DOE/ER-0046/8
Vol. 1

Damage Analysis and Fundamental Studies

Quarterly Progress Report
Oct-Dec 1981

February 1982

U.S. Department of Energy
Assistant Secretary for Energy Technology
Office of Fusion Energy
Washington, DC 20545

DISCLAIMER

NOTICE

Printed in the United States of America
Available from
National Technical Information Service
U.S. Department of Commerce
5285 Port Royal Road
Springfield, VA 22161

NTIS price codes
Printed copy: A 12
Microfiche copy: A01

DOE/ER-0046/8
UC-20,20c
Vol. 1

DOE/ER--0046/8 Vol. 1

DE82 013572

Damage Analysis and Fundamental Studies

Quarterly Progress Report
Oct-Dec 1981

February 1982

U.S. Department of Energy
Assistant Secretary for Energy Technology
Office of Fusion Energy
Washington, DC 20545

PREFACE

This two-volume report contains two special contributions. Appended to Volume 1 is a critical assessment of the role of charged particle research in the Damage Analysis and Fundamental Studies (DAFS) program, prepared by several DAFS program participants under the leadership of G. R. Odette. Volume 2 contains the proceedings of a workshop on advanced experimental techniques for radiation damage analysis arranged under the DAFS program by P. Wilkes, F. V. Nolfi and J. A. Spitznagel. The participation of the various contributors, most of whom were not working on Office of Fusion Energy programs, is gratefully acknowledged.

FOREWORD

This report is the sixteenth in a series of Quarterly Technical Progress Reports on Damage Analysis and Fundamental Studies (DAFS), which is one element of the Fusion Reactor Materials Program, conducted in support of the Magnetic Fusion Energy Program of the U. S. Department of Energy (DOE). The first eight reports in this series were numbered DOE/ET-0065/1 through 8. Other elements of the Materials Program are:

- Alloy Development for Irradiation Performance (ADIP)
- Plasma-Materials Interaction (PMI)
- Special Purpose Materials (SPM).

The DAFS program element is a national effort composed of contributions from a number of National Laboratories and other government laboratories, universities, and industrial laboratories. It was organized by the Materials and Radiation Effects Branch, Office of Fusion Energy, DOE, and a Task Group on Damage Analysis and Fundamental Studies, which operates under the auspices of that Branch. The purpose of this series of reports is to provide a working technical record of that effort for the use of the program participants, the fusion energy program in general, and the DOE.

This report is organized along topical lines in parallel to a Program Plan of the same title so that activities and accomplishments may be followed readily, relative to that Program Plan. Thus, the work of a given laboratory may appear throughout the report. The Table of Contents is annotated for the convenience of the reader.

This report has been compiled and edited under the guidance of the Chairman of the Task Group on Damage Analysis and Fundamental Studies, D. G. Doran, Hanford Engineering Development Laboratory (HEDL). His efforts, those of the supporting staff of HEDL, and the many persons who made technical contributions are gratefully acknowledged. M. M. Cohen, Materials and Radiation Effects Branch, is the DOE counterpart to the Task Group Chairman and has responsibility for the DAFS Program within DOE.

D. L. Vieth, Chief
Materials and Radiation Effects Branch
Office of Fusion Energy

THIS PAGE

WAS INTENTIONALLY

LEFT BLANK

CONTENTS

CONTENTS (Cont'd)

CONTENTS (Cont'd)

CONTENTS (Cont'd)

FIGURES

FIGURES (Cont'd)

FIGURES (Cont'd)

FIGURES (Cont'd)

FIGURES (Cont'd)

FIGURES (Cont'd)

TABLES

TABLES (Cont'd)

CHAPTER 1

IRRADIATION TEST FACILITIES

THIS PAGE

WAS INTENTIONALLY

LEFT BLANK

RTNS-II IRRADIATIONS AND OPERATIONS

C. M. Logan and D. W. Heikkinen (Lawrence Livermore National Laboratory)

1.0 Objective

The objectives of this work are operation of OFE's RTNS-II (a 14-MeV neutron source facility), machine development, and support of the experimental program that utilizes this facility. Experimenter services include dosimetry handling, scheduling, coordination, and reporting. RTNS-II is dedicated to materials research for the fusion power program. Its primary use is to aid in the development of models of high-energy neutron effects. Such models are needed in interpreting and projecting to the fusion environment engineering data obtained in other neutron spectra.

2.0 Summary

Irradiations were performed on a total of five different experiments. The 50-cm target assembly was installed. Also installed was the modified two zone furnace from HEDL. Unscheduled outage of three weeks occurred due to unexpected problems with the 50-cm target assembly.

3.0 Program

Title: RTNS-II Operations (WZJ-16)
Principal Investigator: C. M. Logan
Affiliation: Lawrence Livermore National Laboratory

4.0 Relevant DAFS Program Plan Task/Subtask

TASK II.A.2,3,4.
TASK II.B.3,4
TASK II.C.1,2,6,11,18.

5.1 Irradiations-C. M. Logan, D. W. Heikkinen and M. W. Guinan (LLNL)

An irradiation of mica samples for J. Fowler (LANL) was completed. An in-situ creep experiment using a Ni sample was done for W. Barmore (LLNL). D. Nethaway (LLNL) irradiated a radioactive target of ^{168}Tm for a cross section measurement. The irradiation for N. Panayotou (HEDL) using the modified two zone furnace continued and was the major user of time during this quarter. A "piggyback" irradiation employing a rabbit system was done for R. Mallon (LLNL). Oil shale activities were measured.

5.2 RTNS-II Status-C. M. Logan and D. W. Heikkinen

During this quarter the new design HEDL furnace and the 50-cm target assembly were installed. The 50-cm target assembly had been tested for ~300 hours with no problems encountered. However, after ~100 hours of operation, problems occurred with the target water feed hub and the rotating vacuum seal. This resulted in approximately three weeks of unscheduled outage. The target problems are under investigation.

6.0 Future Work

Irradiations are scheduled for H. Vonach (Vienna), R. Borg (LLNL), G. Woolhouse (ARACOR, Inc.), D. Kaletta (Karlsruhe), R. Mallon (LLNL), N. Panayotou (HEDL), R. VanKonynenberg (LLNL) and C. Snead (BNL).

7.0 Publications

Stress Calculations for RTNS-II 50-cm Targets, B. J. Schumacher and P. A. House (UCRL 53148)

RTNS-II Targets: Cooling Channel Collapse Under Simulated Bonding Conditions, W. D. Ludemann, R. L. Brady and B. J. Schumacher (UCRL 53206)

Analysis of Bond-Failures in RTNS-II Targets, W. D. Ludemann, G. A. Harter and B. J. Schumacher (UCRL 53184)

NUCLEAR DATA FOR DAMAGE STUDIES AND FMIT (AVC)

D. L. Johnson and F. M. Mann (Hanford Engineering Development Laboratory)

1.0 Objective

The objective of this work is to supply nuclear data needed for damage studies and in the design and operation of the Fusion Materials Irradiation Testing (FMIT) Facility.

2.0 Summary

Estimates were made of damage and heating rates that might occur in the FMIT target backing plate due to protons created in the lithium target which penetrate to the plate. The upper limits of proton-induced damage and heating rates are comparable at the surface of the backing plate to estimated neutron-induced rates. This indicates that proton effects should be included in a comprehensive analysis of the behavior of the backing plate.

3.0 Program

Title: Nuclear Data for Damage Studies and FMIT (WH025/EDK)
Principal Investigators: D. L. Johnson and F. M. Mann
Affiliation: Hanford Engineering Development Laboratory

4.0 Relevant DAFS Program Plan Task/Subtask

All tasks that are relevant to FMIT use, with emphasis upon:

Subtask	II.A.2.3	Flux Spectra Definition in FMIT
Task	II.A.4	Gas Generation Rates
Subtask	II.A.5.1	Helium Accumulation Monitor Development
Subtask	II.B.1.2	Acquisition of Nuclear Data

5.0 Accomplishments and Status

5.1 Estimates of Proton-Induced Damage and Heating Rates in the FMIT Target Backing Plate

5.1.1 Introduction

The Fusion Materials Irradiation Test (FMIT) Facility is currently being designed for use in the study of neutron radiation effects in fusion reactor materials. The facility will make use of the intense source of high energy neutrons produced by a 100-mA beam of 35-MeV deuterons incident upon a thick target of liquid lithium. The deuterons stop in about 15 mm whereas the lithium is 19 mm thick and is backed by a stainless steel plate 1.6 mm thick.

The backing plate will experience the highest neutron-induced damage and heating rates of the target structure. These effects are being reviewed for a comprehensive analysis of the behavior of the backing plate. Protons will also be produced in the lithium and some will have enough energy to penetrate to the backing plate. The objective of this work was to establish whether or not proton induced effects need to be included with neutron induced effects in estimating the behavior of the backing plate in the high radiation field.

5.1.2 Evaluation of Proton Flux Incident Upon the Backing Plate

In the forward direction, the neutron spectrum from the FMIT source peaks near 14 MeV as in a fusion device. However, in the FMIT facility, the neutron energy spectrum will be much broader and there will be a significant number of neutrons emitted with energies up to about 30 MeV. A small fraction will be emitted with even higher energies, up to a maximum of 50 MeV. An evaluation of the neutronic characteristics of this source and calculations of displacement damage and helium production that would result are presented in Reference 1.

High energy protons will also be produced in the lithium target via reactions with the incident deuterons. There are few experimental data on proton production

by deuterons of the appropriate energies incident upon lithium. For scoping estimates, it can be assumed that the yield, spectra and angular distributions of most of the protons emitted following reactions with monoenergetic deuterons are the same as the the neutrons emitted. However, there are significant differences expected between neutrons and protons emitted at the extreme upper ends of the spectra where, for neutrons, the yield is relatively small. In this regime, monoenergetic deuterons produce sharply peaked neutron and proton spectra due to reactions leading to long-lived states of the residual nuclei. However, there are more peaks in the proton spectra than in the neutron spectra and their magnitudes and energies are different. The highest energy neutron peak is about 10 MeV above the highest energy proton peak for the same deuteron energy.

The flux of protons that penetrate to the backing plate was estimated by assuming that the protons were created with the same characteristics as the neutrons except at the extreme upper end of the spectrum. There, the maximum proton energy was assumed to be 10 MeV less than the maximum neutron energy for monoenergetic deuterons and details of the upper portions of the spectra were neglected. The initial proton yield and spectra depend upon the penetration depth in the lithium because the residual deuteron energy decreases with depth. It was found that only the upper end of the initial proton spectrum for each particular depth could penetrate through the remaining lithium to the backing plate. For example, at the front surface of the lithium, the 35-MeV deuterons produce a proton spectrum up to 40 MeV, but only protons greater than 29 MeV can penetrate through 19 mm of lithium to the backing plate.

The proton flux that penetrates to the backing plate was found to be somewhere between an upper limit of about 5% of the neutron flux and a lower limit of about 1%. The highest neutron flux on the backing plate is calculated to be about 3×10^{15} n/cm^2-sec. Hence, the upper limit of the proton flux is 1.5×10^{14} protons/cm^2-sec ($\sim$24 μA/cm^2).

The proton spectrum that is incident upon the backing plate is quite different from the neutron spectrum because of energy losses of the protons in the lithium.

The maximum proton energy incident upon the backing plate is only about 24 MeV. The spectrum on the plate is not accurately known since the upper portions of the initial proton spectra are not know. It was roughly estimated to decrease linearly with increasing proton energy to zero at 24 MeV.

5.1.3 Formalism for Evaluation of Proton Induced Damage and Heating Rates

At a particular point within the backing plate, the displacement rate, helium production rate and heating rate can be expressed in the following equations which are analogous to those used for calculations of neutron induced damage and heating. However, special provisions are needed to treat the rapid variations of the spatial and energy dependence of the proton flux in the backing plate.

$$\text{dpa/sec} = \int \sigma_d(E_p)\ \phi_p(E_p) dE_p \tag{1}$$

$$\text{appm He/sec} = 10^{-6} \int \sigma_{He}(E_p)\ \phi_p(E_p) dE_p \tag{2}$$

$$\text{watts/gram} = 1.602(10^{-13}) \int \frac{dE}{d\rho x}(E_p)\ \phi_p(E_p) dE_p \tag{3}$$

Here, $\phi_p(E_p)$ is the flux spectrum of protons (p/cm^2-s-MeV) for a particular location within the backing plate, $\sigma_d(E_p)$ is the displacement cross section (cm^2/atom), $\sigma_{He}(E_p)$ is the helium production cross section, and $dE(E_p)/d\rho x$ is the energy loss per unit path length (units of MeV/(gm/cm^2)) as a function of energy for protons in the backing plate material. The local density of the material is ρ(gm/cm^3) and dx is an increment of path length (cm).

Using the flux spectrum of protons that was estimated to be incident upon the surface of the backing plate, the proton flux was evaluated as a function of penetration depth. This was done using the BRAGG [2] code which calculates the residual energy and relative flux as a function of penetration for charged particles incident upon a material. It makes use of the well known energy dependence of the stopping power for charged particles on materials.

5.1.4 Evaluation of Displacement Rates

The displacement cross section for protons on stainless steel was assumed to be the same as that associated with Rutherford scattering of protons by iron. This cross section is very large for low energy protons and decreases roughly as 1/E for increasing proton energies. The methods for evaluation of such cross sections are described in Reference 3.

It was estimated in earlier work at HEDL that for energies somewhat above the Coulomb barrier for protons on the materials in stainless steel ($\sim$7 MeV) the displacement cross section becomes increasingly larger than that due to Rutherford scattering alone. However, for an incident proton spectrum similar to what was estimated in this work, it can be shown that using the Rutherford displacement cross section is a very good approximation.

Figure 1 shows the displacement rate profiles for monoenergetic protons of 6, 12, 18 and 24-MeV incident upon thick nickel. Here one sees that, for all incident energies, the displacement rate peaks near the end of the proton range where the residual energies are very low and the displacement rate is due exclusively to Rutherford scattering which is known very accurately. Only near the incident surface for monoenergetic protons greater than $\sim$12 MeV is the displacement rate much larger than that predicted for Rutherford scattering alone. However, near the incident surface, the displacement rate profile for a spectrum of incident protons similar to that estimated here will be dominated by contributions from low energy protons which produce displacements by Rutherford scattering.

Note that the energy spectrum of atoms displaced by the protons is much softer than that produced by the neutrons. As a result of this, the number of defects produced per calculated displacement is expected to be larger for the protons than for the neutrons. Recent work in which initial damage rates were measured for a variety of low energy ions suggests an upper limit of a factor of three for this effect. For the present application, a factor of 1.5 to 2 might be appropriate because not all displaced atoms are at low energy. This is consistent

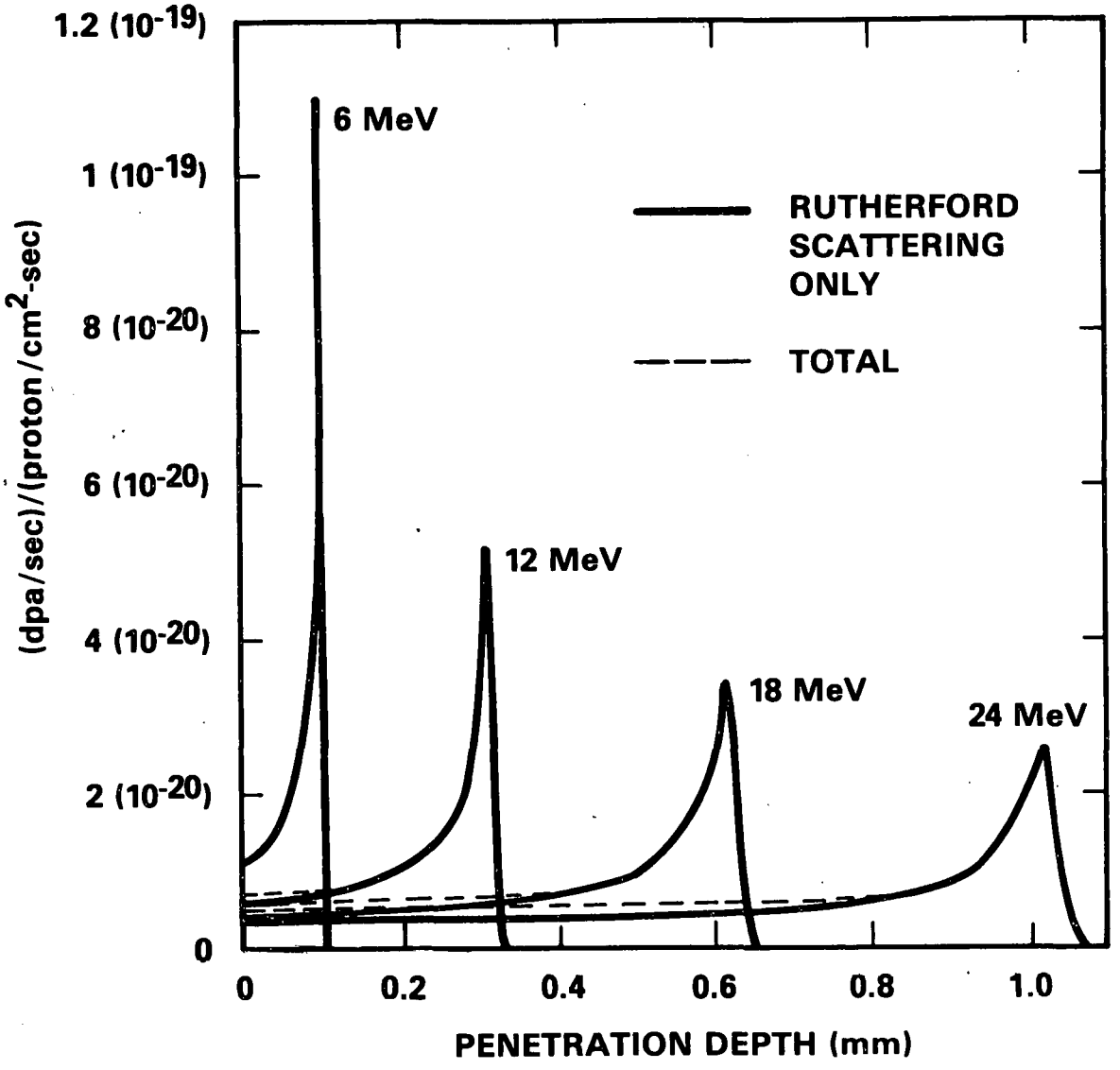

FIGURE 1. Displacement Rate Profiles Versus Penetration Depth for Monoenergetic Protons Normally Incident Upon Thick Nickel.

with an estimate, corroborated by one experiment, of the difference in creep rates produced by neutrons and light ions.[4] For comparison to neutron induced displacements, the effective displacement rate calculated for the protons in this study was increased rather arbitrarily by a factor of two.

The displacement rate profile was evaluated for the estimated proton flux spectrum described earlier. Figure 2 shows the profiles for proton fluxes of 5 and 1% of the neutron flux at the point of highest flux on the backing plate. Also shown is an estimate of the neutron induced displacement rate which was taken from data associated with Reference 1.

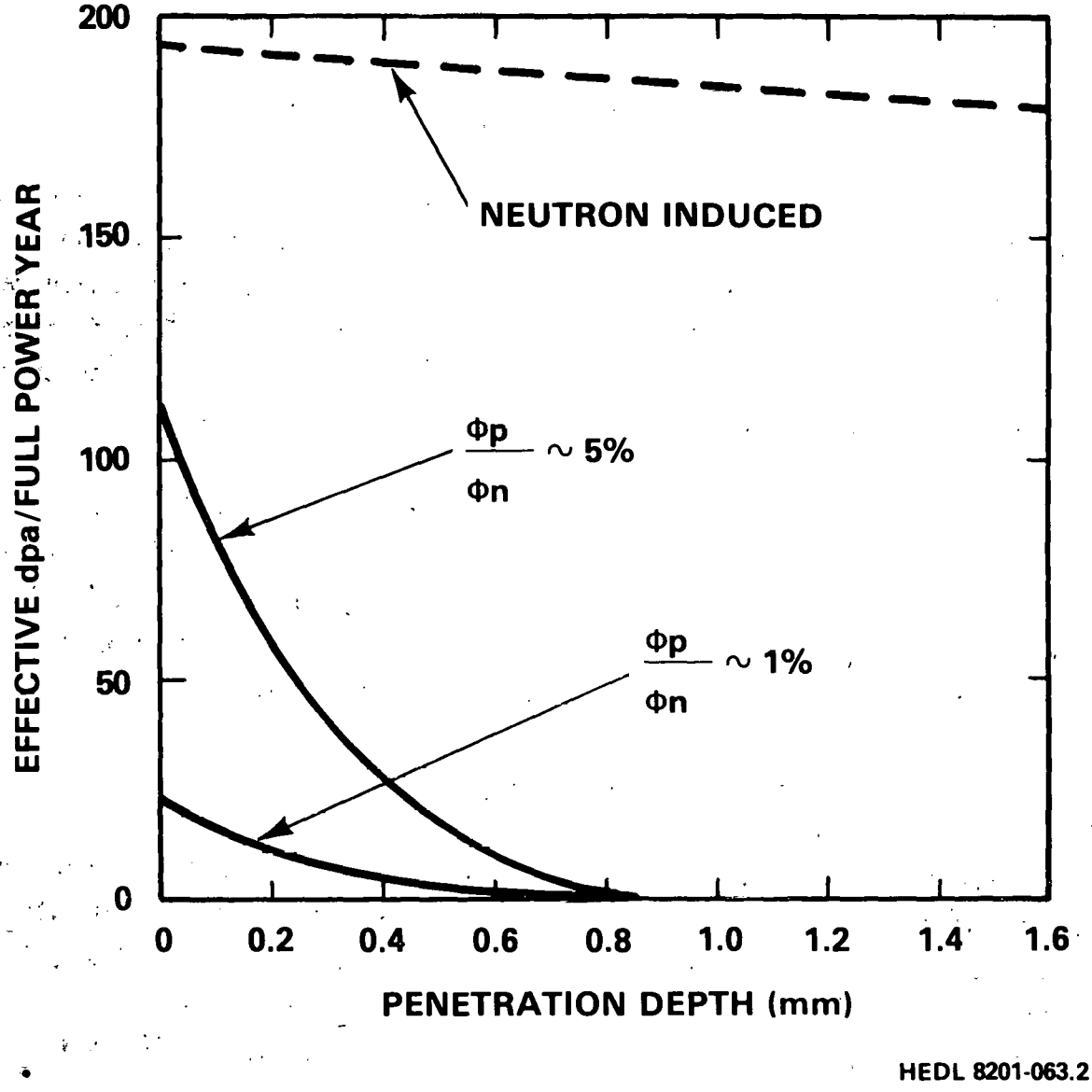

FIGURE 2. Effective Displacement Rate Profiles Versus Penetration Depth for the Estimated Spectrum of Protons Incident Upon the Center of the Backing Plate. Also shown is the neutron-induced displacement rate profile.

Here one sees that at the surface of the backing plate the effective proton induced displacement rate may be as large as ∿120 dpa/full power year. This is comparable to the neutron induced displacement rate of about 190 dpa/full power year. However, the effective proton induced displacement rate rapidly drops to zero about halfway through the 1.6 mm thickness of the backing plate. Thus the sum of the neutron and proton induced displacement rate profiles has a significant gradient.

5.1.5 Evaluation of Helium Production Rates

Figure 3 shows the helium production rate profiles along the centerline (highest flux location) of the backing plate for proton fluxes of 5 and 1% of the neutron flux. Also shown is an estimate of the neutron-induced helium production rate. The proton-induced helium production cross section was obtained from data in Reference 5 and is shown in Figure 4. The profiles were obtained using this cross section plus an estimated 50% (2σ) uncertainty.

One sees that the proton-induced helium production rate may be as large as about 420 appm He/full power year at the surface of the backing plate. However, this is only about 20% of the neutron-induced helium production rate (∿2000 appm He/full power year). Hence, the proton induced helium production does not seem to be very significant compared to the neutron induced rate.

5.1.6 Evaluation of Heat Deposition Rates

Figure 5 shows the heating rate profiles along the centerline of the backing plate for proton fluxes of 5 and 1% of the neutron flux. The heating rate profiles for monoenergetic incident protons were obtained from the BRAGG [2] code and are similar in shape to the displacement rate profiles shown in Figure 1. Also shown in Figure 5 is an estimate of the neutron-induced heating rate.

Here one sees that, at the surface of the backing plate, the proton-induced heating rate may be as large as about 900 watts/gram. This far exceeds the

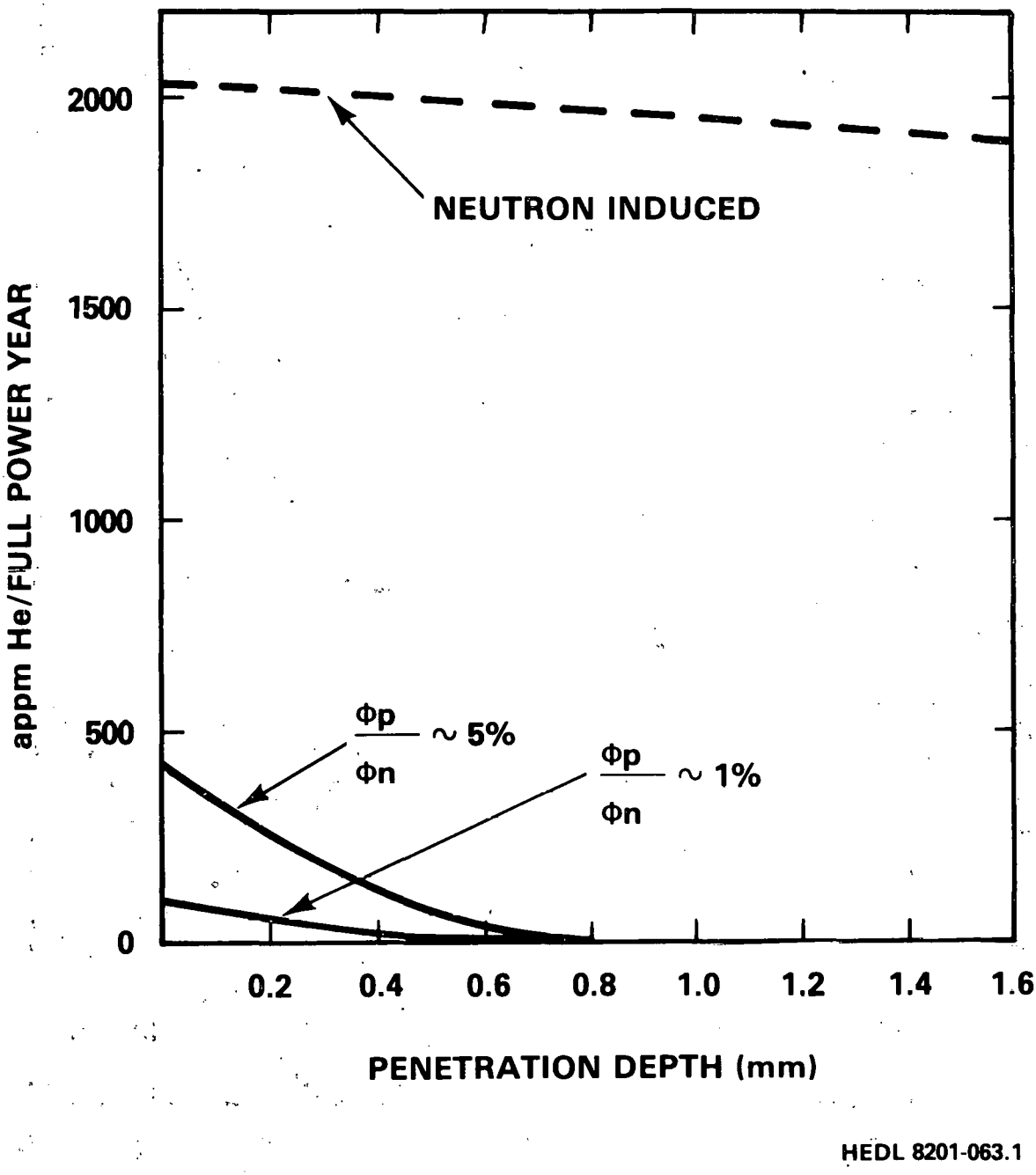

FIGURE 3. Helium Production Rate Profiles for the Estimated Spectrum of Protons Incident Upon the Center of the Backing Plate. Also shown is the neutron-induced profile.

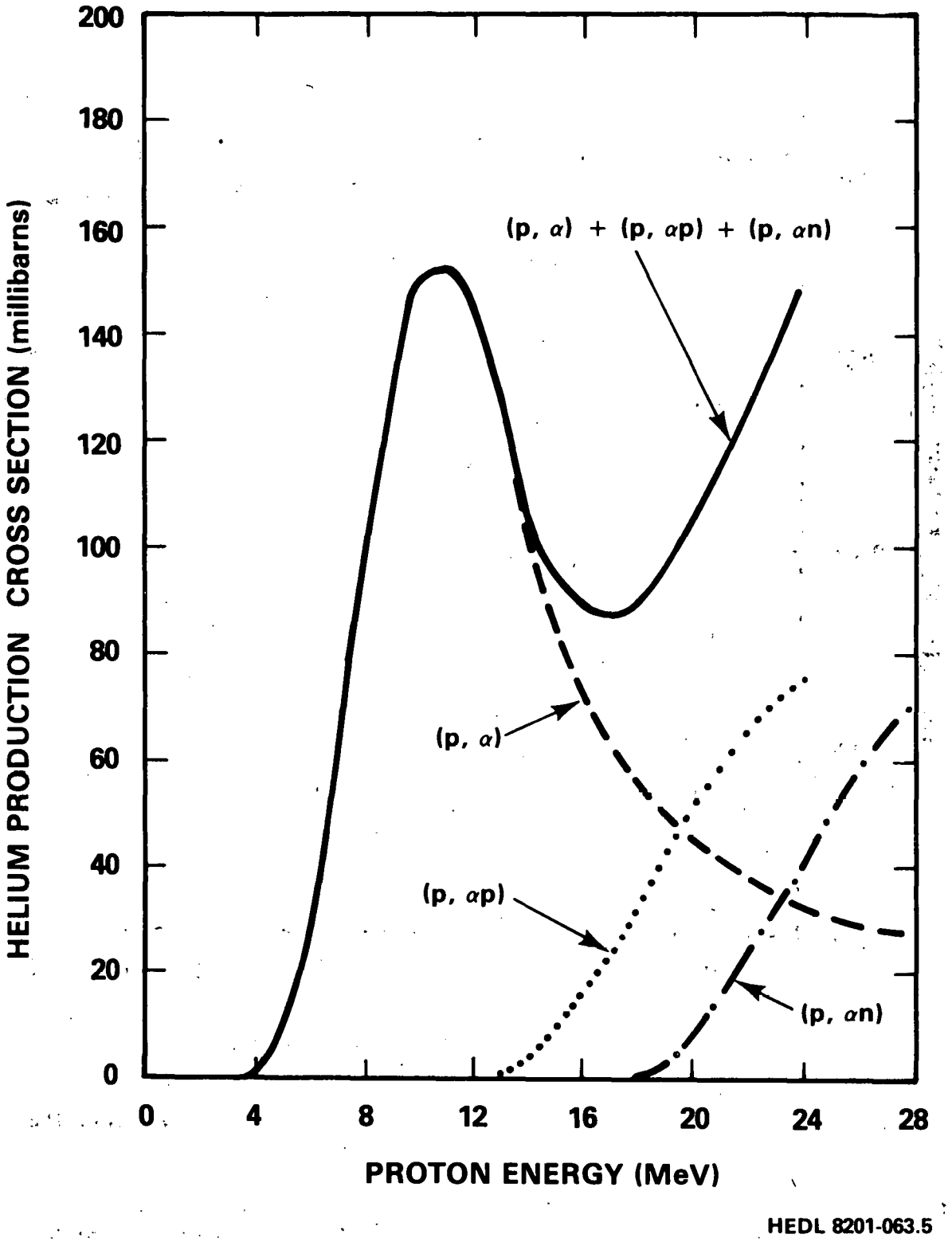

FIGURE 4. Estimated Helium Production Cross Section for Protons on Stainless Steel.

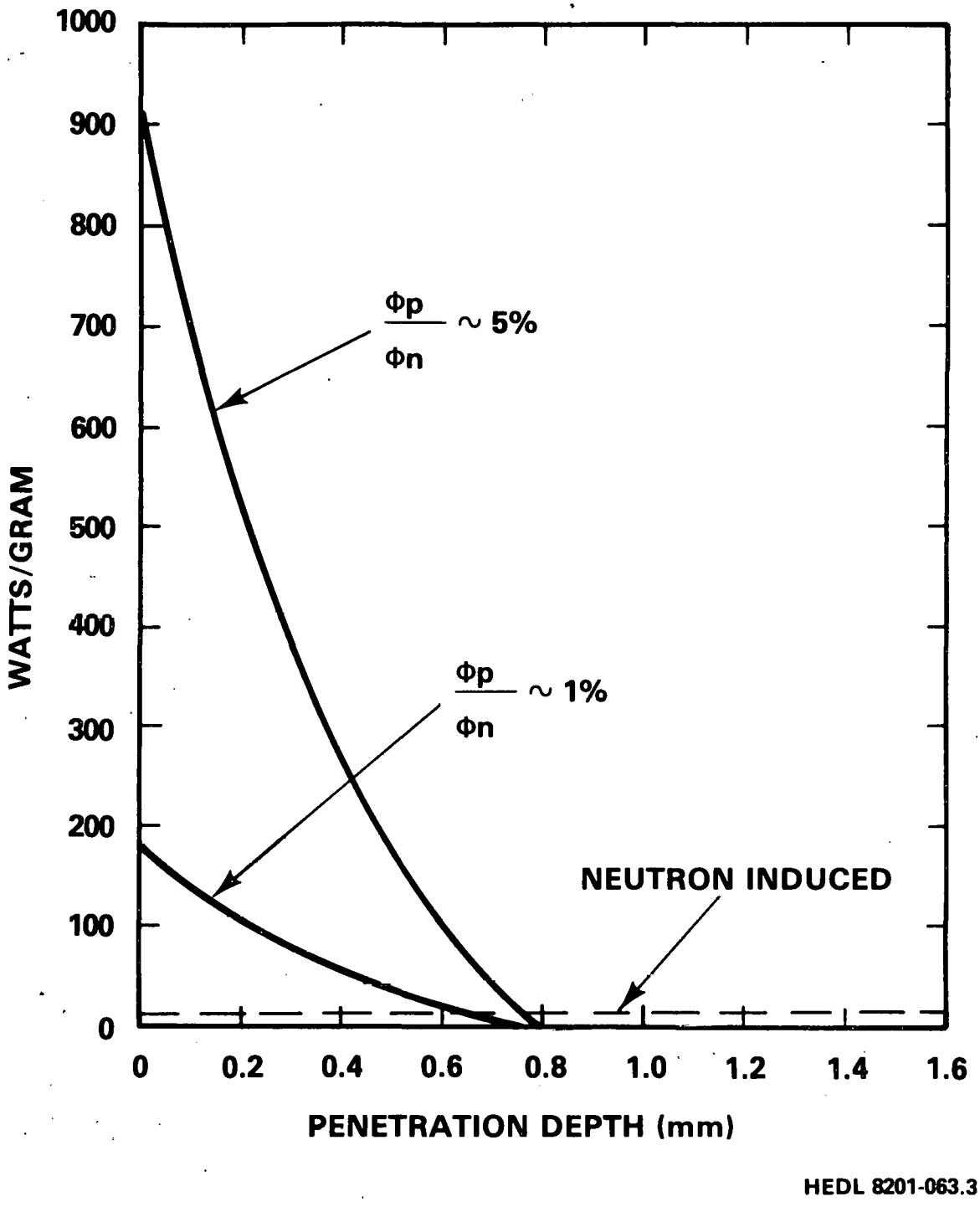

FIGURE 5. Heating Rate Profiles Versus Penetration Depth for the Estimated Spectrum of Protons Incident Upon the Center of the Backing Plate. Also shown is the neutron-induced rate profile.

neutron-induced rate of about 10 watts/gram. However, the proton-induced heating rate rapidly drops to zero about halfway through the backing plate just as the displacement rate does.

5.1.7 Conclusions

It appears that at the surface of the backing plate the upper limit of the proton-induced heating rate far exceeds the neutron rate and that the proton-induced displacement rate is comparable to the neutron rate. Therefore, it is likely that proton effects must be included in the analysis of the behavior of the backing plate during irradiation in the FMIT facility.

6.0 References

1. F. M. Mann, F. A. Schmittroth and L. L. Carter, "Neutron Environment in d + Li Facilities," Symposium on Neutron Cross Sections from 10 to 50 MeV, Brookhaven National Laboratory, May 12-14, 1980, BNL-BCS-51245, July 1980, pp. 517-537.

2. G. M. Litton, "Program BRAGG, a FORTRAN-IV Program for Calculating Bragg Curves and Flux Distributions," UCRL-17391, February 1967.

   G. M. Litton, J. Lyman and C. A. Tobias, "Penetration of High Energy Heavy Ions with the Inclusion of Coulomb, Nuclear and Other Stochastic Processes," UCRL-17392, Rev. 1, May 1968.

3. D. G. Doran, J. R. Beeler, Jr., N. D. Dudey and M. J. Fluss, "Report of the Working Group on Displacement Models and Procedures for Damage Calculations," HEDL-TME 73-76, December 1973.

4. T. C. Reilly and P. Jung, "The Simulation of Irradiation Creep," in Radiation Effects in Breeder Reactor Structural Materials, M. L. Bleiberg and J. W. Bennett (Eds.), AIME, 1977, p. 295.

5. K. A. Keller, J. Lange and J. Münzel, "Estimation of Unknown Excitation Functions and Thick Target Yields for p, d, ^{3}He and α Reactions," Landolt-Börnstein, Group I, Volume 5, Part C, Sprtinger-Verlag, Berlin-Heidelberg-New York, 1974.

CHAPTER 2

DOSIMETRY AND DAMAGE PARAMETERS

THIS PAGE

WAS INTENTIONALLY

LEFT BLANK

FISSION REACTOR DOSIMETRY

L. R. Greenwood (Argonne National Laboratory)

1.0 Objective

To establish the best practicable dosimetry for fission reactors and to provide dosimetry and damage analysis for OFE experiments.

2.0 Summary

Final results are presented for the ORR-MFE4A experiments. Samples have been counted from HFIR-CTR32.

3.0 Program

Title: Dosimetry and Damage Analysis

Principal Investigator: L. R. Greenwood

Affiliation: Argonne National Laboratory

4.0 Relevant DAFS Program Plan Task/Subtasks

Task II.A.1 Fission Reactor Dosimetry

5.0 Accomplishments and Status

The status of all fission reactor dosimetry is given in Table 1.

5.1 Dosimetry Results for the ORR-MFE4A Experiment

Preliminary dosimetry results were reported for the MFE4A experiment in ORR in our August 1981 Quarterly Report (DOE/ER-0046/6). The irradiation was

conducted between June 12, 1980 and January 20, 1981 with an exposure of 5471 MWD. Dosimetry wires were provided by ORNL; additional wires were also provided by ANL and are still being irradiated.

TABLE 1

STATUS OF REACTOR EXPERIMENTS

Facility/Experiment	Status/Comments
ORR - MFE1	Completed 12/79
- MFE2	Completed 6/81
- MFE4A	Completed 12/81
- MFE4B,C	Irradiation in Progress
- TBC07	Completed 7/80
- TRIO	Test Planned 1/82
HFIR - CTR 32	Samples Counted 12/81
- CTR 30, 31	Irradiation in Progress
- CTR 34, 35	Samples Provided 9/81
- T1,T2,T3	Irradiation in Progress
- RB1,RB2,RB3	Samples Provided 9/81
Omega West - Spectral Analysis	Completed 10/80
- HEDL1	Completed 5/81
EBR II - X287	Completed 9/81
IPNS - LASL1 (Hurley)	Planned for 2/82

One problem noted in our previous analysis was that the cobalt samples indicated a higher thermal flux than the iron samples. This was contrary to our previous experience where cobalt and iron were always in excellent agreement. Since the cobalt samples were in the form of a new Co-V alloy provided by ORNL, we requested a simultaneous activation experiment in the HFIR rabbit tube with our Co-Al alloys. The results of this experiment are listed in Table 2.

TABLE 2

COBALT-ALLOY ACTIVATION TESTS IN HFIR

Sample (Source)	% Co	Relative Activity
Co-Al (NBS)	0.116 ± 0.002	1.000
Co-Al (RE)	0.504	0.957
Co-V (ORNL)	0.085	1.156

As can be seen, the Co-V activity is much too high. If we adopt the NBS sample as a standard (since the others have no certifiable error analysis), then the Co-V alloy contains 0.098% cobalt rather than the 0.085% cobalt analysis by ORNL. This difference is very close to that reported in our earlier report where the ratio of cobalt to iron thermal flux was 1.142. The $^{59}Co(n,\gamma)^{60}Co$ activity rate for ORR-MFE4A would thus be reduced to 6.20×10^{-9} atoms/atom-sec. The ratio to the MFE2 experiment is 1.040 compared to 1.053 for $^{58}Fe(n,\gamma)^{59}Fe$. We thus conclude that the ORNL cobalt analysis is

incorrect and that the cobalt and iron monitors now measure the same thermal flux, as expected from previous experiments in ORR. Since we assumed that the iron values were correct and rejected the old Co-V activities, no changes are required in the thermal flux values for ORR which we reported previously.

Since the flux wires were located near the maximum flux position in ORR it was expected that the gradients would be rather flat along the 6" sections of dosimetry wire. Whereas the fast flux was indeed found to be flat within a few percent, disturbing oscillations were found in the thermal values. A second nickel wire was thus cut into uniform 1/2" long sections to study these thermal gradients in more detail. The results are listed in Table 3.

The gradients in Table 3 show that the ^{58}Co decreases near the top while the ^{60}Co increases and the ^{57}Co is nearly flat. These trends can be explained by changes in the thermal flux since ^{58}Co is converted to ^{60}Co. The flat ^{57}Co trend means that the fast neutron flux gradient is quite small, <7% over 6", <2% over the top 5". The increase in the thermal flux near the top of the wire is also seen in helium measurements by Rockwell International (DOE/ER-0046/7 - p. 26). The helium gradient is steeper than our changes in the nickel since helium depends on the thermal flux squared in a two-step reaction. This unusual behavior in the thermal flux gradient is probably due to neutron shadowing by the experimental assemblies. However, the net effect is rather unimportant ($\sim$5% in thermal flux, $\sim$10% in He production in nickel).

In conclusion, the fluences reported earlier still appear to be accurate and our predictions of helium production in nickel are in excellent agreement with

TABLE 3

NICKEL ACTIVITY GRADIENTS FOR ORR-MFE4A
$\sigma\phi$ (ATOM/ATOM-S)

	$^{58}Ni(n,p)^{58}Co$	$^{60}Ni(n,p)^{60}Co$	$^{58}Ni(n,np)^{57}Co$
Sample	(x 10^{-12})	(x 10^{-13})	(x 10^{-14})
1-Bottom	3.99	5.14	2.24
2	4.00	5.31	2.29
3	3.98	5.54	2.34
4	3.99	5.60	2.35
5	4.06	5.55	2.38
6	4.01	5.67	2.37
7	4.03	5.61	2.35
8	4.03	5.55	2.37
9	3.99	5.71	2.39
10	3.91	5.80	2.35
11-Top	3.85	5.89	2.38

measurements at Rockwell International. However, the radiometric and helium values are still about 30% lower than neutronic calculations made by ORNL (Gabriel and Lillie).

6.0 References

None.

7.0 Future Work

Further measurements are planned in the MFE4B and C experiments. More complete dosimetry sets will also be analyzed at the end of the MFE4 experiment.

Samples have been counted from the HFIR-CTR32 experiment. Test experiments will be conducted in ORR for the TRIO tritium-breeding experiment in January. Some insulator materials will be irradiated at IPNS at cryogenic temperatures in February.

8.0 Publications

None.

CHARACTERIZATION OF SPALLATION NEUTRON SOURCES

L. R. Greenwood (Argonne National Laboratory)

1.0 Objective

To characterize the neutron flux, spectrum, and damage parameters for spallation neutron sources.

2.0 Summary

The Neutron Scattering Facility (NSF) of the Intense Pulsed Neutron Source (IPNS) has been characterized for radiation damage experiments. As expected, the spectrum is softer and damage rates are lower than in the Radiation Effects Facility (REF); however, longer exposure times will be possible at the NSF. The first fusion materials irradiations are planned for February 1982.

3.0 Program

Title: Dosimetry and Damage Analysis

Principal Investigator: L. R. Greenwood

Affiliation: Argonne National Laboratory

4.0 Relevant DAFS Program Plan Task/Subtasks

Task II.A.2 High-Energy Neutron Dosimetry

5.0 Accomplishments and Status

The Intense Pulsed Neutron Source (IPNS) at ANL became operational in July 1981 and dosimetry experiments were conducted in the Radiation Effects Facility (REF) which has a ^{238}U target surrounded by a lead reflector. Neutrons are generated from spallation reactions by a 400-500 Mev proton beam of about 8 μA. The total neutron flux was measured to be 1.6×10^{12} n/cm^2-s (1.0 x 10^{12} above 0.1 MeV). Spectral measurements, gradients, and damage rates were reported last quarter (DOE/ER-0046/7).

Since the IPNS devotes most of the operational time to the Neutron Scattering Facility (NSF) it was decided to also characterize this facility for damage experiments. Two holes are available near the target (named H2 and F6), although the holes are not instrumented at present. Dosimetry packages were irradiated from September 23 to October 2, 1981 for a total exposure of 7.73 x 10^{18} protons on target.

Twenty-five activation reactions were measured using Ge(Li) gamma spectroscopy. The STAYSL computer code was then used to adjust the neutron spectrum which was crudely based on neutronics calculations. The low energy flux was estimated from calculations with Be moderators only roughly similar to the configuration in the NSF.

The unfolded neutron spectrum is shown in Figure 1 and compared to the REF in Figure 2. The spectrum in the NSF is clearly much softer than in the REF, especially below 0.1 MeV. However, the total neutron flux is roughly the same. This difference is due to the Be moderator in the NSF compared to a Pb

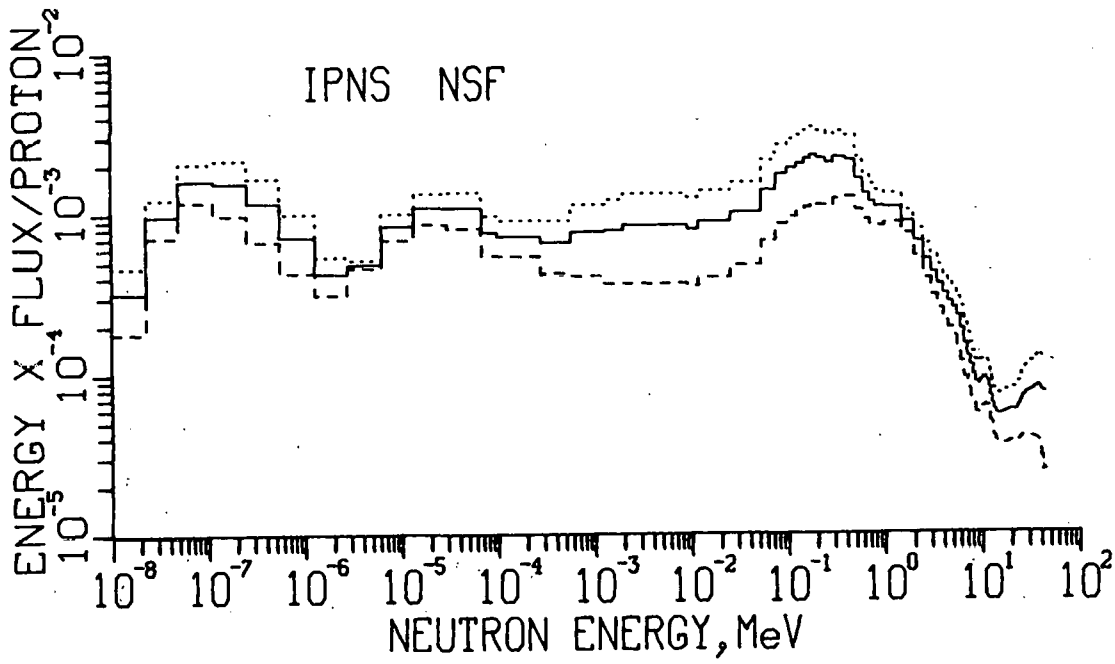

FIGURE 1. Neutron Energy Spectrum for Position H2 of the IPNS-NSF. The dotted and dashed lines represent one standard deviation for each energy group. The flux above 44 MeV is not shown.

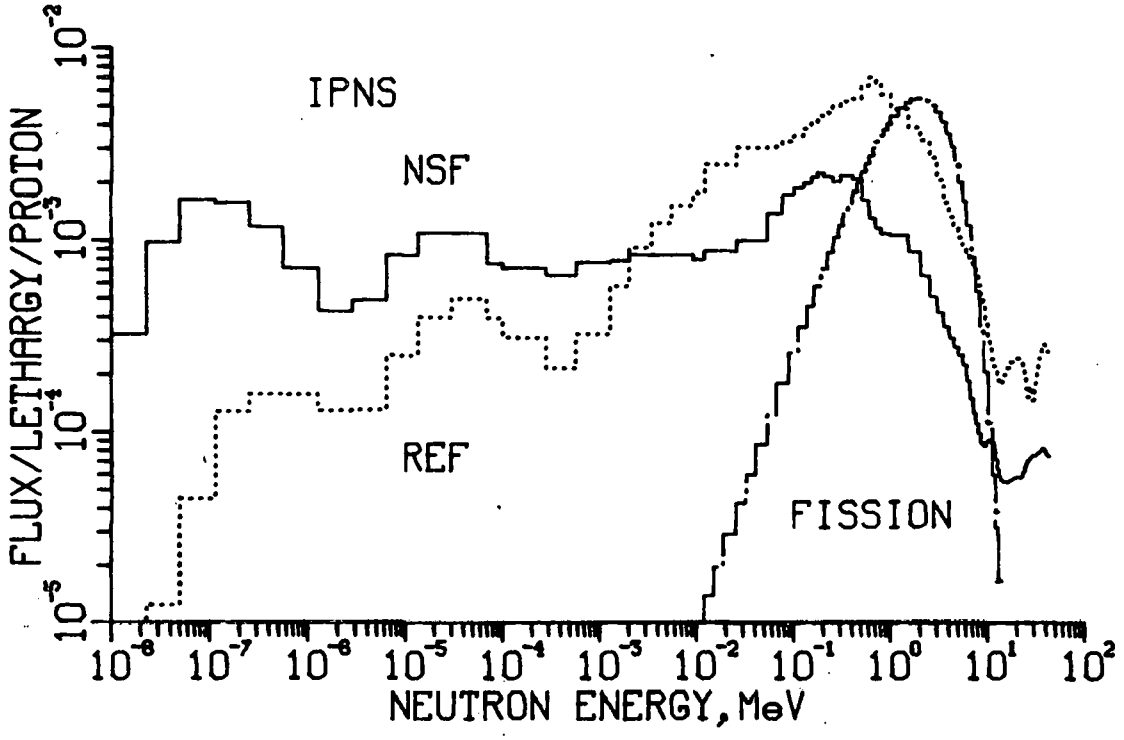

FIGURE 2. Spectra are Compared for the IPNS-REF (VT2), NSF (H2), and a Pure Fission Spectrum. The NSF spectrum is much softer than the REF, although the total integral flux is comparable.

reflector in the REF. In very crude terms, neglecting very high-energy neutrons, the REF spectrum resembles a fast reactor like EBR II whereas the NSF spectrum is more like a mixed-spectrum reactor like ORR.

Flux values are reported for both facilities in Table 1. The total flux in the NSF is about 67% of that in the REF; however, the fast flux (>0.1 MeV) is only 30% of the REF while the thermal flux is 17.6 times higher. Since the H2 and F6 sample tubes point directly in towards the target, gradients need only be measured along the tube. The fast flux (>0.1 MeV) was found to decrease a factor of two in a distance of two inches going away from the target. Spectral gradients were not measured, although it is assumed that experimenters would place samples as close to the target as possible in the 5/8" O.D. sample tube.

6.0 References

None.

7.0 Future Work

The first fusion materials experiment will be conducted by G. Hurley (LANL) during February or March of 1982. Organic insulators will be irradiated at cryogenic temperatures. Since gamma exposure is also of interest, heating and TLD measurements are now being made and compared to calculations.

8.0 Publications

1. M. A. Kirk, R. C. Birtcher, T. H. Blewitt, L. R. Greenwood, R. J. Popek, and R. R. Heinrich, Journal Nucl. Mater. 96, 37 (1981).

TABLE 1

INTEGRAL FLUX RATES FOR IPNS

A proton current of 8 μA at 500 MeV is assumed.

Percent standard deviations are given in parenthesis.

Energy Range	NSF (H2)		REF (VT2)		Ratio
	(x 10^{11})		(x 10^{11})		(NSF/REF)
Total	10.5	(12)	15.6	(13)	0.67
>0.1 MeV	2.97	(22)	9.92	(17)	0.30
Thermal	2.37	(17)	0.135	(17)	17.6
0.5 eV-0.1 MeV	5.18	(18)	5.60	(23)	0.92
0.1-1 MeV	2.27	(27)	6.79	(25)	0.34
1-5	0.58	(11)	2.64	(11)	0.22
5-10	0.056	(24)	0.29	(23)	0.20
10-15	0.016	(14)	0.048	(19)	0.32
15-20	0.0086	(21)	0.036	(23)	0.24
20-30	0.014	(25)	0.043	(15)	0.32
30-44	0.016	(28)	0.049	(26)	0.34
>44	∿0.038[a]		∿0.11[a]		

[a]Estimated from neutronics calculations.

HELIUM GENERATION CROSS SECTIONS FOR 14.8-MeV NEUTRONS

B. M. Oliver, D. W. Kneff, M. M. Nakata, and H. Farrar IV (Rockwell International, Energy Systems Group)

1.0 Objective

The objectives of this work are to measure helium generation rates of materials for Magnetic Fusion Reactor applications in the ~14.8-MeV T(d,n) neutron environment, to characterize the T(d,n) neutron field of the Rotating Target Neutron Source-II (RTNS-II), and to develop helium accumulation neutron dosimeters for this test environment.

2.0 Summary

The total helium generation cross sections have been measured for the pure elements Si, Co, Sn, and Pt, irradiated by ~14.8-MeV T(d,n) neutrons at RTNS-II.

3.0 Program

Title: Helium Generation in Fusion Reactor Materials
Principal Investigators: D. W. Kneff and H. Farrar IV
Affiliation: Rockwell International, Energy Systems Group

4.0 Relevant DAFS Program Plan Task/Subtask

Subtask II.A.2.2 Flux-Spectral Definition in RTNS-II
Subtask II.A.4.2 T(d,n) Helium Gas Production Data

5.0 Accomplishments and Status

Total helium generation cross section measurements have been completed for Si, Co, Sn, and Pt, irradiated in the ~14.8-MeV T(d,n) neutron spectrum of

RTNS-II. The irradiation was a joint experiment with Argonne National Laboratory (ANL) and Lawrence Livermore National Laboratory (LLNL), and both the experiment and previous cross section measurements have been detailed in earlier reports.[1,2] The cross sections were determined by analyzing multiple samples of each material by high-sensitivity gas mass spectrometry for generated helium, and combining the helium results with the neutron fluence at each sample's irradiation position. The fluence values were derived from a neutron fluence map constructed for the irradiation volume, using passive dosimetry incorporated in the experiment. The fluence mapping was supported by the Office of Fusion Energy of the U.S. Department of Energy (DOE), and the cross section measurements were supported by the DOE's Office of Basic Energy Sciences.

The cross section results for these four materials are given in Table 1. The absolute values were normalized to the niobium radiometric foil dosimetry results, for which the $^{93}Nb(n,2n)^{92m}Nb$ cross section was assumed to be 463 ± 19 mb.[3] Most of the ^{4}He measurements had absolute 1σ uncertainties of about 2%. The exception was platinum, whose higher cross section uncertainties were due in part to the significantly lower helium concentrations (~2×10^{-10} atom fraction) in this material. The neutron fluence determinations contributed about 7% to the final cross section uncertainties.

TABLE 1

HELIUM GENERATION CROSS SECTIONS FOR ~14.8-MeV NEUTRONS

Material	Measured Cross Section (mb)	Material	Measured Cross Section (mb)
Si	218 ± 11	Sn	1.5 ± 0.1
Co	40 ± 3	Pt	0.74 ± 0.11

Cobalt is of particular interest for helium accumulation neutron dosimetry. This element has the highest priority for radiometric dosimetry in the Fusion Materials Irradiation Test Facility (FMIT), because several neutron-induced reactions [(n,γ), (n,2n), (n,3n), (n,4n), (n,p)] with different energy responses lead to long-lived radioactive products. Helium accumulation provides an additional dosimetry reaction in the same material with a different energy sensitivity for neutron spectrum unfolding. This can be used to help minimize the number of different materials needed for passive dosimetry. Silicon is of interest for fusion materials as a component of candidate insulators and for optical materials, and tin is a component of candidate superconductors. The platinum cross section was measured to provide a background correction for the analysis of several platinum-encapsulated materials in RTNS-II.

6.0 References

1. D. W. Kneff, B. M. Oliver, M. M. Nakata, and H. Farrar IV, "Characterization of the RTNS-II Neutron Field," in Damage Analysis and Fundamental Studies, Quarterly Progress Report July-September 1980, DOE/ER-0046/3, U.S. Department of Energy, 25 (1980).

2. B. M. Oliver, D. W. Kneff, M. M. Nakata, and H. Farrar IV, "Helium Generation Cross Sections for 14.8-MeV Neutrons," in Damage Analysis and Fundamental Studies, Quarterly Progress Report July-September 1981, DOE/ER-0046/7, U.S. Department of Energy, 28 (1981).

3. D. R. Nethaway, "The $^{93}Nb(n,2n)^{92m}Nb$ Cross Section," J. Inorg. Nucl. Chem., 40, 1285 (1978).

7.0 Future Work

The helium analyses of RTNS-irradiated materials will continue, with emphasis on lead and selected platinum-encapsulated materials. The latter will include PbO, Nb_2O_5, PbF_2, LiF, ^6LiF, and ^7LiF, to determine the cross sections of Li, ^6Li, ^7Li, O, and F.

HELIUM GENERATION CROSS SECTIONS FOR Be(d,n) NEUTRONS

D. W. Kneff, B. M. Oliver, M. M. Nakata, and H. Farrar IV (Rockwell International, Energy Systems Group)

1.0 Objective

The objectives of this work are to measure helium generation rates of materials for Magnetic Fusion Reactor applications in the Be(d,n) neutron environment, to characterize this neutron environment, and to develop helium accumulation neutron dosimeters for routine neutron fluence and energy spectrum measurements in Be(d,n) and Li(d,n) neutron fields.

2.0 Summary

Helium analyses have been completed for the pure elements Cr, Co, and Nb irradiated in the Be(d,n) neutron field, and average integral cross sections have been determined.

3.0 Program

Title: Helium Generation in Fusion Reactor Materials
Principal Investigators: D. W. Kneff and H. Farrar IV
Affiliation: Rockwell International, Energy Systems Group

4.0 Relevant DAFS Program Plan Task/Subtask

Subtask II.A.2.1 Flux-Spectral Definition in the Be(d,n) Field
Subtask II.A.4.3 Be(d,n) Helium Gas Production Data

5.0 Accomplishments and Status

Helium analyses have been completed for the pure elements Cr, Co, and Nb, irradiated in the Be(d,n) neutron field for 30-MeV deuterons. The measured

helium concentrations were combined with integral neutron fluence values for the individual sample locations to derive average helium generation cross sections. These cross sections extend the tabulation of measured Be(d,n) cross sections presented in the previous Quarterly Report.[1] The measurements are based on a joint Rockwell International-Argonne National Laboratory (ANL)-Lawrence Livermore National Laboratory (LLNL) irradiation experiment that has been described in detail previously.[2] The helium measurements were performed by high-sensitivity gas mass spectrometry, and the integral neutron fluence distributions were calculated by L. R. Greenwood at ANL,[2] using the least-squares analysis code STAY'SL.

The new cross section results are presented in Table 1, where they are given in two forms: spectrum-integrated total helium production cross sections evaluated for the total Be(d,n) neutron fluence, and spectrum-integrated cross sections evaluated for the neutron fluence above 5 MeV. The cross sections representing the total neutron yield provide a means of estimating the helium generation in these materials for any similar Be(d,n) or Li(d,n) spectrum if the total neutron fluence is known. Those cross sections evaluated using a 5-MeV neutron energy cutoff provide a rough estimate of the average differential total helium generation cross sections for high-energy neutrons.[1] The Table 1 cross section values are averages based on multiple samples of each element located at different positions within the irradiation volume. The cross section value varies with sample location, because of the spatial dependence of the neutron spectrum shape and the neutron energy sensitivity of the differential cross sections. The uncertainties in the tabulated cross sections for a given Be(d,n) irradiation position have thus been estimated to be ~±35% for the total fluence and ~±18% for the fluence above 5 MeV.[1]

The cross sections determined for fluences >5 MeV are similar to those measured for T(d,n) neutrons (34, 40, and 14 mb, respectively, for Cr, Co, and Nb). This correlation was also observed for previous Be(d,n) results.[1]

TABLE 1

INTEGRAL HELIUM GENERATION CROSS SECTIONS
FOR THE ~0-32-MeV Be(d,n) NEUTRON
SPECTRUM PRODUCED BY 30-MeV DEUTERONS

	Average Cross Section*	
Material	Total Fluence	Fluence > 5 MeV
Cr	13 mb	31 mb
Co	13 mb	34 mb
Nb	5 mb	12 mb

*The cross section uncertainty for a given Be(d,n) irradiation position is ~±35% for the total fluence and ~±18% for the fluence above 5 MeV, reflecting the changing neutron spectrum and thus cross section with source angle.

6.0 References

1. D. W. Kneff, B. M. Oliver, M. M. Nakata, and H. Farrar IV, "Helium Generation Cross Sections for Be(d,n) Neutrons," in Damage Analysis and Fundamental Studies, Quarterly Progress Report July-September 1981, DOE/ER-0046/7, U.S. Department of Energy, 34 (1981).

2. D. W. Kneff, H. Farrar IV, L. R. Greenwood, and M. W. Guinan, "Characterization of the Be(d,n) Neutron Field by Passive Dosimetry Techniques," in Proc. Symp. on Neutron Cross-Sections from 10 to 50 MeV, M. R. Bhat and S. Pearlstein, eds., BNL-NCS-51245, Brookhaven National Laboratory, N.Y. (1980), p. 113.

7.0 Future Work

The helium analysis of Be(d,n)-irradiated materials will continue, and correlations will be made between the integral helium generation results and helium production cross section evaluations.

8.0 Publications

None.

EFFECTS OF TEMPERATURE IN BINARY COLLISION SIMULATIONS OF HIGH ENERGY DISPLACEMENT CASCADES

H. L. Heinisch (Hanford Engineering Development Laboratory)

1.0 Objective

The objective of this work is to develop computer models for the simulation of high energy cascades which will be used to generate defect production functions for correlation analysis of radiation effects.

2.0 Summary

Several hundred cascades ranging from 1 to 500 keV were generated using the binary collision code MARLOWE for primary knock-on atoms (PKAs) with randomly chosen directions in both a nonthermal copper lattice and one having atomic displacements representative of room temperature. To simulate the recombination occurring during localized quenching of the highly excited cascade region, an effective spontaneous recombination radius was applied to reduce the number of defect pairs to be consistent with values extracted from resistivity measurements at 4K. At room temperature fewer widely separated pairs are produced, thus the recombination radius is smaller, however, the recombination radii were found to be independent of energy over the entire energy range investigated for both the cold and room temperature cases. The sizes and other features of the point defect distributions were determined as a function of energy. Differences between cold and room temperature cascade dimensions are small. The room temperature cascades tend to have a greater number of distinct damage regions per cascade, but about the same frequency of widely separated subcascades.

3.0 Program

Title: Irradiation Effects Analysis (AKJ)
Principal Investigator: D. G. Doran
Affiliation: Hanford Engineering Development Laboratory

4.0 Relevant DAFS Program Plan Task/Subtask

Subtask II.B.2.3 Cascade Production Methodology

5.0 Accomplishments and Status

5.1 Introduction

Computer simulations of radiation damage are done using models of varying degrees of exactness. A simplifying assumption often employed, even in fully dynamical models, is to neglect the thermal displacements of atoms and assume the atoms are initially arranged on a perfect lattice. It is usually assumed that the temperature of the lattice affects only the low energy aspect of a displacement cascade, namely the displacement threshold and focusing phenomena which are dictated by the lattice symmetry. Since lattice symmetry effects are not so important in high energy collisions, the net effect of thermal displacements on the set of high energy collisions which occur in a cascade is expected to be small when averaged over many cascades, even though individual high energy collisions may be greatly influenced by slight changes in their impact parameters.

Dynamical simulations with thermal vibrations [1-3] have demonstrated the effects of thermal vibrations for primary knock-on atom (PKA) energies up to about 100 eV. The lengths of collision sequences are reduced, and the displacement energy for a given direction has a distribution of values. Higher energy cascades, greater than a few keV (in copper), have so far defied investigation with fully dynamical models, with or without thermal effects, simply because of the large computational demands.

The use of less exact models, employing the binary collision approximation, permits computers to accommodate PKAs with energies up to hundreds of keV, but the ability to deal exactly with the many-body aspects of low energy collisions is sacrificed. However, the widely-used binary collision code MARLOWE [4] contains parametric representations of some low energy phenomena which can be set to yield the appropriate results. MARLOWE also has the capability of simulating a lattice at

a finite temperature by imposing on the lattice a Gaussian distribution of uncorrelated displacements in the Debye model. Recently the low energy behavior of the MARLOWE code was investigated by Robinson for PKA energies up to 500 eV in copper.[5] MARLOWE parameter values were chosen so as to give a reasonable fit to replacement sequence lengths evaluated with the dynamical code COMENT.[6] Anomalies in the production of defect pairs associated with <111> collision sequences were removed when the computations were done with the atoms given thermal displacements corresponding to room temperature. Thus, Robinson concluded that thermal displacements should be included in MARLOWE to give correct low energy behavior.

MARLOWE has been used to investigate high energy cascades in copper from 1 to 500 eV, with the parameters set as in the study above, but without thermal displacements.[7] In that investigation the gross characteristics of the spatial distributions of defects in cascades, i.e., the cascade shapes and sizes, were described quantitatively as a function of PKA energy. The present work is a similar investigation of the spatial characteristics of high energy cascades in copper, but including thermal displacements in the MARLOWE calculations.

5.2 Computations

More than five hundred cascades, ranging in energy from 1 to 500 keV, were generated in copper using MARLOWE with thermal displacements representative of a temperature of 300 K, using a Debye temperature of 314K.

In MARLOWE there is an energy parameter, E_d, which is the minimum energy an atom must receive in a collision if its trajectory is to be followed beyond that collision. To achieve appropriate lengths for focused collision sequences in the low energy events it is necessary to set E_d as low as 5 eV.[6] While this value of E_d allows for replacement sequence propagation resulting in widely separated defect pairs, it also leads to the production of many close pairs which are ultimately subject to spontaneous recombinations. For PKA energies above 100 keV the large number of pairs produced as a result of this low value

of E_d presents computational difficulties. Without making substantial changes to the code, the only way to economically handle cascade energies greater than 100 keV is to increase the value of E_d. The result of using a higher E_d value is fewer pairs and smaller average separations. However, if spontaneous recombination is accounted for in such a way that the number of remaining pairs is independent of E_d, then the spatial distributions of remaining vacancies are fairly independent of E_d also. The average separation of remaining pairs is, of course, greater for cascades generated with a low E_d value. Since setting E_d at 5 eV results in more realistic cascades, this value was used wherever practical. These runs were used to calibrate a more computationally efficient MARLOWE version with E_d = 17 eV, which was used to extend the work to PKA energies above 100 eV.

The cascades as produced by MARLOWE are a simulation of the initial production of displacements occurring in the first $\sim 10^{-13}$ sec of the cascade development. What happens during the subsequent dissipation of energy or "quenching" of this highly energetic cascade region can be properly simulated only by careful application of a dynamical model. However, a crude simulation of the pair recombination which occurs during the quenching of the cascade has been done with MARLOWE cascades by simply recombining the closest pairs until the proper number of residual pairs is reached.[7-8] It was found in the previous simulations (for E_d = 5 eV) that if defect pairs separated by less than 5.75 lattice parameters are recombined, the number of remaining pairs is equal to the value extracted from resistivity measurements on copper irradiated at $\sim$4K, independent of the PKA energy.

In the present simulations using thermal displacements, recombination was also used to simulate quenching of the cascades. Even though these cascades were produced in a lattice at 300K, they were recombined so as to have the number of pairs derived from the results of the experiments at $\sim$4K. It is assumed that this value accounts for the recombination occurring only during the very rapid dissipation of energy in the localized cascade region. At 4K further rearrangement is not possible because of defect immobility. The influence of the temperature of the surrounding lattice on the immediate recombination in the quench is probably a second-order effect, hence the recombination due only

to quenching should be about the same at higher temperatures as at 4K. At 300K, where defects are fairly mobile, more recombination is expected to occur during normal thermally activated diffusion, but the present investigation is concerned only with the effects of temperature on initial cascade structure.

The dimensions of the recombined cascades were determined for the distributions of vacancies only. Thus on the average, about the same number of vacancies, representing those surviving the quench, were in the cascades at a given energy, regardless of the temperature of the model used to generate it.

5.3 Results

The average pair separations at 300K were 10% less than when thermal displacements were not included. The recombination representing the quenching of the cascade was simulated by a recombination radius of 4.75 lattice parameters. As with the nonthermal cascades, the number of pairs in the recombined thermal cascades matched the resistivity results at all energies. The sizes of the resulting vacancy distributions were measured, and the average values of the results are compared at each energy with the nonthermal cascades in Table 1. The maximum dimension of the cascade, R_{max}, in lattice parameters, is the distance between the two most widely separated vacancies. The dimension Δz is the maximum dimension of the cascade along the initial PKA direction, and the aspect ratio, A, is the ratio $\Delta z/((\Delta x^2 + \Delta y^2)/2)^{\frac{1}{2}}$, where Δx and Δy are the maximum dimensions transverse to the PKA direction. Thus, the dimensions Δx, Δy, and Δz define a rectangular parallelepiped which just encloses the cascade, and the aspect ratio A is a measure of the depth relative to the average transverse dimension. The values in Table 1 are averages of fairly broad distributions of values. The aspect ratios vary from about 0.2 to 4.0 for the 100 keV cascades. At all energies the vacancy distributions of the cascades generated at 300K have a 10-15% greater average maximum extent than the nonthermal cascades. The average aspect ratios of the parallelepipeds enclosing the 300K cascades are smaller at every energy.

TABLE 1

DIMENSIONS OF ROOM TEMPERATURE AND NONTHERMAL SIMULATED CASCADES

PKA Energy, keV	$\langle R_{max} \rangle$, a		$\langle R_{max}/\Delta z \rangle$		$\langle A \rangle$	
	NT	300 K	NT	300 K	NT	300 K
1	3.0	3.5	1.4	2.3	2.0	1.2
2	5.7	6.0	1.3	1.9	1.8	1.1
5	12	13	1.4	1.9	1.3	1.2
10	22	23	1.4	1.9	1.6	1.1
20	34	45	1.5	1.7	1.3	1.2
30	43	56	1.4	1.9	1.4	1.1
50	69	84	1.4	1.7	1.5	1.2
100	117	129	1.4	1.6	1.6	1.2
200	196	232	1.3	2.0	1.9	1.1
500	443	488	1.2	1.7	1.9	1.7

The irregularity of the defect distributions, especially at the higher energies, makes quantitative descriptions difficult. To facilitate analysis, the cascades were broken down into some basic components or segments which could be quantified. As in the previous nonthermal cascade study the distinct cascade segments were classified into three categories: 1) widely-separated subcascades for which the edge-to-edge separation of damage areas is at least as large as the subcascade diameter (center-to-center separations typically greater than 90 lattice parameters), 2) close subcascades for which the edge-to-edge separation is at least six lattice parameters (about the average diameter of a 2 keV cascade), and 3) lobes, which are contiguous but identifiably separate parts of the cascade (for example, an L-shaped distribution of defects might be considered to have two lobes). The number and center-to-center separations of the

distinct segments of which the cascades are composed were determined from defect density maps as in the nonthermal case.

In Figure 1 the average number of lobes and subcascades per cascade is plotted as a function of energy for the cascades at 300K. For comparison, the dashed lines are the results for nonthermal cascades. The cascades at 300K are composed of greater numbers of both lobes and subcascades. On the average, the 300K cascades have 30-40% more lobes per cascade, hence the average size of individual lobes is smaller.

Additional comparisons show other, slight differences between the 300K and nonthermal cascades. The average center-to-center spacing of lobes is 5-10% smaller at 300K, and as with the nonthermal cascades it is approximately constant ($\sim$40 lattice parameters) over the 50-500 keV energy range. The frequency of occurrence of widely spaced subcascades is about the same with or without thermal displacements, varying from a few percent at 50 keV to about 50% at 500 keV. The average separation of all widely-separated cascades is 6% less at 300K than for the nonthermal cascades.

5.4 Discussion

Thermal displacements remove the perfect crystal symmetry which is a simplifying artifact in most computer simulations of radiation damage. The expected result of including thermal displacements, confirmed by studies of low energy events, is the disruption of focused collision sequences along high symmetry directions.[2] The net effect of this disruption should be a decrease in the average vacancy-interstitial separation, and this effect was observed to occur, independent of PKA energy, in the MARLOWE cascades when thermal displacements were included.

The inclusion of thermal displacements apparently has an effect on the gross features of the cascade configurations. These are the features directly influenced by high energy collisions in the cascade. With thermal displacements there are more lobes per cascade, and the lobes have smaller average separations. In the previous work on nonthermal cascades[7] it was concluded that a high

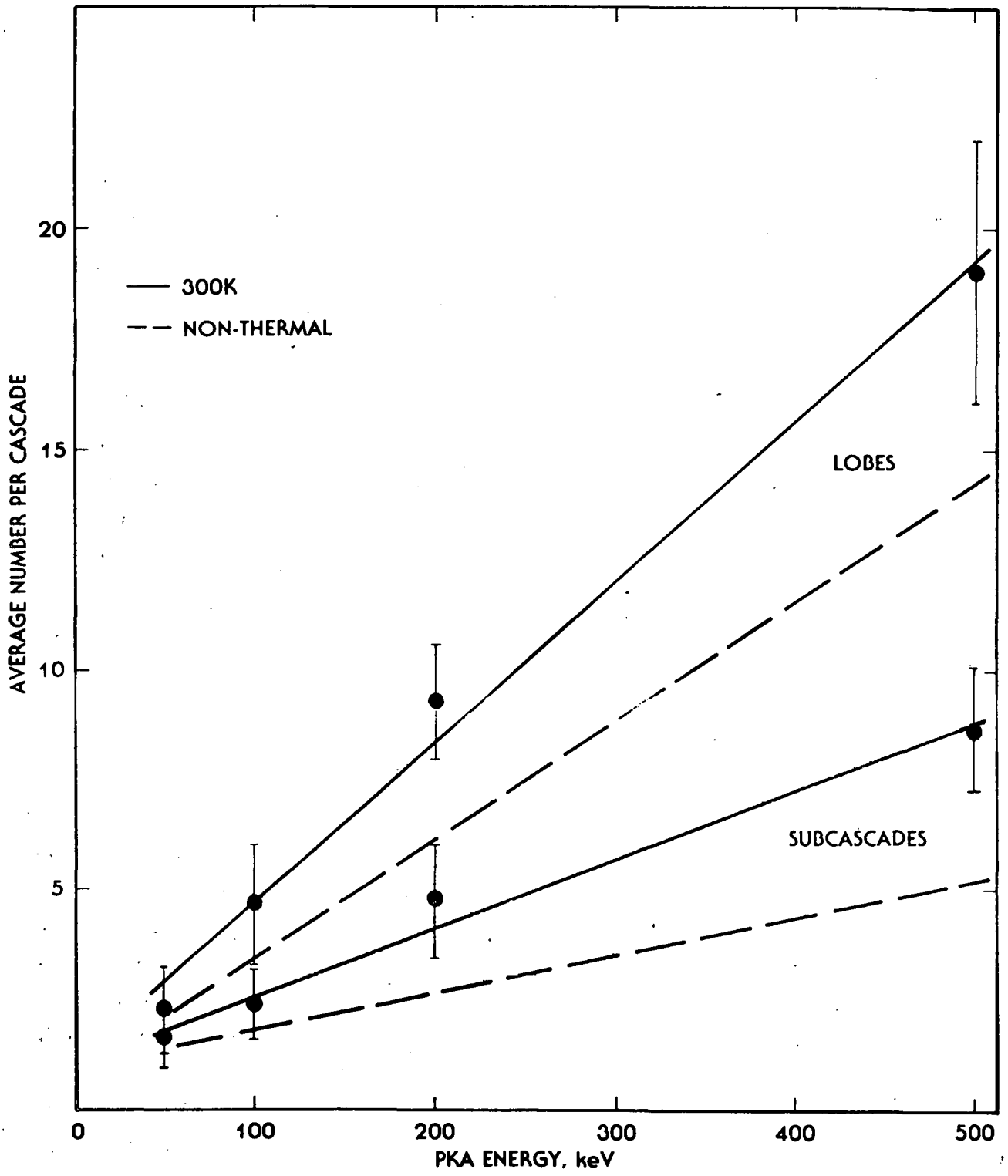

FIGURE 1. The Average Number of Subcascades and Lobes per PKA in Copper Cascades at 300K as a Function of PKA Energy. "Lobes" are the total number of lobes in the cascades regardless of the subcascade structure. "Subcascades" includes both close and widely separated subcascades.

energy cascade can be characterized as a collection of mostly-connected 5-30 keV cascades, and that the number of lobes per cascade is approximately the PKA energy divided by 35 keV. As illustrated in Figure 1, when thermal displacements are included, there is about one lobe for every 25 keV. However, there is a good deal of subjectivity involved in determining what constitutes a lobe and, if anything, there may have been a tendency to distinguish too many regions as separate. Thus, 25-35keV per lobe is probably an appropriate range of values.

If one assumes that the vacancies in individual lobes or subcascades can collapse to form loops, then it follows from the results here that the number of loops per cascade should increase with cascade energy, and that the distribution of loop sizes remains independent of energy. This behavior is observed in self-ion experiments in copper [9] where there were three times as many loops observed with 90 keV self-ions as with 30 keV self-ions, and the size distributions were quite similar. It should be noted, however, that the experiments were performed at room temperature, where vacancies are somewhat mobile in copper. Also, only those defects large enough to be imaged in an electron microscope could be measured.

It is interesting to speculate on whether the effects of thermal displacements on the high energy aspects of cascades observed here are consistent with what one might expect from the disruption of crystal symmetry produced by thermal displacements. The lobed structure of the cascades in copper is apparently a manifestation of the mean free path for collisions involving large energy transfers. The addition of thermal displacements appears to slightly shift to smaller values the distribution of impact parameters available to an atom with random position and direction, creating an increased probability of very energetic collisions, hence, a smaller mean free path. This results in more lobes per cascade and closer spacing of lobes. This would also explain the increased probability of major collisions early-on in the cascade development, resulting in the smaller values of the average aspect ratio.

On the other hand, the widely-spaced subcascades may be a manifestation of channeling, hence these events are not subject to the same mean free path

considerations as lobes. The small differences in impact parameters encountered by ions within the channels are apparently not enough to seriously affect the channeling capability. This is reasonable, since channeling is experimentally observed to occur over long distances at finite temperatures. There is however a slight tendency for somewhat shorter subcascade separations, evidently due to the increased probability of dechanneling by atoms thermally displaced.

The major effects of including thermal displacements in binary collision simulations of high energy cascades are the decreased average pair separations and the increased number of distinct damage regions (lobes) in the cascades. These effects are not significant enough to change any of the earlier conclusions about the basic nature of high energy cascade configurations which were based on nonthermal simulations.[7] However, the behavior of the defects subsequent to their initial production, i.e., during quenching and short term annealing, may depend very strongly on their actual configurations even at the level of exactness of MARLOWE and the simple short term annealing simulation models which have been applied to MARLOWE cascades.[8]

6.0 References

1. R. N. Stuart, M. W. Guinan and R. J. Borg, Radiation Effects, 30 (1976) 129.

2. A. Tenenbaum, Phil. Mag., A 37 (1978) 731.

3. J. R. Beeler and M. F. Beeler, Proceedings of the International Conference on Fundamental Aspects of Radiation Damage in Metals, Volume 1 (1976) 21.

4. M. T. Robinson and I. M. Torrens, Phys. Rev. B, 9 (1974) 5008.

5. M. T. Robinson, DAFS Quarterly Progress Report, January-March 1980, DOE/ER-0046/1, U.S. Department of Energy (1980) 55.

6. J. O. Schiffgens, D. M. Schwartz, R. G. Ariyasu and S. E. Cascadden, Radiation Effects, 39 (1978) 221.

7. H. L. Heinisch, Proceedings of the Second Topical Meeting on Fusion Reactor Materials, Seattle, WA, August 1981, J. Nucl. Mat., in press.

8. H. L. Heinisch, D. G. Doran and D. M. Schwartz, Effects of Radiation on Materials, ASTM Special Technical Publication 725 (1981) 191.

9. M. M. Wilson, Phil. Mag., 24 (1971) 1023.

7.0 Future Work

Interactions of cascades during short term annealing will be investigated along with simple models of cascade quenching.

8.0 Publications

This paper was presented at the International Conference on Neutron Irradiation Effects, November 9-12, 1981, Argonne National Laboratory, and it will be included in the conference proceedings to appear in the Journal of Nuclear Materials.

14-MEV NEUTRON IRRADIATION OF COPPER ALLOYS

S. J. Zinkle and G. L. Kulcinski (University of Wisconsin-Madison)

1.0 Objectives

The objectives of this experiment are to: 1) determine defect survivability in copper alloys irradiated at room temperature and the influence of solute additions and neutron fluence, and 2) determine whether resistivity measurements can provide useful information when used in conjunction with TEM and microhardness measurements to study the dependence of defect survivability on neutron energy and solute additions. In particular, this experiment is an attempt to use resistivity analysis to explain the difference in hardness increase and microstructure as viewed by TEM of Cu and Cu alloys examined previously by HEDL.

2.0 Summary

Resistivity foils and TEM disks of pure copper and 3 copper alloys (Cu+5% Al, Cu+5% Mn, Cu+5% Ni) have been irradiated at room temperature at the RTNS-II facility. Resistivity measurements and TEM disks have been obtained for each metal at fluences of approximately 1×10^{16}, 3×10^{16}, 1×10^{17}, 3×10^{17} n/cm^2. The change in resistance for the pure copper sample was found to be proportional to the square root of the neutron fluence.

The results for the copper alloys show a decrease in the foil resistivity with neutron fluence up to about 1×10^{17} n/cm^2. At a fluence of 3×10^{17} n/cm^2, the foil resistivity increased and became greater than the pre-irradiation value for the Al and Ni solute alloys. This tends to indicate that the overall resistivity is due to a superposition of a negative resistivity process which saturates at high fluence, and a positive resistivity process.

3.0 Program

Title: Radiation Effects to Reactor Materials
Principal Investigators: G. L. Kulcinski and R. A. Dodd
Affiliation: University of Wisconsin

4.0 Relevant DAFS Program Task/Subtask

Subtask II.B.3.2 Experimental Characterization of Primary Damage State; Studies of Metals
Subtask II.C.6.3 Effects of Damage Rate and Cascade Structure of Microstructure; Low-Energy/High-Energy Neutron Correlations
Subtask II.C.16.1 14-MeV Neutron Damage Correlation

5.0 Accomplishments and Status

5.1 Introduction

This study is a continuation of research on copper alloys which was initiated by researchers at HEDL. In their study,[1] the authors used a combination of microhardness and TEM analysis in an attempt to quantify defect survivability and microstructure, and the influence of neutron fluence and solute additions on these parameters. The irradiation-induced microhardness changes were found to be independent of the type of alloy. In their TEM analysis, they found that the Cu+5% Al had about twice as many visible clusters per calculated PKA as compared to the other alloys. We anticipated that a resistivity analysis in conjunction with microhardness and TEM work might help to resolve this puzzle.

The current study, therefore, tries to duplicate the experimental conditions of the previous work. TEM disks have again been irradiated, along with resistivity foils.

5.2 Experimental Procedure and Results

Samples of the alloys in the form of 10 mil thick foils were obtained from HEDL. A detailed description of the composition of these alloys has been previously reported.[2,3] In order to obtain accurate resistivity results, the thickness of the foils had to be reduced. This was accomplished by cold-rolling, with 6 passes required to achieve the final thickness of about 1 mil. TEM disks were punched out, deburred, and enscribed with an identifying number. Resistivity foils were cut to a width of about 10 mils, measured, and weighed. The samples were then annealed under a partial atmosphere of high-purity argon and allowed to air cool. The pure copper samples were annealed at 400°C for 15 minutes. The Cu alloys were annealed at 750°C for 1/2 hour. This duplicated the stress relieved condition for the foils from the HEDL study. After the anneal the pure copper had a RRR = 380.

Standard resistivity measuring equipment supplied by M. W. Guinan of LLNL was used to measure the resistance increments. The potentiometer used in the experiment had a resolution of 10 nV. The resistivity foils were connected in series so that the same current flowed through all samples. The current through the foils was maintained at about 10 mA, and was read directly by a Dana digital multimeter. Readings were taken with the current going both ways through the samples in order to cancel out the effect of thermal emfs. There was some difficulty with the stability of the current supply, so several readings were taken and the results were averaged. The effect of this instability has been included in the error analysis.

A schematic of the sample holder used in the experiment is shown in Figure 1. For simplicity, the voltage leads are not shown. Niobium dosimetry foils were placed between each resistivity foil and between the TEM disks to determine the 14 MeV neutron fluence. The TEM disks were spaced away from the neutron source at four different distances such that at the end of the experiment the total dose received by the disks was approximately 1×10^{16},

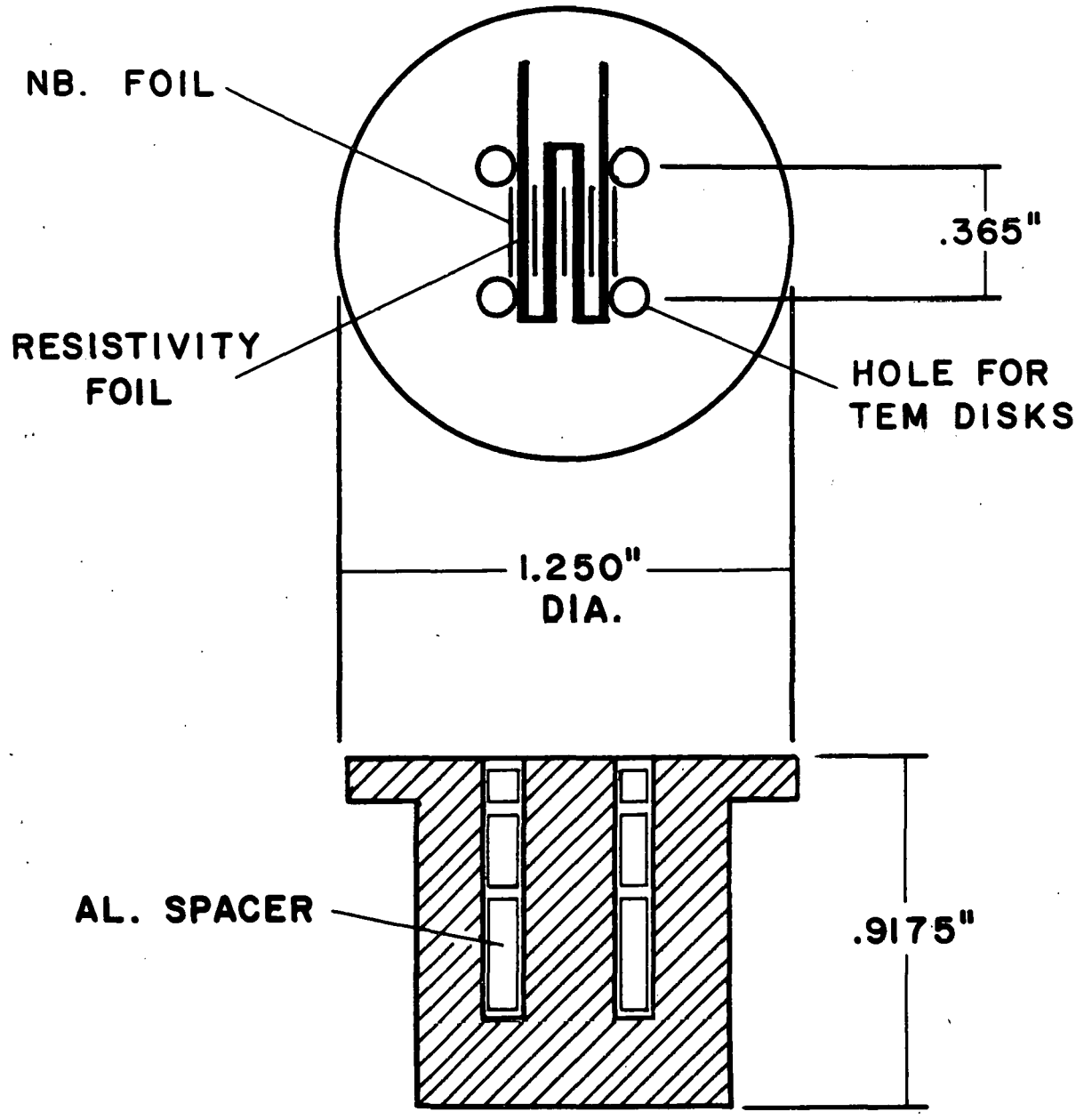

FIGURE 1. Specimen Mounting Flange.

3×10^{16}, 1×10^{17}, 3×10^{17} n/cm^2 for each alloy. The variation of neutron fluence across the resistivity samples was approximately 15%.

The experimental procedure consisted of irradiating the samples at room temperature to a certain fluence level, then the entire sample assembly was removed and the foils were immersed in liquid helium while the resistivity measurements were being made. When the measurement was finished, the sample assembly was repositioned in front of the neutron source and the next increment of fluence was started. Ion chamber readings were recorded at the end of each leg of the experiment. After the experiment was over, the Nb foils were removed and counted to determine the total neutron fluence received by the samples. By taking the ratio of the ion chamber readings at each stopping point of the experiment, the fluence level for each leg could be determined. The sample assembly was designed so that repositioning errors between legs of the experiment were negligible.

The fluence levels achieved for each of the 4 resistivity samples is given in Table I. The integrated fluence received by each of the foils was approximately 2.9×10^{17} n/cm^2, which corresponds to about 0.001 dpa. The unirradiated resistivity value (4.2°K) for each of the samples is also given in Table I. The fluence levels for the TEM disks is given in Table II. The maximum fluence achieved was about 2×10^{17} n/cm^2. This value is less than the maximum fluence for the resistivity foils because of geometrical positioning.

A size effect correction had to be made for the pure copper foil. This was readily done following the procedure of reference 4. A value of $K = 7.0 \times 10^{-16}$ Ω-m^2 was used.[5] The magnitude of the size effect correction varied from 18% to 7% with increasing fluence level of the foil.

The conversion from the measured macroscopic resistance values to resistivity values was accomplished as follows. The foil length and width were measured with a travelling microscope, and the foil was weighed with a

TABLE I

DATA FOR RESISTIVITY SAMPLES

Alloy	$\rho_0(\Omega\text{-cm})$	$\Phi_1(n/cm^2)$	$\Phi_2(n/cm^2)$	$\Phi_3(n/cm^2)$	$\Phi_4(n/cm^2)$
Cu	4.49×10^{-9}	0.98×10^{16}	3.03×10^{16}	9.8×10^{16}	2.93×10^{17}
Cu+5% Al	3.96×10^{-6}	0.97×10^{16}	3.0×10^{16}	9.7×10^{16}	2.91×10^{17}
Cu+5% Mn	1.08×10^{-5}	0.93×10^{16}	2.9×10^{16}	9.35×10^{16}	2.80×10^{17}
Cu+5% Ni	5.16×10^{-5}	0.96×10^{16}	2.98×10^{16}	9.6×10^{16}	2.88×10^{17}

TABLE II

FLUENCE LEVELS OF TEM SAMPLES

Alloy	$\Phi_1(n/cm^2)$	$\Phi_2(n/cm^2)$	$\Phi_3(n/cm^2)$	$\Phi_4(n/cm^2)$
Cu	1.41×10^{16}	4.29×10^{16}	1.07×10^{17}	1.85×10^{17}
Cu+5% Al	1.42×10^{16}	4.60×10^{16}	1.18×10^{17}	2.08×10^{17}
Cu+5% Mn	1.42×10^{16}	4.48×10^{16}	1.16×10^{17}	1.99×10^{17}
Cu+5% Ni	1.46×10^{16}	4.42×10^{16}	1.17×10^{17}	2.24×10^{17}

microbalance. Using the handbook value for the density of copper,[6] the foil thickness was deduced. The geometry factor for the pure copper sample was $A/L = 1.95 \times 10^{-6}$ m. This value was checked by an alternative method: The conversion factor can be determined directly from the ratio ρ_0/R_0, where ρ_0 is the handbook resistivity value[6] at 20°C, and R_0 is the measured unirradiated sample resistance at 20°C. The results of these two methods agreed to within 1%.

The resistance change as a function of fluence for pure copper and the copper alloys is shown in Figures 2 and 3, respectively. Representative error bars are as indicated.

A post-irradiation isochronal anneal was attempted in order to obtain more information about the defects, but difficulties with the sample holder prevented any conclusive results from being obtained.

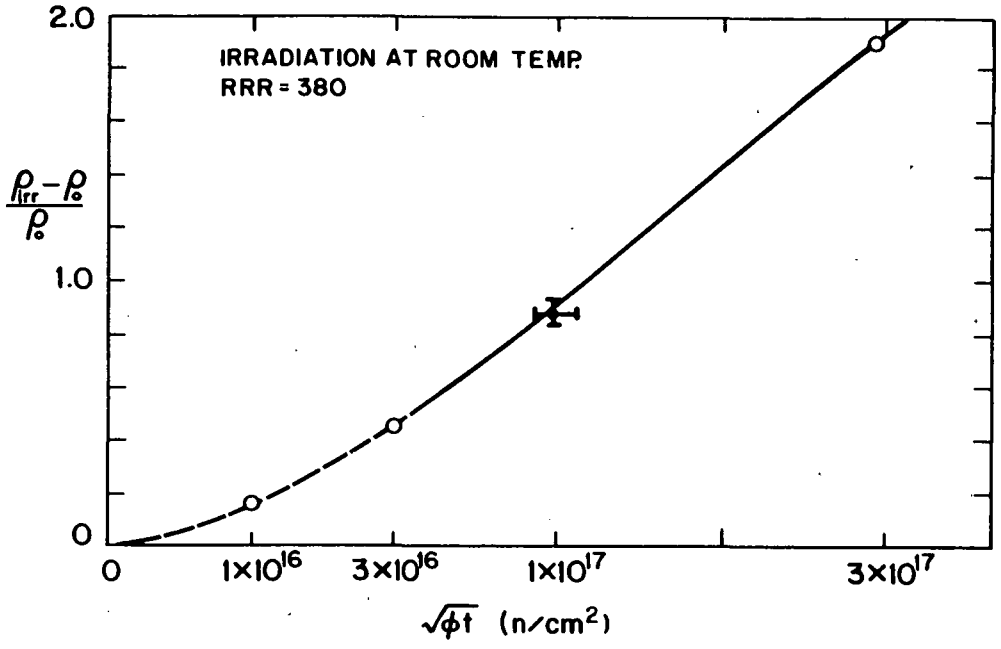

FIGURE 2. Resistance Change vs. 14-MeV Neutron Fluence for Copper.

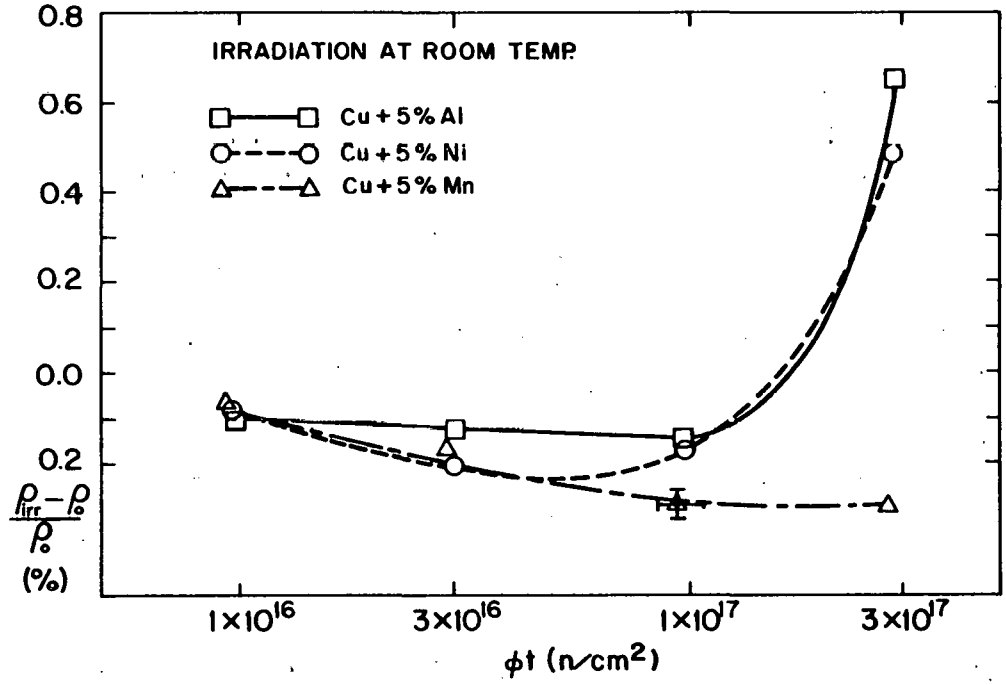

FIGURE 3. Resistance Change vs 14-MeV Neutron Fluence for Copper Alloys.

5.3 Discussion

The resistivity change of the pure copper is proportional to the square root of fluence. This is a generally well known result for irradiation temperatures where the interstitial is mobile.[7,8]

Irradiation of the copper alloys initially produced a decrease in the foil resistivity. At higher fluences, the resistivity increased and became greater than the pre-irradiation value for the Al and Ni solute alloys at a fluence of 3×10^7 n/cm^2. This effect has also been observed by other researchers[8,9] for both electron and neutron irradiations. The resistivity change rate is composed of 2 competing processes: a positive change rate due to Frenkel defect production and a negative one due to solute segregation or short range ordering. The negative process probably saturates at high fluence but future tests and analysis are being conducted on these alloys to clarify the mechanism.

6.0 References

1. H. R. Brager et al., "Damage Development and Hardening in 14-MeV Neutron Irradiation of Copper Alloys at 25°C," paper presented at the Second Topical Meeting on Fusion Reactor Materials, August 9-12, 1981, Seattle, WA. Proceedings to be published in J. Nucl. Mat.

2. H. R. Brager et al., "Microstructural Development in Copper Irradiated in RTNS-II," 9th DAFS Quarterly Technical Progress Report (May 1980), DOE/ER-0046/1, p. 76.

3. N. F. Panayotou et al., "RTNS-II Irradiation Program Status," DAFS Quarterly Technical Progress Report,DOE/ET-0065/5 (Jan.-Mar. 1979), p. 112.

4. F. Dworschak et al., Phys. Stat. Sol., 21, 741-745 (1967).

5. R. Coltman et al., Journal of Nuclear Materials, 99, 284 (1981).

6. Weast, CRC Handbook of Chemistry and Physics, 59th ed., (1978-79), CRC Press Inc.

7. D. S. Billington, "Radiation Damage in Solids," Proceedings of the International School of Physics, (Enrico Fermi) Course XVIII, p. 594, (1962).

8. J. Corbett, "Electron Radiation Damage in Semiconductors and Metals," Solid State Physics - Supplement 7, Academic Press (1966).

9. R. Poerschke and H. Wollenberger, Journal of Nuclear Materials, 74, 48-61 (1978).

7.0 Future Work

An attempt will be made to determine the number of defects surviving using appropriate resistivity models. Future plans include TEM analysis and microhardness in a cooperative effort with HEDL.

NEUTRON-IRRADIATION PLAN FOR CALIBRATION OF GAMMA AND NEUTRON DAMAGE EFFECTS IN ORGANIC INSULATORS

G. F. Hurley, J. D. Fowler, Jr., and D. M. Parkin* (Los Alamos National Laboratory)

1.0 Objective

This study is being carried out to determine the effects of neutron-irradiation at 4.2 K on epoxy and polyimide insulators, and to compare these effects with those from gamma-irradiations at the same temperature, and in the same materials.

2.0 Summary

A plan for a preliminary calibration of damage effects from neutron-irradiation with those from gamma irradiation of organic insulators has been developed. In this first experiment, G-10CR, G-11CR, two polyimide-based analogues of G-10, kapton films, and glass-filled Epon 828 are being prepared for irradiation in IPNS. Damage effects will initially be calibrated primarily by a phenomenological comparison of mechanical and electrical properties.

3.0 Program

Title: Radiation Damage Analysis and Computer Simulation (Radiation Effects in Organic Insulators)
Principal Investigator: G. F. Hurley
Affiliation: Los Alamos National Laboratory

4.0 Relevant DAFS Program Plan Task/Subtask

Task II.B.4: Damage Production in Insulators
Subtask II.B.4.3: Experimental Validation/Calibration of Theory

*Currently on assignment to DOE/Germantown

5.0 Accomplishments and Status

5.1 Introduction

Organic insulation is specified for the superconducting ohmic heating coils, toroidal field coils, and equilibrium field coils in many tokamak reactor designs, including the Fusion Engineering Device (FED). The essential requirements for organic insulation, and implications of the work carried out to date, have recently been reviewed.[1] Much work of a scoping nature has been carried out in which candidate insulators have been irradiated to high doses ($\geq 10^6$Gy) in fission reactors which supply most of the dose from γ absorption.[2-5] This work has defined limitations for epoxy-based materials which fall in the dose-range of interest, 10^6- 10^8 Gy. At the same time, analogous polyimide materials have shown satisfactory retention of properties in this dose range.

Limitations in using the existing data to predict insulator behavior in fusion reactors can be seen by comparing the conditions under which this data was obtained with the operating environment in fusion devices. Specifically, magnet insulation in service is exposed to both neutron and gamma irradiation at liquid helium temperatures. The total dose is expected to be in the range 10^7-10^8Gy as specified for a number of designs (Table 1). A substantial part of the total dose (50-90% by various estimates) is contributed by the neutrons.

TABLE 1

SPECIFIED DOSE TO THE ORGANIC INSULATORS IN 3 CONTEMPORARY FUSION REACTOR DESIGNS

MACHINE	DOSE(Gy)
FED	1×10^7
INTOR	1×10^8
STARFIRE	$1\text{-}2 \times 10^7$

During operation of the magnets, the insulation is required to withstand pulsed electrical and mechanical stresses, with the latter being the more demanding. Mechanical stresses will be multiaxial, with tensile, shear, and compressive components. Finally, the magnets will be periodically warmed to room temperature, a factor which is likely to affect the insulator's radiation response.

By contrast, studies in this country[2-4] have concentrated on candidate materials after liquid helium irradiations, with most of the dose from γ-ray absorption. Mechanical testing was conducted at 77 K after samples had been warmed to room temperature. A survey of irradiation effects in epoxy and polyimide materials in Japan[5], has suggested that mechanical properties show greater loss when tested at 4.2 K, without warmup.

Based on this comparison it is clear that several areas for investigation require attention, just to assess expected radiation performance of materials which have already been examined. A key area for consideration is the nature of the radiation, and how the mechanism of radiation-induced structural change might be affected when a much larger fraction of the dose comes from neutrons.

Other aspects of the problem which have not been addressed concern the effect of other operating conditions on the perceived degradation, partly reflecting the influence of the operating environment on the mechanism. These problems include the thermal history, atmosphere during warmed-up periods, dose rate, and the complex stress state expected during magnet service.

In our work, of which this is the initial report, we will address the first of these subjects, the effect of the type of irradiation on the degradation of those polymers which are already candidates for magnet service and for which some data for degradation in γ-fluxes already exists. The first study will be a calibration based on a phenomenological comparison of this data with that obtained after neutron irradiation in IPNS and RTNS-II. This initial study will be followed by work of a more fundamental nature to determine the mechanism of degradation.

5.2 Irradiation Experiments

5.2.1 IPNS

An initial irradiation has been scheduled for IPNS, to be carried out in late February or early March of CY 1982. In addition, a tentative plan has been made for a second irradiation in RTNS-II.

In the first irradiation, preparations for which are underway or completed, samples will be irradiated which will mirror those tested at ORNL after γ-irradiation. The materials which will be studied are listed in Table 2.

TABLE 2

DESCRIPTION OF MATERIALS FOR IPNS IRRADIATION

Material	Description	Tests
G-10CR	Glass-cloth reinforced epoxy. Meets NEMA G-10 specification as modified for cryogenic service	Mechanical and electrical
G-11CR	Similar to G-10CR; epoxy differs in the nature of its cure.	Mechanical and electrical
Spaulrad™	Polyimide matrix analogue of G-10CR; product of the Spaulding Fiber Co., Tonawanda, NY	Mechanical and electrical
Norplex NP-530	Similar to above; product of Norplex Division, LaCrosse, WI	Mechanical and electrical
Silica-filled	Epoxy resin with 40 wt % filler and 0.5% 3-(2-Amino-ethylamino) propyl trimethoxysilane coupling agent, cured with the Shell Z (blended aromatic) curing agent. Duplex cure at 355 K followed by 425 K.	Mechanical and electrical
Kapton	Non-reinforced polyimide film material (Dupont)	Electrical
Aluminized Kapton	Candidate thermal insulation material	Qualitative

These materials are the same as those studied in the latest work at ORNL,[2,3] in γ-irradiations, and have been selected for this study for a phenomenological comparision of the damage after IPNS irradiation, with that occurring after γ-irradiation.

Figure 1 illustrates the types of samples which have been prepared for irradiation. Elongated bars were machined from sheet materials with the warp direction parallel to the sample axis, or cast from epoxy with the aid of the fixture shown in Fig. 2. Eight samples of each material will be irradiated, of which six will be evaluated in flexure testing to fracture, and two will be used for tensile modulus determination. Modulus changes are a sensitive indicator of structural changes in polymers.

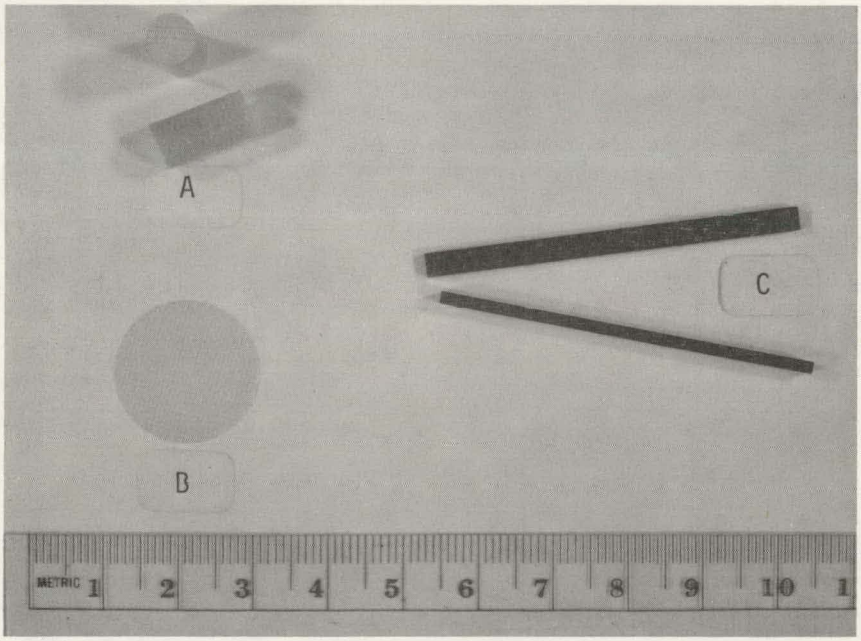

FIGURE 1. Sample Forms for IPNS Irradiation.
A. G-10CR compression samples.
B. G-11CR disks for electrical tests.
C. NP-530 bars for tension and bend tests.

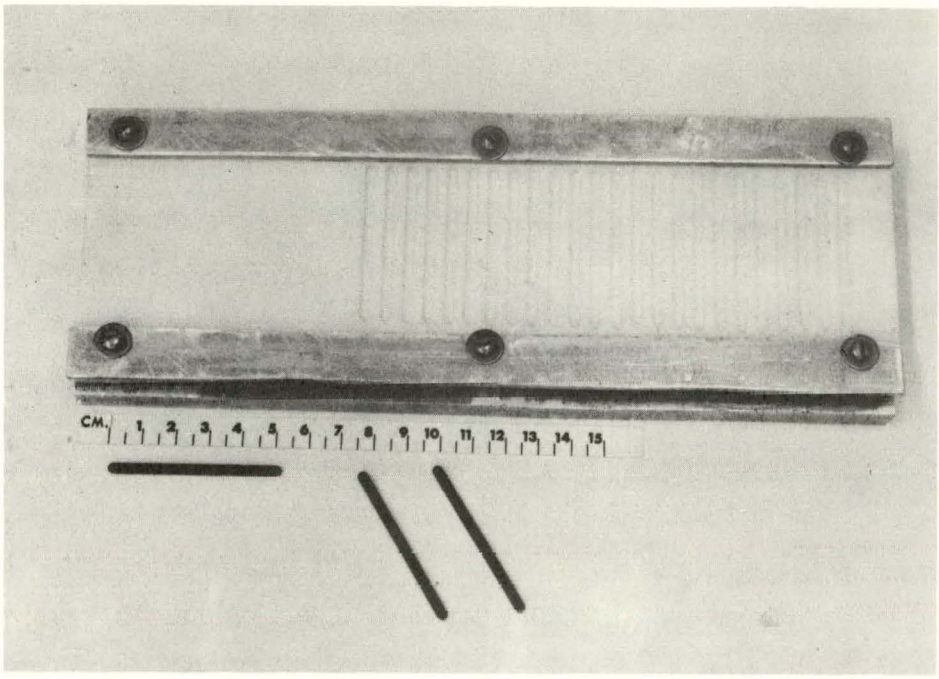

FIGURE 2. Casting Fixture for Epoxy Flexure Samples.

Compression samples were machined from the reinforced materials with their axes parallel to the fabric warp direction, so that the stress during testing will be in the plane of the reinforcements. Epoxy samples are being machined from rods cast in tubular teflon molds (Fig. 3). Six samples of each material will be irradiated, and compression modulus and fracture strength and mode will be determined. These tests as well as flexure testing will be carried out at 77 K.

Electrical properties characterization will be carried out in two distinct areas: measurement of dielectric breakdown strength and determination of low-field AC and DC conductivity. The former will be done at room temperature in an atmosphere of pressurized gas to reduce the likelihood of flashover. Disks 19mm in diameter have been prepared for these measurements, by punching from thin sheets of the fiberglass materials containing only a single layer of glass cloth. No dimpling of these samples will be used (to reduce the thickness in the area of applied high voltage) due to the laminar nature of the

material. Epoxy samples are being sliced from large bar castings (Fig.3) and will be dimpled to leave ≈ 0.1 mm thickness. Four samples of each material will be tested.

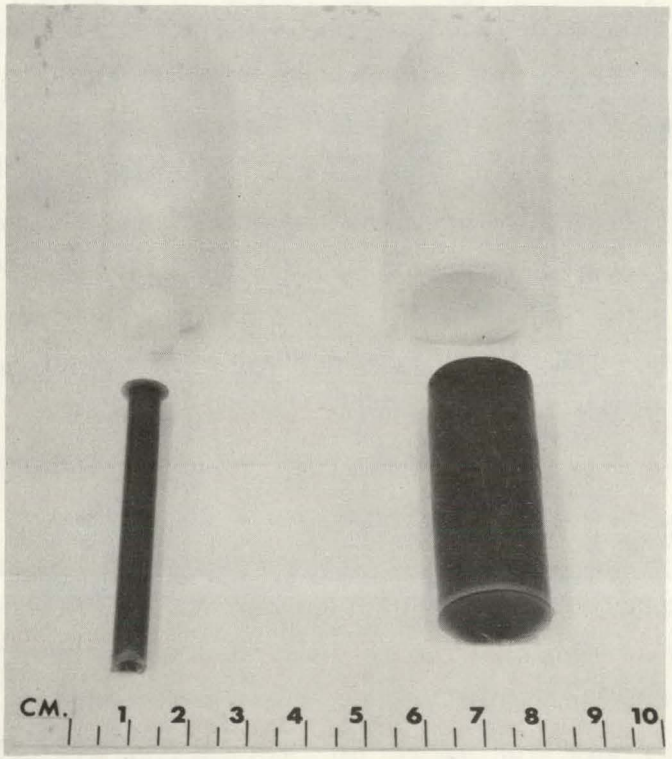

FIGURE 3. Rod Molds. A. 6.4-mm diam for compression samples
B. 19-mm diam for electrical specimens

Conductivity measurements will be made using 19mm disks with tradiational 3-terminal electrodes applied to the surface with a silver paste. AC and DC measurements will be made at room temperature. AC and somewhat less sensitive DC measurements will also be made at temperatures between 80 and 300 K in order to determine temperature dependence and gain an understanding of changes in polymer structure through study of any activation processes which may be found. These samples have been punched from thicker reinforced sheets, typically 0.5 mm thick. Epoxy samples are being sliced from cast bars.

A low temperature apparatus, consisting of two concentric brass cylinders containing a sample holder and thermocouple, has been constructed and tested. This will allow conductivity and loss tangent measurements over a continuous temperature range from 80 to 300 K.

Prior to irradiation samples will be placed in a copper irradiation can, of welded construction, now being fabricated. This can will be placed in the IPNS cryostat, immersed in a static helium pool. The latter is in turn cooled by liquid helium flowing in a loop. To insure that the samples are held at liquid helium temperature, the can itself will be helium filled. After irradiation (5 days, attaining $5 \times 10^{21} m\ m^{-2}$) the samples will be permitted to warm to room temperature. A gas sample will be collected at this time, and again after 1 month. Dosimetry for this experiment will be supplied by L. Greenwood of the Argonne National Laboratory.

5.2.2 RTNS-II

If possible, a second irradiation will be carried out later this year. The purpose of this experiment will be to continue the calibration of property degradation after neutron irradiation against existing data for degradation after γ- or mixed-irradiation data. In this case we will be seeking comparison with some of the recent work of Kato and co-workers at the JAERI.[5]

Although preparations for this work are not as advanced as for the IPNS irradiation, considerable progress has been made in the preparation of sample casting fixtures and a mechanical test device for cryogenic testing. Materials which will be irradiated are unfilled epoxy, with aliphatic amine aromatic amine, and acid anhydride hardeners. Samples will be 1.5 mm diam x 3 mm long cylinders which will be tested in compression. A fixture for casting these samples has been fabricated in the form of a split mold, as shown in Fig. 4. The castings, shown at the bottom in Fig. 4, are then trimmed to size with the aid of the fixture in Fig. 5

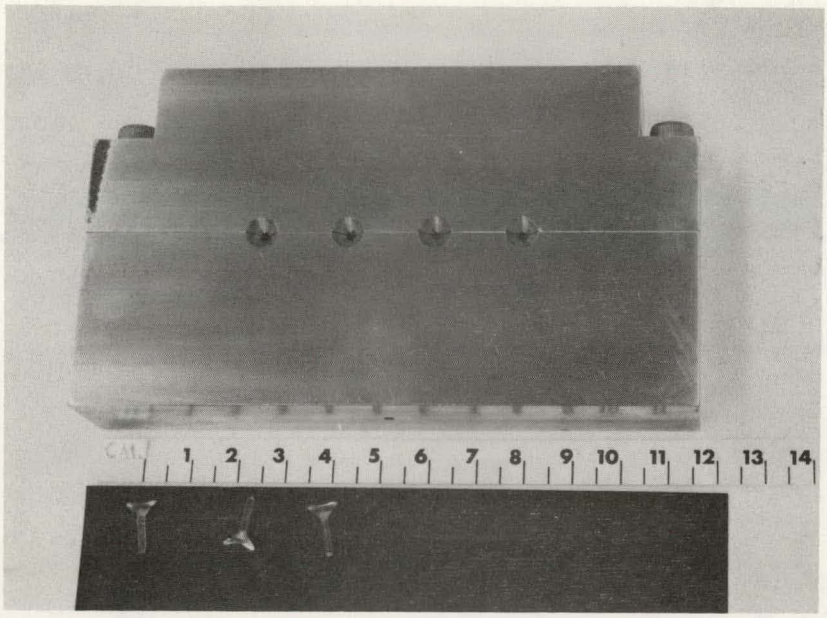

FIGURE 4. Split Mold for Casting Small Compression Samples. Several as-cast samples are shown below the mold.

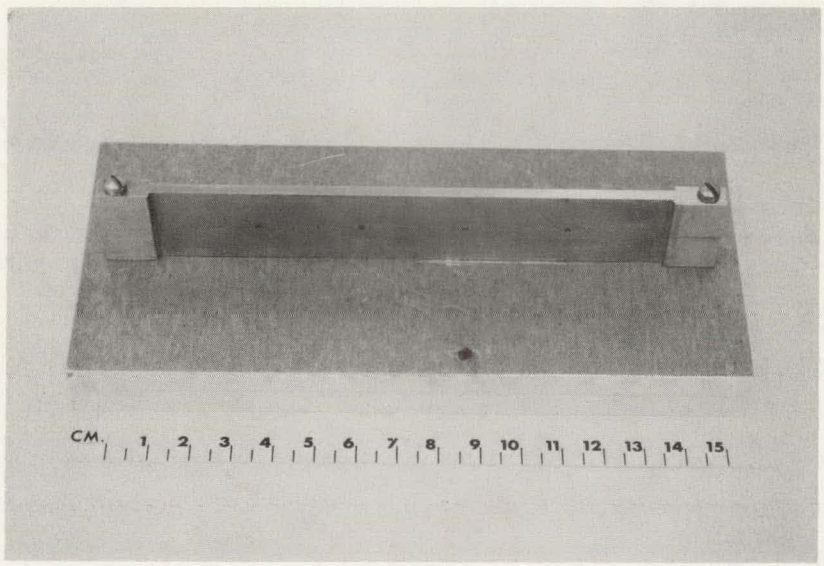

FIGURE 5. Fixture for Trimming the Samples Shown in Fig. 4. Samples are clamped and then cut off and ground with their length secured by the thickness of the plate.

Compression tests yielding modulus and fracture strength will be carried out at 77 K after irradiation. A cryogenic test fixture suitable for testing these small samples has been designed (Fig. 6) and is being fabricated. This device will employ a displacement transducer for the measurement of strain.

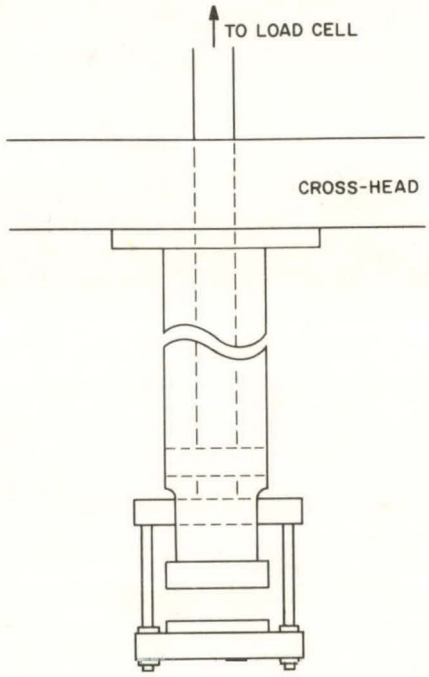

FIGURE 6. Schematic Illustration of the Cryogenic Test Fixture Now Under Construction. This device is lowered into a dewar during testing.

Samples in this study will also be irradiated at liquid helium temperature. A Helitran cold end* and associated hardware, which are compatible with the arrangement for cryogenic irradiations at RTNS-II, are on order. Some modification to this apparatus will be necessary, after its receipt, for accommodating the samples.

*Air Products Co., Allentown, PA 18105

5.3 Concluding Remarks

A program to investigate radiation damage in organic insulators of interest to the magnetic fusion program has been initiated. The initial stages of the investigation will aim at calibrating neutron damage effects on physical properties of organics irradiated at liquid helium temperature against those measured after similar γ-irradiation. Preparations for the first irradiation, in IPNS, are nearly complete, and the irradiation should be carried out during the next quarter.

6.0 References

1. F. W. Clinard, Jr. and G. F. Hurley, "Ceramic and Organic Insulators for Fusion Applications", Second Topical Meeting on Fusion Reactor Materials, Aug. 1981, Seattle, WA. To be published in J. Nucl Materials.

2. R. R. Coltman, Jr. and C. E. Klabunde, "Mechanical Strength of Low-Temperature-Irradiated Polyimides: A Five-to-Tenfold Improvement in Dose Resistance Over Epoxies," Second Topical Meeting on Fusion Reactors, Aug., 1981, Seattle, WA. To be published in J. Nucl Materials.

3. R. R. Coltman,Jr., C. E. Klabunde, and C. J. Long, "The Effect of a 100 MGy (10^{10} Rads) Gamma-ray Dose at 5 K on the Strength of Polyimide Insulators", Special Purpose Materials Annual Progress Report for 1980, USDOE Report, in press.

4. R. R. Coltman, Jr., C. E. Klabunde, R. H. Kernohan, and C. J. Long, "Radiation Effects on Organic Insulators for Superconducting Magnets," Oak Ridge National Laboratory Report ORNL/TM-7077 (November 1979).

5. T. Kato and S. Takamura, "Effect of Low Temperature Reactor Irradiation on Organic Insulators in Superconducting Magnets (I), (II), and (III)," Cryogenic Engineering, 13 243-249 (1978), 14 178-183 (1979); and 15 173-178 (1980).

7.0 Future Work

The IPNS irradiation will be carried out during the next quarter. Measurements on the control samples will begin concurrently. An RTNS-II irradiation is in the planning state.

8.0 Publications

F. W. Clinard, Jr. and G. F. Hurley, "Ceramic and Organic Insulators for Fusion Applications", Second Topical Meeting on Fusion Reactor Materials, Aug., 1981, Seattle, WA. To be published in J. Nucl. Materials.

CHAPTER 3

FUNDAMENTAL MECHANICAL BEHAVIOR

THIS PAGE

WAS INTENTIONALLY

LEFT BLANK

QUANTITATIVE LOAD-ELONGATION CAPABILITIES OF AN IN-SITU HOT TENSILE STAGE FOR HVEM USE

R. D. Gerke and W. A. Jesser (University of Virginia)

1.0 Objective

The objective of this report is to describe the capabilities of the quantitative load-elongation tensile rod that is used in an HVEM to conduct in-situ studies of the nature of crack propagation in irradiated materials, and to indicate the type of data that can be obtained by such an apparatus.

2.0 Summary

It has been demonstrated that load-elongation data can be obtained from thick (40 μm) areas of small tensile specimens while simultaneously observing crack propagation characteristics and microstructural interactions through HVEM video recordings obtained from the thin (< 1 μm) regions of the specimen.

3.0 Program

Title: Simulating the CTR Environment in the HVEM
Principal Investigators: W. A. Jesser and R. A. Johnson
Affiliation: University of Virginia

4.0 Relevant DAFS Program Plan Task/Subtask

Task 11.C.13 Effects of Helium and Displacements on Crack Initiation and Propagation

5.0 Accomplishments and Status

5.1 Introduction

The embrittling process due to radiation damage produced during the normal operation of a reactor has been extensively studied through engineering tests of irradiated bulk specimens that are designed to characterize the brittle nature of the bulk specimens. This characterization is accomplished through the use of such parameters as fracture toughness, elongation (total and uniform), stress intensity factor K, J-integral and crack opening displacement COD. Only COD has any direct microstructural relationship to the fracture mechanism. In order to better understand the mechanisms of fracture and the causes of embrittlement, in-situ deformation experiments are being conducted on thin, electron transparent specimens inside transmission electron microscopes. In this case, typical parameters which characterize the fracture are: crack angles, crack tip radius, plastic zone width and plastic zone lengths[1-4]. There are serious challenges which must be met when attempting to relate the in-situ TEM fracture parameters of thin specimens to those parameters appropriate to the bulk specimen tests. Specimen dimensions (primarily thickness) are important when comparing bulk specimens to thin specimens because of the different stress state created in each (plane stress vs. plane strain). Comparison of the fracture parameters of thin specimens to that of bulk specimens is difficult because of not only the different stress state present but the fact that quantitative tensile data are very difficult to obtain from specimens deformed inside a TEM. The aim of this work is to develop a quantitative load-elongation hot tensile stage and to use it as a tool to suggest methods for linking accepted tensile measurements obtained from bulk specimens to the parameters used to describe ductility in thin foil specimens. This link can ultimately be used to quantitatively measure the ductility of in-situ deformed materials in the TEM which could be a very valuable tool when used in studying the complex fracture process found in radiation damaged materials.

5.2 Hot Tensile Stage Description

The quantitative load-elongation tensile stage has been designed to be used in-situ with the HVEM-accelerator link constructed at this facility[5-8] which means that it is constructed so that it may be tilted to 45° (to the electron beam) so that simultaneous helium ion irradiation and viewing may be performed. A schematic drawing of the tensile rod is shown in Figure 1.

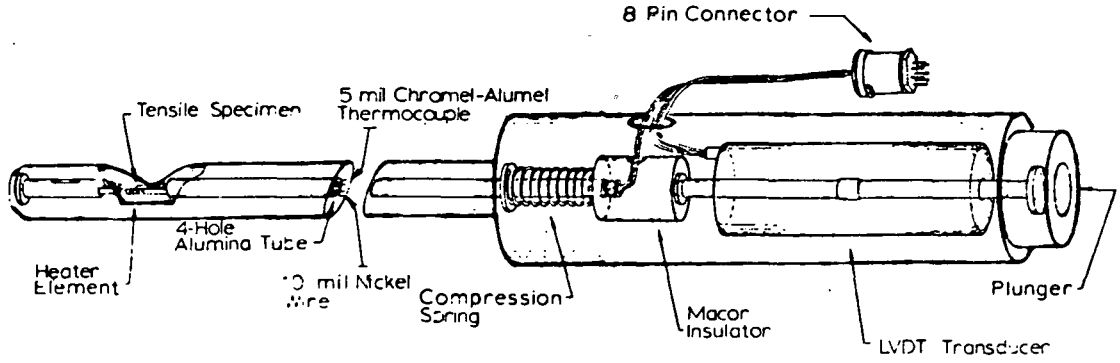

Figure 1. Schematic Drawing of the Quantitative Load-Elongation Tensile Rod.

There is a compact heating element and a thermocouple located in the vacuum area of the HVEM at the tip of the rod and two transducers, to determine load and elongation, at the opposite end of the rod outside of the HVEM (only the elongation transducer is shown in Figure 1). Voltage outputs from the transducers are continually recorded by use of an x-y plotter and a two pen strip chart recorder which is primarily used to maintain a record of the elongation rate. The tensile rod consists of two concentric stainless steel tubes. The outer tube is fixed in place and holds the tensile specimen, while the center portion, which acts as the pulling section, is connected directly to a spring. A hydraulic system compresses and restrains the spring and controls the spring expansion rate and hence the elongation rate of the system, which is not constant. The original design of a hydraulically controlled tensile rod was developed by Wilsdorf[9] and has been modified by Horton[3].

5.3 Primary Tensile Rod Capabilities

5.3.1 Specimen Heaters

The heating element was made in house from nichrome wire and was designed after that of Philips Co. It has a bifilar winding circular in nature and positioned beneath the electrothinned region of the specimen. The electron beam passes through the center of the 3.5-mm diameter element which requires only 1 ampere to produce a recommended maximum specimen temperature of 700° C. Equilibrium time at this temperature is on the order of 15 minutes.

5.3.2 Thermocouple

A standard chromel-alumel thermocouple is mounted near the tip of the specimen stage and is primarily used to monitor the specimen temperature by use of a calibration curve which relates the specimen temperature to the thermocouple reading. Since this tensile rod may be used in simultaneous in-situ He^+ ion irradiation and specimen deformation experiments, a way of monitoring the ion beam by using the thermocouple wires was devised. The center (pulling section) of the rod was electrically insulated from the main body by extensive use of ceramics and provides a method to continuously monitor an effective ion-beam current.

5.3.3 Load and Elongation

The unique aspect of this apparatus is that it can quantitatively measure load and elongation of micro-tensile specimens much like tensile testing machines do on bulk specimens. Measurement of load and elongation is accomplished by use of two transducers: a D.C. operated linear variable differential transformer (LVDT) to determine total elongation, crosshead speed and total pulling force provided by the spring, and a pressure transducer used to determine load exerted on a specimen. In the present configuration, loads up to approximately 10 kg. are possible.

5.4 Tensile Specimen Geometry

The specimens studied are punched from a 1.5 mil (~ 40 μm) sheet which produces a rectangular shaped ribbon specimen, 12.5 x 2.5 mm in dimensions, with a small hole used for gripping at each end. The specimen is annealed and then electo-thinned in the center, approximately 2 mm diameter, leaving a 'thick' portion on each side of the electropolished region. Because of the electropolish configuration, the ribbon specimen can be thought of as the classic 'dogbone' configuration typically used in the tensile testing of bulk specimens, if one neglects the small contribution due to the electropolished region, as shown in Figure 2. This indicates that the load supported by the

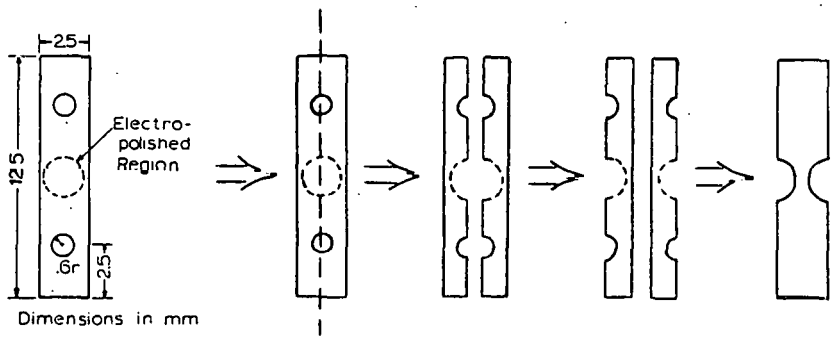

Figure 2. Schematic Illustration Showing the Similarity Between an Electro-thinned HVEM Specimen and a Conventional Tensile Specimen.

specimen is primarily carried by the portion of the specimen not electropolished which means that the tensile data is obtained from these relatively thick regions while microstructural observations, viewed in the HVEM, come from the electro-thinned region. Correlations between the two may be possible. Also, the electro-thinned region is not uniformly thin but exhibits a thickness gradient, 'bowl' shaped, which begins with the thickness of the foil and tapers toward the center of the specimen where a perforation is made. This complicated geometry is present in every specimen that is tensile tested. When a specimen is tensile tested it is secured at both ends with steel clamps, by placing small screws through the clamp and then through the specimen, thus securing the specimen across its entire width.

5.5 Experimental Results

5.5.1 Experimental Procedure

In this study all specimens were type 316 stainless steel and were solution annealed at 1000° C for one hour, and electropolished to electron transparency for 400 kV electrons. The specimens were then tensile tested in an HVEM under three different conditions: 1) unirradiated, tested at room temperature (4 specimens tested), 2) unirradiated, tested at 400° C (3 specimens tested), and 3) neutron irradiated at the LLL RTNS II facility (total fluence $\sim 1 \times 10^{22}$ n/m^2) and tested at room temperature (1 specimen). It should be noted that all unirradiated specimens were electropolished in the same batch at the University of Virginia, while the neutron irradiated specimens were electropolished at ORNL.

5.5.2 Load vs. Elongation

Quantitative load and elongation measurements have been taken from each specimen tensile tested by the apparatus previously described and have been compiled to produce load vs. elongation curves for each specimen condition. The load vs. elongation curves are shown in Figure 3 where the shaded regions in the unirradiated graphs represent one standard deviation of the data. It should be noticed that the data for the unirradiated specimens is closely spaced, indicating that the original cross-sectional area of these specimens are very close which suggests that the consistency of the electropolish from sample to sample is good. Because of the reproducibility of the data obtained from the unirradiated specimens, it is believed that it is meaningful to make a comparison between the curves of the unirradiated specimens and the one curve produced by the RTNS II specimen, even though the cross-sectional area may be different from that of the unirradiated specimens.

The resultant load vs. elongation curves and the specimen's load bearing capabilities depend on the cross-sectional area of the specimen. In order to

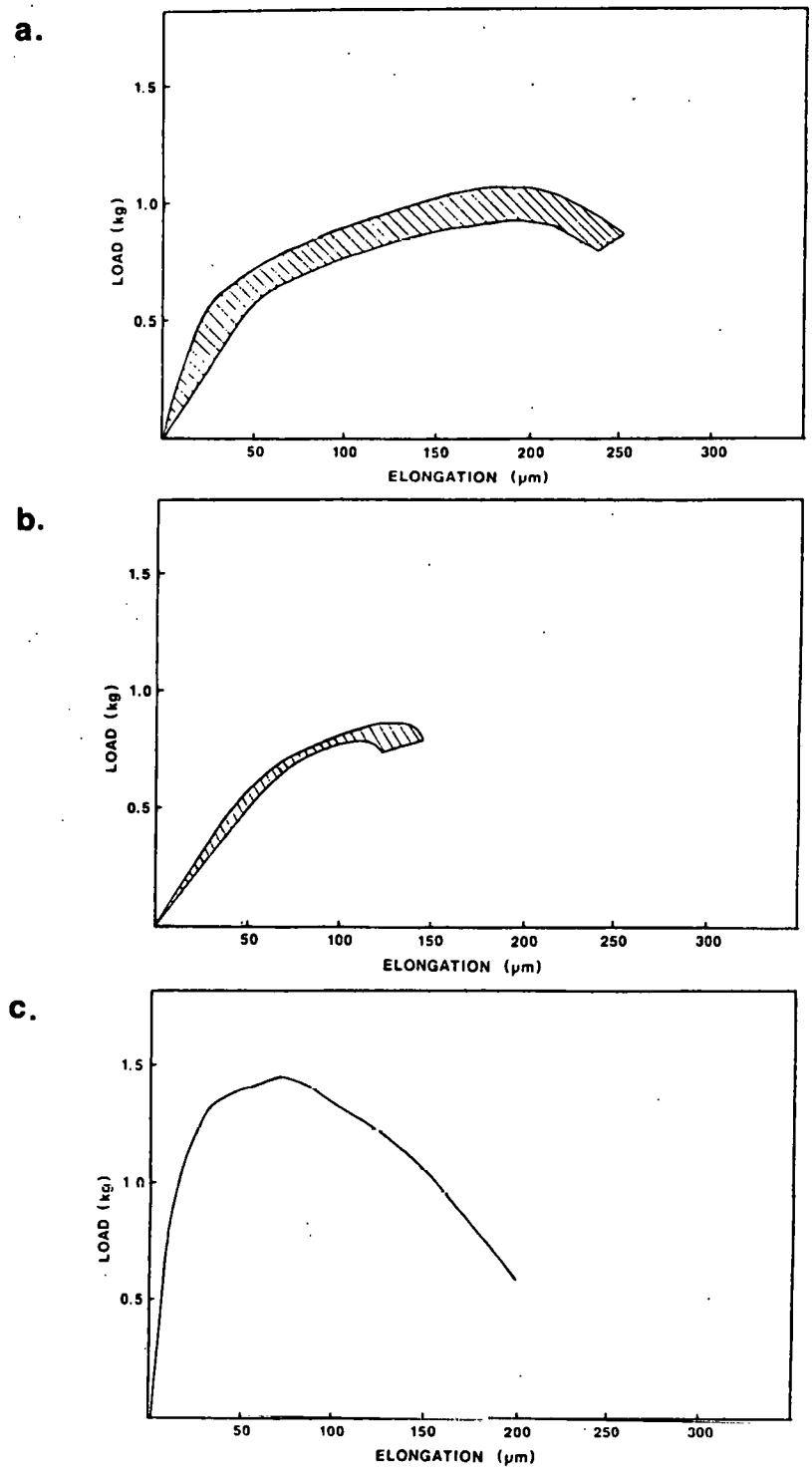

Figure 3. Graphs of Load-Elongation Data Obtained From a) R. T. Unirradiated, b) 400° C Unirradiated, and c) R. T. RTNS II (neutron irradiated to $\sim 1 \times 10^{22}$ n/m^2) specimens.

measure this area several specimens were observed in an SEM. In the unirradiated case, cross-sectional areas were determined by observing specimens after failure as well as a non-tensile tested specimen that was cut in half by a razor blade. Each method deforms the specimen from its original state but yields a way of comparing cross-sections. The cross-sections agreed to within 1% with each other. The cross-sectional area of the neutron irradiated specimen was determined by using the already tensile tested specimen and was found to be 15% greater than that of the unirradiated specimens.

After obtaining cross-sectional areas it is possible to calculate ultimate tensile strengths (UTS) and yield strengths (YS) for the micro-tensile specimens and compare them to the accepted values for bulk specimens. The pertinent values are shown in Table 1.

TABLE 1

Comparison of the Mechanical Properties of HVEM and Bulk Tensile Specimens

Specimen	# tested	Cross-sectional Area ($\times 10^{-2}$ mm^2)	Elongation to Failure (μm)	Maximum Load (kg)	Experimental Foil UTS (MPa)	Experimental Foil YS (MPa)	Bulk[10] UTS (MPa)	Bulk[10] YS (MPa)
R. T. Unirradiated	4	4.38	245 ± 7	0.99 ± 0.07	220 ± 20	97	540	240
400° C Unirradiated	3		133 ± 12	0.83 ± 0.05	190 ± 10	120	460	120
R. T. neutron Irradiated	1	5.04	200	1.46	280	190	---	350*

* Calculated from (11).

5.6 Discussion

A quantitative comparison of the mechanical properties of small and large specimens encounters many difficulties; however, several features of the data are apparent. There is a high degree of similarity between each of the load-elongation curves for equivalent specimens tested under equivalent conditions. The reproducibility of the experiment suggests that there are no uncontrolled

variables. The significant differences between the curves for the different groups of specimens suggests that the variables which are being controlled have a pronounced effect and hence should permit a correlation to be made between the microscopic crack propagation behavior and the data from load-elongation curves.

The effect of neutron irradiation by 14-MeV neutrons to a fluence of 10^{22} m^{-2} increases the room temperature yield stress of bulk specimens by 110 MPa.[11] The increase measured for the room temperature yield stress of the HVEM specimens was 97 MPa. While these relative values show agreement between bulk and HVEM specimens the absolute values are not in agreement. Similarly the change in elongation to fracture with neutron irradiation in the HVEM specimens is consistent with that measured in the bulk specimens.

From the above results one can reasonably expect that when quantitative mechanical property comparisons are made among HVEM specimens subjected to various irradiation conditions, these comparisons should semi-quantitatively reflect bulk specimen data. Because of this agreement between HVEM and bulk specimens a more valid correlation between microstructural behavior and mechanical properties may be made particularly with regard to flow localization mechanisms.

5.7 Conclusions

1. From load-elongation curves obtained from HVEM ribbon specimens 40 μm thick by 2.5 mm wide and 12.5 mm long, it is possible to obtain reproducible data on such mechanical properties as tensile strength, yield strength and total elongation.

2. Relative changes in the measured mechanical properties agree with tests on bulk specimens; however, absolute values agree less well with those from bulk specimens.

3. Video recordings of crack propagation characteristics may be obtained from

the thin regions of the specimen and correlated to the load-elongation curves.

6.0 Future Work

The above techniques for obtaining quantitative mechanical properties of ribbon specimens tensile tested in the HVEM will be applied to type 316 stainless steel specimens which have been neutron irradiated. Correlations between crack propagation characteristics and mechanical properties obtained simultaneously from the same specimen will be made in order to better understand the mechanisms of flow localization.

7.0 References

1. J. I. Bennetch and W. A. Jesser, "Room Temperature Helium Embrittlement in Type 316 Stainless Steel," DAFS Quarterly Progress Report, DOE/ER - 0046/3 (1980) 113.

2. D. S. Gelles, L. E. Thomas, and R. W. Powell,"HVEM In Situ Deformation of Neutron Irradiated Fe - 0.3 Cu," 109th AIME Annual Meeting, Las Vegas, NE (Feb. 24-28, 1980).

3. J. A. Horton, Ph.D. Thesis, Materials Science Department, Univ. of Va. (Jan. 1980).

4. J. I. Bennetch, Ph.D. Thesis, Materials Science Department, Univ. of Va. (May 1981).

5. W. A. Jesser, J. A. Horton and L. L. Scribner, "Adaptation of an Ion Accelerator to a High Voltage Electron Microscope," Radiation Effects 29 (1976) 79.

6. J. I. Bennetch, J. A. Horton, and W. A. Jesser, "Ion Accelerator - HVEM Link," Proceedings 35th Annual Meeting EMSA, ed. by G. W. Bailey (Baton Rouge, LA: Claitor's Publishing Div., 1977) 96.

7. W. A. Jesser, J. A. Horton, J. I. Bennetch, L. L. Scribner, and H. G. F. Wilsdorf, "Instrumentation for SAMI Studies," Proceedings of the US - Japan Seminar on New Applications and Extensions of the Unique Advantages of the HVEM for Physical and Materials Research, University of Hawaii, Honolulu, Hawaii (1976).

8. W. A. Jesser, "Light Ion Accelerator - High Voltage Electron Microscope Facility for CTR Radiation Damage Studies," 1978 Conference on the Applications of Small Accelerators in Research and Industry, North Texas State University, Denton, Texas (Nove. 6-8, 1978); IEEE Transactions on Nuclear Science NS-26 (1979), 1252.

9. H. G. F. Wilsdorf, Rev. Sci. Inst., 4 (1958) 323.

10. W. F. Simmons and H. C. Cross, "Reports on the Elevated-Temperature Properties of Stainless Steels," ASTM Spec. Tech. Pub. No. 124, 1952.

11. R. R. Vandervoort, E. L. Raymond, and C. J. Echer, "High-Energy Neutron Irradiation Effects on the Tensile Properties and Microstructure of 316 Stainless Steel," Radiation Effects 45 (1980) 191.

MECHANICAL BEHAVIOR EVALUATION USING THE MINIATURIZED DISK BEND TEST

M. P. Manahan, A. S. Argon, and O. K. Harling (Massachusetts Institute of Technology)

1.0 Objective

The purpose of this research has been to develop test techniques capable of extracting postirradiation mechanical behavior information from disk-shaped specimens no larger than those used for Transmission Electron Microscopy.

2.0 Summary

1) A new Miniaturized Disk Bend Test (MDBT) has been designed, constructed and is being developed for postirradiation determination of mechanical behavior. This new test is potentially capable of determining most of the mechanical property information needed to screen alloys in the postirradiated state.

2) Experimental reproducibility has been demonstrated between room temperature and 500°C. Various techniques for postirradiation specimen identification have been investigated and laser engraving has been shown to be superior in general.

3) A finite element computer model has been developed utilizing a friction-gap boundary condition to accurately model the MDBT to convert the experimental central load-deflection curves into stress/strain information. Preliminary results using small strain theory show excellent agreement with experimental data.

3.0 Program

Title: Alloy Development for Irradiation Performance in Fusion Reactors
Principal Investigators: O. K. Harling and N. J. Grant

Affiliation: Nuclear Reactor Laboratory and Materials Science and Engineering Department, Massachusetts Institute of Technology

4.0 Relevant DAFS Program Plan Task/Subtask

Task II.C.7 Effects of Helium and Displacements on Flow
II.C.8 Effects of Helium and Displacements on Fracture
II.C.9 Effects of Hydrogen on Fracture
II.C.10 Effects of Solid Transmutation Products on Fracture Behavior
II.C.11 Effects of Cascades and Flux on Flow
II.C.12 Effects of Cycling on Flow and Fracture
II.C.13 Effects of Helium and Displacements on Crack Initiation and Propagation
II.C.15 Effect of Near Surface Damage on Fatigue
II.C.19 Comparison of *In Situ* and Postirradiation Fracture Behavior

5.0 Accomplishments and Status

5.1 Introduction

There exist many promising advanced alloy systems for possible Controlled Thermonuclear Reactor applications and, of course, within each system myriads of thermomechanical treatments and processing conditions can be developed. The mechanical behavior of prime candidates from each of these alloy systems needs to be readily determined in the postirradiated state in a timely and cost effective fashion. To this end, a Miniaturized Disk Bend Test (MDBT) is being developed, which is potentially capable of determining from biaxial measurements:

1. plastic stress/strain response
2. ductility
3. stress relaxation behavior
4. creep response
5. creep ductility

6. S-N fatigue response
7. ductile/brittle transition temperature

Disk-shaped specimens are used which are no larger than those used for Transmission Electron Microscopy (TEM). In addition, information on cyclic behavior could be obtained by use of the standard low cycle fatigue formalisms using information from the tensile response of the material, or directly via measurements using the MDBT procedure to generate S-N curves. In the MDBT measurements, the stress field is biaxial, and the analytical modeling of the experiment accounts for multiaxial stress states. Therefore it is readily possible using the MDBT to report biaxial behavior as well as referencing back to the more conventional uniaxial behavior.

Thus, outside of fracture toughness, the MDBT could potentially provide most of the mechanical behavior information desired to screen many alloy systems in the postirradiated state. There are two principal conceptual innovations present in the MDBT. The first innovation is to use bending to extract mechanical behavior information from a very small sample as opposed to the more standard approach of using uniaxial tensile loading requiring gripping extensions. The second innovation is the use of the finite element method to extract useful engineering information from the experimental data. While the former innovation has been suggested and used also by others[1-3,5] with analytical modeling, the latter was first proposed by Manahan and Argon[4] and derives its motivation from the impression creep and impression fatigue tests described by Li and coworkers[6-8].

The determination of a stress/strain curve from a pure bending test, using analytical expressions, was first reported by Herbert[1] for cast iron bars. More recently, Crocker[2] has obtained stress/strain information for large deflections and plastic strains using a three point rotary bend test. He uses the same analytical expressions as Herbert and implements a progressive reconstruction technique to transfer the moment-angle measurements into a stress/strain relationship. Stelson et al.[3] have used an adaptive controller to measure force and displacement during brakeforming to estimate

workpiece parameters with a microcomputer, which are then used in an analytical elastic-plastic material model to predict correct final punch position. Although these earlier developments have been useful, particularly in the metals-forming industry, they are not readily adaptable to postirradiation mechanical behavior testing because of large size and awkward loading configuration. For this application we have proposed earlier[4] a simply supported miniaturized disk of the size of TEM specimens, which we have now developed much further. We are aware that a similar specimen and loading configuration to provide for ductility screening has also been under development at the Hanford Engineering Development Laboratory (HEDL), using small strain analytical expressions[5]. The advantage of the finite element method for data inversion that we are developing is that it permits the extraction of both plastic resistance and creep resistance from the raw data in addition to the information on ductility from irradiated samples exhibiting moderate to large levels of strain to fracture and with a minimum of material. Recent progress on the task of generating stress/strain and ductility information using the MDBT will be reported in Sections 5.3-5.5. Section 5.2 provides a brief discussion of the experimental approach taken. The reader is referred to References 4 and 9 for further details.

5.2 Experimental Approach

In the MDBT the simply supported disk is centrally loaded. The specimen disk, which has dimensions of 3.0 mm x 0.25 mm, rests in a cylindrical die and the alumina punch presses the disk into the cavity as shown schematically in Figure 1.

The actual test apparatus has been adapted to an Instron 1331 servo-hydraulic machine with environmental chamber and induction furnace as shown schematically in Figure 2. During the test, either the applied load of the punch vs time under constant impression velocity, or the punch displacement vs time under constant applied load are measured. Deflections are measured external to the environmental chamber with MTS axial extensometers (Type 632.12). The

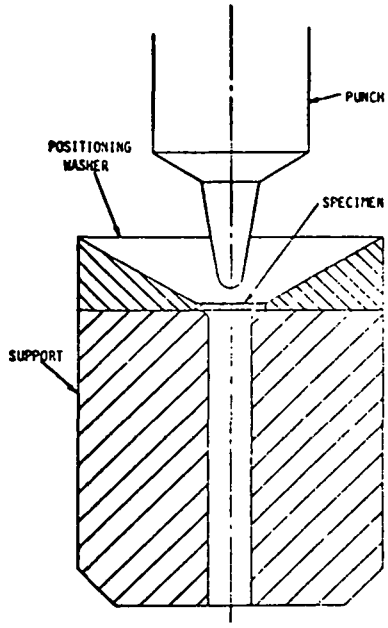

FIGURE 1. Schematic of Miniaturized Disk Bend Test Showing Simply Supported Central Loading.

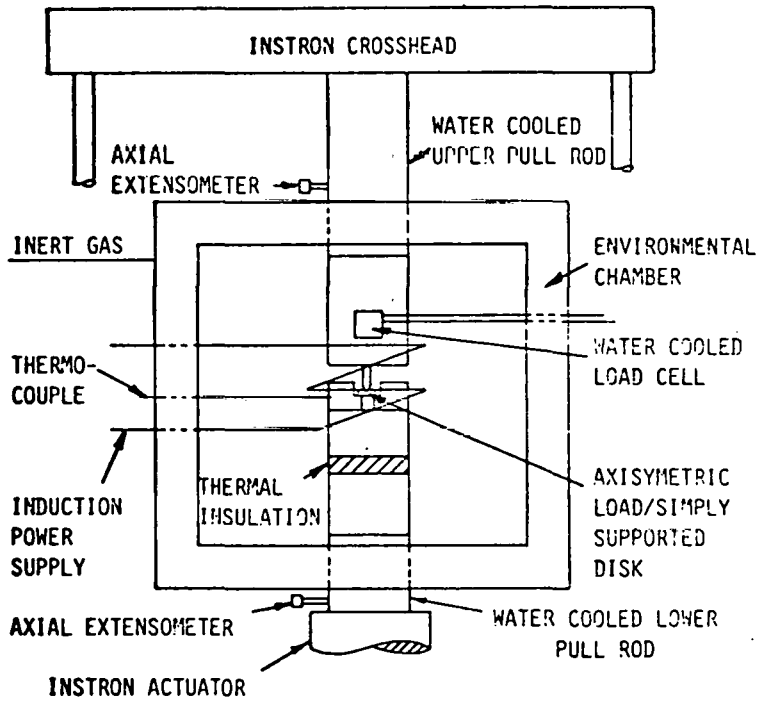

FIGURE 2. Miniaturized Disk Bend Test Experimental Configuration.

maximum error in deflection measurement over the entire calibrated range is 0.00254 mm. A water cooled load cell using semi-conductor strain gauges provides accurate load measurement. The maximum error in load measurement over the entire calibrated range is 6.67 N. The water cooling eliminates any apparent strain effects due to temperature drifts. The load cell is placed in the environmental chamber to eliminate effects due to frictional forces at the upper bellows seal.

The test apparatus is shown in Figure 3 in exploded view. Most interfaces in the load train are prestressed to minimize nonlinear contact forces. High density alumina was chosen for the punch and die material because of its large compressive strength, good wear resistance, and low thermal conductivity compared with the steel specimens. Invar was chosen for the load train material because its low thermal expansion coefficient matches that of the strain gauges and thus essentially eliminates apparent strain effects from temperature variations. The positioning washer and upper disk support structure were fabricated from 304SS to provide some thermal expansion and thus maintain simply supported conditions at elevated temperatures. Since the compression rods are water cooled, heat loss via conduction through them is reduced by using ceramic washers in the load train. A suction operated handling system has been designed to facilitate radioactive specimen handling and positioning.

The MDBT has been designed to operate at elevated temperatures. There are two thermocouples (TC) permanently attached to the upper disk support structure; one for control, and one for recording. For calibration purposes, a small diameter TC was silver soldered to the disk and the temperature calibrated with the permanent control TC, which is located in the upper disk support structure. With the present design of the MDBT apparatus, testing is currently carried out in an inert gas atmosphere after the environmental chamber has been pumped down and flushed several times.

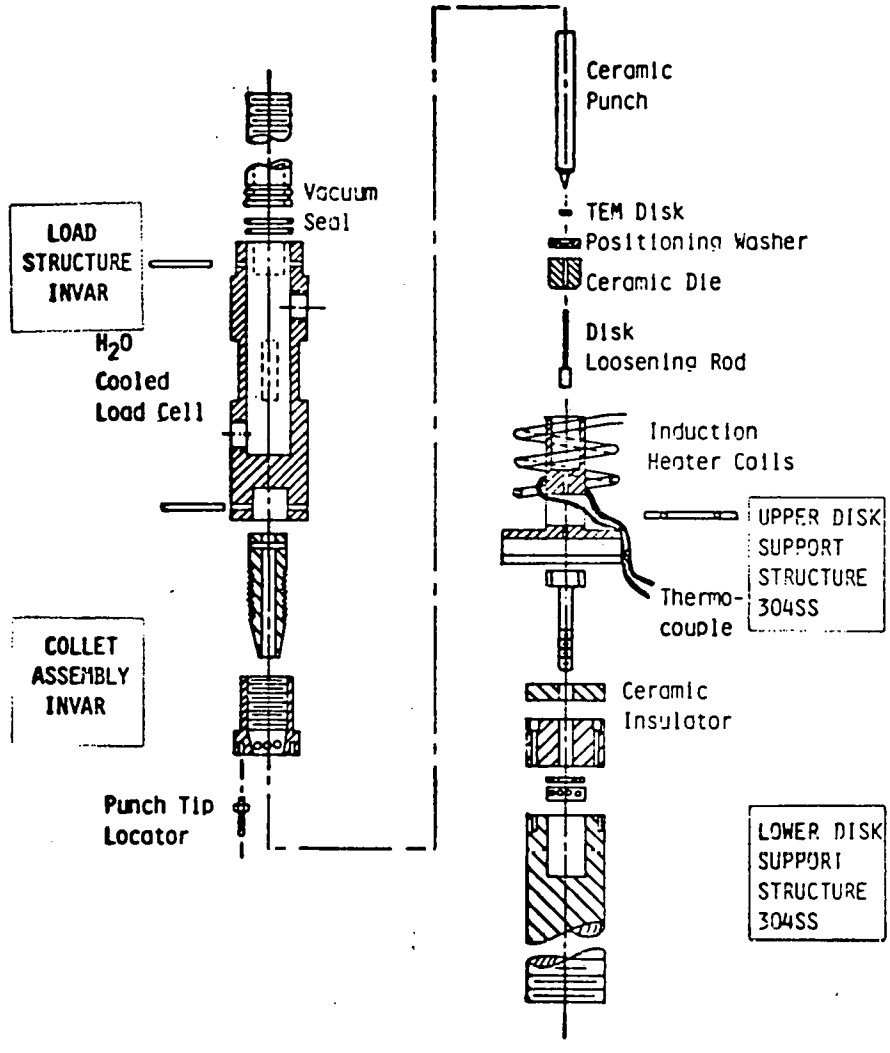

FIGURE 3. Miniaturized Disk Bend Test Apparatus.

5.3 Experimental Reproducibility

Experimental Reproducibility for ten separate tests at room temperature is shown in Figure 4. The tested material was 316SS with 20% cold work (CW).[1] This material was chosen because the mechanical behavior has been well

[1]Material obtained from HEDL in rolled sheet 0.348 mm thick; heat designation 87210; HEDL N-LOT. For this we are grateful to Dr. J. Straalsund, Dr. R. W. Powell, and Dr. M. Paxton.

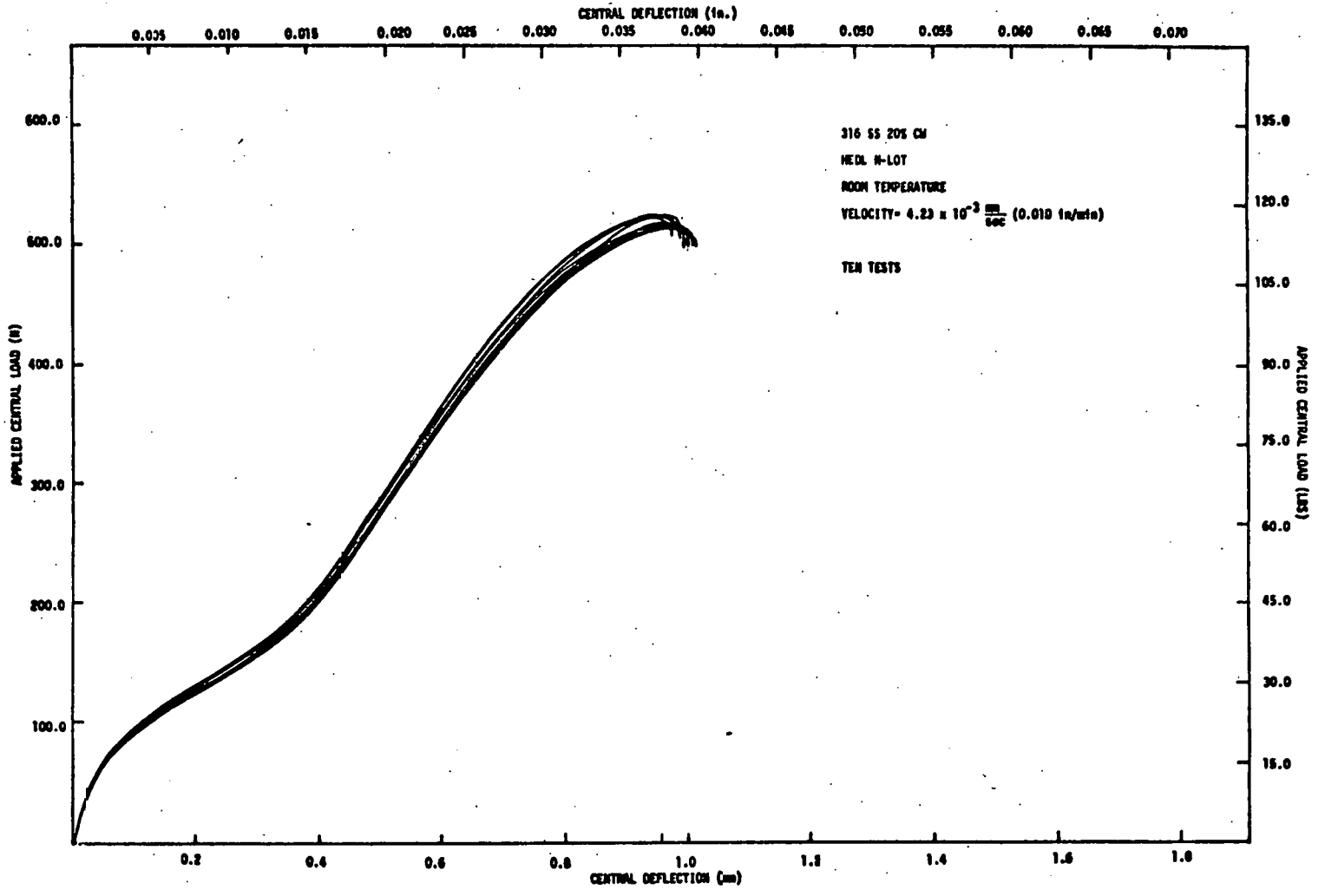

FIGURE 4. Miniaturized Disk Bend Test Reproducibility for Room Temperature, Ten Separate Tests. All Curves are Within 1.8% of the Mean Along the Entire Curve.

characterized and should serve as a good validation of the MDBT. The specimens were stamped from rolled sheet to a diameter of 3.0 ± 0.0076 mm and subsequently precision lapped to a thickness of 0.254 ± 0.00254 mm.

Alignment of the punch and die as well as specimen centering are critical since disk stiffness increases with eccentricity of loading. There are two basic contributions to total eccentricity which are of prime importance: 1) punch axis of symmetry not coincident with die axis of symmetry, and 2) design tolerances for die, positioning washer, upper disk support structure, and specimen outer diameter. The former eccentricity has been reduced by using a precision alignment fixture, and the latter, by careful experimentation and by accurate machining of key components. The total eccentricity of loading was measured and found to be approximately 0.0178 mm for all the curves in Fig. 4. For this eccentricity, the central load-deflection curves for the ten tests fell within a band that is only 1.8% of the mean along the entire curve. An earlier reproducibility investigation with a total eccentricity of approximately 0.0635 mm was reported in Ref. 9 for room temperature on ten samples of the same material. In this case, the reproducibility band was 3.0% of the mean along the entire curve.

The central load-deflection reproducibility is as good as or better than that normally attainable in conventional mechanical behavior testing of materials from a given heat. The American Society for Testing and Materials (ASTM) is developing quantitative estimates of the precision and accuracy of the methods set forth in Standard E8, "Tension Testing of Metallic Materials"[10]. The ASTM currently advises that statements on accuracy should be limited to the documented performance of particular laboratories. Ref. 11 reports axial tensile data for Fast Test Reactor prototypic fuel cladding lots. Nine tests at room temperature were reported for the N-LOT material. For purposes of comparison with MDBT data, 95% confidence limits, assuming a normal distribution, were calculated for the 0.2% yield stress and the engineering Ultimate Tensile Strength (UTS) from the data in Ref. 11. The confidence limits were found to be ± 1.75% of the mean for the 0.2% yield stress, and ± 0.95% of the mean for the UTS. Likewise, 95% confidence limits for the load response were calculated

using the MDBT data in Fig. 4 for a central deflection of 0.76 mm. The confidence limits in this case were found to be ± 0.52% of the mean. Work is currently underway to determine the accuracy of the finite element model in converting the experimental data into stress/strain information.

The reproducibility for 500°C tests is shown in Fig. 5 for the same material. This material has been shown to have negligible strain rate dependence at this temperature[12] for strain rates in the range of $10^{-5}sec^{-1}$ to 10 sec^{-1} and, therefore, a convenient punch velocity of 4.23 x 10^{-3} mm/sec was chosen. This velocity corresponds to a strain rate of approximately $10^{-3}sec^{-1}$. The total eccentricity was approximately 0.178 mm, and the five central load-deflection curves all fell within 1.4% of the mean along the entire curve. Experimental reproducibility in general has been judged to be quite good and total eccentricities of less than 0.0254 mm are achievable in practice and produce errors in test results which are comparable to or less than other experimental and analytical modeling uncertainties.

Demonstration of elevated temperature reproducibility is, of course, of prime importance since all experimental, geometric and material variables contribute to the data spread. In particular, grain size effects can be quite limiting for miniaturized samples. However, this is not the case for the MDBT as evidenced by the reproducibility curves. Two of the reproducibility samples in the pre- and post-bent state were sectioned, polished, and examined using a Bausch and Lomb optical research metallograph. There were approximately six grains through the thickness and approximately 70 grains across the diameter for the N-LOT material. Considering that about 10 grains probably represents a lower limit to achieve continuum behavior, it is clear that in the through thickness direction this is not the case. However, the stress components and the plastic strains that lead to fracture are approximately tangent to the curvature throughout the deformation. Therefore, the number of grains across the diameter is more important than the number through the thickness. This is one of the main reasons why this loading configuration was chosen. For materials with smaller grain sizes, such as those produced by rapid solidification, these considerations are of even less concern since, in general, continuum behavior through the thickness is achieved there as well.

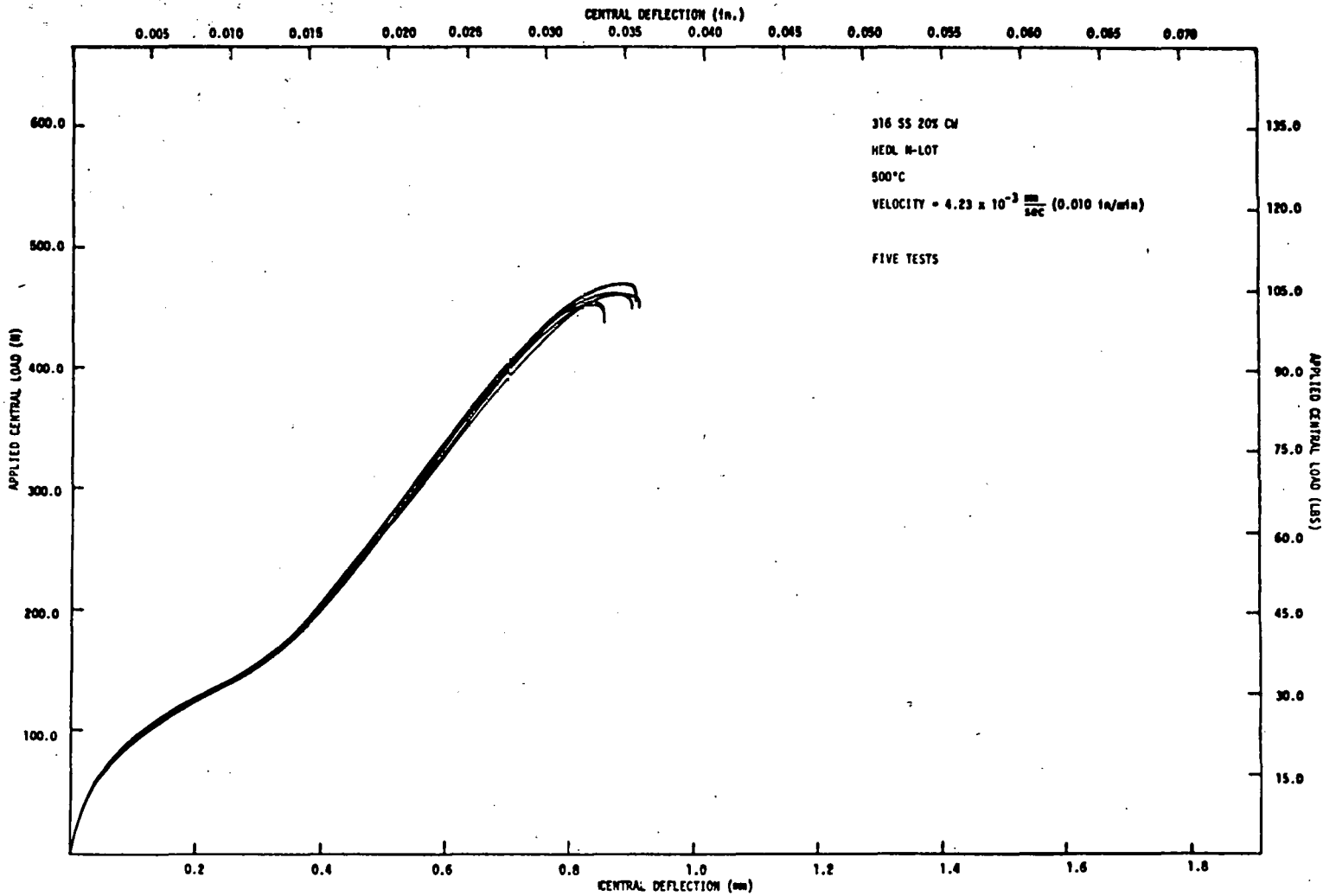

FIGURE 5. Miniaturized Disk Bend Test Reproducibility for Elevated Temperature, Five Separate Tests. All Curves are Within 1.4% of the Mean Along the Entire Curve.

5.4 Specimen Identification Study

Since the MDBT is being developed primarily for postirradiation applications, it is imperative that a method of identifying specimens without altering the kinematic response be investigated. A second criterion to be considered is that the identification characteristic be visible on remote closed circuit television cameras for hot cell sorting of the samples. Three methods of identification have been investigated: 1) radial slitting, 2) stylus engraving and 3) laser engraving.

5.4.1 Radial Slitting

Three radial slits 0.254 mm wide were cut through the thickness on the outer specimen edge approxiamtely 0.254 mm apart. The radial depths of the slits for a given specimen were 0.254 mm and 0.127 mm respectively. The latter radial depth is just visible in remote cameras in normal practice. The former radial depth was chosen because it is the length of the portion of the specimen which initially rests on the flat part of the die in the MDBT. The specimens were fabricated from 316SS with 20% CW (N-LOT) and tested at room temperature. In both cases the central load-deflection curves fell below the reproducibility band for the same material, as shown in Figure 6. The removal of material from the outer edge results in a decrease in plate stiffness. No cracks were found near the slits. This method of identification has been abandoned for all future irradiations.

5.4.2 Stylus/Laser Engraving

An alternative method of specimen identification is to engrave alphanumeric characters on one or both specimen surfaces. Stylus engraving ploughs the material and leaves a track with a material lip protruding above the specimen surface. Laser engraving exfoliates the material by ablation and also leaves a track with a protruding lip. We can quantify these processes somewhat by measuring the height of the lip from the specimen surface, the width of the

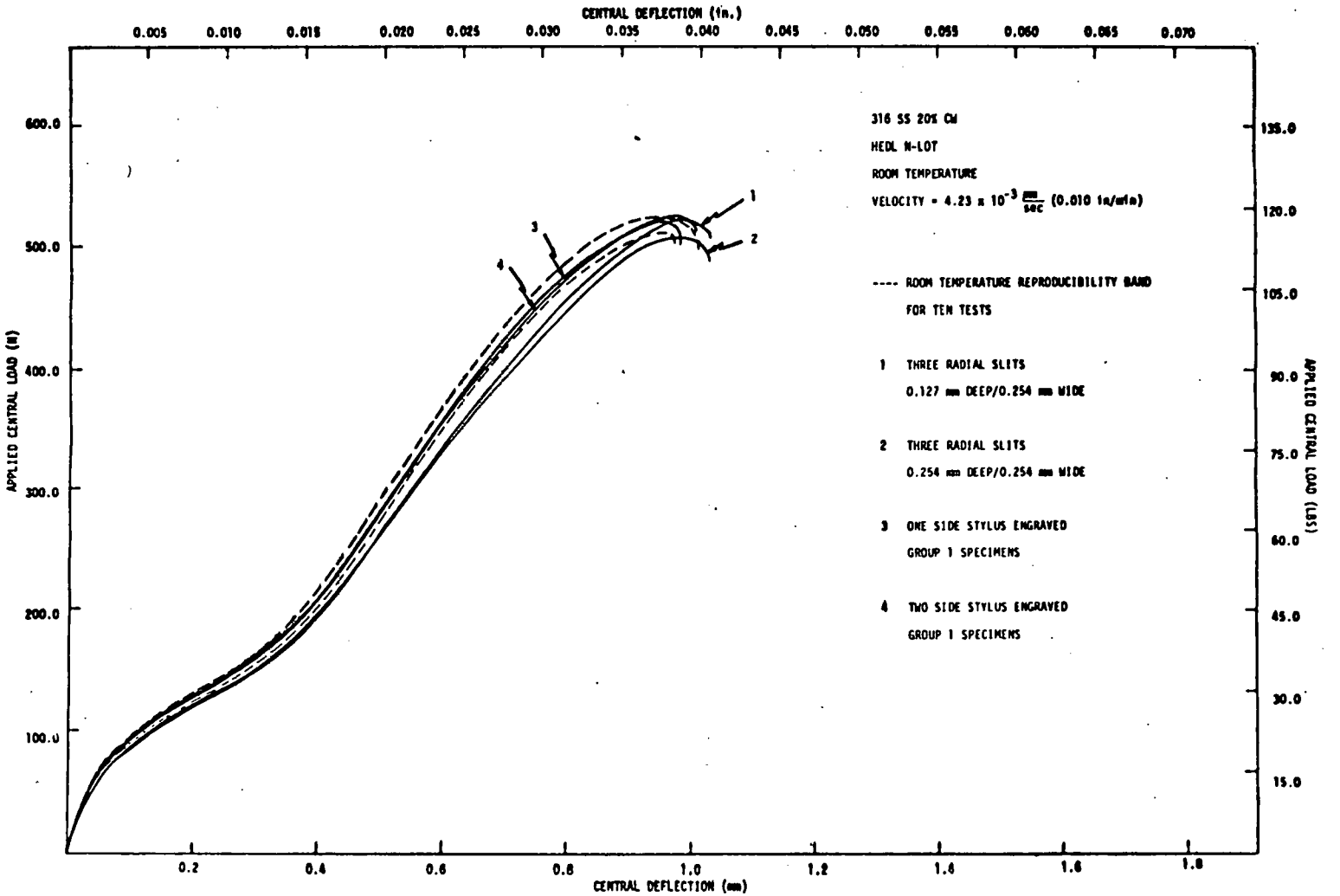

FIGURE 6. Miniaturized Specimen Identification Study Results for Radial Slitting and Stylus Engraving. Results Are Compared to a Series of Tests With Unmarked Specimens of the Same Material.

track at the specimen surface, and the depth of the track from the specimen surface. Table I lists measurements of these parameters for the three specimen groups examined. The measurements were made using an optical depth micrometer. Group 1 was engraved by hand at M.I.T. and the tracks were relatively shallow and narrow. Tests on N-LOT material at room temperature were performed on specimens with one and two sides engraved and the central load-deflection curves were found to be within the reproducibility band for this material, as shown in Figure 6.

Group 2 specimens were prepared at Hanford Engineering and Development Laboratory (HEDL)[1] and were stylus engraved. The tracks were one sided and relatively wide and deep. These specimen dimensions were 3 mm x 0.31750 mm and the material was N-LOT. The central load-deflection curves for the engraved samples were found to be quite different from the unengraved samples at room temperature and at 500°C, as shown in Figure 7.

Group 3 specimens, having the same dimensions as those of Group 2, were also prepared and laser engraved on one side at HEDL. The central load-deflection curves for the engraved and unengraved Group 3 samples were found to be within expected reproducibility bands for room temperature and 500°C.

In summary, stylus engraving is in general acceptable provided the character tracks are relatively narrow and shallow. Wide and deep tracks cause a plate stiffness reduction. However, one-sided laser engraving is somewhat more desirable because the exfoliated lip height is greater than the lip obtained by shallow stylus tracks and is therefore more visible for hot cell sorting after irradiation.

5.5 Finite Element Modeling

The finite element analysis of the MDBT data is essential for the conversion of the experimentally determined central load-deflection curve to stress/strain information. In order to accurately analyze this highly nonlinear

[1]We are grateful to Dr. D. Peterson for specimen preparation.

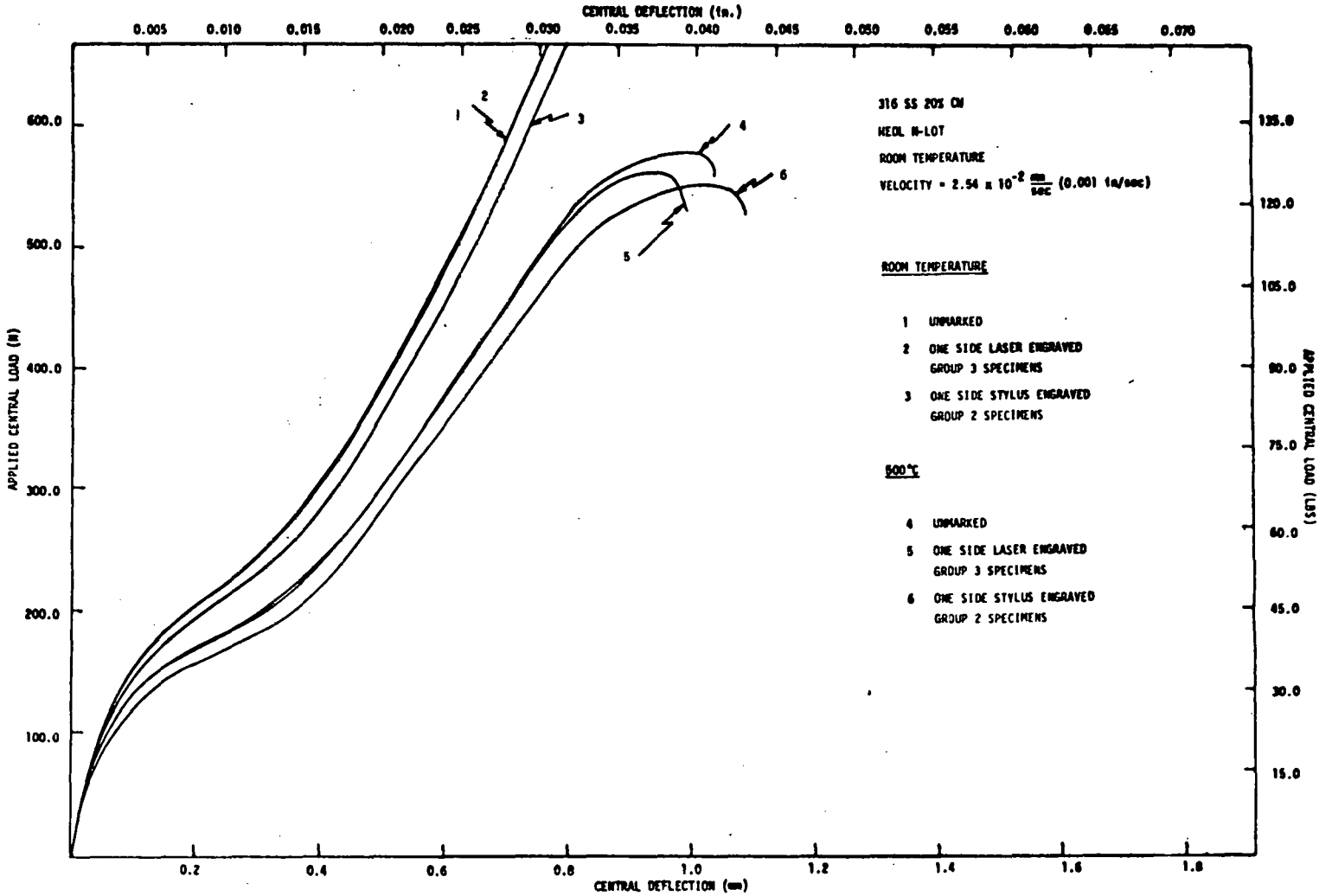

FIGURE 7. Miniaturized Specimen Identification Study Results for Stylus and Laser Engraving.

TABLE I

STYLUS/LASER-ENGRAVED PARAMETER MEASUREMENTS

Parameter \ Specimen Group	1 Stylus Engraved		2 Stylus Engraved		3 Laser Engraved	
	(mm)	(in)	(mm)	(in)	(mm)	(in)
Character height from specimen surface	0.00381-0.00762	0.00015-0.0003	0.0127-0.02032	0.0005-0.0008	0.03048-0.04572	0.0012-0.0018
Track width at specimen surface	0.0254-0.0762	0.001-0.003	0.127-0.254	0.005-0.010	0.02032-0.02794	0.0008-0.0011
Track depth from specimen surface	0.00381-0.01016	0.00015 0.0004	0.0127-0.03302	0.0005-0.0013	0.00254-0.00508	0.0001-0.0002

boundary value problem with shifting contacts, a model to reproduce the frictional contact has been developed for the support[13]. A similar model with the additional boundary condition of punch velocity has also been developed. There is experimental evidence that suggests that at the center of loading the specimen may separate from the punch and leave only an annular section in contact for a punch tip radius of 0.508 mm. In all experiments using this size punch, the specimen was stuck on the punch tip after large plastic strains. In addition, fracture has been observed to occur at a radial location of approximately 0.254 mm for 302SS shim stock. This is due to the fact that the punch tip is of finite radius and causes an abrupt change in specimen curvature at this location. Thus, it is anticipated that the friction-gap model, applied at the support and also at the punch, will prove essential in accurately predicting the specimen curvature as a function of central deflection and also in predicting the fracture location. Further experimental evidence illustrating the importance of accurately modeling the punch boundary condition is shown in Figure 8, where the punch tip radius is varied while all other experimental variables are held constant.

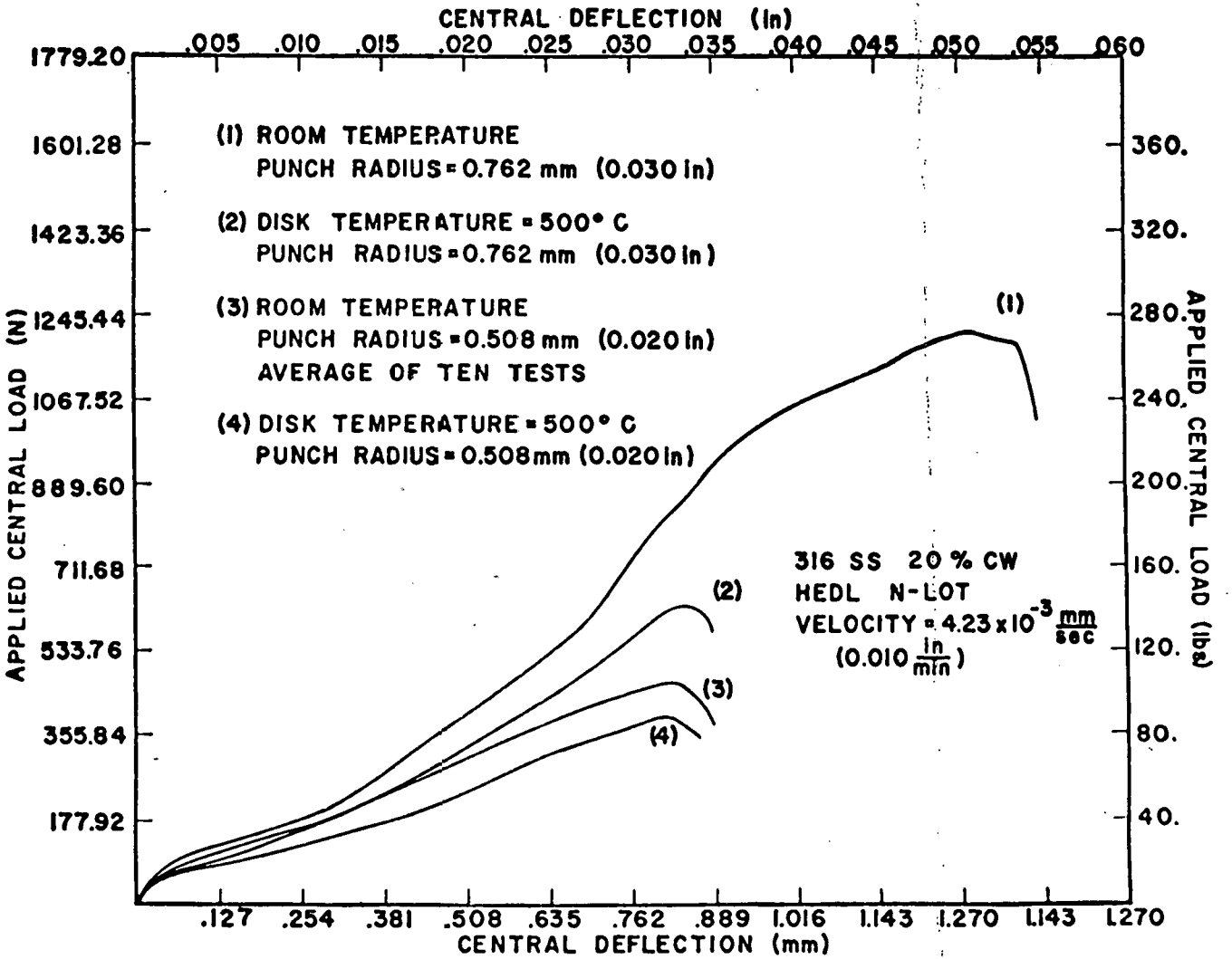

FIGURE 8. Miniaturized Disk Bend Test Results for Two Different Punch Radii.

The ABAQUS[14] computer code was chosen for this modeling application because of its superior nonlinear capabilities and the fact that it already contains a simple two body single node frictional-gap model applicable to Cartesian space. The code uses classical Colomb friction with a stiffness in stick method to aid convergence. This simple model can be used as a basic building block to accurately represent multiple node friction contact boundary conditions for essentially any geometry by the introduction of the shadow node concept that helps monitor the region of contact between a rigid support and a deforming structure in contact with it. The details of this finite element development will be presented in future reports and papers. It will suffice here to state that the multipoint constraint equations due to such sliding contacts have been incorporated into the ABAQUS program as subroutines.

The validity of the MDBT must be demonstrated for a material with well characterized tensile properties before it can be safely used in practice. The N-LOT material was chosen for this purpose. Of course, once this is accomplished, the MDBT can be used to determine mechanical behavior. The known tensile properties of the N-LOT material were used as code input. The problem at hand, therefore, reduces to that of generating the central load-deflection curve using the finite element method. Preliminary finite element results are shown in Figure 9. Twenty eight-noded two dimensional axisymetric continuum elements were used for this analysis and the punch and die friction-gap models were implemented. Multilinear hardening was used. The small strain theory in ABAQUS-3 was used and is valid up to approximately 5% strain. It was found that significant portions of the plate had exceeded 5% strain for central deflections less than 0.254 mm. It is obvious that finite strain theory is necessary to analyze materials with moderate to large ductility. Work is currently underway to implement the finite strain version of ABAQUS. Also, the convergence parameters were quite generous for the results shown in Figure 9. Nevertheless, the agreement of the finite element model with the experimental data is shown to be quite good. It is anticipated that further mesh refinement, tighter convergence parameters, and finite strain modeling will enable analytical model prediction of the entire experimental curve.

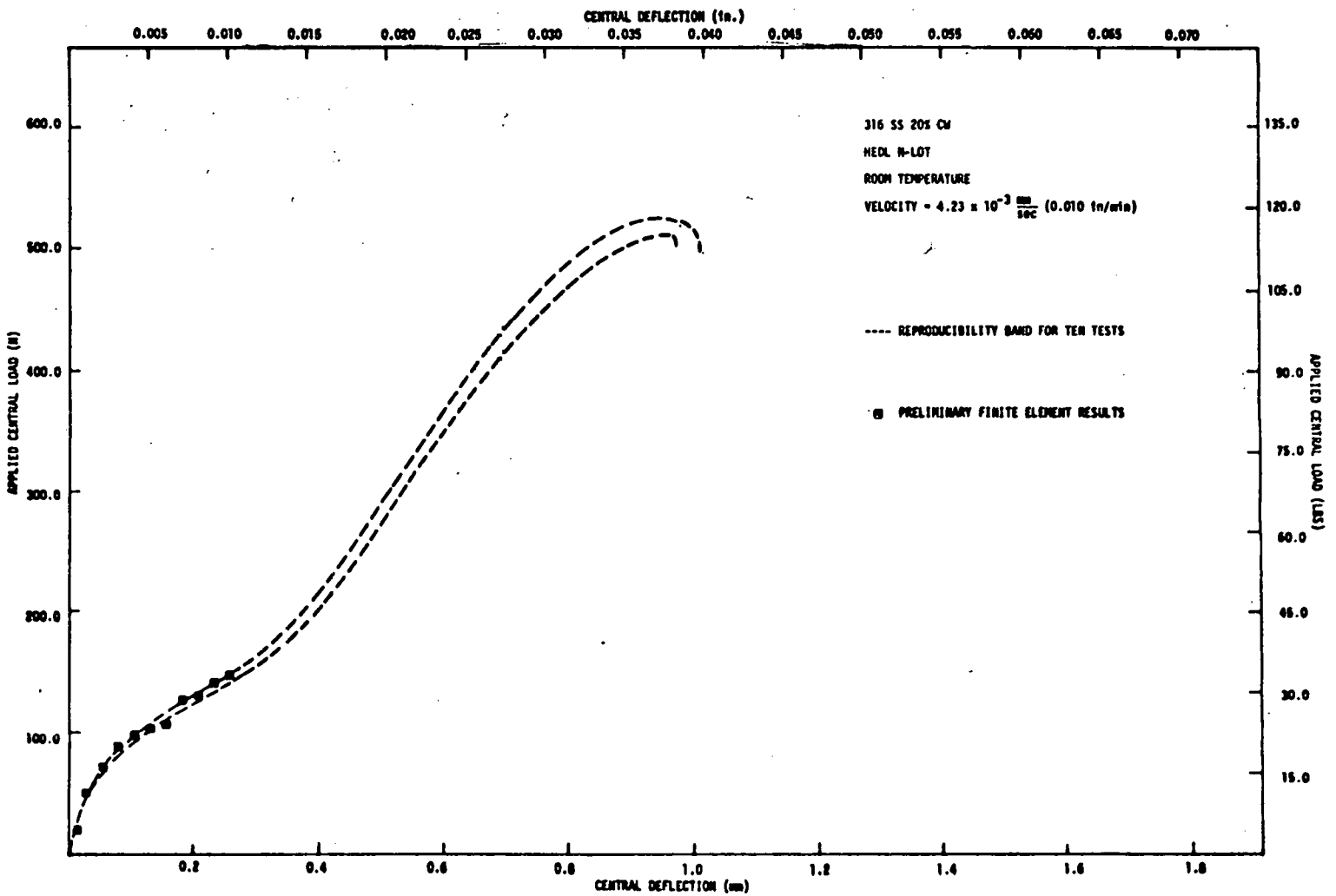

FIGURE 9. Preliminary Finite Element Results for Modeling of Miniaturized Disk Bend Test.

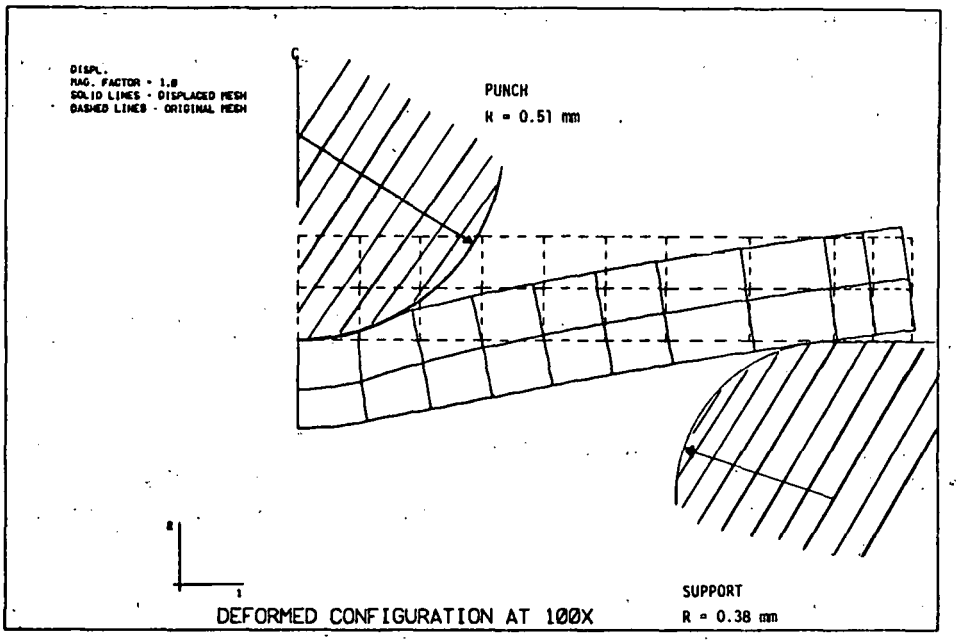

FIGURE 10. Finite Element Model Prediction of Displaced Disk for Central Punch Displacement of 0.254 mm.

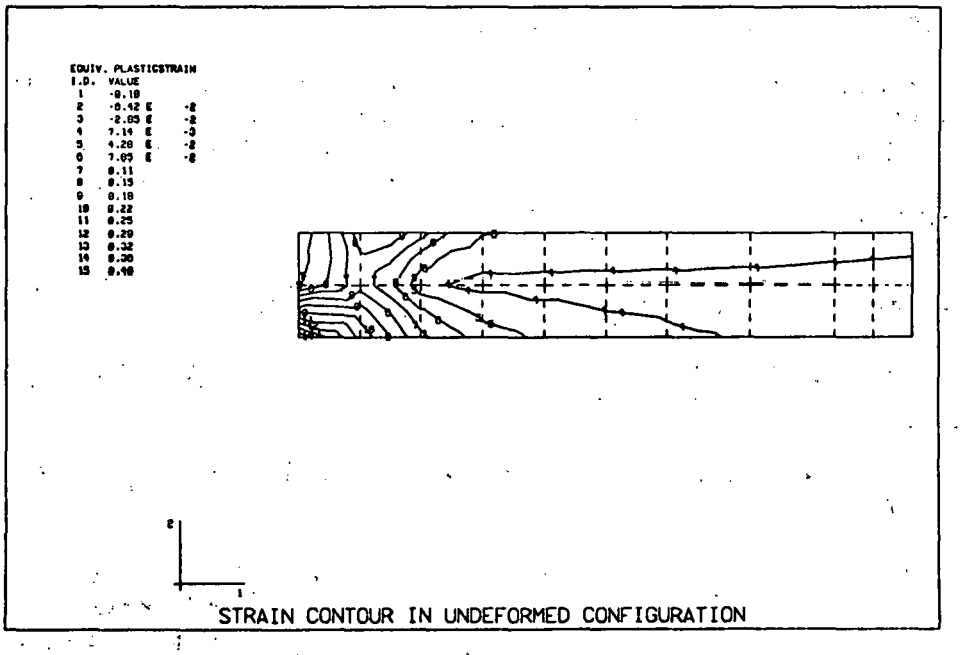

FIGURE 11. Finite Element Model Prediction of Equivalent Plastic Strain Contour for Punch Displacement of 0.254 mm, Referenced Back to Underformed Configuration.

The deformed configuration of half the plate superimposed on the undeformed configuration is shown in Figure 10 for a central deflection of 0.254 mm. The model predicts separation of the punch and plate at the center when the punch displacement is 0.0762 mm. Figure 11 presents strain contours in the undeformed configuration corresponding to a central deflection of 0.254 mm.

6.0 References

1. Von H. Herbert, "Ueber den Zusammenhang der Biegungselastizitat des Gusseisens mit seiner Zug- and Druckelastizitat," Mitt. u Forschungsarb, Ver. deut. Ing., 89, 1910.

2. W. H. Crocker, "Obtaining a Stress/Strain Relationship from a Rotary Three-Point Bend Test with Large Plastic Displacement," submitted in partial fulfillment of the requirements for the M.S. Degree at M.I.T., August 1979.

3. K. A. Stelson and D. C. Gossard, "An Adaptive Pressbrake Control Using an Elastic-Plastic Material Model," Proceedings of the 1981 Joint Automatic Control Conference, 11, June 17-19, 1981, Charlottesville, Va.

4. Annual Report of Alloy Development for Irradiation Performance in Fusion Reactors, by M.I.T. Project Staff, Alloy Development Project, O. K. Harling and N. J. Grant, Co-Principal Investigators, September 1979-September 1980, Report No. MITNRL-006 and DOE/ER-10107-1, December 1980.

5. That a ductility test has been developed by HEDL and used on irradiated metals since 1978 for alloy ductility screening has been privately communicated by G. Wire to M. P. Manahan, October 1980, and has also been disclosed in HEDL-SA-2438, "Bend Testing for Miniature Disks," to be published in the J. of Nucl. Tech.

6. H. Yu and J. C. M. Li, "Computer Simulation of Impression Creep by the Finite Element Method," J. Mater. Sci., 12, 2214 (1977).

7. S. N. G. Chu and J. C. M. Li, "Impression Creep; a New Creep Test," J. Mater. Sci., 12, 2200 (1977).

8. S. N. G. Chu and J. C. M. Li, "Impression Fatigue," Scripta Met., 13, 1021 (1979).

9. M. P. Manahan, A. S. Argon and O. K. Harling, "The Development of a Miniaturized Disk Bend Test for the Determination of Postirradiation Mechanical Properties," presented at the Second Topical Meeting on Fusion Reactor Materials, August 9-12, 1981, Seattle, Washington, and to be published in a special topical report of the J. of Nucl. Mater.

10. Standard E8, "Tension Testing of Metallic Materials," 1980 Annual Book of ASTM Standards, Part 10, Metal-Physical, Mechanical, Corrosion Testing (American Society for Testing and Materials).

11. M. M. Paxton, "Mechanical Properties of Annealed and Cold Worked Type 316 Stainless Steel Fast Reactor Tubing," HEDL-TME 74-11, February 1974.

12. Nuclear Systems Material Handbook, No. TID 26666, U. S. Department of Energy.

13. M. P. Manahan, "The Development of a Friction Gap Boundary Condition Model," submitted in partial fulfillment of the requirements for M.I.T. Course 2.093, Computer Methods in Dynamics (May 1981).

14. ABAQUS, developed by Hibbit and Karlsson, Inc., Providence, Rhode Island.

7.0 Future Work

Finite strain theory will be implemented in the analytical modeling and the results compared with experimental data for the N-LOT material. Once the validity of the MDBT is demonstrated, the method will be applied to irradiated samples to determine their tensile behavior.

8.0 Publications

Annual Report of Alloy Development for Irradiation Performance in Fusion Reactors, by M.I.T. Project Staff, Alloy Development Project, O. K. Harling and N. J. Grant, Co-Principal Investigators, September 1979-September 1980, Report No. MITNRL-006 and DOE/ER-10107-1, December 1980.

M. P. Manahan, A. S. Argon and O. K. Harling, "The Development of a Miniaturized Disk Bend Test for the Determination of Postirradiation Mechanical Properties," presented at the Second Topical Meeting on Fusion Reactor Materials, August 9-12, 1981, Seattle, Washington, and to be published in a special topical report of the J. of Nucl. Mater.

AN APPROACH TO SMALL SCALE DUCTILITY TESTS

M. Dooley, G. E. Lucas, J. W. Sheckherd (University of California, Santa Barbara)

1.0 Objective

The purpose of this aspect of the program is to develop test techniques to extract mechanical property information from small volume specimens either being used or planned for use in neutron irradiation experiments for the fusion materials development program.

2.0 Summary

A study was undertaken to investigate the potential applicability of a bulge test for extracting ductility information from small, thin sheet specimens. A bulge testing apparatus was fabricated and used to test to failure 13 different materials under balanced biaxial tension. Uniaxial tensile data were also obtained for these materials. The bulge test was found to be useful in characterizing plastic instability and in evaluating a ductile failure parameter.

3.0 Program

Title: Damage Analysis and Fundamental Studies for Fusion Reactor Materials Development

Principal Investigators: G.R. Odette and G.E. Lucas

Affiliation: University of California, Santa Barbara

4.0 Relevant DAFS Program Plan Task/Subtask

Subtask B Fundamental Mechanical Properties
Subtask C Correlation Methodology

5.0 Accomplishments and Status

5.1 Introduction

Near term devices which are (or will be) available to provide high energy neutron irradiation environments for the fusion materials development program have, by their nature, somewhat limited test volumes. A need therefore exists to develop small volume specimens and the test techniques necessary to extract both microstructural and mechanical property information from them. One such test is a ductility test.

Quantitatively, ductility has numerous definitions which has, at times, led to some ambiguity in discussions of ductility. However, qualitatively, ductility is taken as the ability of a material to plastically deform without failing. Changes in ductility with neutron irradiation are of particular interest to the fusion materials program for several reasons. Ductility has some engineering significance for structural design. Moreover, ductility is sensitive to certain microstructural features, especially small second phase particles and extended defects; thus ductility changes can be used to monitor microstructural and microchemical evolution. Finally, ductility parameters may serve as important input to fracture correlation models and failure criteria [1].

In addition to the standard tensile test a number of techniques have been developed to measure ductility. Many of these have been developed in conjunction with the sheet metal forming industry to address the question of stress state effects. Such tests include the hydraulic bulge test [2], sheet stretching over hemispherical punches [3], the Swift [4], Fukui [5],

and Marciniak [6] cup tests, sheet bend tests [7] and punch tests [8]. More recently a disc bend test has been developed to assess the relative ductility of irradiated TEM discs [9]. In addition, a considerable literature has evolved to address the question of interpreting the data generated in these tests in terms of a metal's ability to deform and its susceptibility to fail under multiaxial stresses.

Of the tests developed, sheet stretching over a hemispherical punch -- referred to here as a bulge test -- has received the most attention, both analytically and experimentally. Consequently, this study was undertaken to assess 1) the adequacy of existing theories and analyses for extracting from the bulge test information pertinent to the fusion materials development program and 2) the potential for scaling the bulge test down to TEM disc-type specimens.

5.2 Background

From a review of existing theories and analyses of the bulge test, it is evident that the bulge test may be generally useful in characterizing two types of phenomena which affect ductility; namely, plastic instability and failure. Typically, plastic deformation prior to failure consists initially of uniform deformation after which plastic instability results in some nonuniform thinning, or necking, of the sample. The nature of this necking may be diffuse or localized [3]. Specifically, then, the bulge test may be useful in characterizing 1) the onset and nature of the plastic instability and 2) the magnitude of the local plastic deformation prior to failure under a specific biaxial stress state. More importantly, however, the possibility exists to use the bulge data in conjunction with instability or failure criteria to predict these phenomena for a general state of stress.

The criterion for plastic instability is still under debate although the picture is improving. Considére [10] originally proposed an instability criterion which was later generalized by Keeler and Backofen [3] to

predict both localized and diffuse necking for uniaxial and biaxial stress states. Although their theory predicted that localized necking would not occur for balanced biaxial tension, such necking was observed experimentally [6]; and considerable theoretical and experimental work to understand this has ensued [6,11,12]. Most recently, Ghosh [13] and Ghosh and Hecker [14] have proposed that the onset of diffuse and localized necking occurs in the bulge test as the result of the particular strain and strain rate distributions which arise from imposed geometric and frictional constraints and not as a consequence of some existing or imposed inhomogeneity in the sample. The theory, supported by experiments, may be applied to predict the onset of local plastic instability <u>if</u> the strain history of the specimen can be predicted, and if the constitutive equation of the material (specifically the strain hardenability and strain rate sensitivity) is known. This may be complicated, however, by the stress state dependence of strain hardening[12].

As in the case of plastic instability, a number of criteria have been proposed to describe ductile failure in thin sheets and thus to predict the <u>total strain</u> to failure under various stress states. Included in these failure criteria are such continuum mechanics relations as the "maximum shear stress" [15], "maximum volume strain" [7], and "maximum tensile work" [16] rules, as well as criteria based on the micromechanisms of ductile fracture, such as the shear linking or coalescence of voids [17,18]. In general, these theories all predict a decrease in the total strain to failure with increasing hydrostatic tension. However, there seems to be conflicting evidence about the applicability and usefulness of these theories, especially with respect to bulge testing of thin sheet samples.

To further evaluate existing instability and failure criteria and to evaluate the scalability of the bulge test itself, a research program was initiated in three parts. The first part of the program was directed at using the finite-difference, finite-element code STEALTH [19] to track the strain history of the bulge sample. This would be quite useful, for

instance, in coupling with the plastic instability criterion of Ghosh and Hecker [14]. This aspect of the program is ongoing and is not reported here. The second part of the program addressed the usefulness of several ductile failure criteria in predicting failure for planar stress states by means of comparisons between uniaxial and balanced biaxial failure data. The third part of the program addressed the scalability of the bulge test to small sample sizes. The results of these latter parts of the program are described below.

5.3 Experimental Procedure

Thirteen metals were selected for testing. These were copper, aluminum, yellow brass, mild steel and stainless steel in various metallurgical conditions ranging from highly cold-worked to recrystallized. All metals were obtained as sheet stock 0.51mm or 0.64mm in thickness.

For baseline data, tensile tests were performed on flat tensile specimens with a gage section 2.54cm long x 0.635cm wide machined from the sheet stock. A square grid of 0.20mm wide lines spaced 1.0mm apart was applied to the gage section of each sample by a photoetch/bluing technique. Three samples of each material type were tested in an Instron 1122 testing machine at a cross head speed of 0.021mm/s. Macroscopic gage length displacements were determined with a clip gage extensometer. Local grid deformations, including deformations at the failure site, were determined along both principal axes by measuring the grids directly with a travelling microscope and by measuring micrographs of the grids. Through-thickness strains were measured with a micrometer and by measuring micrographs of the sample after it had been sectioned and mounted on its side in a metallographic mount. The data were analyzed to determine K and n (in the parabolic hardening relation $\sigma = K\varepsilon^n$, where σ is the flow stress at a true plastic strain ε), R (the planar anisotropy coefficient), the uniform tensile strain ε_u^t, and the three principal strains at failure ε_f^t, ε_{2f}^t and ε_{3f}^t (where 1 = test axis, 2 = width, 3 = thickness direction). In all cases, a final localized neck formed which was smaller

in extent than the grid. Hence ε^t_{1f} was taken as the negative sum of ε^t_{2f} and ε^t_{3f}. A typical tensile sample and its corresponding photomicrographs are shown in Fig. 1.

Bulge tests were performed on samples large relative to TEM discs to facilitate testing and to develop a working understanding of the test parameters important for scaling down the sample size. The bulge test apparatus, which is shown in Fig. 2, was used in the following way. The two plates were used to clamp square samples of various sizes beneath a right cylindrical hole in the upper plate and over a tapered hole in the bottom plate. The radius of the taper shoulder was 0.635 cm, the same as the cylindrical hole. The assembly was mounted in an MTS 810 testing machine, which was used to force a small ram, tipped with a 1.27cm diameter steel ball, through the top hole and into the sample. By backing the sample with a neoprene sheet, the sample could be forced to fail at the tip of the ram where the stress state was one of balanced biaxial tension. Failure was signaled by a sudden load drop.

The most important scaling parameters were found to be the ratio of the sample width to the hole diameter and the ratio of the sample width to thickness. For samples with width-to-thickness ratios below 30 and a width-to-hole-diameter ratio less than 3 (i.e., a sample width less than 4.0 cm) there was insufficient material around the edges to keep the sample clamped in place during bulging.

To facilitate strain analysis of bulged samples, a square grid of 0.05 mm wide lines spaced 0.25 mm apart was applied to each specimen by the same photoetch/bluing technique used for the tensile samples. Following failure the sample was removed and grid deformations analyzed as described above. The sample was then sectioned, mounted in a metallographic mount and photographed, and the specimen thickness as a function of distance from the failure site was measured from the photomicrographs. Unlike the tensile tests, there were only two materials for which a localized neck formed prior to failure. In these cases the extent of the neck was again

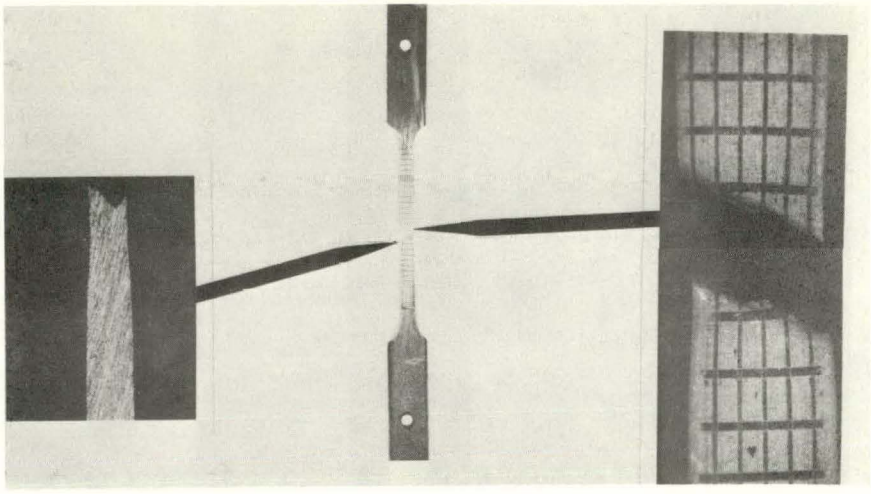

FIGURE 1. Photograph of a Gridded Tensile Sample Tested to Failure and the Corresponding Photomicrographs of the Grid and Sample Thickness at the Failure Site.

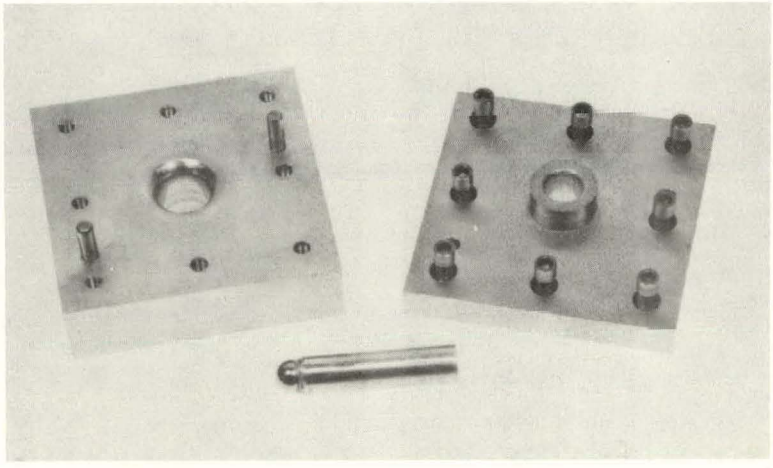

FIGURE 2. Bulge Testing Apparatus.

smaller than grid, and ε_{1f}^{b} was taken as $-\frac{1}{2}\varepsilon_{3f}^{b}$ [18]. A typical bulged specimen and its corresponding photomicrographs are shown in Fig. 3.

5.4 Results

Results of the uniaxial tension tests are given in Table 1. Several points are notable. Not all the metals exhibited strictly parabolic hardening; some instead exhibited a transition in K and n after some accumulated strain (e.g., SA1, SA2, SSA3 and SSA4). For these metals the values given for K and n are those after the transition.

In all of the materials the onset of plastic instability appeared to occur by the formation of a diffuse neck. In most cases the uniform axial strain was approximately equal to the strain hardening exponent, i.e. $\varepsilon \cong n$, in agreement with the criterion of Keeler and Backofen [3]. For the materials SAR, SSAR, SSA1, and SSA2, there was poor agreement with such a relationship. This may be largely due to the low ductility and hence greater uncertainty in both ε and n.

The results of the biaxial tests are also given in Table 1. Here ε_{m}^{b} is defined as the principal grid strain accumulated prior to failure in grids adjacent to the failure site; hence, ε_{m}^{b} contains both uniform and diffuse neck strains but not the local necking strain. In agreement with earlier findings [3], the biaxial strains ε are all larger than the corresponding values of ε_{u}^{t}. That is , with the suppression of local necking and the extension of diffuse necking strains in biaxial tests, the macroscopic deformation of bulge samples was considerably enhanced over uniaxial samples; this was particularly true for the materials exhibiting very small values of ε_{u}^{t} (i.e., SAR, SSAR, SSA1 and SSA2).

In all but two of the materials, CUAR and ALAR, $\varepsilon_{m}^{b} \cong \varepsilon_{1f}^{b}$, indicating the samples failed without local necking. For CUAR and ALAR $\varepsilon_{m}^{b} < \varepsilon_{1f}^{b}$, indicating local necking took place prior to failure. These observations were consistent with the through-thickness profiles of the bulged samples.

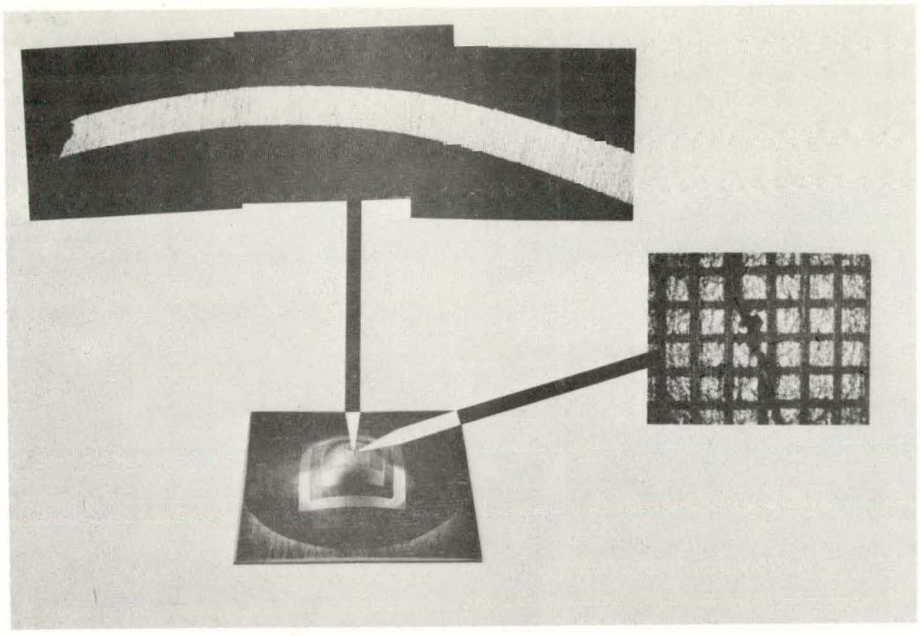

FIGURE 3. Photograph of a Gridded Bulge Sample Tested to Failure and the Corresponding Photomicrographs of the Grid and Sample Thickness at the Failure Site.

TABLE 1

TENSILE AND BIAXIAL TEST DATA

Sample	Uniaxial Data							Biaxial Data		
	K (MPa)	n	R	ε^t_u	ε^t_{1f}	$-\varepsilon^t_{2f}$	$-\varepsilon^t_{3f}$	ε^b_m	ε^b_{1f}	$-\varepsilon^b_{3f}$
CUAR	352	.28	.52	.310	1.01	.22	.79	.42	.52	1.04
ALAR	196	.24	.16	.140	.93	.18	.75	.37	.56	1.11
BAR	565	.18	.18	.207	.84	.16	.69	.37	.35	.71
BA1	550	.19	.51	.191	.82	.19	.62	.38	.38	.76
BA2	641	.25	.92	.225	.76	.19	.57	.35	.37	.73
SAR	765	.02	3.00	.005	.64	.02	.63	.14	.17	.34
SA1	513	.16	.45	.217	1.22	.32	.90	.67	.66	1.31
SA2	508	.20	.71	.252	1.38	.37	1.01	.67	.64	1.28
SSAR	2534	.11	.94	.012	.50	.21	.29	.16	.13	.25
SSA1	1552	.05	.55	.012	.47	.11	.36	.13	.11	.22
SSA2	1410	.06	.12	.015	.53	.05	.43	.18	.21	.41
SSA3	1636	.34	.60	.404	.93	.31	.62	.49	.45	.90
SSA4	1436	.17	.78	.270	.71	.32	.40	.27	.24	.48

For example, the sample shown in Fig. 3 failed with no local necking; after diffuse necking, failure occurred abruptly by shear.

These data were used to test the applicability of the failure criteria listed earlier, with the exception of the criterion of McClintock [17], for which inclusion size, shape and spacing and microvoid growth rate information are required. All the other criteria could be tested with the available data by using them to predict a biaxial strain to failure from the uniaxial data.

The criterion of Ghosh [18] was the only one which adequately fit the data. This failure criterion is based on the linkage of growing microvoids when a critical shear stress is achieved in the material between the voids. It is given by

$$(1 + \alpha)\ \sigma_1^2 = K_{cr} \qquad (1)$$

where $\alpha = \sigma_2/\sigma_1$, σ_1 and σ_2 = principal stresses, and K_{cr} is a material parameter which accounts for inclusions and second phase particle size and shape distributions and microvoid growth rates. In theory, if one can determine K_{cr} in one type of test (i.e. at one stress state) it can be used to predict failure (and failure strains) under other conditions, given a stress state, a constitutive equation, and a flow rule.

For the particular case at hand, the bulge (biaxial) failure strain ε_{1f}^{b} should be predicted from the uniaxial tension failure strain ε_{1f}^{t} by

$$\varepsilon_{1f}^{b} = \left[\frac{(1+\alpha_u)}{2}\left\{\frac{2-P'}{1+\alpha_u^2-P'\alpha_u}\right\}^{\frac{1}{2n}}\right]\left[\frac{1+\rho_u^2+P'\rho_u}{2+P'}\right]^{\frac{1}{2}}\varepsilon_{1f}^{t}$$

where:

$$P' = \frac{2R}{1+R}$$

$$\rho_u = \varepsilon^t_{2f}/\varepsilon^t_{1f} \qquad (2)$$

$$\alpha_u = \frac{[(1+R)\ \rho_u + 2R]}{[2 + 2R + R\rho_u]}$$

A comparison of the predicted values of ε with the observed values is shown in Fig. 4 along with the 45° line representing a perfect fit.

As can be seen the agreement is quite good, indicating the validity of the Ghosh criterion for this application.

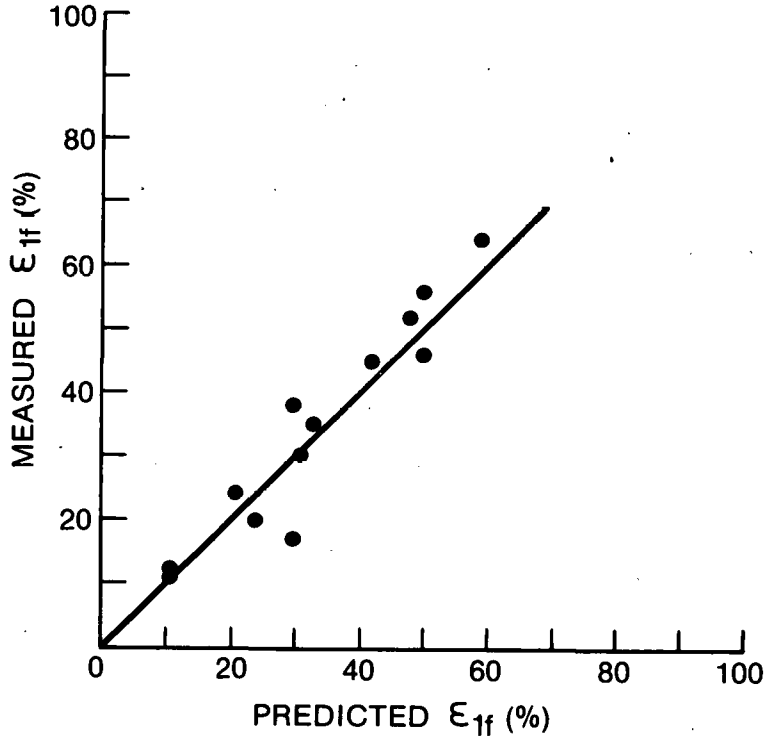

FIGURE 4. Comparison of the Predicted and Measured Values of the Principal Strain to Failure in the Bulge Test.

5.6 Conclusions

A considerable amount of information has been developed in the literature to describe the deformation and failure of thin metal sheets. Much of this appears applicable to bulge testing small thin metal sheet samples and thus to providing information for the selection of metals to be used in thin-walled structures like the first wall of a fusion reactor. There are currently analytical and semi-empirical methods of predicting the onset of plastic instability in such samples for a variety of planar stress states, although these have yet to be tested for irradiated material.

Moreover, the ductile failure criterion of Ghosh appears to be quite successful in correlating uniaxial with biaxial data.

The bulge test, or some modification of the bulge test, is a potentially attractive test for extracting ductility information. Although the samples and the punch used in this study were relatively large (4.0cm square samples and a 1.27cm diameter punch), it should be relatively straight-forward to scale this down to smaller sample and punch sizes.

For example, using the scaling rules determined in this study, bulge testing should be feasible with a 0.75cm x 0.75cm x .025cm thick sample and a 0.25cm diameter punch. Such a sample would be of the order of TEM discs in size. Moreover, the test data could be used in conjunction with flow properties obtained either from other tests or from some extension of the test itself to determine a failure parameter like K_{cr}. Such a parameter would actually have more utility than some direct measure of ductility since it 1) has a direct microstructural relationship, 2) can be used to predict ductilities under various stress states and 3) could be used in place of ductility as an input parameter for some correlation model for fracture.

6.0 References

1. Odette, G.R., Ritchie, R.O., McConnel, P., Server, W., 2nd Topical Meeting on Fusion Reactors Materials, Seattle, WA, Aug. 8-12, 1981.

2. Ranta-Eskola, A.J., Int. J. Mech. Sci., 21 (1979) 457.

3. Keeler, S.P. and Backofen, W.A., Trans. ASM, 56 (1963) 25.

4. Newby, J.R., ASTM-STP-647 (1978) 4.

5. Moore, G.G. and Wallace, J.F., J. Inst. of Metals, 93 (1964-65) 33.

6. Marciniak, Z. and Kuczynski, K., Int. J. Mech. Sci., 9 (1967) 609.

7. Weiss, V., Proc. Third Int. Conf. Mech. Behavior of Mater., Kyoto, Japan, (1971) 458.

8. Ludwigson, D.C., J. Test Eval., 7, 6 (1979) 301.

9. Mañahan, M.P., Argon, A.J., Harling, O., 2nd Topical Meeting on Fusion Reactors Materials, Seattle, WA, Aug. 8-12, 1981.

10. Considére, A., Ann. Ponts Chaussées, 9, 6 (1885) 574.

11. Azrin, M., and Backofen, W.A., Met. Trans., 1 (1970) 2857.

12. Ghosh, A.K., and Backofen, W.A., Met. Trans., 4 (1973) 1113.

13. Ghosh, A.K., Met. Trans. 5 (1974) 1607.

14. Ghosh, A.K., and Hecker, S.S., Met. Trans., 6A (1975) 1065.

15. Marin, J., Mechanical Behavior of Engineering Materials (Prentice Hall, London, 1963).

16. Cockroft, M.G., Ductile Fracture in Cold Working Operations, in Ductility (ASM, Metals Park, Ohio, 1968).

17. McClintock, F.A., J. Appl. Mech., 35 (1968) 363.

18. Ghosh, A.K., Met. Trans., 7A (1976) 523.

19. Hofman, R., EPRI-NP-260, Electric Power Research Institute, (1976).

7.0 Future Work

The computer program STEALTH is being used to model plastic flow in the bulge test. Some analytical work will be done with STEALTH before attempts are made to scale the bulge test down. In addition the investigation of a shear punch test to determine strength and ductility information is being continued.

8.0 Publications

1. M. Dooley, G.E. Lucas, J.W. Sheckherd, "Small Scale Ductility Tests," to be published in J. Nucl. Mater. as part of Proceedings of the Second Topical Meeting on Fusion Reactor Materials, Seattle, Aug. 8-12, 1981.

AN EVALUATION OF THE APPLICATION OF FRACTURE MECHANICS PROCEDURES TO FUSION FIRST WALL STRUCTURES

G.R. Odette (UC Santa Barbara), R.O. Ritchie (UC Berkeley), P. McConnell and W. Server (Fracture Control Corporation)

1.0 Objective

The objective of this work is to establish the procedures which will allow reliable prediction of conditions leading to the fracture of fusion first wall structures.

2.0 Summary

An analysis of the application of J integral based elastic-plastic fracture mechanics procedures to fusion structures is carried out. Some limiting flaw-structure geometries are specified along with estimates of upper- and lower-bound service properties of a martensitic stainless steel. Size requirements for J procedures in unconstrained flow geometries and for low strain-hardening conditions result in a small range of valid application even for lower-bound properties. In constrained deformation geometries, the range of application is extended for lower-bound properties. Failure of J procedures is shown to coincide with approach to fully plastic fracture, which can be treated partly with limit-load or net-section stress criteria.

3.0 Program

Title: Damage Analysis and Fundamental Studies for Fusion Reactor Materials Development

Principal Investigators: G.R. Odette and G.E. Lucas

Affiliation: University of California, Santa Barbara

4.0 Relevant DAFS Program Plan Task/Subtask

Subtask B. Fundamental Mechanical Properties

5.0 Accomplishments and Status

5.1 Introduction

Major problems facing development of fusion power are the limitations in the performance, reliability and service life of blanket support and vacuum barrier first wall structures. In this paper, a preliminary assessment is made of one potential failure mode, extension of a pre-existing flaw to leak or break conditions due to monotonic applied loads; no attempt is made to assess fatigue or cyclic crack growth failure, although these are likely to be the proximate causes of formation of critically sized flaws.

Fracture mechanics often focusses on the problem of measuring a presumed material property, such as toughness, from small, idealized test specimens and then applying the properties to predict fracture conditions for real structures (1-3). When the structures are large, some of the basic assumptions of fracture mechanics are likely to be reasonably met (e.g., plane-strain and small-scale yielding). In the case of fusion first wall structures, large size scales in the thickness dimension are not anticipated. Hence, fracture resistance may not be readily represented by a single toughness property and some "easily" computed local stress characterizing parameter, e.g. the linear elastic stress intensity factor K.

Of course, size is only one of a number of considerations which confound fracture analysis. In general, there are: complex multiaxial stress-

states and stress gradients; non-standard three-dimensional flaw geometries; complex load histories; variable structure compliance/ secondary stresses; and non-ideal constitutive behavior. Further, the microstructure, hence mechanical properties, of fusion alloys will evolve in service due to neutron irradiation and other environmental factors. The most appropriate high energy neutron irradiation test facilities will have very limited volumes requiring the use of small test specimens; this compounds the normal difficulty of both remote radioactive specimen testing and interpretation of test data.

Thus it is important to ascertain if approaches such as elastic-plastic fracture mechanics, will be applicable for material and structural conditions, and fracture modes pertinent to fusion systems. We begin with a brief review of fracture mechanics, emphasizing constraints implicit in its application; while the results we present are not new, some are recent and not widely appreciated by the metallurgical community.

5.2 Formal Fracture Mechanics Methods

Fracture mechanics is based on the presumption that a fundamental material property (i.e., toughness) can represent the fracture response of a material to a uniquely determined stress-strain field in the fracture process zone in the vicinity of a flaw. There are several basic assumptions implicit in obtaining unique fields, primarily related to size and geometry requirements needed to constrain the deformation.

In the case of Linear Elastic Fracture Mechanics (LEFM), the test specimen or structure is loaded grossly only in the linear elastic regime. Here an elastic 'K' field surrounds and dominates a small plastic region which inevitably forms ahead of the crack. For LEFM conditions, unique stress-strain fields can be defined for limiting states of plane stress and strain; the amplitudes of these fields are uniquely defined by K. Any process in the fracture zone is controlled by deformation in the elastic

'K' field, resulting in a critical value of the applied K for extension of the crack in the process zone - viz. fracture. From a microscopic perspective, at the critical stress intensity K_{IC}, local fracture stress/strain criteria are reached over a microstructurally significant distance.

The major advantage of LEFM is that applied K values are readily computed from expressions contained in handbooks. However, the major limitation of the application of LEFM procedures are size requirements for 'K' field dominance (4); since these sizes are generally much larger than critical fusion structure dimensions (< 1 cm) we will not pursue analysis of LEFM approaches further.

In lower strength materials the size of the plastic zone increases and may grow to the point where large scale yielding occurs before fracture, intersecting the boundaries of the specimen or structure. In this case, the stress-strain fields may or may not be uniquely definable by a single calculable parameter which is a function of the remote load and the test specimen or flawed structure geometry. Rice (5), Rice and Rosengren (6), and Hutchinson (7) have shown that, based on certain assumptions, a new field characterizing parameter, J, can define the scalar amplitude of a unique stress-strain field in the intensely deformed process zone near the crack. These are commonly referred to as HRR fields (after Hutchinson (7) and Rice and Rosengren (6)). The crack driving characterizing parameter J* is a function of the remote stresses, crack length, external dimensions, yield stress and strain-hardening; crack extension in plane-strain mode I initiates at a uniquely defined J_{Ic}.

---

* J is sometimes interpreted as a generalized energy release rate calculated by means of a path independent integral. J reduces to $J = G = K(1-\nu)/E$ (where E is Young's Modulus and ν Poisson's Ratio) in the elastic limit (1-3). We also note that J is directly related to other elastic-plastic fracture parameters, notably crack tip opening displacement.

The assumptions used in this analysis include:
1) constitutive behavior which can be represented reasonably by deformation theory plasticity or non-linear elasticity; this implies monotonic increasing and proportional loading (i.e., stress is uniquely determined by the existing strain); 2) finite strain hardening; 3) smooth crack blunting as the initially sharp crack opens; 4) independence of the specific flow field geometry or, equivalently, sufficiently constrained deformation with a HRR singularity dominance. Further, there is an implicit assumption that J values (like other parameters used as crack driving forces, e.g. K) can be calculated for pertinent structure and crack geometries.

Assumptions 2 and 4 are particularly significant. Consider two limiting slip field lines in Figure 1. Figure 1a shows the fields associated with a specimen with an applied bending moment (e.g. a compact tension specimen, CT) where the deformation is constrained; in this case the stress-state is highly triaxial with a hydrostatic/flow stress ratio of 2.4 for rigid-perfectly plastic behavior. In contrast, Figure 1b shows the unconstrained deformation field for a center crack panel (CCP) of finite width; here deformation may be characterized by large shear strains localized in inclined bands. These bands extend long distances and may intersect freely displacing surfaces. In this case the deformation fields are not unique. The maximum stress triaxiality is < 1 for such fields, and the crack tips often tend to be sharp vertices formed by alternate sliding off and on slip bands. The stress state, the tendency to localize deformation (which is influenced by strain-hardening), and the shape of crack tips are all known to be important factors in the micromechanisms of fracture in the process zone (8).

These effects have been investigated recently by a number of authors (8-11) using both experimental and analytical (i.e. finite element) techniques. The clear conclusion of this work is that there are also size limitations to the measurement and application of J dominated crack

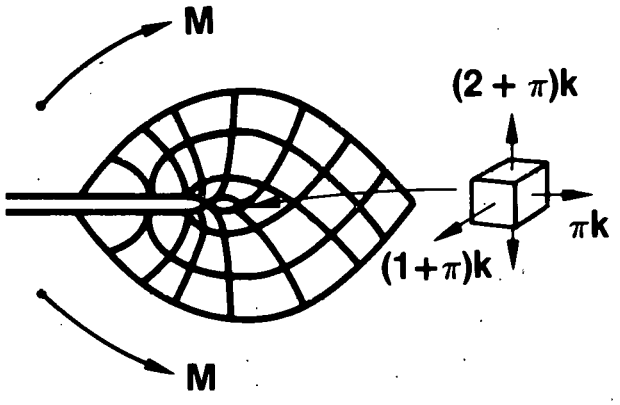

(a)

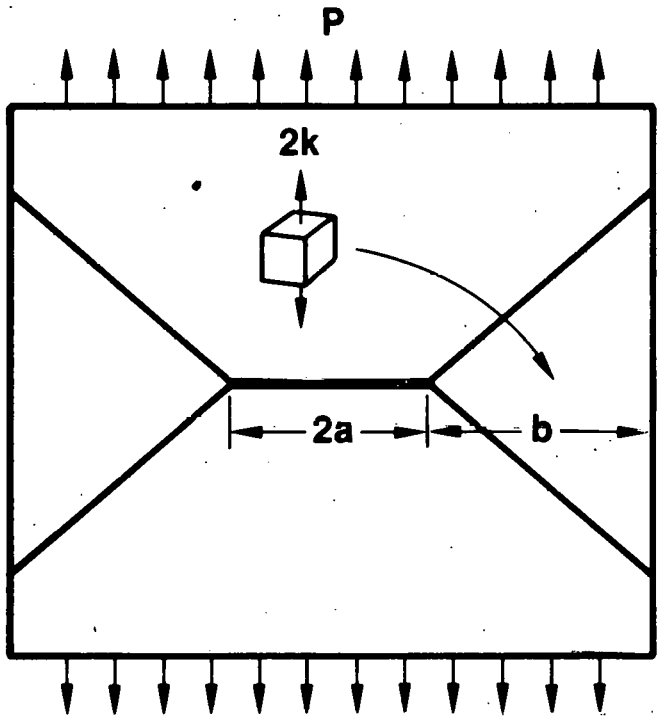

(b)

FIGURE 1. Slip Field Lines for (a) Highly Constrained Deformation of High Triaxiality and (b) Unconstrained Deformation and Low Triaxiality.

initiation which vary with the basic characteristics of the gross deformation field.

For constrained (e.g., CT) field type cracks it is suggested that (11)

$$a, b > 25\text{-}50\ J_{Ic}/\sigma_0 \qquad (1a)$$

while for unconstrained geometry (e.g., CCP) (11)

$$a, b > 200\ J_{Ic}/\sigma_0 \qquad (1b)$$

Hancock and Cowling have carried out a convincing set of experiments which demonstrate these points in quenched and tempered steels similar to HY80 (8). Using six specimen geometries with varying degrees of constraint, they found nominal J_{Ic} values ranging from ~ 147 to 570 kN-m in spite of the fact that the specimens generally met the generally accepted size requirements of Equation 1a.

In both cases, the thickness must be B > a,b to maintain plane-strain if that is desired. The state of plane-stress can be approached in the specimens with B < a, b, but this may not be asymptotically determinate; indeed, if the specimen becomes too thin, fracture may shift to a type III antiplane shear mode with lower toughness values. Largely because of primary application to large structures, plane-stress J analysis procedures are not yet developed.

With respect to the other assumptions: low strain-hardening and in the limit perfectly plastic behavior formally preclude application of J based elastic-plastic fracture theory (3,8-11); however, in practice, low strain-hardening may not severely limit J application to bend type geometries. In contrast, the CCP type geometries, size requirements have

been found to be very sensitive to strain-hardening; indeed, the size requirement for J dominance in Equation 1b assumes low strain-hardening (n ~ 0.1 for $\sigma_t \propto \varepsilon_t^n$ where σ_t is the true flow stress and ε the true strain); however, this might not be sufficient for even more perfectly plastic materials. The significance of the monotonic loading requirement lies primarily in the fact that since unloading inevitably follows crack growth, J_{Ic} procedures cannot be directly used to characterize continued crack extension. In reality, ductile materials often display, a very rapidly rising J_R resistance to continued crack extension, viz. - stable crack growth. Hence, initiation values may be a conservative measure of the actual fracture load or displacement. Paris (12,13) and others have suggested this can be treated using another possible material property, the tearing modulus $T \propto dJ_R/da$, when the stable growth of the crack is J-controlled. Use of T introduces new size and geometry considerations (3) and may not be very useful since it is limited to small crack growth (<6%); and dJ_R/da may be small for irradiated steels (14).

Finally, even if we can accurately characterize J_{Ic} (or T) as a material parameter, we must also be able to calculate J_I (applied) as a valid crack driving characterizing parameter for the flawed fusion structure. In this case the formal definition of J_I as a path independent energy integral must usually be invoked (5). Calculation of J_I is not trivial; indeed, this has not been carried out for many important crack-structure geometries. However, estimation procedures which combine elastic and fully plastic solutions (obtainable from approximate analytic or finite element calculations) which are characterized in terms of the yield stress, work hardening exponent and specimen-flaw geometry have been systematically developed in handbook format for a number of standard specimen geometries (15); these general approaches may be extended to conditions pertinent to fusion structures, but this would require considerable effort.

5.3 Fusion Structures and Material Properties

It is necessary to specify flaw-structure geometries and some basic material properties. Of course, these must be viewed as tentative, since an irradiated materials property base is just now being developed* and fusion reactor designs are, at best, schematic.

In the most general sense, flaw geometries might be expected to be part through surface, cracks; such flaws would probably be subject to a range of primary and secondary stresses with both tensile and bending moment components. The magnitude and character of the stresses would vary with time due to dimensional changes resulting from swelling and irradiation creep and various programmed and accidental transients. Few J solutions for such surface part through cracks are available at this time, even for simple loading conditions. Further, the critical small dimension of fusion structures will probably be ~2-10 mm. Hence, we consider the two limiting deformation field geometries shown in Figure 1 for both plane-stress and plane-strain stress states to bracket important regimes of flaw geometry with respect to deformation constraint and stress-state.

We will assume the structure is made of HT-9, which is a quenched and tempered martensitic stainless steel. Estimates of the yield strength, σ_y, and toughness K_{Ic} ($=\sqrt{J_{Ic}E/(1-\nu)}$), of HT-9 are shown in Figure 2. These curves are constructed from limited data from several sources (16-19). The irradiated curves are for 'saturated' properties of steels irradiated to moderate fluences T < 400°C. While not highly accurate, these might represent reasonable upper and lower bounds of the in-service

---

* Indeed, because it is essentially impossible to simulate actual in-service conditions, and since properties are very sensitive to the specific alloy condition, any test data base must be considered an approximate representation of the actual material state of a fusion component.

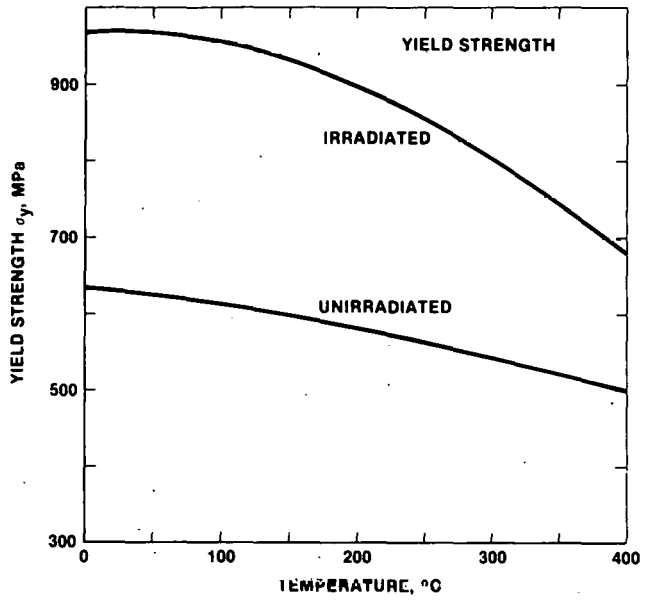

(a)

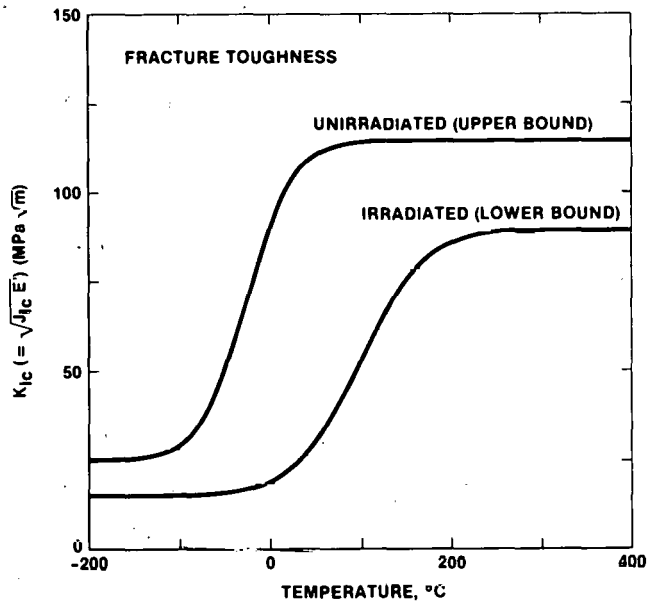

(b)

FIGURE 2. Estimates of the (a) Yield Strength and (b) Fracture Toughness for HT-9 (Upper and Lower Bound).

behavior of alloys in early fusion engineering test reactors or improved alloys subject to more aggressive conditions in commerical reactors.

Irradiation also causes a large reduction in the strain-hardening and ductility parameters, particularly uniform elongation (20). This is accompanied by a microscopic reduction in the homogeneity of slip -- viz. severe localization of deformation in coarse bands, known as channels. The ultimate manifestation of this termed channel fracture has been observed in some highly irradiated stainless steels; here, the deformation is almost entirely confined to very narrow bands (<1μm) resulting in essentially zero ductility and a brittle fracture surface appearance (21). Hence, while we will not quantitatively define these parameters, it will be assumed that the strain-hardening exponent and uniform ductility will be less than ~ 0.1.

5.4 Evaluation of Fracture Mechanics Procedures

Equations 1a and 1b can be used to determine size requirements for J controlled fracture in fusion structures. We assume the condition a = b, hence the minimum dimension will be t = 2a. Figure 3 shows the required t for J dominance, (i.e., valid J_{Ic}) for both M = 50 and 200, i.e., for highly constrained and unconstrained deformation fields, respectively. Note again that the use of M = 200 may be somewhat conservative for unirradiated upper bound type properties and not sufficiently conservative for very low strain-hardening irradiated alloys.

Upper-bound properties (unirradiated), even J_{Ic} approaches, would be limited to use for low temperature and constrained flow field cases. For the lower-bound toughness properties (irradiated) J_{Ic} based fracture analysis would appear to be useful over range of temperature for the constrained flow fields; however, for unconstrained flow fields, the applicability of J procedures may be limited to fairly low temperatures, even with the degraded properties.

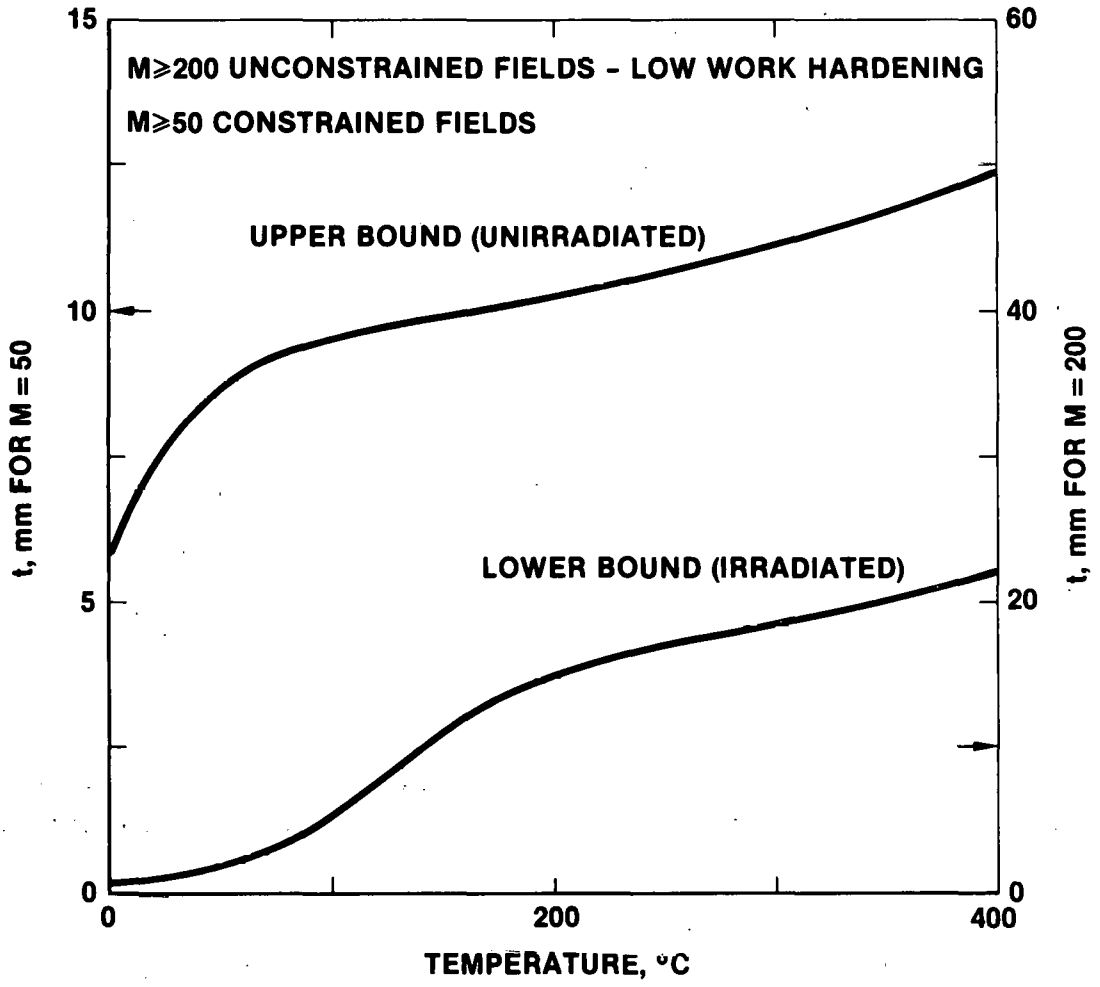

FIGURE 3. Required Minimum Structural Dimension for J-Controlled Fracture for Both Constrained and Unconstrained Deformation Fields.

Fracture stresses estimated using J_{Ic} criteria outside the range of valid application will generally be conservative; that is, actual fracture will occur at limit loads by fully-plastic collapse governed by the strength level and constraint factors. A semi-quantitative assessment of this can be made using one of the several procedures (22-27) (all implicitly based on simplified crack tip strip yield models (26)) which interpolate between elastic LEFM fracture and fully plastic collapse. For a plane-stress CCP type crack-loading geometry, these yield an expression in the form

$$\frac{\sigma_N}{\sigma_y} = \frac{2}{\pi} \cos^{-1} \{\exp(-A)\} (1 - a/t)^{-1} \tag{2a}$$

where

$$A = \frac{\pi}{8}\left(\frac{K_{IC}}{\sigma_y}\right)^2 \frac{1}{a} \tag{2b}$$

and where σ_N is the net section stress at fracture. Application of the results of Smith (27) show that the effects of finite width are small in these geometries.

If we assume fully plastic fracture occurs at $\sigma_N/\sigma \geq 0.9$ (large A) and brittle fracture at $\sigma_N/\sigma \leq 0.6$ (small A), the temperature/thickness regimes of various fracture modes (plastic, elastic-plastic, fully plastic) can be mapped. Inserting appropriate values, we find that even in the case of lower-bound properties there is essentially no significant regime of elastic fracture; and a very limited regime, at $T < 100°C$ and $t \gtrsim 2$ mm, which would exhibit elastic-plastic fracture. Smith has also shown that the net section fraction stress is only weakly geometry dependent in the fully-plastic case (28).

While the basic model does not strictly apply to constrained deformation field geometries and plane-strain conditions, expressions of the form of Equation 2 have been widely applied to interpolate fracture between modes in these cases; at least in simple test specimen geometries these procedures have met some success (23-26). For constrained flow geometries σ_y must be multiplied by a constraint factor, M; typical values of M are ~ 2 in CT type geometries. Figure 4 shows a t-T fracture regime map for M = 2 and a/t = 0.5 (the results are only weakly dependent on a/t). These results suggest that for constrained flow geometries while there is still a major T-t regime of fully-plastic fracture, there is also a potentially significant regime of elastic-plastic fracture. The dashed line in Figure 4 shows the size requirement for application of J_{Ic} fracture criteria which are met in the elastic-plastic fracture regime.

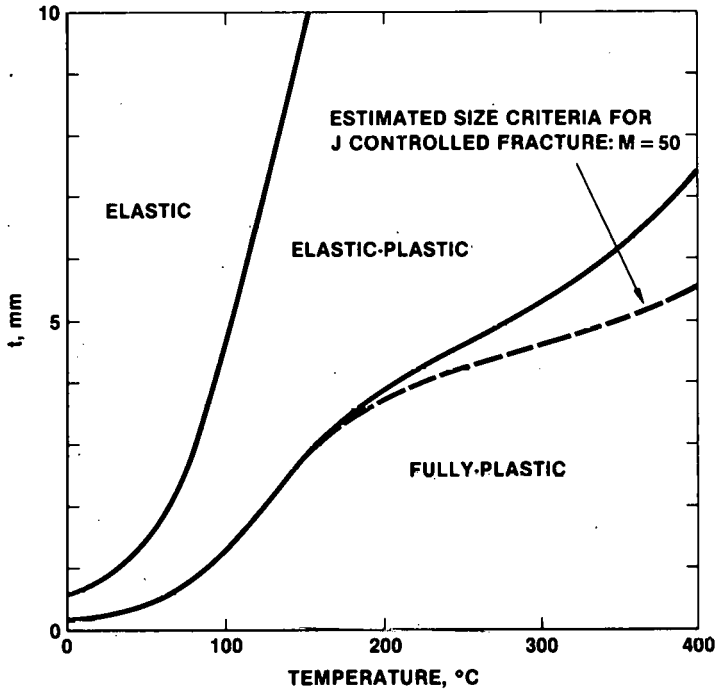

FIGURE 4 Estimated Fracture Regimes for Constrained Deformation Field Geometries.

Thus, fracture in relatively thin fusion structures may take place predominantly by plastic collapse. Our analysis also showed that fracture stresses for the irradiated condition always exceed the tensile yield stress of the unirradiated condition in t-T regimes of practical interest. Hence, unirradiated strength levels may be a useful and conservative design parameter.

5.5 Summary and Conclusions

Our analysis has shown a limited region of structural applicability for elastic-plastic J procedures. These limits are primarily associated with the potentially low strain-hardening capacity of irradiated steels coupled with the possibility of unconstrained deformation fields, e.g. the type formed in center-cracked-panels with finite widths. Other problems include: analysis of short or shallow cracks; treating possible stress-states other than plane-strain; and calculating J crack driving parameters for actual structures, viz. - part-through cracks. Indeed it has yet to be demonstrated that crack initiation or stable growth can be predicted for the complex conditions encountered in structures from conventional laboratory test specimens (29).

There is a regime in which one would anticipate fully-plastic collapse; in this case, limit load analysis might be sufficient and relatively easily applied (30). However, while secondary stresses should not contribute significantly to fracture in the fully plastic regime, they must be considered in treating elastic-plastic fracture (25). Even in the fully plastic regime the question of ductility in deformation or displacement controlled fracture remains. In this case, accurate fracture predictions would require appropriate measures of "ductility", - viz., test procedures which provide a proper interaction between macroscopic and micromechanical deformation and fracture processes. Simple tensile ductility parameters are probably not sufficient.

Two approaches to ascertaining more useful ductility parameters might be considered. One is to attempt to simulate directly limiting flaw-structure geometries pertinent to fusion components in suitably conditioned non-standard specimens. The second is to conduct more fundamental studies of the micromechanics of fracture as a function of microstructure, stress-state and macroscopic deformation path (31). Of course, J_{Ic} measurements of fracture with well-characterized crack tip fields are very valuable in this regard. Since the micromechanisms of deformation and fracture in highly irradiated alloys are likely to be atypical (e.g. phenomena such as flow localization and even channel fracture), better understanding may be important to long-term efforts to develop more accurate methods of predicting performance limits of fusion structures and better alloys to extend these limits.

6.0 References

1. J.F. Knott, Fundamentals of Fracture Mechanics, Halsted Press (1973).

2. S.T. Rolfe and J.M. Barson, Fracture and Fatigue Control in Structure, Prentice Hall (1977).

3. J.W. Hutchinson, A Course on Non-Linear Fracture Mechanics, Technical University of Denmark (1979).

4. ASTM Standard E-399-78a "Standard Test Method for Plane-Strain Fracture Toughness of Metallic Materials", ASTM Book of Standards, Part 10 (1978).

5. J.R. Rice, Journ. Appl. Mech., Trans ASME, 35 (1968) 379.

6. J.R. Rice and G.F. Rosengren, Journ. Mech. Phys. of Solids, 16 (1968) 1.

7. J.W. Hutchinson, Ibid 13.

8. J.W. Hancock and M.J. Cowling, Metal Science, 5 (1980) 293.

9. F.A. McClintock, Fracture, An Advanced Treatise, Vol. 3, Academic Press (1971) 47.

10. R.M. McMeeking, Journ. Mech. Phys. Solids, 25 (1977) 357.

11. R.M. McMeeking and D.M. Parks, ASTM STP 668 (1978) 175.

12. P.C. Paris, H. Tada, A. Zahoor and H. Ernst, Ibid 11 (1978) 5.

13. J.W. Hutchinson and P. Paris, Ibid 11 (1978).

14. D.M. Norris, T.U. Marston, R.L. Jones and S.W. Tagart, Jr., Pressure Boundary Program: Progress 1979, EPRI NP-1540-SR (1980).

15. C.F. Shih and J.W. Hutchinson, J. Eng. Mat. Tech., 98 (1976) 289.

16. F.A. Smidt, J.R. Hawthorne and V. Provenzano, ADIP-QPR, March 1980 DOE/ER-0045/2 (1980) 163.

17. R.L. Klueh and J.M. Vitek, ADIP-PRQ, March 1981, DOE/ER-0045/6 (1980), 139.

18. T.A. Lechtenberg and S. Helfrich, ADIP-QPR, June 1980, DOE/ER-0045/3 (1980) 201.

19. F.H. Huang and G.L. Wire, Ibid, 18 (1980) 236.

21. E.E. Bloom, Radiation Damage in Metals, S.D. Petersen and Harkness, eds., ASTM STP 295, (1975) 295.

22. R.L. Fish, J.L. Straalsund, C.W. Hunter and J.J. Holmes, ASTM STP 529, (1973).

23. P.T. Heald, G.M. Spink and P.J. Worthington, Mat. Sci. and Engr., 10 (1972) 129.

24. J.M. Bloom, Int. Journ. of Press. Ves. and Piping, 8 (1980) 215.

25. B.J.L. Parkson, Advances in Elasto Plastic Fracture Mechanics, L.H. Larsson, Ed., Appl. Sci. Pub. (1980) 319.

26. C.G. Chell, Ibid 25 (1980) 359.

27. B.A. Bilby, A.H. Cottrell and K.H. Swinden, Proc. Roy. Soc. (London) A272 (1963) 304.

28. E. Smith, Proc. Roy. Soc. (London) A285, (1965) 46.

29. T.U. Marston, EPRI NP-1734, Project 601-1 Final Report (1981).

30. E. Smith, Int. J. of Pres. Ves. and Piping, 8 (1980) 303.

31. M.A. Dooley, G.E. Lucas and W. Sheckherd, "Small Scale Ductility Tests", to be published in the Proceedings of the Second Topical Meeting on Fusion Materials, Seattle, WA, August 1981.

7.0 Future Work

Experiments are being designed to test the predictions of this analysis, with emphasis on the behavior of part-through cracks.

8.0 Publications

The content work was presented at the Second Topical Meeting on Fusion Reactor Materials, Seattle, Washington, August 9-12, 1981 and will be included in the Proceedings of that Conference.

A FATIGUE TEST FOR SPECIMENS FROM SIMULTANEOUSLY ION-BOMBARDED AND STRESS/TEMPERATURE-CYCLED 316 SS PRESSURIZED TUBES

G. Kohse and O. K. Harling (Massachusetts Institute of Technology)

1.0 Objective

The objective of this study is to understand and quantify the effects of near surface damage and implanted gas on the performance of the fusion reactor first wall.

2.0 Summary

A fatigue test to supplement information gained from microscopic analysis of simultaneously ion-bombarded and stress/temperature cycled 316SS pressurized tube specimens has been developed. This will allow testing of a larger number of fatigue specimens from each irradiated tube. Using unirradiated specimens, a viable approach with load controlled to produce stresses of approximately 95% of yield with $R \simeq 0.05$ and a frequency of 20-50 HZ has been established.

3.0 Program

Title: Effects of Near Surface Damage and Helium on the Performance of the First Wall

Principal Investigator: O. K. Harling

Affiliation: Nuclear Reactor Laboratory, Massachusetts Institute of Technology

4.0 Relevant DAFS Program Plan Task/Subtask

Task II.C.5 Effects of Cycling on Microstructure
II.C.8 Effects of Helium and Displacement on Fracture
II.C.12 Effects of Cycling on Flow and Fracture
II.C.13 Effects of Helium and Displacement on Crack Initiation and Propagation
II.C.15 Effects of Near Surface Damage on Fatigue

5.0 Accomplishments and Status

5.1 Introduction

The aims, procedures and initial results of the scoping experiment have been described in previous DAFS reports and elsewhere[1,2,3]. Briefly, pressurized tube specimens are irradiated in the M.I.T. research reactor, surrounded by a ^{10}B film to provide ion bombardment from $^{10}B(n,\alpha)^{7}Li$. The temperature of the specimens is cycled, which produces a concurrent stress cycle in the sample walls. Previous work has centered on microscopic analysis of sample surfaces and cross-sections to determine whether or not the ion-bombarded surface layer enhances the initiation of possibly fatal fatigue cracks. The pressurized tubes are not cycled to failure in the reactor due to the relatively long cycle period (~3.5 min). A postirradiation fatigue test has therefore been developed to supplement the microscopic investigation of the evolution of the ion-bombarded surfaces, and possible crack initiation under cyclic conditions. The establishment of a suitable test method is described in this report.

5.2 Test Development

The primary constraints on the postirradiation test are: 1) that it be sensitive to the presence of short cracks on the outer surface of the samples; 2) that it provide as many samples as possible from each test capsule; 3) that it not supplant the microscopic investigation; and 4) that it be adaptable to the techniques necessary for the handling of radioactive specimens without damage to the highly embrittled ion-bombarded surface. It is also desirable that the test preserve the range of data available from each pressurized tube specimen as a result of the varying wall thickness, which produces a range of stresses along the sample axis (see Figure 1). In other words, it should be possible to fatigue test to failure a section from any axial position on the tube.

The test which has been designed meets all these criteria and utilizes equipment which has been developed under the ADIP program at the M.I.T. Nuclear Reactor Laboratory for the Miniaturized Disk Bend Test (MDBT).[4] Essentially,

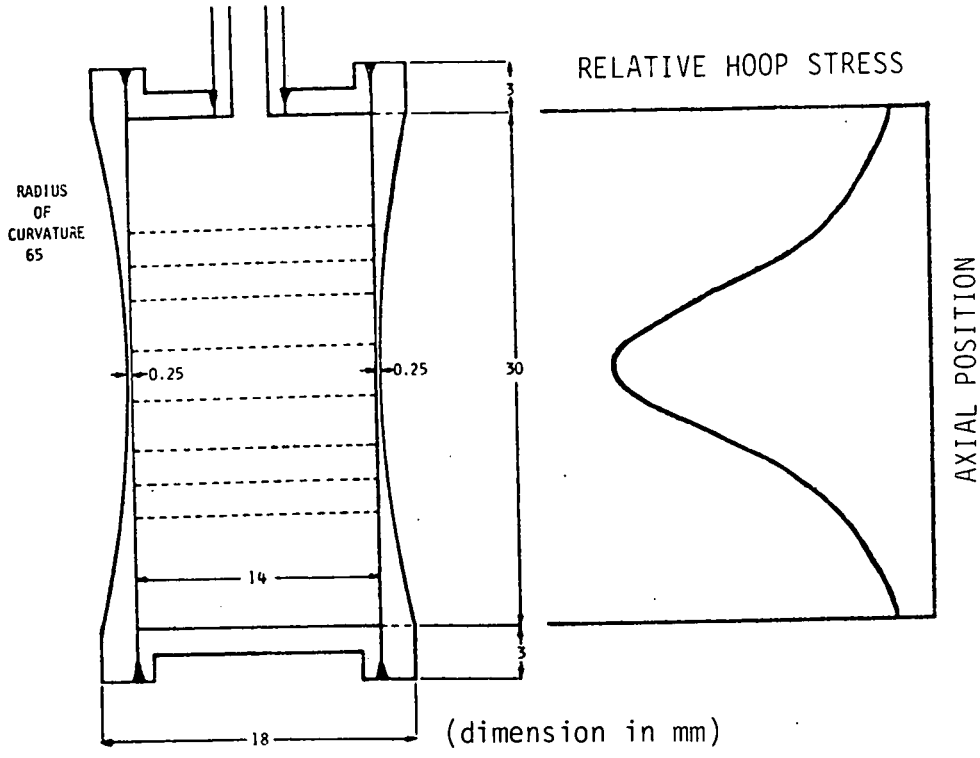

FIGURE 1. Pressure Capsule Showing Sectioning Cuts and Hoop Stress Variation.

this equipment consists of an Instron 1331 servohydraulic testing machine equipped with a low-load (0-150 lb) load cell and fixtures for holding a punch and die. In the standard MDBT, the punch and die are both axisymmetric, with the punch acting on the center of a 3 mm disk supported around the edges (see Ref. 4). The configuration of the punch and die for the current test is shown in Figure 2a. Samples are sections cut from the rings indicated in Figure 1, and the test therefore involves three point bending of a small curved beam with dimensions dependent on the segment of the initial sample tube from which it is cut. A typical fatigue specimen is shown in Figure 2b.

Developmental testing has been carried out using both the 3 mm disks and miniature "beams." The test configuration permits loading in one direction only, and tests are therefore performed in a load regime where plastic deformations are small. Stable control can be maintained with the current equipment at

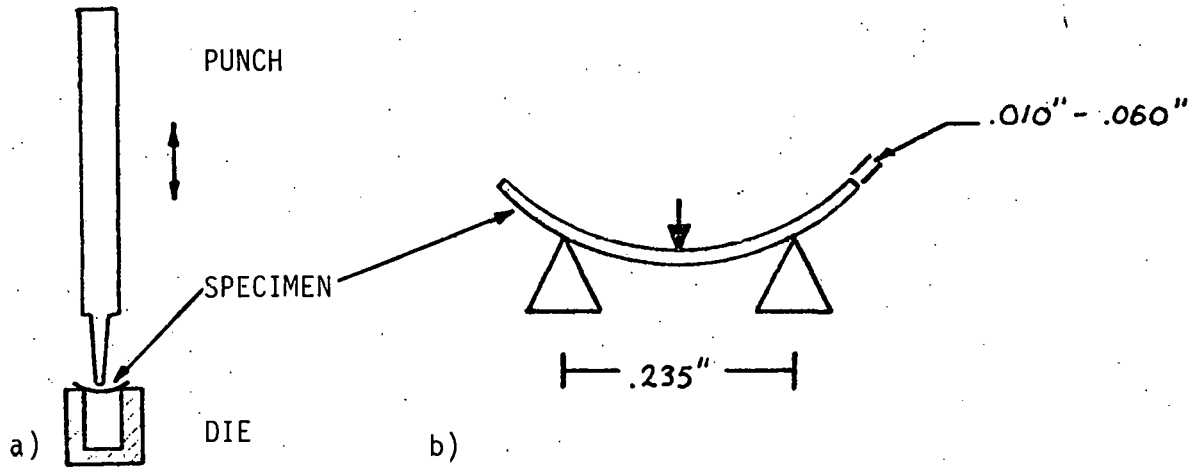

FIGURE 2. a) Punch and Die for Fatigue Test of Partial Ring Specimens.
b) Test Configuration for Partial Ring Specimen.

test frequencies up to 50 HZ, in both stroke control and load control modes. The test parameters which have been established on nonradioactive specimens indicate a test at 20-50 HZ, with maximum stress of approximately 95% of the yield stress and R ≃ 0.05. As currently planned the test will be carried out in load control and the maximum stroke will be monitored to detect failure.

6.0 References

1. H. Andresen and O. Harling, DAFS Quarterly Progress Report, October-December 1978 (DOE/ET-0065/4).

2. G. Kohse, S. G. DiPietro, O. Harling and H. Andresen, DAFS Quarterly Progress Report, January-March 1981 (DOE/ER-0046/5).

3. H. Andresen, G. Kohse, A. S. Argon and O. K. Harling, "A Scoping Experiment to Investigate the Effects of Simultaneous Multi-Energy Ion Bombardment, Neutron Irradiation and Stress Temperature Cycling on 316SS," to be published in J. Nucl. Mater. Proceedings of the Second Topical Meeting on Fusion Reactor Materials, Seattle, Washington, 1981.

4. M. P. Manahan, A. S. Argon and O. K. Harling, "The Development of a Miniaturized Disk Bend Test for the Determination of Postirradiation Mechanical Properties," to be published in J. Nucl. Mater. Proceedings of the Second Topical Meeting of Fusion Reactor Materials, Seattle, Wa., 1981.

7.0 Future Work

Testing of specimens cut from the four pressurized tubes described in Reference 3 will commence immediately following the necessary modifications for routine testing of radioactive specimens. Two of these specimens were ion-bombarded and stress/temperature cycled as described above, while two were stress/temperature cycled in a reactor without ion-bombardment. Direct comparison between ion-bombarded and non-ion-bombarded specimens of similar geometry and thermal and stress history will be undertaken. Twenty to thirty specimens are expected to be available from each pressurized tube sample.

8.0 Publications

H. Andresen and O. K. Harling, "Fusion Reactor First-Wall Performance Under Ion Bombardment and Cyclic Stresses," invited paper, American Nuclear Society, 26th Annual Meeting, MGM Grand Hotel, Las Vegas, Nevada, June 8-12, 1980.

H. Andresen, S. G. DiPietro, G. Kohse and O. K. Harling, "The Behavior of Boron Coatings Under Simultaneous Ion Bombardment and Temperature Cycling," paper presented at Second Topical Meeting on Fusion Reactor Materials, The Park Hilton, Seattle, Washington, August 9-12, 1981.

H. Andresen, G. Kohse, A. S. Argon and O. K. Harling, "A Scoping Experiment To Investigate the Effects of Simultaneous Multi-Energy Ion Bombardment, Neutron Irradiation and Stress/Temperature Cycling on 316SS," paper presented at Second Topical Meeting on Fusion Reactor Materials, The Park Hilton, Seattle, Washington, August 9-12, 1981.

CHAPTER 4

CORRELATION METHODOLOGY

THIS PAGE

WAS INTENTIONALLY

LEFT BLANK

FISSION FUSION CORRELATIONS FOR SWELLING AND MICROSTRUCTURE IN STAINLESS STEELS: EFFECT OF THE HELIUM TO DISPLACEMENT PER ATOM RATIO

G.R. Odette (U.C. - Santa Barbara), P.M. Maziasz (Oak Ridge National Laboratory) and J.A. Spitznagel (Westinghouse Research and Development Center)

1.0 Objective

The objective of this work is to review the data base on the influence of helium on microstructural evolution in charged particle and neutron irradiations; and to develop predictive models of the behavior of stainless steels at helium to displacement per atom ratios characteristic of fusion first wall structures.

2.0 Summary

The irradiated fusion materials data base will be initially developed in fisson reactors. Hence, predictions of the in-service performance of materials in fusion reactors must account for the effect of a number of variables which differ between fission and fusion environments. Ideally such fission-fusion correlations should reflect sound mechanistic understanding. In this paper we review the effects of the helium to displacement per atom ratio on microstructural evolution, with emphasis on austenitic stainless steels. Charged particle data is analyzed to determine mechanistic trends. These results appear to be consistent with a more detailed comparison made between data from neutron irradiations of type 316 stainless steel in EBR-II (low helium) and HFIR (high helium). Finally, a model calibrated to the fission reactor data is used to extrapolate to fusion conditions.

3.0 Program

Title: Damage Analysis and Fundamental Studies for Fusion Reactor Materials Development
Principal Investigators: G.R. Odette and G.E. Lucas
Affiliation: University of California, Santa Barbara

4.0 Relevant DAFS Program Task/Subtask

Subtask C Correlation Methodology

5.0 Accomplishments and Status

5.1 Introduction

The irradiation environments in which engineering data can be obtained for structural alloys differ from fusion conditions in a variety of potentially important ways. Systematic development of a basis for predicting the in-service behavior of fusion alloys will require: judicious use of existing fission reactors; extrapolation of fission data to fusion conditions using physically based models; and use of both fission reactors and special irradiation facilities to help develop, and ultimately verify, correlation procedures. These facilities include high energy neutron sources and the dual-ion charged particle irradiation devices (1,2).

Recently, emphasis has been placed on conditions pertinent to near term fusion devices; namely low temperatures (< 350°C for which very little data exists) and low-to-intermediate exposures (< 60 dpa). Proposed alloys include 20% cold-worked (CW) and titanium modified type 316 austenitic stainless steels (SS), and martensitic stainless steel alloys (e.g. HT-9). Correlations for 20% CW type 316 SS have been formulated for a number of properties. These will be included in the Fusion Materials Handbook (3).

This paper emphasizes the data base and mechanistic understanding pertinent to developing a stress free swelling correlation for this alloy. We focus on the effect of only one of the several environmental variables, the ratio of helium (He) to displacements per atom (dpa), or the He/dpa ratio.* Even this narrow exercise demonstrates the challenges to developing reliable fission-fusion correlations.

To begin, however, it is useful to list the environmental variables other than temperature, dpa and He/dpa ratio which may be important. These include: stress (4); damage rate (4); history effects (4); pulsing (5); and neutron spectrum [due to the influence of primary recoil distributions (6), solid transmutants (7) and hydrogen (8)]. Commercial stainless steels often have highly heterogeneous microstructures both prior to and after irradiation (9). Further, irradiation response is sensitive to many metallurgical variables (4,10). Therefore, correlations must ultimately be developed for specific alloys, and treat factors which lead to heat-to-heat variablity.

We first review charged-particle studies of helium effects to determine trends found in a wide range of metals and alloys for a variety of experimental conditions. This demonstrates that helium is an important, and in some cases necessary, factor in the formation of observable cavities. Increased He/dpa ratios lead to higher cavity densities and smaller cavity sizes. The degree of refinement varies with the He/dpa ratio in systematic ways, which can be described using simple scaling laws.

The effect of helium on total cavity volume, or swelling, is more complex and depends on the coupled behavior of other microstructural components as well as other variables. Microstructures which are

*The He/dpa ratio is always given here in units of atom parts per million per displacement per atom.

dominated by high densities of cavities, which can be induced by large concentrations of helium, often result in lower swelling and retarded precipitation. In contrast, at intermediate cavity densities, associated with higher temperatures and/or intermediate helium concentrations, enhanced swelling is often observed.

These results are consistent with rate theory interpretations, and indicate the important elements which must be considered in formulation of swelling models which incorporate helium effects. These include: helium partitioning and inventory calculations; bubble-to-void conversion critical radius criteria; and microstructurally complete descriptions of void growth kinetics. In particular, the importance of considering concurrent precipitate evolution, and precipitate-cavity association is demonstrated. The charged-particle data suggests that helium can significantly influence the general character of the microstructure; this may vary from cases of dominance of high densities of small matrix bubbles to cavity microstructures characterized by large voids attached to precipitates.

These observations guide and strengthen our interpretation of limited data on neutron irradiations of type 316 SS. This analysis involves a detailed comparison of microstructures formed in fast- and mixed-spectrum reactors which produce lower and higher concentrations of helium relative to fusion conditions, respectively. The trends in the neutron irradiations are very similar to the charged-particle results. Specifically, the high helium concentrations produced in mixed spectrum irradiations leads to accelerated nucleation of a refined, cavity dominated microstructure. This appears to result in earlier swelling at low rates for intermediate exposures (< 60 dpa). In contrast, fast reactor irradiations result in much lower cavity densities, with large voids attached to precipitates. In this case, incubation exposures prior to the onset of swelling are large, but the high exposure (> 60 dpa) swelling rates are high.

The experimental observations are used to guide the construction of a theoretical model which incorporates the elements noted above. The model is calibrated to the neutron irradiation data, and used to interpolate to actual fusion He/dpa ratios. The results suggest that environments which generate very high and low helium concentrations may not result in swelling which brackets behavior in fusion environments. Finally, this analysis should be considered tentative. The limitations of both the current data base and understanding of basic mechanisms are discussed briefly.

5.2 Charged Particle Studies of the Effect of Helium on Microstructural Evolution

5.2.1 Background

Charged-particle studies using single or multiple beams of high energy ions or electrons to implant helium and produce displacement damage possess several unique capabilities. In particular, they provide for precise and independent control of a number of experimentalvariables (e.g. temperature, dpa rate and pulsing) for any material. However, experience has shown that these techniques cannot generally directly simulate neutron effects; and that a number of critical factors, such as damage rate, must be considered in interpreting charged-particle data (11-13). Several promising experimental and theoretical efforts are underway to establish charged- particle-neutron data correlations (13). However, at this time, these techniques are most useful for studying critical mechanisms and parameters. Reviews of some of the charged-particle literature have been published (6,14).

Charged-particle studies have been conducted on a wide variety of metals and alloys with He/dpa ratios up to 500, dpa rates from about $2x10^5$ to $3x10^3$ dpa/s, and temperatures from about 0.3 to 0.6 of the melting point. The general trends found in this data base are grouped into three broad

categories: helium to displacement per atom effects on the size and number density of microstructural features; scaling laws; and consequences to cavity volume. Further, the effects of beam history are reviewed briefly. We analyse experiments in which helium is preinjected followed by charged-particle irradiation to generate displacement damage, and dual-ion studies in which simultaneous helium implantation and displacement damage is produced using two (or more) particle beams.

5.2.2 Helium Induced Microstructural Refinement

Increasing the He/dpa ratio refines the microstructure in the sense of causing cavity and loop formation to occur on a finer scale; that is, higher number densities and smaller sizes (14-47). Further, helium often promotes the formation of bimodal cavity size distributions (14-24). Distinct upper limits on the size of the small component of the bimodal cavity distributions, which are presumably gas bubbles, is commonly observed (15-23). This has important implications with respect to the mechanism of void formation which will be discussed in Section 5.4. In complex alloys containing precipitates, the balance between matrix cavities (usually small) and those associated with precipitates (usually large) often shifts in favor of the small matrix cavities with higher He/dpa ratios (17,19,25,26).

Varying degrees of loop enhancement with helium implantation have been reported (14,17,19,22-24). The effects are more pronounced for preinjected than for dual-ion conditions (14,17,19,24) and for commerical type 316 SS compared to a high purity Fe-Ni-Cr model alloy (18,22). However, the total dislocation density is relatively insensitive to the He/dpa ratio and injection mode (16-19,21-23,27).

The influence of helium on precipitation has also been studied for some stainless steels alloys (17,19,23,26,28,29). Precipitation appears to be highly coupled to cavity and loop microstructures. Segregation to these

features of solutes such as silicon and nickel, sometimes leading to precipitates or precipitate shells, is well established (19,26). In some cases, early loop formation appears to set the stage for subsequent phase instability and swelling (19). When cavity and loop microstructures are refined, solutes partition to more sites. This can lead to a finer distribution and a lower volume fraction of second phase (17,19,23,26,28,29). These observations are summarized schematically in Table 1.

TABLE 1

A SCHEMATIC REPRESENTATION OF HELIUM-INDUCED MICROSTRUCTURAL REFINEMENT TRENDS OBSERVED IN CHARGED-PARTICLE IRRADIATIONS

	Increasing He/dpa Ratio		
Feature	(1)	(50)	(500)
Cavity Density	N_c	$10\text{-}50N_c$	$20\text{-}100N_c$
Loop Density	N_L	$1\text{-}3N_L$	$2\text{-}4N_L$
Network Dislocation Density	ρ_d	$0.5\text{-}2\rho_d$	$0.5\text{-}2\rho_d$
Precipitate Volume Fraction*	V_p	$0.5\text{-}1V_p$	~0

*Irradiation induced or modified

The results of a number of studies can be used to quantify the influence of the He/dpa ratio on some microstructural features. Such scaling laws provide insights into critical mechanisms. Figure 1 shows one example for type 304SS dual-ion irradiated at 700°C (23). The total cavity number density has been normalized by dividing by the square root of the helium concentration [He] (note that the [He] is proportional to the helium injection rate K_{He}). The normalized quantity exhibits a small dependence on the helium injection rate over two orders of magnitude. Thus, the cavity density N_c can be crudely related to the helium concentration [He]

in terms of a simple power dependence p as

$$N_c \alpha [He]^p \quad (1)$$

where p ~ 0.5. Such scaling is consistent with other experimental observations (19,30,31). However, some studies suggest different scaling dependence. Values of p ~ 0.25 (27,32), 1(22,33) and 2(17,18) have been observed.

Some of these variations may result from inconsistent definitions of what constitutes a cavity or failure to resolve small bubbles. However, cavity scaling behavior is probably dependent on a number of variables. For example, the existing dislocation and precipitate microstructure is expected to influence the balance between homogeneous and heterogeneous nucleation of cavities. Further, cavity densities often decrease at high exposures due to void coalescence. The concentration of residual gases,

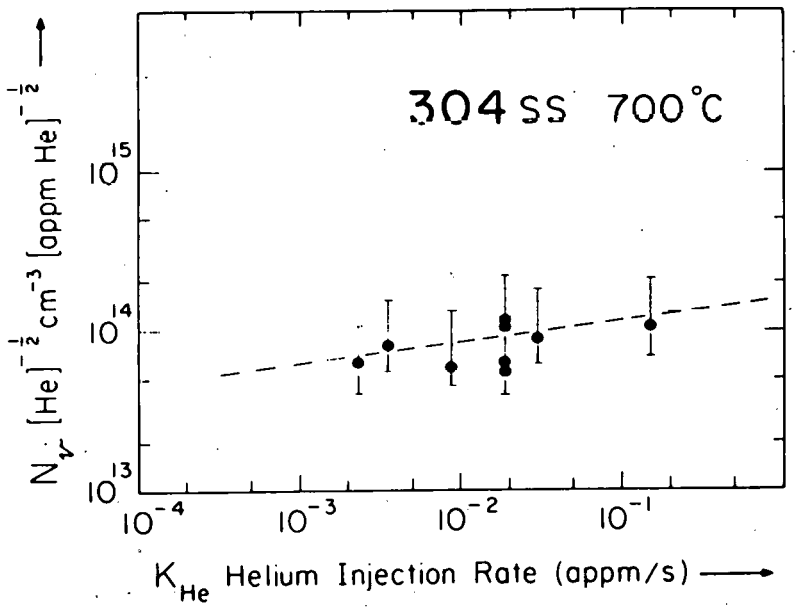

FIGURE 1. The Cavity Density Normalized by Dividing by the Square Root of the Helium Concentration Versus the Helium Injection Rate for a 700°C Dual-Ion Irradiation of Type 304SS.

which may act as a surrogate for helium, seems to be an important factor (14,34). Finally, the temperature and sequence of helium implantation are significant as discussed below. Scaling laws for loops and precipitates have not been established.

5.2.3 Consequences of the Refined Microstructure

Within the framework of the kinetics of point defect segregation and clustering (i.e., rate theory) the major effect of helium on macroscopic properties such as cavity swelling is due to perturbed point defect absorbtion / emission balances at sinks. The net effect of increasing the He/dpa ratio on swelling varies depending on the circumstances as summarized in Table 2.

TABLE 2

THE EFFECT OF INCREASING HE/DPA RATIO ON SWELLING FOUND IN CHARGED-PARTICLE IRRADIATIONS

Effect on Swelling	References
Increase	8,22,25,27,28,35-37
Decrease	16,18,25,30,38,39
Variable*	14,19,27,32,34,40,41

*Depending on the temperature, exposure and He/dpa ratio.

The sign and magnitude of swelling changes appears to depend on the degree of refinement of the microstructure. For example, in one dual-ion experiment increasing the He/dpa ratio from 15 to 50 increases the post-incubation swelling by a factor of ~3 at 20 dpa in a solution annealed and aged type 316SS irradiated at 625°C (22). In this case, the density of small cavities did not change much with increased He/dpa ratio and the number of large cavities increased only by a factor of about 3. In contrast, in a 700°C dual-ion irradiation of a Fe-Ni-Cr model alloy an increase in the He/dpa ratio of 16 to 55 resulted in an increase in cavity

density by a factor of ~20; swelling decreased by a factor of ~8 at 20 dpa (18). Notably, the bimodal cavity size distribution did not continue beyond the incubation regime for the lower He/dpa ratio in this case. In part, the complex behavior described above may be due to He/dpa induced shifts in the temperature-dependence of swelling as found in a pure stainless steel (i.e. a Fe-Ni-Cr-Mo alloy) as illustrated in Figure 2 (34). Here the temperature of the peak swelling rate is shifted upwards with respect to a single-ion bombardment by ~50°K for dual-ion irradiation at a He/dpa ratio of 20. Other studies of the temperature-dependence of swelling suggest that increased He/dpa ratios decrease swelling below the peak temperature (39) and extend swelling to higher temperatures (37). However, helium induced extentions of swelling to lower temperatures has also been reported (37). The effect of helium on the swelling and swelling temperature-dependence is different for preinjection and dual-ion conditions (16,17,37).

Further, simple monotonic changes in swelling as a function of He/dpa ratio are not always observed. That is, an increased He/dpa ratio does not lead to a steady increase or decrease in swelling. We cite two examples.

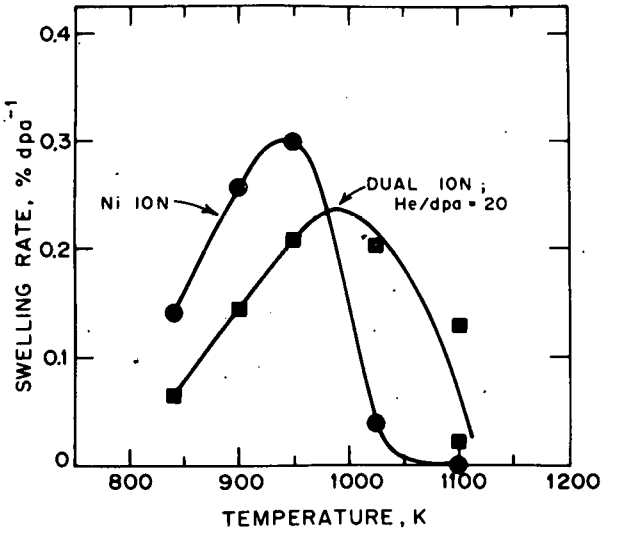

FIGURE 2. The Temperature-Dependence of the Swelling Rate For Single and Dual-Ion Irradiations of a Pure Stainless Steel. (32)

Figure 3 shows the effect of a dual-ion experiment on a titanium-modified type 316SS irradiated to 70 dpa at 625°C at He/dpa ratios of 0, 0.2 and 20 (19). As indicated in the Figure 3, this alloy is swelling resistant in the absence of helium (swelling ~0). A low He/dpa ratio of ~0.2 provides sufficient impetus for the nucleation and rapid growth of cavities (swelling ~3.5%). However, raising the He/dpa ratio to ~20 results in reduced swelling (~ 1.8%). Perhaps an even more striking example is the observation of precipitate and cavity alignment in dual-ion bombarded solution annealed type 316SS at 600°C (26). This phenomenon, which can apparently lead to large swelling through rapid coalescence of aligned cavities, can be totally suppressed by either increasing or decreasing the He/dpa ratio.

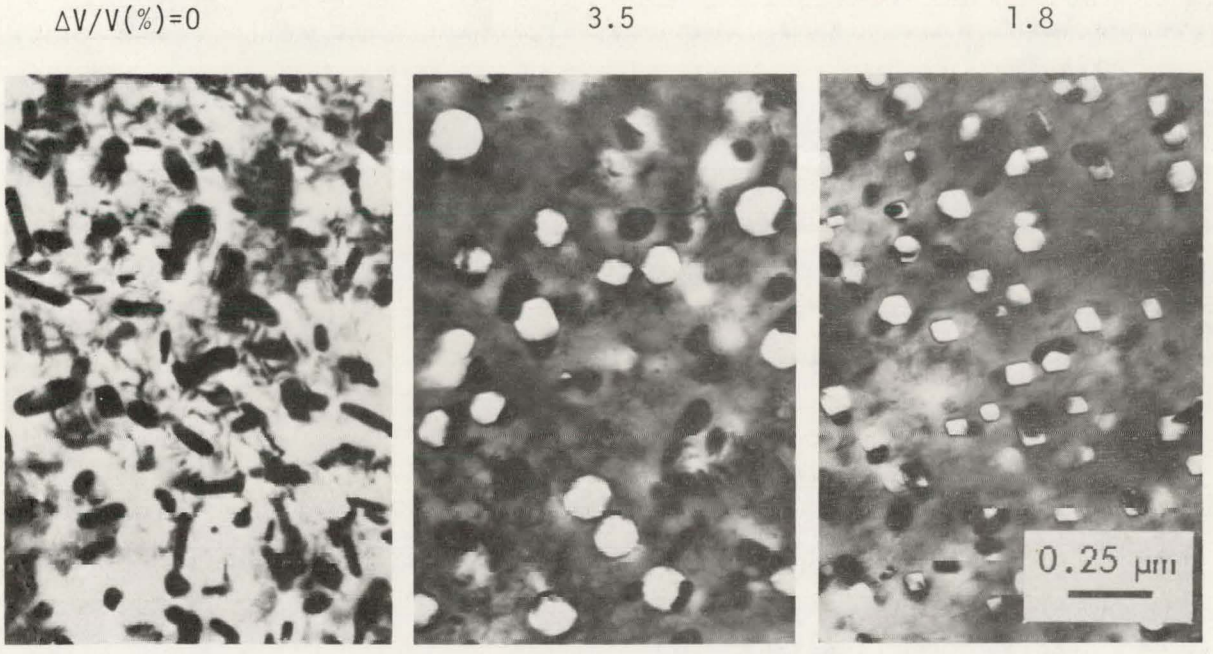

FIGURE 3. Micrographs Showing the Effect of the He/dpa Ratio on the Microstructure of a Titanium-Modified Stainless Steel Dual-Ion Irradiated at 625°C to 70 dpa. (19)

In general, charged-particle experiments suggest that small amounts of helium promote cavity nucleation and increase cavity volume fractions, particularly in swelling resistant alloys. Larger amounts of helium may increase cavity and loop densities to the point where swelling is retarded. In some cases even more helium may reverse this trend and result in increased cavity volume. High cavity and loop densities also retard precipitation of nickel and silicon rich phases.

5.2.4 Beam Scheduling and Rate Dependence

Microstructural evolution is influenced by the time and temperature history of helium implantion. The most extreme case, which also results in the most dramatic microstructural differences, is observed for cold preinjection (near room temperature) conditions. Such experiments generally result in higher cavity and loop densities than are produced by dual-ion or hot preinjection (near the temperature at which displacement damage is generated) irradiations (16,18,19,24,27,37,41). There are concomitant effects on swelling and precipitation. Indeed, these tend to be suppressed by the very high cavity and loop concentrations found in some cold preinjection experiments (16,18,19,24,32,39,41). Differences between hot preinjection and dual-ion microstructures have also been reported (24,29).

Dual-ion experiments have been used to study the effect of the helium implantation schedule (23,42). This is useful for analyzing mixed spectrum fission reactor experiments in which there is a time dependent He/dpa ratio. The available data indicates that, with one exception, those microstructural features which are most subject to refinement by helium are also most sensitive to beam history. Cavity size distributions, interstitial dislocation loops, and precipitation of nickel and silicon rich phases all depend on beam history, while the total dislocation density is unaffected. The exception, noted above, is total

cavity density which appears to be unaffected by beam schedule, despite its dependence on the He/dpa ratio (23).

Several studies of low displacement rate neutron irradiations following cold preinjection of various pure metals and alloys have been reported (43-47). These results are qualitatively consistent with the high displacement rate charged-particle data discussed above. Most notably, cold preinjection of helium appears to refine cavity and loop microstructures and usually retards cavity swelling.

In summary, the charged-particle studies demonstrate both systematic trends in the response of the microstructure to variations in the He/dpa ratio and a well defined sequence of events. However, discussion of the mechanistic implications of these results will be deferred to Section 4 to permit comparison with the data from mixed and fast spectrum neutron irradiations.

5.3 A Comparison of Type 316 Stainless Steel Irradiated in Fast and Mixed Spectrum Reactors

5.3.1 Background

Because of the need for bulk mechanical properties and the limitations of charged-particle studies, fission neutron irradiations will form the primary basis for generating engineering data for fusion alloys. Substantial information is available on the microstructural response, particularly swelling, of austenitic stainless steel alloys in fast-spectrum reactors such as the Experimental Breeder Reactor-II (EBR-II) (10,48,49). Unfortunately, these environments have low He/dpa ratios of ~ 0.35 for stainless steel relative to nominal fusion values of ~ 10 (50). Note, however, that depending on the position in the blanket and details of the reactor design, fusion He/dpa ratios may vary from ~1 to 30. Existing fast reactor data is also primarily limited to temperatures greater than 370°C. In contrast, mixed-spectrum reactors

produce copious amounts of helium in nickel bearing alloys by the two-stage ^{58}Ni (n_{th}, γ) ^{59}Ni (n_{th}, α) reaction (50). In the mixed-spectrum High Flux Isotope Reactor (HFIR) the He/dpa ratio for stainless steel containing 13% Nickel is $\sim$ 70 for exposures greater than 10 dpa (50). Hence, the fast-and mixed-spectrum fission environments bracket nominal fusion He/dpa ratios.

The fast reactor data base shows that irradiation induced microstructural evolution is sensitive to a number of material variables associated with composition and alloy condition (4,10,48,49). Hence, it is important to minimize the material as well as irradiation parameter variations in comparing fast and mixed spectrum data. Unfortunately, the data available for such a comparison consists only of a single heat of type 316 SS in both 20% CW and solution-annealed (SA) conditions (51-58). The composition of this steel, specified as DO Heat, is as follows (weight percent):

Fe	C	Cr	Ni	Mo	Mn	Si	Ti	N
63	.05	18	13	2.6	1.9	.8	.05	.05

Note that DO Heat is slightly enriched in silicon relative to typical breeder steels (0.8% versus ~ 0.5%) (57).

Direct comparison of even this limited data is confounded by several factors which include: 1) a relatively small overlap in dpa and temperature; 2) significant uncertainties in temperature and potential effects of complex temperature histories; 3) a time-dependent He/dpa ratio in HFIR increasing from 15 at ~1 dpa and saturating at ~70; 4) different solid transmutant generation in the two environments; [For example, HFIR produces vanadium ~ .7% and depletes manganese from ~ 1.9 to .9% at 50 dpa (7)]; and 5) characterizing the average microscopic behavior and correlating this with bulk properties is somewhat uncertain for the highly heterogeneous microstructures found in cold-worked stainless steels.

Probably the most serious problems are items 1, 2 and 4. Only additional data will resolve item 1. With respect to item 2, the previously reported temperatures for HFIR are now known to be low by ~50-100°C or more. This conclusion is primarily based on a revised estimate of gamma heating rates (59). Perhaps more significantly, a rationalization of observed temperature regimes of loop formation, dislocation recovery, recrystallization, and precipitation in EBR-II and HFIR results if the HFIR temperatures are increased by ~75-100°C. Conversely, if such temperature adjustments are not assumed, there appear to be large and surprising differences between HFIR and EBR-II irradiations for phemomena such as recrystalization.

Therefore, we apply an increase to the HFIR temperatures of 75°C plus rounding to the nearest 50°C increment (e.g., the temperature of 460°C was shifted to a nominal 550°C). There are residual temperature uncertainties in both the HFIR and EBR-II of ~25-50°C. Further, the irradiations were not isothermal in all cases. The EBR-II data is assigned nominal temperatures of 520 and 620°C. In order to minimize the impact of the uncertainties in the irradiation temperatures, we compare the EBR-II data with the HFIR data at both adjacent higher and lower nominal temperatures.

With respect to item 4, the data presented in Reference 7 suggests a small effect of manganese burn-out on swelling in CW type 316 SS in the composition range transgressed. Further, the generation of vanadium does not result in formation of vanadium MC carbides. Thus, we do not feel that the solid transmutants should be a major factor in the validity of data comparisons.

The data presented in this section is primarily taken from References 51-58. Note, however, that the HFIR temperature correction discussed above has not been applied in these publications. In addition, some of the data is from previously unpublished work of one of the authors (Maziasz).

5.3.2 Precipitation in the 20% CW Do Heat

We cannot do justice here to the complex microchemical evolution which takes place during irradiation of the 20% CW DO Heat. Table 3 provides a brief summary of EBR-II and HFIR data at intermediate exposures of 36 to 54 dpa.* There appears to be a general similarity in the precipitate structure and composition in the two environments. However, HFIR irradiations do result in higher densities of second phase particles and, in some cases, slightly smaller sizes. In general, the silicon concentrations of the phases induced in HFIR are lower than those formed in EBR-II and similar to those found in thermally precipitated eta and Laves. Further, there is a substantially lower nickel concentration in Laves phase formed at 550°C and 42 dpa in HFIR compared to the enrichment found at 520°C and 36 dpa in EBR-II. Preliminary measurements of EBR-II specimens irradiated to 75 dpa at 620°C show a substantial nickel enrichment in Laves phase compared to the relatively low concentrations found for either 550°C and 54 dpa or 650 and 42 dpa irradiations in HFIR. Laves phase formed by thermal precipitation has a low nickel concentration. However, it can become highly enriched with this element under irradiation. Hence, Laves phase is believed to be a good monitor for solute segregation. Therefore, these differences may indicate an effect of the high cavity sink density, formed in HFIR irradiations, minimizing solute segregation induced partitioning of nickel and silicon to the precipitates.

Precipitation is not a steady evolution, particularly in HFIR. Rather, it can involve marked cycles of precipitation, dissolution and reprecipitation, as is observed for tau phase in HFIR. These cycles appear to be closely coupled to the evolution of the cavity microstructure. Garner has proposed that rapid void swelling is largely

*The precipitate sizes, number densities and volume fractions reported in this section are subject to considerable uncertainty. Further, we note that Brager and Garner have reported a somewhat different precipitate structure for the 20% CW DO Heat for the same irradiation conditions (57).

TABLE 3

A SUMMARY OF PRECIPITATE STATISTICS FOR HFIR AND EBR-II IRRADIATIONS AT 36 TO 54 DPA

Spectrum-Phase	Temperature (°C)	Exposure (dpa)	Composition (%) Nickel	Silicon	Density ($\#/m^3$)	Size (nm)	Volume Fraction	Comments
HFIR-eta	550	54	20	4	10×10^{19}	50-120	.014	A thermal phase naturally rich in nickel and silicon. Primarily forms on the subgrain structure. Has a very high association with bubbles in both environments. Dominant phase in HFIR at 450°C (0.03 volume fraction at 49 dpa) with a high cavity association.
	650	42	30	4	3	100-200	.012	
EBRII-eta	520	36	25	7	3	70-200	.013	
	620	36	25	7	3	70-250	.016	
HFIR-Laves	550	54	12	5	25	70-400	.03	Found between the subgrain structure. Irradiation induced at 520 to 550°C and enhanced in volume fraction at 620 to 650°C in both environments. Variable nickel and silicon composition. Observed to be highly enriched in nickel at both 520 and 620°C in EBR-II at 70-75 dpa. High association with large cavities (voids) in EBRII and small cavities (bubbles) in HFIR.
	650	42	7	5	13	90-300	.043	
EBRII-Laves	520	36	19	7	4	100-350	.005	
	620	36	8	5	3	80-500	.02	

Description of Minor Phases (< 0.01 volume fraction)

Phase	Spectrum	Comments
σ	HFIR	A nickel poor phase found at a volume fraction of ~.01 in the form of a relatively low density of large particles at 650°C and 42 dpa in HFIR.
	EBR-II	Observed as a small volume fraction (<.001) of very large, very sparse particles at 620°C and 36 dpa.
γ'	HFIR	A nickel and silicon rich irradiation induced phase which forms only briefly in HFIR at 450°C at ~ 10 dpa, redissolving at higher exposures.
	EBR-II	Observed only at 70 dpa and 520°C at a low volume fraction (< 0.002).
τ	HFIR	A chromium and molybdenum rich phase which forms early in HFIR at 550°C as blocky particles, but appears to dissolve and subsequently reprecipitate as a very fine dispersion at 54 dpa; also observed at 650°C and 42 dpa.
	EBR-II	Observed at a small volume fraction (<.005) at 36 to 75 dpa at both 520 and 620°C.
G	EBR-II	Observed only in EBR-II at 70 dpa and 520°C at a low volume fraction (< .003). Not observed in HFIR.

triggered by removal of a critical amount of silicon and nickel from the matrix (4). Specifically, he reports that voids generally occur when matrix regions are depleted by precipitation to less than ~10-11% nickel as measured by microanalytical procedures. Using this thesis, he has been able to rationalize, qualitatively,a number of disparate observations (4). However, there are indications that the overall process may be somewhat more complex than this; e.g., mechanisms may also involve the direct action of precipitates as nucleation sites. Further, the cavities themselves provide sites for solute segregation.

The micrograph in figure 4 compares regions with varying levels of precipitation of eta and Laves phases for the EBR-II specimen irradiated to 36 dpa at 620°C. It illustrates the highly heterogeneous microstructures found in cold-worked stainless steels. Voids form preferentially in the less heavily precipitated regions (often on Laves particles). However, from mass-balance considerations of the nickel enrichment of the eta phase, and from direct matrix measurements, the void free regions are lower in nickel (9.5-11.5%) and the regions containing voids are higher in nickel (12-13%).

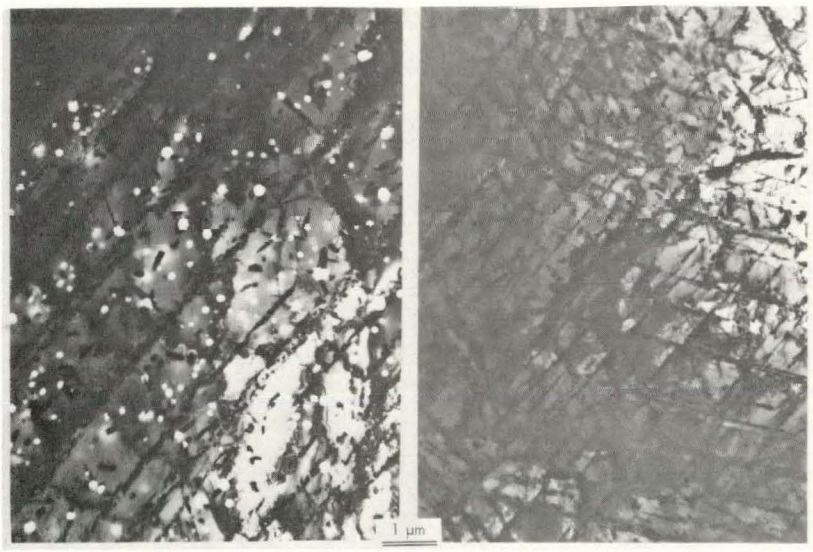

FIGURE 4. Micrographs Illustrating the Heterogeneous Precipitate and Cavity Microstructure in the 20% CW DO-Heat Irradiated in EBR-II to 36 dpa at 620°C.

Clearly, additional experiments are required to understand the causes and consequences of microchemical evolution. Data that can be analysed quantitatively in terms of point defect and solute mass balances within pertinent local microstructural volumes is critically needed. This requires measurements of precipitate volumes and composition, matrix composition and the defect statistics.

Another difference between the two environments is the rate of precipitation, which appears to be accelerated in HFIR as illustrated in Figure 5. Only the data for a nominal temperature of 620°C for EBR-II and nominal bounding temperatures of 550 and 650°C for HFIR is shown both here, and in the following section. In all cases, the results at nominal EBR-II temperature of 520°C (and 450 and 550°C for HFIR) show similar trends. We have constructed average trend curves using the convention of dashed lines for HFIR and solid lines for EBR-II. Since the HFIR data is for a range of temperatures, and because of the uncertainties in the data, these curves are only meant to serve as rough guides and to highlight similarities or differences between the two environments. Figure 5 shows that at ∿10 dpa precipitate volume fractions in HFIR are ~ .005 at 550°C and ~ .07 at 650°C. Essentially no second phases are observed in EBR-II

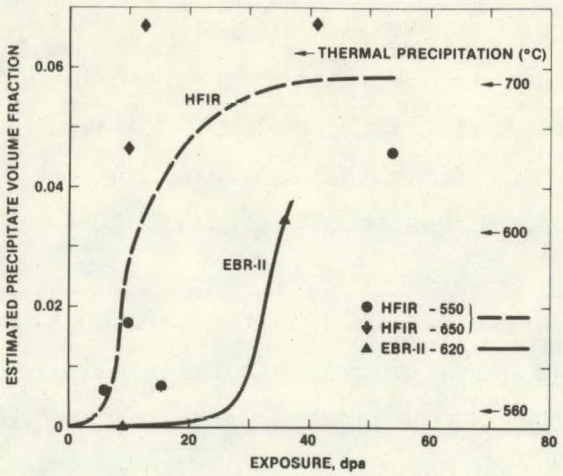

FIGURE 5. The Exposure Dependence of the Total Precipitate Volume Fraction for the 20% CW DO-Heat Irradiated in HFIR and EBR-II in the Temperature Range of 500 to 650°C as Indicated.

at similar exposures at 620°C. At 36 dpa considerable precipitation has occurred in both environments.

5.3.3 Microstructures in the 20% CW DO Heat

No dislocation loops are observed at exposures greater than 10 dpa and above temperatures of 450°C in either environment. The network dislocation density recovers rapidly in both cases, saturating at levels of ~1 to 2 x $10^{14}/m^2$.

There is a fundamental difference in the cavity microstructures in HFIR and EBR-II. This is illustrated in the micrograph shown in Figure 6. In EBR-II (at 36 dpa and 620°C), cavities tend to be heterogeneous and larger. The largest (~50% of the large cavities) are found on precipitates and they dominate the swelling. In HFIR (at 42 dpa and 650°C) a much higher density of smaller cavities form. These are more homogeneous and predominently located in the matrix.

Figure 7a shows the fluence dependence of the cavity densities. Observable cavity formation is accelerated as well as greatly enhanced (by a factor of ~30) in HFIR. Figure 7a also shows a relatively high density (~ $10^{14}cm^3$) of small cavities (~ 5-7 nm) in EBR-II at ~36 dpa and 620°C. Note that for these conditions in EBR-II, there is a trimodal distribution of large cavities on precipitates, and both intermediate and small cavities in the matrix. It appears that most of the smallest cavities, which are probably bubbles at 36 dpa, convert to voids at 75 dpa.

Figure 7b shows that the average cavity diameters are much smaller in HFIR than in EBR-II. Finally, we note the preliminary results of a recent high voltage electron microscopy (thick area) study of the EBR-II samples irradiated at 70-75 dpa at 520 and 620°C; this work indicates that many areas contain a lower density of much larger voids (several hundred nm diameters) than reported in Reference (57). Measurement of the detailed cavity statistics is in progress.

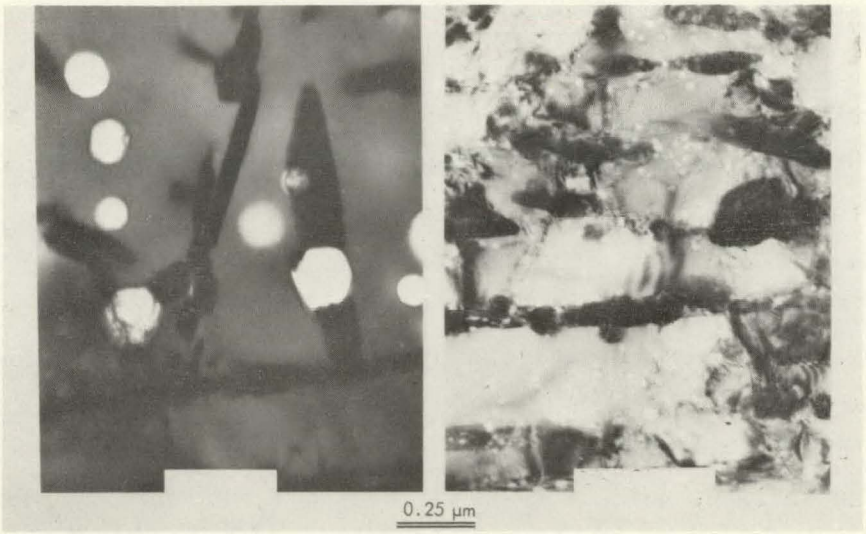

FIGURE 6. Micrographs Illustrating the Microstructures Formed in the 20% CW DO-Heat of Irradiations in EBR-II to 36 dpa at 620°C (Left) and in HFIR at 650°C to 42 dpa (Right).

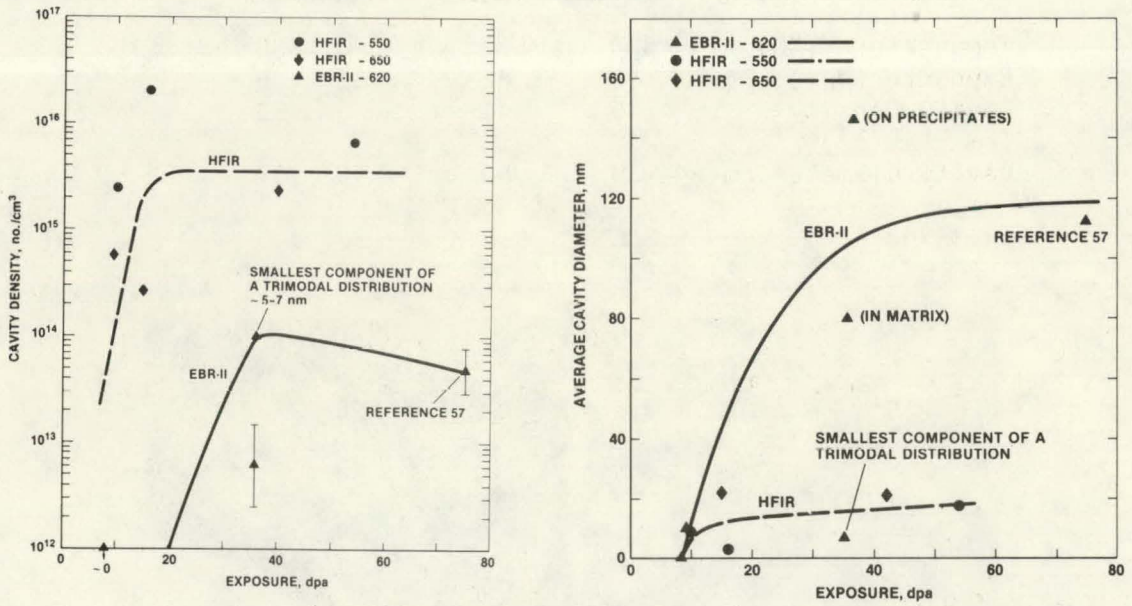

Figure 7. The Exposure Dependence of the (a) Cavity Density and (b) Average Cavity Diameter in the 20% CW DO-Heat Irradiated in HFIR and EBR-II in the Temperature Range of 550 to 650°C as Indicated.

5.3.4 Solution Annealed DO Heat Cavity Evolution

Even less data is available on solution-annealed DO heat. The micrographs in Figure 8 compare the cold-worked (CW) and solution-annealed (SA) conditions for irradiations in HFIR to 42-54 dpa at 550°C. In contrast to the cold-worked condition, the cavities in the SA DO Heat are lower in density (a factor of 4-6) and larger in size. The largest are found on precipitates. The overall swelling in the solution-annealed condition is ~8-9% compared to ~2% for the 20% cold-worked alloy. A comparative summary of EBR-II and HFIR induced cavity microstructures in the SA DO Heat is given in Table 4.

TABLE 4

A COMPARISON OF SA DO HEAT CAVITY STATISTICS FOR IRRADIATIONS IN HFIR AND EBR-II

SPECTRUM	HFIR		EBR-II	
Temperature (°C)	550	650	520	620
Exposure (dpa)	42	42	31	36
Cavity Density ($cm^{-3} \times 10^{13}$)	140	44 (.12)	5	.63
Cavity Diameter nm	39	50 (3350)	49	137
Swelling (%)	8.8	8.5	.37	1.5

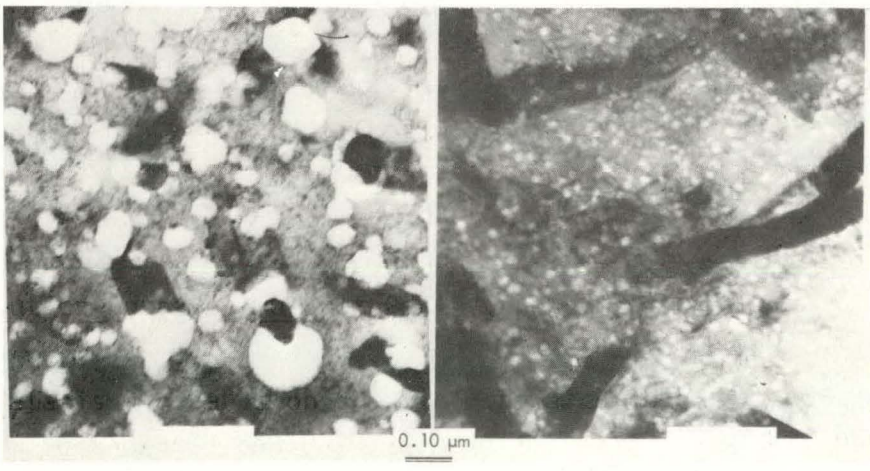

FIGURE 8. Micrographs Illustrating the Microstructures Formed in HFIR Irradiations of SA DO-Heat to 36 dpa at 520°C (Left) and 20% CW DO-Heat to 54 dpa at 550°C (Right).

5.3.5 Swelling Behavior of the 20% CW DO Heat

While the analysis of the total microstructure given in the previous sections is useful for improving basic understanding, (including the mechanisms of irradiation induced changes in mechanical properties), designers require simpler formulations of effects such as swelling.

Figure 9 shows the EBR-II swelling data at the nominal irradiation temperatures of 520 and 620°C along with the bounding HFIR data. Both void volume fractions derived from transmission electron microscopy (TEM) and immersion density data are included. Both techniques are believed to have relatively large uncertainties. The uncertainties in the TEM measurements primarily derive from the highly heterogeneous microstructures of cold-worked stainless steels. Immersion density uncertainties are related to the details of the measurement procedures, which have improved significantly in recent years.

Immersion density data for the MFE Reference Heat of 20%CW type 316 SS, is also shown in Figure 9 (60). We have noted the problem of comparing different heats of steel. However, the most important difference between

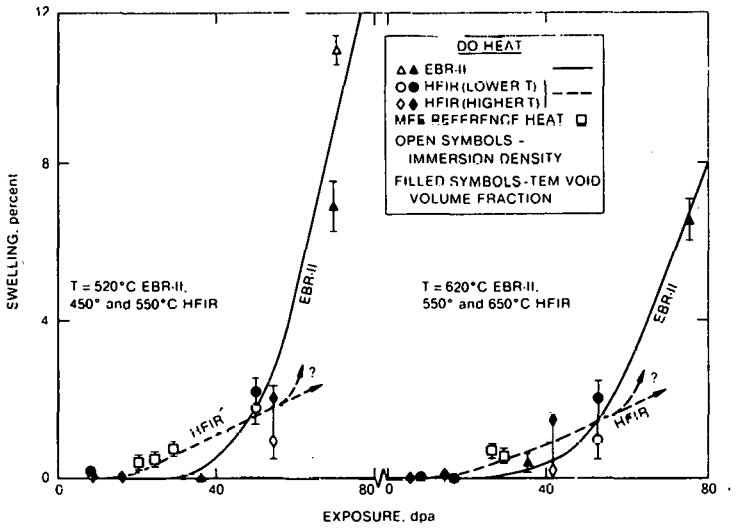

FIGURE 9. A Comparison of Swelling in the 20% CW DO-Heat Irradiated in HFIR and EBR-II in the Temperature Range of 450 to 650°C as In Indicated.

the Reference and DO Heats is probably due to the lower (~ 0.67 versus 0.80%) silicon content in the former. The data in Reference 61 suggests this difference should not have a large effect on swelling for the conditions shown in Figure 9.

Since comparison is made for the void volume fractions, the immersion density swelling values are increased slightly (0.1%) to reflect probable densification due to carbide precipitation (57). The trend curves for the EBR-II irradiations are constructed using the same bilinear form and curvature parameter recommended for several heats of breeder steels (10). However, it is necessary to impose longer incubation times and different swelling rates to approximately fit the DO Heat data. The HFIR curves are drawn as rough averages of all of the available data. The magnitude of swelling in HFIR is reasonably consistent with predicted helium bubble volumes, if it is assumed that most of the helium partitions to the cavities.

This very limited data suggests that the HFIR irradiations result in more swelling than EBR-II exposures at less than 50 dpa. The swelling in HFIR may be primarily due to helium bubbles. Extrapolation of the results to above 50 dpa would imply a much lower swelling rate in HFIR than in EBR-II. A plausible physical basis for such behavior is discussed in Section 4. However, no high fluence data exists to confirm this prediction. Indeed, an alternate position is that additional precipitation (and concomitant nickel and silicon removal) will accelerate HFIR swelling rates at higher exposures (57).

Another possible difference between EBR-II and HFIR irradiations is in the temperature-dependence of swelling at low-to-intermediate exposures. Figure 10 shows the HFIR data for 7 to 16 and 42 to 60 dpa. Due to the limited data, it is not possible to establish the temperature-dependence for swelling of the DO Heat in EBRII. Hence, we represent the shape of the fast spectrum swelling temperature-dependence using a correlation for EBR-II irradiations of several heats of breeder steels (10). While this

correlation is directly applicable to only a limited number of heats of 20% CW type 316SS, the existence of swelling peak(s) for fast reactor irradiations in the temperature range from ~450 to 650°C appears to be generic to commerical stainless steels at exposures less than 60 dpa (48,49). Thus, the analysis shown in Figure 10 suggests a possible inversion in the temperature-dependence of swelling. That is, the minimum swelling in HFIR occurs in the range of peak swelling in EBR-II.

However, the enhancement of swelling for high He/dpa ratios at low temperatures does not appear to be general, since the 20% CW Reference Heat swelling increases monotonically with temperature in HFIR (60). Further, we have already noted that little fast reactor swelling data exists below 370°C. Conversely, the increase in swelling at high temperatures in HFIR is consistent with a helium bubble mechanism. Thus, the existence of a high temperature enhancement of swelling in HFIR appears to be well established. However, more data is needed to determine the temperature-dependence and magnitude of swelling below 400°C in both environments.

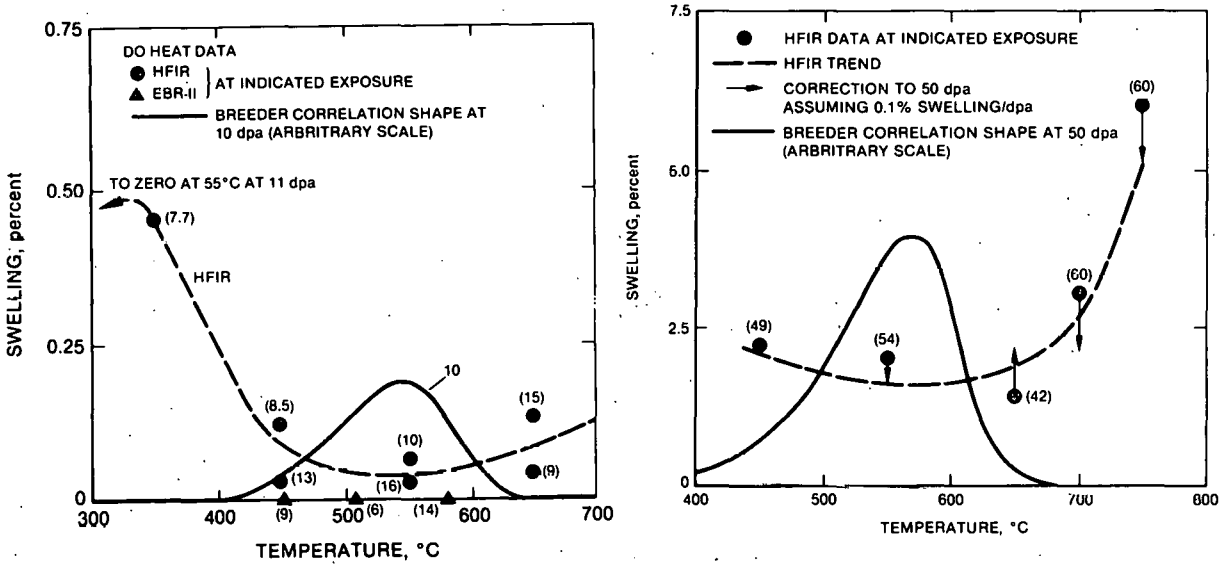

FIGURE 10. The Temperature Dependence of Swelling in the 20% CW DO-Heat Irradiated in HFIR in the Range of 350-750°C at the Indicated Exposures. The shape of the EBR-II swelling temperature-dependence from Reference (10) is shown for comparison.

5.3.6 Design Correlations for 20% CW 316 SS

The practical implications of the present state of understanding to design equations is illustrated in Figure 11, where two swelling correlations proposed for inclusion in the Fusion Materials Handbook are presented. The solid curves, developed by Garner et. al. (62), are based on the premise that fast reactor data can reasonably represent stress free swelling for fusion environments. This contention is supported by an analysis which suggests relatively small swelling differences between EBR-II and HFIR (57). A clear strength of this formulation lies in the large amount of data that it represents.

An alternate position developed by Maziasz and Grossbeck (63) is shown as dashed lines. These curves model the behavior of the 20% CW DO Heat in HFIR. Note that this requires interpolation between ~350°C and 55°C (no swelling is observed at 55°C and 10 dpa in HFIR). Further, the high fluence behavior is based on extrapolating the low swelling rates found in HFIR at intermediate exposures in the temperature range of 450 to 650°C. The major advantage of this correlation is that it is derived from an environment with a high He/dpa ratio.

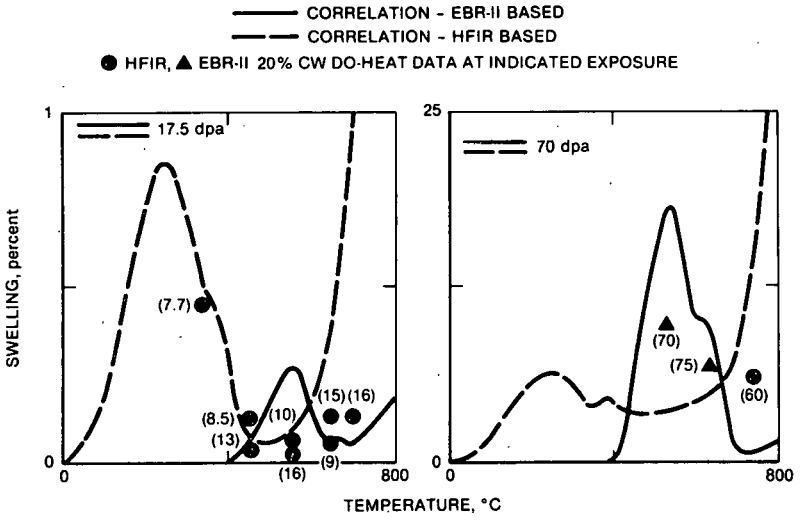

FIGURE 11. Swelling as a Function of Temperature at Two Exposures Based on Two Proposed Correlations for 20% CW SS. The 20% CW DO-Heat data for irradiations in HFIR and EBR-II is also shown.

There are probable limitations of both representations. At very high and, possibly, low temperatures, swelling may be underpredicted by the EBR-II based correlation. The HFIR based curve may underpredict swelling at intermediate temperature and high exposures. Clearly, the two correlations represent very different types of behavior. Perhaps most significantly, neither represents a realistic fusion environment, even in terms of the He/dpa ratio.

However, it is important to maintain some perspective on the practical importance of uncertainties in swelling in various fluence and temperature regimes. As noted above, near-term fusion devices will probably operate at low to intermediate exposures (<60 dpa) as well as at low temperatures where very little data is available. Hence, obtaining data for these conditions should be the focus of research on existing commerical alloys. Conversely, if high exposures do result in large amounts of swelling in cold-worked type 316 steels, then these alloys will almost surely be inadequate for use in higher performance fusion devices. Hence, for these applications, emphasis should be placed on developing fission-fusion correlations for advanced low-swelling alloys.

5.4 Mechanisms and Models of the Effect of Helium on the Microstructure of Stainless Steel

5.4.1 Mechanisms Defining the Sequence of Events in Cavity Evolution

The data reviewed in the previous sections demonstrates a well-defined sequence of events. Further, the similarity in behavior under both charged-particle and neutron conditions is striking. The qualitative trends in the data are consistent with mechanisms and models based on rate theory. A comprehensive conceptual model has been presented previously (64). The elements in this sequence and associated mechanistic interpretations are summarized in Table 5.

TABLE 5

ELEMENTS IN THE SEQUENCE OF EVENTS FOUND IN CAVITY EVOLUTION

EXPERIMENTAL OBSERVATIONS	THEORETICAL PREDICTIONS
OBSERVABLE CAVITY FORMATION	
Tiny cavities form first and grow slowly. They are often found on dislocations and precipates. Cavity density increases with helium concentration as $N_c \propto [He]^p$, $p \sim 0.5$ (0.25-2). A population of small cavities can persist up to high exposures with little change in size and number density.	The small cavities are gas bubbles which can grow only with the addition of helium. Bimolecular kinetics predict a cavity scaling exponent of $p \sim 0.5$. Helium trapping and bubble formation on dislocations and precipitates is energetically favored (65).
BUBBLE TO VOID CONVERSIONS	
Above a critical size, d_c, there is a transition to rapid cavity growth which can result in bimodal cavity size distributions. Based on maximum small cavity sizes or helium inventory estimates, d_c increases with increasing temperature and decreasing damage rate. For temperatures less than 700°C, values of d_c range from ~ 3-15 nm in charged particle studies to more than 20 nm in HFIR.	Bubbles convert to voids above a critical d_c, which increases with increasing temperature and decreasing damage rate. Calculated values of d_c are in reasonable agreement with experiment. Only a fraction of the bubbles may convert, leading to bimodal size distributions. Incubation exposures reflect the helium accumulation required to grow the bubbles to r_c (66,67,68).
VOID GROWTH KINETICS AND SWELLING	
Swelling is influenced by the overall microstructure, including cavity densities at extremely high and low values. In the range of low cavity densities (e.g. at low helium concentrations and high temperatures) increases often tend to enhance swelling. Conversely, at very high cavity densities (e.g. at high helium concentrations and low temperature) additional increases often tend to reduce swelling.	The observed influence of cavity density on swelling is consistent with theory. Very high cavity densities can retard swelling due to: reduction of the effective bias; higher vacancy emission rates; and recombination at bubbles. Rate theory is qualitatively consistent with most trends in the swelling data, provided complete descriptions of the microstructure are used (68,69).
CONCURRENT COUPLED EVOLUTION	
Dislocation loop and network evolution is a precursor to cavity and microchemical evolution. Bubble-to-void conversions take place first and the largest cavities are found on precipitates. Irradiation induced microstructures are often sites for precipitate formation. Irradiation induced or enhanced precipitation and swelling may be suppressed by cavity dominated microstructures. High densities of small matrix cavities can suppress void formation on precipitates.	Bubbles on precipitates require less helium to convert to voids and grow more rapidly thereafter. Solute depletion removes trapping sites and may increase effective bias. Microstructural and microchemical evolutions are in principle, highly coupled due to defect conservation and solute flows induced by defect fluxes as mediated by microstructural sinks. For example, at high sink densities solutes may partition more uniformly, thereby reducing irradiation induced or modified precipitation (64).

There still are very large gaps in our knowledge. Of particular significance, is a continuing lack of basic quantitative understanding of: helium diffusion and trapping mechanisms, or the factors which govern helium partitioning; quantitative defect-solute mass balances; and the thermodynamics and kinetics of the evolution of cavities at small sizes. Further, the current analytical modeling tools are underdeveloped.

5.4.2 A Model Based Fission-Fusion Correlation

An extended rate theory model developed to treat the effects of the He/dpa ratio on some important aspects of cavity evolution is described elsewhere (69). Briefly, the model calculates the partitioning of helium to an initial distribution of small bubbles. The bubbles grow slowly with the addition of helium, but at a critical size become unstable and grow as voids. The number of size classes which convert to voids (if any) is governed by the cavity concentrations, total helium concentration and the point defect fluxes as determined by the overall microstructure (bubbles, voids, dislocations and subgrain structure). Selection of the microstructural parameters (total cavity densities, subgrain structure, and dislocation density) is based on experimental observations. Interpolation of total cavity densities to fusion conditions assumes a scaling of $N_c \alpha [He]^{0.5}$.

In order to treat observed void-precipitate association, an effective surface energy is used for the EBR-II calculations. Nominal matrix surface energies are used in the calculations for HFIR. We postulate that these differences arise because the high density of matrix cavities in HFIR prevents the nucleation and rapid growth of voids on precipitates. That is, there are two alternate paths of cavity evolution, namely, matrix-dominated or precipitate-associated. The matrix-dominated path, observed in HFIR, could be triggered by reductions in helium and excess vacancy fluxes at the precipitates resulting from the competing cavity

dominated sink structure. Perturbations in the microchemical evolution may also contribute to this effect.

Void growth rates are calculated using standard rate theory equations. The model is calibrated to the HFIR and EBR-II 20% CW DO Heat swelling data and used to calculate swelling for fusion He/dpa ratios. The results of the calibration are illustrated in Figure 12. Of course, the predictions are not unique and, to some degree, depend on the model mechanisms and parameters. Nevertheless, this analysis yields some interesting qualitative results.

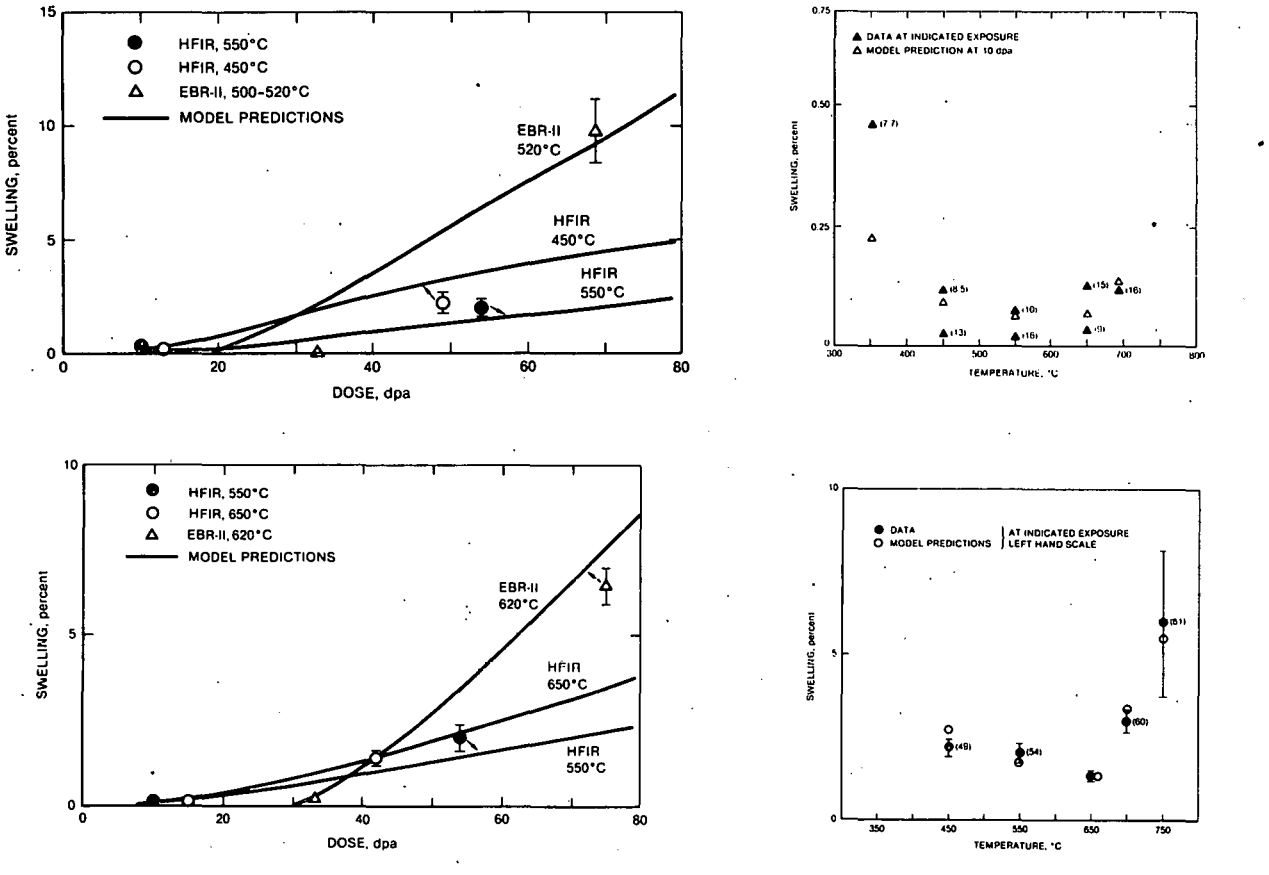

FIGURE 12. Swelling as a Function of Exposure Predicted by the Model Compared to 20% CW DO-Heat Data for Irradiations in HFIR and EBR-II at the Indicated Temperatures.

Figure 13 shows the predicted swelling in various environments at 600°C. The HFIR environment has a slightly higher swelling at low fluences (< 20 dpa) and a lower steady-state swelling rate up to 80 dpa. The lower swelling rate in HFIR is the result of both the cavity dominated sink microstructure and higher vacancy emission rates from smaller matrix cavities. Indeed, above 500°C the cavities in HFIR are predicted to be near equilibrium bubbles. The model does not treat any high fluence microchemical evolution which might occur. The use of time-independent model parameters which do not account explicitly for microchemical evolution is clearly approximate (69).

It is not known which of the possible paths (matrix-dominated or precipitate- associated) of cavity evolution will occur for the intermediate fusion He/dpa ratio. Therefore, calculations are presented for both possibilites. For the precipitate-associated case 15 600°C, steady-state swelling rates are similar for fusion and EBR-II conditions. However, the fusion He/dpa ratio results in a much lower incubation time, hence, significantly higher swelling. For the matrix-dominated case at 600°C, the incubation time is increased, and the steady-state swelling

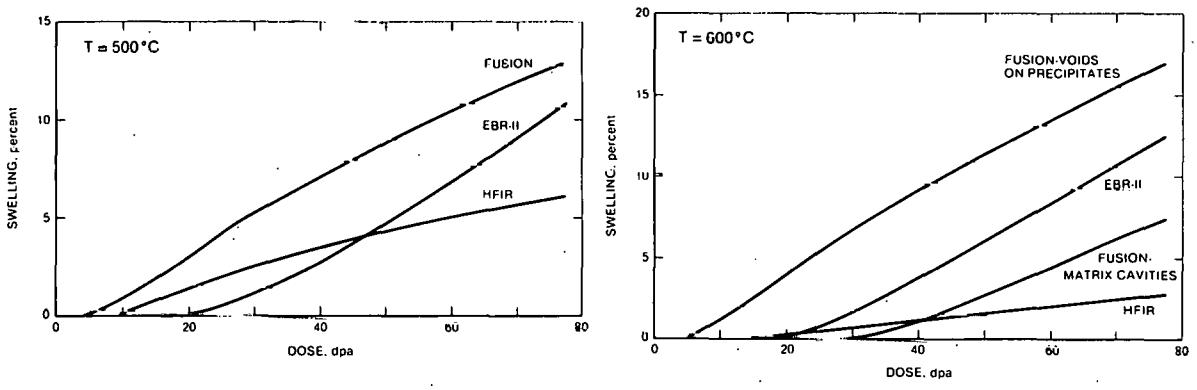

FIGURE 13. A Comparison of Swelling as a Function of Exposure at 500 and 600°C Predicted for EBR-II, HFIR, and Fusion Irradiations. See text for an explanation of the two fusion curves.

rate is somewhat less than in EBR-II. At exposures greater than 40 dpa EBR-II and HFIR swelling bracket the fusion predictions. At 500°C no distinction is made between the two paths; the swelling is predicted to be highest for the fusion He/dpa ratio, due to a small incubation time and relatively high swelling rate (similar to that predicted for the EBR-II He/dpa ratio).

The quantitative results should not be taken too seriously. However, there are two important qualitative conclusions. First, there may be different paths of cavity evolution; which path is followed is largely governed by the He/dpa ratio. Second, that irradiations in available fission environments may not result in swelling which brackets behavior at intermediate fusion He/dpa ratios.

While there is no neutron data at intermediate He/dpa ratios, both dual-ion and preinjection data are consistent with our conclusions. In addition, the rapid swelling of the SA DO Heat in HFIR can be rationalized on the basis of the observation of a lower density of matrix cavities for this condition than found in the 20% CW DO Heat. Similarly, the effectiveness of MC carbides in titanium modified steels, which trap helium in the form of a high density of small bubbles, resulting in low swelling, support our interpretation (70,71). Finally, we note the results of an experiment reported by Gelles and Garner where swelling in a region of higher helium concentration ($\sim$ a factor of 3 due to (n,α) reactions in a nearby particle containing boron) is compared to matrix swelling (72). The alloy was a precipitation strengthened 30%Ni-10%Cr steel irradiated in EBR-II at 430°C. At $\sim$35 dpa the higher helium level enhances the swelling by a factor of 3-4, primarily by increasing the void density.

5.5 Summary and Conclusions

A review of a broad array of charged-particle data and a more limited set of fast-and mixed-spectrum reactor neutron data shows that interactions between helium and displacement damage can have important system-atic effects on several microstructual fea-tures. While increased He/dpa ratios almost always increase the number densities of cavities, total swelling may be increased, decreased or remain unaffected. For a specific alloy condition, the influence of the He/dpa ratio depends on temperature and exposure. In particular, swelling does not appear to be a simple monotonic function of the He/dpa ratio. The qualitative path of cavity evolution also appears to be influenced by the He/dpa ratio.

These observations are consistent with a rate theory model and a postulate that high densities of matrix cavities, which can be induced by high He/dpa ratios, may supress the formation of large voids on precipitates. The theoretical results also suggest non-monotonic swelling changes with increases in the He/dpa ratio, and indicate that the swelling in HFIR and EBR-II may not always bracket fusion behavior.

However, significant gaps remain in detailed understanding of critical mechanisms such as helium transport, and the idealized models are far from complete. The need to develop interim property correlations for fusion reactor designers is clearly recognized. However, much more data and a much better understanding of the underlying physical processes and their interactions will be required before such correlations can be considered reliable.

6.0 References

1. The Fusion Reactor Materials Program-II Damage Analysis and Fundamental Studies, DOE/ET 0032/2 (1978).

2. J.J. Holmes and J.L. Straalsund, J. Nucl. Mat. 85 & 86 (1979) 447.

3. J.W. Davis, "Materials Handbook for Fusion Energy Systems", to be published in the Proceedings of the Second Topical Meeting on Fusion Reactor Materials, Seattle, WA, August, 1981.

4. F.A. Garner, Irradiation Effects on Phase Stability, J.R. Holland, L.K. Mansur and D.I. Potter, eds. TMS-AIME (1981) 165.

5. N.M. Ghoniem and G.L. Kulcinski, "A Critical Assessment of the Effects of Pulsed Irradiation on the Swelling, Microstructure and Irradiation Creep of Materials", Nucl. Tech./Fusion (to be published April 1982.)

6. J.A. Spitznagel, F.W. Wiffen, and F.V. Nolfi,Jr., J. Nucl. Mat. 85 & 86 (1979) 629.

7. J.F. Bates, F.A. Garner and F.M. Mann, "The Effect of Transmutation Products on Swelling in 316 Stainless Steel", to be published in the Proceedings of the Second Topical Meeting on Fusion Reactor Materials, Seattle, WA, August, 1981.

8. M.J. Makin, J.A. Hudson, D.J. Mazey, R.S. Nelson, G.P. Walters, and T.M. Williams, Radiation Effects in Breeder Reactor Materials, M.L. Bleiberg, and J.W. Bennett, eds., TMS-AIME (1977) 645.

9. P.J. Maziasz, ADIP Quart. Prog. Rep. 13 DOE/ER045/6 (1981) 70.

10. J.F. Bates, and M.K. Korenko, Nucl. Tech. 48 (1980) 303.

11. See several papers contained in the Proceedings of the Workshop on Correlation of Neutron and Charged Particle Damage, J.O. Stiegler, ed., CONF-760673, (1976).

12. "ASTM Standard Recommended Practice for Neutron Radiation Damage Simulation by Charged-Particle Irradiation", ASTM E521-77, Annual ASTM Standards, Part 45, (1980) 1087.

13. G.R. Odette, J.A. Spitznagel, A.P.L. Turner, and W.A. Jesser, "Critical Assessment of Dual Ion and Charged Particle Research in the Fusion Materials Program", this report.

14. K. Farrell, Radiation Effects 53-3&4 (1980), 175.

15. J.A. Spitznagel, S. Wood, N.J. Doyle, W.S. Choyke, J.N. McGruer, J.R. Townsend, and R.B. Irwin, "Helium Partitioning to Extended Defects in Dual Ion Bombarded 304 & 316SS," to be published in the Proceedings of the Second Topical Meeting on Fusion Reactor Materials, Seattle, WA, August, 1981.

16. N.H. Packan, and K. Farrell, J. Nucl. Mat. 85 & 86 (1979) 677.

17. W.J. Choyke, J.N. McGruer, J.R. Townsend, J.A. Spitznagel, N.J. Doyle, and F.J. Vanskytis, ibid. 647.

18. F.J. Agarwal, G. Ayrault, D.I. Potter, A. Taylor and F.V. Nolfi, Jr., ibid. 653.

19. E.A. Kenik, and E.H. Lee, Irradiation Effects on Phase Stability, J.R. Holland, L.K. Mansur, and D.I. Potter, eds. TMS-AIME (1981) 493.

20. D.J. Mazey, and R.S. Nelson, J. Nucl. Mat. 85 & 86 (1979) 671.

21. K. Farrell, and N.H. Packan, "Damage Structure in Nimonic PE16 Alloy Ion Bombarded to High Doses and Gas Levels, to be published in the Proceedings of the Second Topical Meeting on Fusion Reactor Materials, Seattle, WA, August, 1981.

22. G. Ayrault, H.A. Hoff, F.V. Nolfi, Jr. and A.P.L. Turner, "Influence of Helium Injection Rate in the Microstructure of Dual-Ion Irradiated Type 316 Stainless Steel", ibid.

23. W.J. Choyke, J.A. Spitznagel, S. Wood, N.J. Doyle, N.J. McGruer, and J.R. Townsend, Nucl. Instr. & Methods 182/183 (1981) 489.

24. J.N. McGruer, W.J. Choyke, J.R. Townsend, J.H. Chang, J.D. Yesso, J.A. Spitznagel, N.J. Doyle, and F.J. Venskytis, Nucl. Mat. 74 (1978) 174.

25. M. Terasawa, M. Shimada, T. Kakuma, T. Yukitoshi, K. Shiraishi, and K. Uematsu, Radiation Effects in Breeder Reactor Materials, M.L. Bleiberg, and J.W. Bennett, eds. TMS-AIME (1977) 687.

26. S. Wood, J.A. Spitznagel, W.J. Choyke, N.J. Doyle, J.N. McGruer, and J.R. Townsend, Scripta Met. 14 (1980) 211.

27. D.J. Mazey, and R.S. Nelson, Radiation Effects and Tritium Technology for Fusion Reactors-I, J.S. Watson, and F.W. Wif-fen, eds. CONF 750989 (1976) 240.

28. E.H. Lee, A.F. Rowcliffe, and L.K. Mansur, "Precipitation and Cavity Formation in Austenitic Stainless Steels During Irradiation", to be published in the Proceedings of the Second Topical Meeting on Fusion Reactor Materials, Seattle, WA, August, 1981.

29. S. Wood, J.A. Spitznagel, W.J. Choyre, N.J. Doyle, J.N. McGruer, and J.R. Townsend, Effects of Radiation on Materials, ASTM STP 725 (1981) 455.

30. H.H. Neeley, and K. Herschback, Radiation Effects 7 (1971) 187.

31. D.W. Keefer, and A.G. Pard, J. Nucl. Mat. 45 (1972) 55.

32. R.S. Nelson, and J.A. Hudson, J. Nucl. Mat. 58 (1975) 11.

33. J.L. Brimhall and E.P. Simonen, J. Nucl. Mat. 68 (1977) 235.

34. K. Farrell and N.C. Packan, J. Nucl. Mat. 85 & 86 (1979) 683.

35. V. Levy, N. Azam, L. Le Naour, G. Didout, and J. Delaplace, Radiation Effects in Breeder Reactor Structural Materials, M.L. Bleiberg, and J.W. Bennett, eds. TMS-AIME (1977) 709.

36. J.L. Brimhall and E.P. Simonen, Trans ANS, 22 (1975) 176.

37. N.H. Packan, K. Farrell, and J.O. Stiegler, J. Nucl. Mat. 78 (1978) 143.

38. E. Kuramoto, N. Yoshida, N. Tsukuda, K. Kitajima, N.H. Packan, M.B. Lewis, and L.K. Mansur, "Simulation Irradiation Studies on Iron", to be published in the Proceedings of the Second Topical Meeting on Fusion Reactor Materials, Seattle, WA, August, 1981.

39. J. Dalaplace, N. Azam, and L. Le Naour, J. Nucl. Mat. 47 (1973) 278.

40. S.C. Agarwal, A. Taylor, and F.V. Nofli, Jr., Trans ANS 27 (1977) 269.

41. H.H. Packan, and K. Farrell, Trans. ANS 33 (1979) 290.

42. S. Wood, J.A. Spitznagel, and W.J. Choyke, DAFS Quart. Prog. Rep. 6 DOE/ET-0065/6 (1979), 118.

43. K. Farrell, A. Wolfenden, and R.T. King, Radiation Effects 8 (1971) 107.

44. M. Cambini, J. Bressers and M. Heerschap, J. Nucl. Mat. 62 (1976) 311.

45. E.E. Bloom and J.O. Stiegler, J. Nucl. Mat. 36 (1979) 331.

46. S.D. Harkness, B.J. Kestel and S.G. McDonald, J. Nucl. Mat. 46 (1973) 159.

47. P.J. Maziasz and B.L. Cox, ADIP Quart. Prog. Rep. 9, DOE/ER-0045/2 (1980) 35.

48. W.K. Appleby, E.E. Bloom, J.E. Flinn and F.A. Garner, Radiation Effects in Breeder Reactor Structural Materials, M.L. Bleiberg, and J.W. Bennett, eds. TMS-AIME (1977) 509.

49. J.I. Bramman, C. Brown, J.S. Watkin, C. Cawthorne, E.J. Fulton, P.J. Barton and E.A. Little, ibid (1979) 479.

50. R.L. Simons, Effects of Radiation on Structural Materials, ASTM-STP 683, J.A. Sprague, and D. Kramer, eds. (1979) 365.

51. P.J. Maziasz, F.W. Wiffen and E.E. Bloom, Radiation Effects and Tritium Technology for Fusion Reactors-I, J.S. Watson and F.W. Wiffen, eds. CONF-750989 (1976) 259.

52. P.J. Maziasz and M.L. Grossbeck, ADIP quart. Prog. Rep. 13, DOE/ER-0045/6 (1981) 28.

53. P.J. Maziasz and M.L. Grossbeck, ADIP Quart. Prog. Rep. 12, DOE/ER-0045/5 (1981) 43.

54. P.J. Maziasz, J.A. Horak and B.L. Cox, Irradiation Effects on Phase Stability, J.R. Holland, L.K. Mansur, and D.I. Potter, eds., TMS-AIME (1981) 271.

55. E.H. Lee, P.J. Maziasz and A.F. Rowcliffe, ibid. 191.

56. P.J. Maziasz and M.L. Grossbeck, "Swelling and Microstructural Development in Type 316 Stainless Steel Irradiated in HFIR and EBR-II", to be published in the Proceedings of the Second Topical Meeting on Fusion Reactor Materials, Seattle, WA, August, 1981.

57. H.R. Brager and F.A. Garner, "Comparison of the Swelling the Microstructural/ Microchemical Evolution of AISI 316 Irradiated in EBRII and HFIR", ibid.

58. E.E. Bloom and J.O. Stiegler, Effects of Irradiation on the Substructure and Mechanical Properties of Metals and Alloys, J. Moteff, ed., ASTM-STP 529 (1972) 360.

59. Private Communication from M.L. Grossbeck, Irradiation Experiments Coordinator for Oak Ridge National Laboratory Fusion Materials Program (1981).

60. R.L. Klueh and M.L. Grossbeck, ADIP Quart. Prog. Rep. 13, DOE/ER045/6 (1981) 58.

61. H.R. Brager and F.A. Garner, Irradiation Effects on Phase Stability, J.R. Holland, L.K. Mansur, and D.I. Potter, eds. TMS-AIME (1981) 219.

62. F.A. Garner, P.J. Maziasz, and W.G. Wolfer, DAFS Quart. Prog. Rep. 11 DOE/ER-0046/3 (1980) 159.

63. P.J. Maziasz, and M.L. Grossbeck, "Equations to Describe Swelling in Type 316 Stainless Steel in HFIR", ADIP Quart. Prog. Rep. 14 DOE/ER-0045/7 (1981) to be published.

64. G.R. Odette, J. Nucl. Mat. 85 & 86 (1979) 533.

65. G.W. Greenwood, A.J.E. Foreman, and D.E. Rimmer, J. Nucl. Mat. 4 (1959) 305.

66. G.R. Odette and M.W. Frei, Proceedings of the First Topical Meeting on the Technology of Controlled Nuclear Fusion, G.R. Hopkins, ed., CONF-740402P2 (1974) 485.

67. M.R. Hayns and M.H. Wood, J. Nucl. Mat. 87 (1979) 97.

68. G.R. Odette and S.C. Langley, Radiation Effects and Tritium Technology For Fusion Reactors-I, J.S. Watson, and F.W. Wiffen, eds. CONF-750989 (1976) 395.

69. R.L. Stoller and G.R. Odette, "A Model Based Fission-Fusion Correlation of Cavity Swelling in Stainless Steel", to be published in the Proceedings of the Second Topical Meeting on Fusion Reactor Materials, Seattle, WA August, 1981.

70. P.J. Maziasz, Scripta Met. 14 (1980) 1251.

71. P.J. Maziasz, and T.K. Roche, "Preirradiation Microstructural Development Designed to Minimize Properties Degradation During Irradiation of Austenitic Alloys", to be published in the Proceedings of the Second Topical Meeting on Fusion Reactor Materials, Seattle, WA, August, 1981.

72. D.S. Gelles, and F.A. Garner, J. Nucl. Mat. 85 & 86 (1979) 689.

7.0 Acknowledgements

The authors were aided by many constructive discussions with their colleagues at ORNL, UCSB and Westinghouse R&D Center. The assistance of the dual-ion irradiation groups at the University of Pittsburgh, ORNL and ANL, in providing paper preprints and offering useful comments, deserves particular thanks. Preprints of several papers of F. Garner, H. Brager and their associates at HEDL were also very helpful. It should be noted

that the results of research supported by the Basic Energy Services Division of DOE, the NSF and other agencies were used in our analysis. Finally preparation of this manuscript, as well as much of the research reviewed here, was supported by the Materials and Irradiation Effects Branch of the DOE OFfice of Fusion Energy.

8.0 Future Work

Work on developing physically based fission-fusion correlations will continue as additional data becomes available. The near term goal is to develop a fission-fusion swelling correlation for 20% CW 316 SS for submission to the Fusion Materials Handbook.

9.0 Publications

The content of this work was presented at the Second Topical Meeting on Fusion Materials in Seattle Washington, August 9-12, 1981 and will be included in the Proceedings of that conference.

Cavity Formation in Single- and Dual-Ion Irradiated HT-9 and HT-9 + 2Ni Ferritic Alloys

G. Ayrault (Argonne National Laboratory)

1.0 Objective

The objective of this work is to determine the microstructural evolution, during irradiation, of first wall materials with special emphasis on the effects of helium production, displacement damage rates, and temperature.

2.0 Summary

Samples of HT-9 and HT-9 + 2Ni ferritic alloys that were single- and dual-ion irradiated in the temperature range 350-600°C have been inspected by TEM. Cavities formed in dual-ion irradiated samples of both alloys at all irradiation temperatures, but significant bias-driven cavity growth occured only at 410 and 470°C. Excess nickel in HT-9 + 2Ni caused swelling suppression at 470°C but did not significantly affect swelling at 410°C. Single-ion irradiation produced essentially no cavities in either alloy at any temperature, showing that helium was essential for cavity nucleation in these alloys.

3.0 Program

Title: Effects of Irradiation on Fusion Reactor Materials
Principal Investigator: A. P. L. Turner
Affiliation: Argonne National Laboratory

4.0 Relevant DAFS Program Plan Task/Subtask

Subtask II.C.2.1 Mobility, Distribution and Bubble Nucleation

5.0 Accomplishments and Status

5.1 Introduction

Irradiation of nickel-bearing alloys in mixed spectrum reactors produces transmutant helium via the two step reaction

$$^{58}Ni(n,\gamma)^{59}Ni$$

$$^{59}Ni(n,\alpha)^{56}Fe \ .$$

In alloys with sufficiently high nickel concentrations (e.g., austenitic alloys) helium production to damage production ratios can reach and exceed those expected in a magnetic fusion reactor (MFR). Thus, mixed spectrum reactor irradiations are often used as a damage simulation technique for nickel-bearing MFR materials.

In the ferritic alloys under consideration for MFR applications, the nickel concentrations are low ($\lesssim$ 0.5 wt. %) and the helium generation rates in mixed-spectrum reactors fall well below the levels expected in MFRs. For this reason current reactor irradiations in the ADIP program include both unmodified ($\lesssim$ 0.5 wt. % Ni) and Ni-modified (with ~ 1 to 2 wt. % additional Ni) ferritic alloys. The nickel additions are specifically aimed at increasing the helium generation rates to levels expected in MFRs.

However isolation of helium effects by comparison of unmodified and Ni-modified samples may be difficult because the additional nickel, in addition to increasing the helium generation rate, may simultaneously alter the irradiation performance of the alloy via other mechanisms. In this study we have used dual-ion irradiation (Ni^+ and He^+) to approximate the MFR environment. This type of simulation is free from the uncertainty mentioned above because the simulated helium production (by injection) is independent of alloy composition. We have dual-ion irradiated unmodified and Ni-modified material under identical conditions and inspected the samples with TEM to assess the effect of Ni addition on irradiation microstructure. In addition we compare single-ion (Ni^+ irradiation only) and dual-ion (Ni^+ with He

injection) irradiated samples to assess the effect of helium.

5.2 Experimental Procedure

The alloys studied were HT-9 (heat no. XAA-3587) and HT-9 + 2Ni (heat no. XAA-3589). The major element composition is shown in Table 1; a more complete analysis can be found in Ref. (1). The material was received in the form of 0.25 mm sheet, from which 3 mm TEM discs were punched. Samples were encapsulated in an argon atmosphere and normalized for 0.5 hours at 1050°C, then air cooled. The HT-9 and HT-9 + 2Ni alloys were tempered for 2.5 hours at 780°C and 5 hours at 700°C, respectively, and air cooled, producing a tempered martensite structure. These heat treat schedules, supplied by R. Klueh, are the same as those used at ORNL in preparing the alloys for reactor irradiations. After heat treatment the samples were mechanically polished and electropolished as final preparation for irradiation.

TABLE 1

		COMPOSITION (wt. %)							
Alloy	Heat	Cr	Ni	Mo	C	W	Mn	V	Si
HT-9	XAA-3587	11.99	0.43	0.93	0.21	0.54	0.50	0.27	0.18
HT-9+2Ni	XAA-3589	11.71	2.27	1.02	0.20	0.54	0.49	0.31	0.14

Samples were irradiated to 25 dpa at a 3×10^{-3} dpa $\cdot s^{-1}$ dose rate. The irradiation temperatures were 350, 410, 470, 530 and 600°C. One set of samples was dual-ion irradiated (3.0 MeV $^{58}Ni^{+}$ and degraded 0.83 MeV $^{3}He^{+}$) with the helium injected at 15 appm He/dpa. A second set was single-ion irradiated (3.0 MeV Ni^{+} alone). After irradiation the samples were prepared for TEM inspection by electrochemically sectioning to a depth of 450 nm (peak damage was at 550 nm) and backthinning to perforation.

5.3 Cavity Formation Under Dual-Ion Irradiation

Microstructures observed in dual-ion irradiated HT-9 and HT-9 + 2Ni are shown in Figs. 1 and 2, respectively. All samples contained cavities, but the cavity sizes, number densities and preferential formation sites were strongly temperature dependent. Cavity microstructures in HT-9 and HT-9 + 2Ni were similar to one another in samples irradiated at 350, 410, 530 and 600°C but 470°C irradiation produced markedly different results in the two alloys.

Samples irradiated at 350°C contained very few visible cavities and these were small ($\lesssim$ 2.5 nm) and nonuniformly distributed in the samples; it was necessary to scan several regions of the samples in order to find any visible cavities at all. In both alloys irradiation at 410°C produced high number densities of intergranular cavities that ranged in size from a maximum of ~ 8 nm to a practical resolution limit of ~ 2 nm. There were variations in both the maximum and mean cavity sizes in different subgrains of the tempered martensite structure in both HT-9 and HT-9 + 2Ni, but there did not appear to be a consistent difference between the two alloys.

Following 470°C irradiation, both HT-9 and HT-9 + 2Ni samples contained high number densities of small cavities ($\lesssim$ 3 nm), most or all of which were associated with radiation-induced dislocations, and lower number densities of large cavities (up to ~ 18 nm). The small-cavity number densities appeared to be quite similar in the two alloys, but the large-cavity number densities were very different. Large-cavity number densities were fairly high in most HT-9 subgrains, Fig. 1c, whereas in HT-9 + 2Ni it was necessary to scan a number of subgrains in order to find a single large-cavity (e.g. in the upper right corner of Fig. 2c).

Irradiations at 530 and 600°C produced small cavities ($\lesssim$ 5 nm) that were preferentially associated with intergranular dislocations and subgrain boundaries. There was no clear and consistent difference in cavity size or number density between 530 and 600°C samples of either alloy, or between samples of the different alloys irradiated at these temperatures. Subgrain-

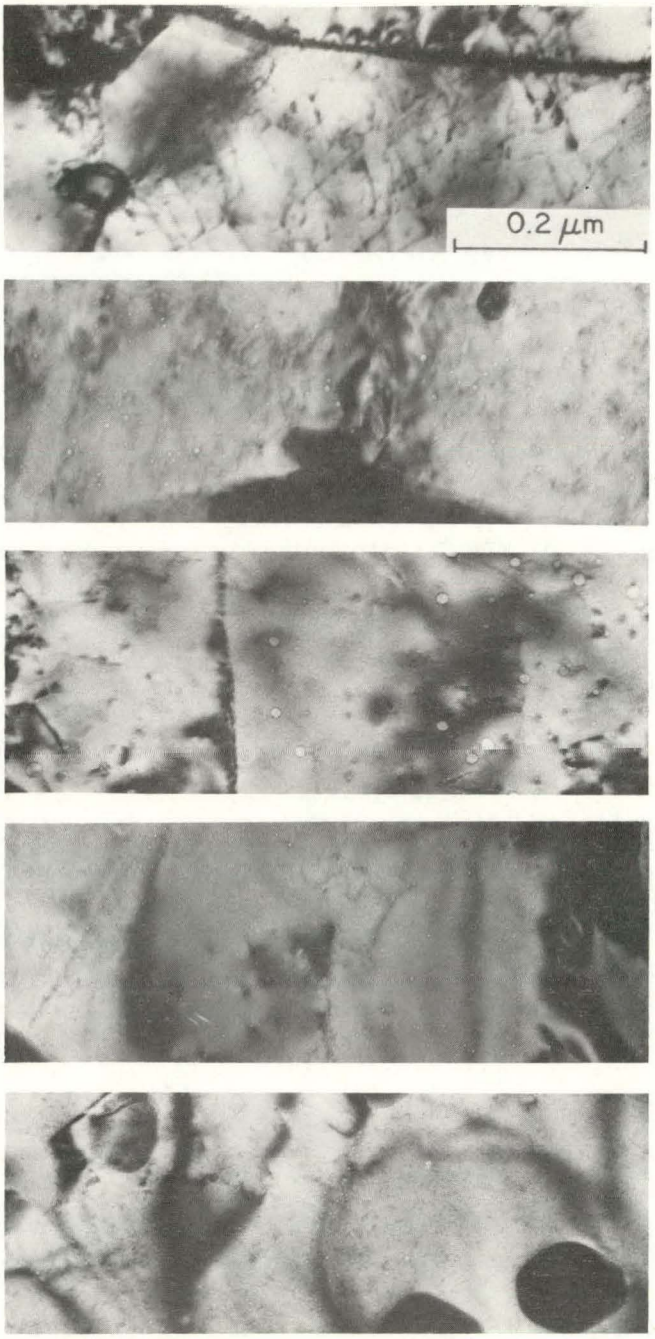

FIGURE 1. HT-9 Ferritic Alloy Dual-Ion Irradiated to 25 dpa with 15 appm He/dpa. (a) 350°C, (b) 410°C, (c) 470°C, (d) 530°C and (e) 600°C.

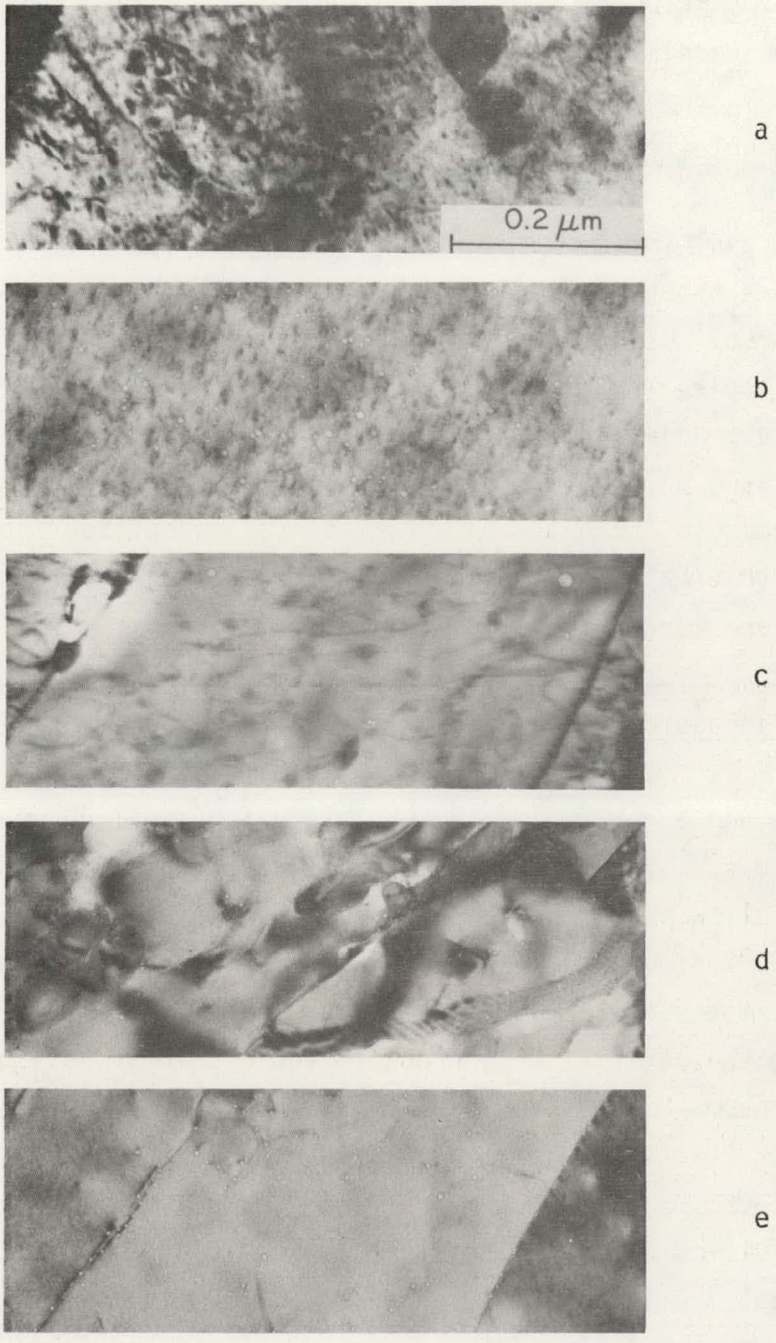

FIGURE 2. HT-9 + 2Ni Ferritic Alloy Dual-Ion Irradiated to 25 dpa with 15 appm He/dpa. (a) 350°C, (b) 410°C, (c) 470°C, (d) 530°C and (e) 600°C.

to-subgrain variations within samples were large enough to mask any consistent dependence on temperature or alloy composition that may exist.

5.4 Single-Ion Irradiated Samples

Based on the dual-ion results, HT-9 and HT-9 + 2Ni samples irradiated at 410 and 470°C were thought to be the most likely to contain cavities so these were inspected first. Large areas of these four samples, and also of HT-9 and HT-9 + 2Ni samples irradiated at 530°C, were carefully inspected for cavities. This search revealed only a single cavity in one of the six samples (HT-9 irradiated at 470°C). Since the single-ion irradiations were identical in all respects to the dual-ion irradiations, except for the helium injection, it is clear that helium was essential to formation of all of the cavities (both small and large) described in section 5.3.

5.5 Discussion

Low swelling and a narrow temperature range for swelling are characteristic of ferritic alloys,[2] and the HT-9 and HT-9 + 2Ni alloys investigated here apparently follow this trend. Under single-ion irradiation in the temperature range 410-530°C, swelling was essentially zero for both alloys. All dual-ion irradiated samples contained cavities, but swelling remained low. At most temperatures the cavities were probably equilibrium or overpressured He bubbles, but some bias-driven cavity growth probably occurred at 410 and 470°C.

The small-cavities located along dislocations and subgrain boundaries in 530 and 600°C dual-ion irradiated HT-9 and HT-9 + 2Ni are likely to be helium bubbles, as are the small-cavities along dislocations in 470°C samples. However, it is probable that the cavities in 410°C samples and the large size fraction of the cavities in the 470°C samples are voids that have grown by bias driven growth after nucleation as He bubbles. The bimodal distribution of cavity sizes at 470°C is indicative of two different mechanisms controlling the growth of the two components of the distribution. It is to be expected

that a higher number density of helium bubbles will be nucleated at lower temperatures. This means that the average bubble size should decrease with decreasing temperature. Furthermore, the equilibrium pressure in a bubble increases with decreasing bubble size so that the injected helium can be accomodated in a smaller volume fraction of equilibrium bubbles when there are more smaller cavities. This means that the helium bubble volume fraction should increase with increasing temperature and decreasing number density. The predicted trends are followed by the results at 530°C or 600°C as compared to the small size fraction of cavities at 470°C. The sizes and volume fractions of cavities at 410°C and 470°C can only be understood if the cavities at 410°C and the large cavities at 470°C have grown substantially beyond the equilibrium bubble size. Thus we conclude that the increases in cavity volume in both alloys at 410°C and in HT-9 at 470°C result from bias-driven cavity growth. However it is clear from the lack of cavities in single-ion irradiated samples that the large bias-driven cavities must have nucleated as helium bubbles.

Since the small-cavity sizes and number densities were similar in HT-9 and HT-9 + 2Ni at 470°C, it seems clear that the additional nickel reduced the degree of bias driven cavity growth at that temperature. The mechanism for this reduction is not clear at present, but it is the same trend noted by Johnston et al.,[2] where addition of 2 wt. % Ni to an Fe-15Cr binary alloy dramatically reduced swelling for 140 dpa, 550°C Ni ion irradiation of helium preinjected samples (550°C was the peak swelling temperature for Fe-15Cr). An interesting feature of the present results is that nickel addition did not appear to significantly reduce bias driven growth at 410°C, i.e., nickel addition appears to suppress swelling mainly on the high temperature side of the void swelling regime.

We conclude, then, that care should be taken in interpretation of swelling differences in reactor irradiated HT-9 nd HT-9 + 2Ni. Helium was found to be essential for cavity nucleation in both alloys, so the increased helium produced by nickel addition could cause swelling increases at some temperatures, particularly on the low temperature side of the void swelling

regime. But at high temperatures the nickel addition itself suppresses swelling, and this suppression cannot be interpreted as a helium effect.

6.0 References

1. M. L. Grossbeck, V. K. Sikka, T. K. Roche and R. L. Klueh, ADIP Quarterly Progress Report for Period Ending Dec. 31, 1979, DOE/ER-0045/1, p. 100.

2. W. G. Johnston, T. Lauritzen, J. H. Rosolowski and A. M. Turkalo, Report No. 76CRD019 (General Electric Research and Development, Schenectady, 1976).

7.0 Future Work

Samples of 9Cr-1Mo and 9Cr-1Mo + 2Ni ferritic alloys irradiated under the same conditions as the HT-9 and HT-9 + 2Ni alloys described in this report will be inspected in TEM in the near future.

Influence of He Injection Schedule and Prior Thermomechanical Treatment on the Microstructure of Type 316 SS

A. Kohyama and G. Ayrault (Argonne National Laboratory)

1.0 Objective

The objective of this work is to determine the microstructural evolution, during irradiation, of first wall materials with special emphasis on the effects of helium production, displacement damage rates, and temperature.

2.0 Summary

The influence of different helium injection schedules on microstructure developement in Ni ion irradiated 316 SS at 625°C is described. Hot- or cold-preinjection followed by single-ion irradiation produced lower swelling than dual-ion irradiation in solution annealed and solution annealed and aged samples, but produced greater swelling in cold-worked material. Dual-ion irradiation to 25 dpa produced strongly bimodal cavity-size distributions in solution annealed and solution annealed and aged samples, whereas single-ion irradiation followed by dual-ion irradiation to the same dose produced a cavity-size distribution with a substantial component of intermediate-size cavities. Dual-ion irradiation produced only very small cavities in 20% cold-worked material, while single-ion followed by dual-ion irradiation produced some intermediate-size cavities, and greater swelling.

3.0 Program

Title: Effects of Irradiation on Fusion Reactor Materials
Principle Investigator: A. P. L. Turner
Affiliation: Argonne National Laboratory

4.0 Relevant DAFS Program Plan Task/Subtask

Subtask II.C.2.1 Mobility, Distribution and Bubble Nucleation

5.0 Accomplishments and Status

5.1 Introduction

Mixed-spectrum reactor irradiation is commonly used for study of helium effects on radiation damage in nickel-bearing alloys. Helium is generated via the two-step reaction

$$^{58}Ni(n,\gamma)^{59}Ni$$

$$^{59}Ni(n,\alpha)^{56}Fe\ .$$

At sufficient neutron doses, the ^{59}Ni concentrations in austenitic alloys can reach levels where the helium generation rate reaches or exceeds the high level expected in magnetic fusion reactors (~ 15 appm He/dpa). However during the earliest phase of microstructure nucleation at the start of irradiation in mixed-spectrum reactors there is no helium generation because no ^{59}Ni has been produced. In contrast, MFR neutrons will generate helium rapidly even at the lowest doses. In this study we have dual-ion irradiated 316 SS samples using helium injection schedules intended to (1) approximate the MFR condition of steady helium generation, and (2) mimic the mixed-spectrum reactor condition of rapid helium production at high dose and no helium production at low dose.

Helium preinjection (usually ~ 10 to 30 appm) is often used to compensate for the aforementioned lack of helium in the early nucleation phase of microstructure development in reactor irradiations, and in ion and electron irradiations as well. In addition to the dual-ion irradiations mentioned above, we have hot- and cold-preinjected 316 SS samples and single-ion irradiated them to test the validity of preinjection alone as a simulation of transmutant helium production.

TEM work has been completed on samples having three thermomechanical histories, each irradiated under the conditions described above. In this report we give a qualitative description of the microstructures. Quantitative

data extracted from the micrographs will be presented in future reports.

5.2 Experimental

The material irradiated was 316 SS from the MFE heat (15893). Irradiations under all of the conditions described below were performed on samples with three prior thermomechanical treatments: solution annealed (0.5 h at 1050°C), solution annealed and aged (1 h at 1050°C, 10 h at 800°C) and 20% cold-worked. All irradiations were performed at 625°C, which is near the peak swelling temperature for the 3×10^{-3} dpa $\cdot s^{-1}$ damage rate employed. Nickel ion irradiation (3.0 MeV $^{58}Ni^{+}$) was used for damage production; all helium injections (simultaneous and preinjection) were performed with a degraded 0.83 MeV $^{3}He^{+}$ beam.

Samples were irradiated with six dose/helium histories. For simplicity, each of these has been assigned a descriptive code (e.g. 5S for (1) below), which is listed with each dose/helium history. The histories were:

(1) single-ion irradiation to 5 dpa (5S),
(2) dual-ion irradiation to 5 dpa with 15 appm He/dpa (5D),
(3) single-ion irradiation to 5 dpa followed by 20 dpa dual-ion irradiation with 18.8 appm He/dpa, giving the same final helium concentration as (4) (25SD),
(4) dual-ion irradiation to 25 dpa with 15 appm He/dpa (25D)
(5) 15 appm (cold) helium preinjection (at room temperature) followed by 25 dpa single-ion irradiation (25CP) and
(6) 15 appm (hot) helium preinjection (at 650°C) followed by 25 dpa single-ion irradiation (25HP).

Histories 3 and 4 (25SD and 25D) are intended to mimic mixed-spectrum reactor and MFR irradiation respectively. Histories (1) and (2) (5S and 5D) provide a view of the microstructures that the 25 dpa samples (25SD and 25D) had at low dose.

5.3 Dual-ion Helium Schedule Microstructure

Typical microstructures for the 5S, 5D, 25SD and 25D samples (histories 1, 2, 3 and 4 respectively) are presented in Figs. 1-6. Figures 1 and 2 show solution annealed (SA) samples; Figs. 3 and 4 show solution annealed and aged (SAA) samples; Figs. 5 and 6 show 20% cold-worked (CW) samples. In all cases the micrographs at left are recorded in a (200) two-beam diffraction condition for dislocation contrast and those at right are recorded in underfocused absorption contrast to image the cavities.

The microstructures in 5 dpa solution annealed samples 5S and 5D, Fig. 1, are quite different from one-another. No visible cavities are present in the single-ion samples, whereas dual-ion irradiation produced significant cavity nucleation and growth. Dislocation structures in both the 5S and 5D samples consist almost entirely of frank loops, but dual-ion irradiation produced a higher number density of smaller loops. Clearly the helium played a major role in nucleation of both cavities and loops.

At 25 dpa the 25SD and 25D samples, Figs. 2a and b respectively have similar dislocation microstructures consisting of both loops and lines. Although the dislocation structure appears to have recovered from differences present at 5 dpa, differences in the cavity microstructure persist. The cavity size distribution in the 25D sample was clearly bimodal in nature, with a high number density of small cavities ($\lesssim$ 3 nm) and a lower number density of large cavities (up to ~ 40 nm) but with very few cavities in the range 3 to 12 nm. The 25SD sample also contained a high number density of small cavities and the maximum cavity size was similar to that in the 25D sample, but the size distribution was not as strongly bimodal as in the 25D sample; there were many cavities in the 3 to 12 nm size range that were absent after continuous dual-ion irradiation. In fact, quantitative analysis (now in progress) may reveal that the cavity size distribution for 25SD irradiation is not bimodal at all, but consists instead of a population whose number density rises monotonically with decreasing size. Despite the difference in cavity size distribution, there is no obvious difference in cavity volume fraction between 25D and 25SD samples.

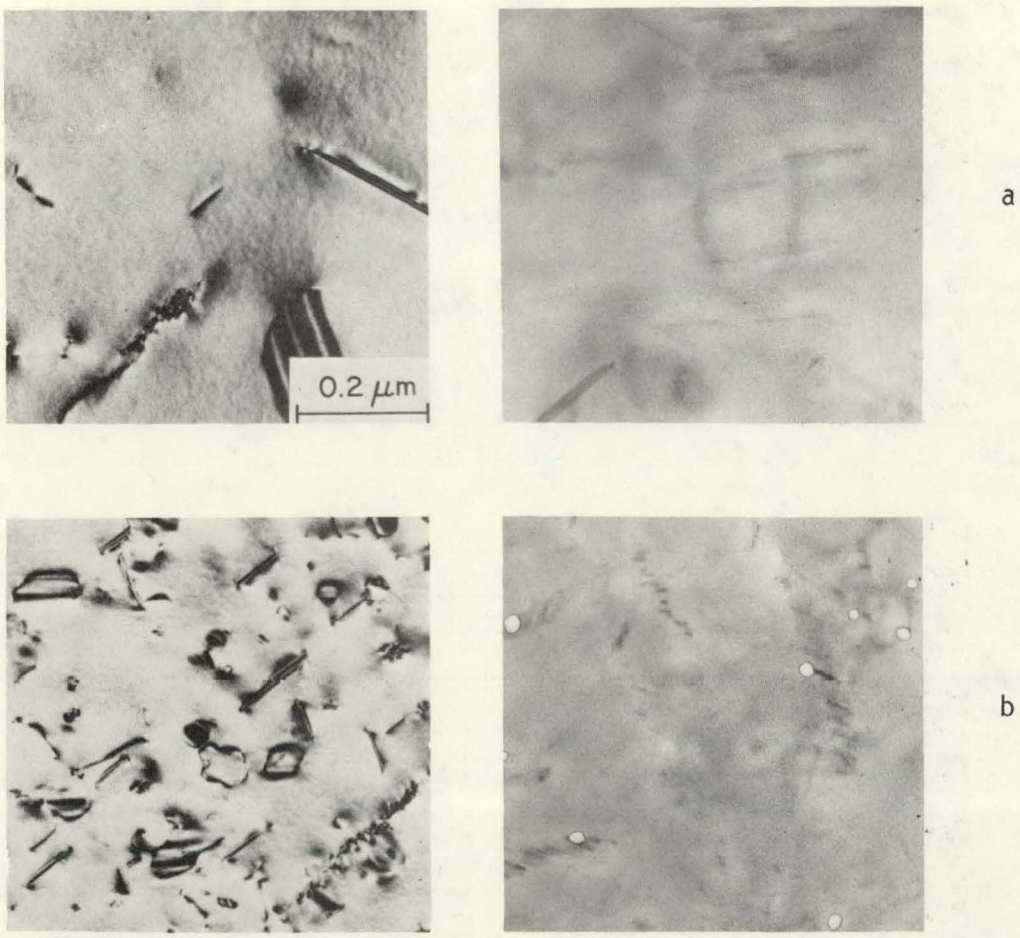

FIGURE 1. Dislocation and Cavity Microstructures in Solution-Annealed 316 SS Irradiated to 5 dpa at 625°C, a) Schedule 5S and b) Schedule 5D.

Microstructure development in solution annealed and aged material, Figs. 3 and 4, closely paralleled that in solution annealed samples. Again no cavities were present in the 5S sample and the loop density was low, while cavity growth was well under way in the 5D sample and higher number densities of smaller loops were present. Also the 25D beam history produced a strongly bimodal cavity-size distribution, whereas cavities of intermediate size were profuse following 25SD irradiation, as in SA material. The most notable difference between SA and SAA samples was the low-dose dislocation

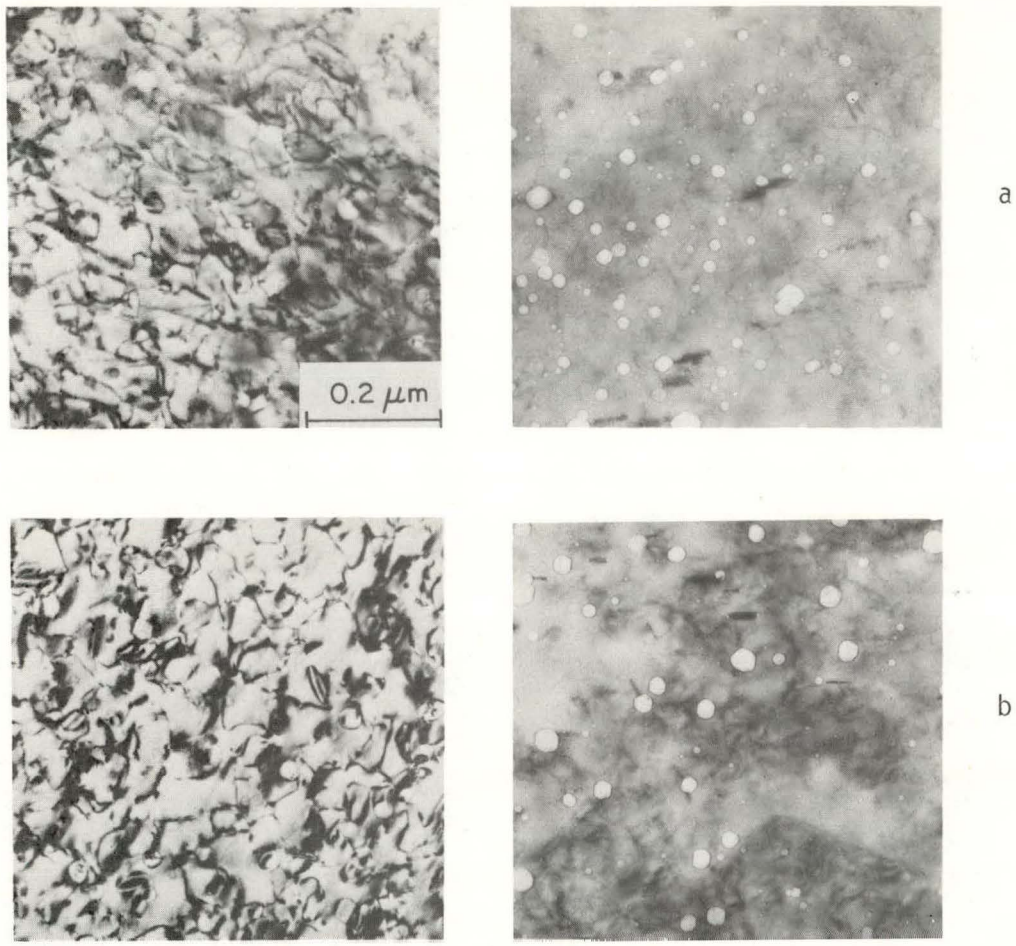

FIGURE 2. Dislocation and Cavity Microstructures in Solution-Annealed 316 SS Irradiated to 25 dpa at 625°C, a) Schedule 25SD and b) Schedule 25D.

microstructure. Loop number densities were lower and loop diameters larger in SA samples than in SAA specimens at 5 dpa after both single- and dual-ion irradiation.

In 20% cold-worked material the dislocation densities were high for all beam histories and swelling was low, as expected. The 5 dpa samples, Fig. 5, looked nearly identical, except that a few very small (barely resolvable) cavities were seen in the 5D sample. At 25 dpa the 25D sample contained no cavities larger than ~ 6 nm. Small cavities ($\leq$ 3 nm) were profuse and most, if not all, were associated with dislocations. The 25SD history produced, in

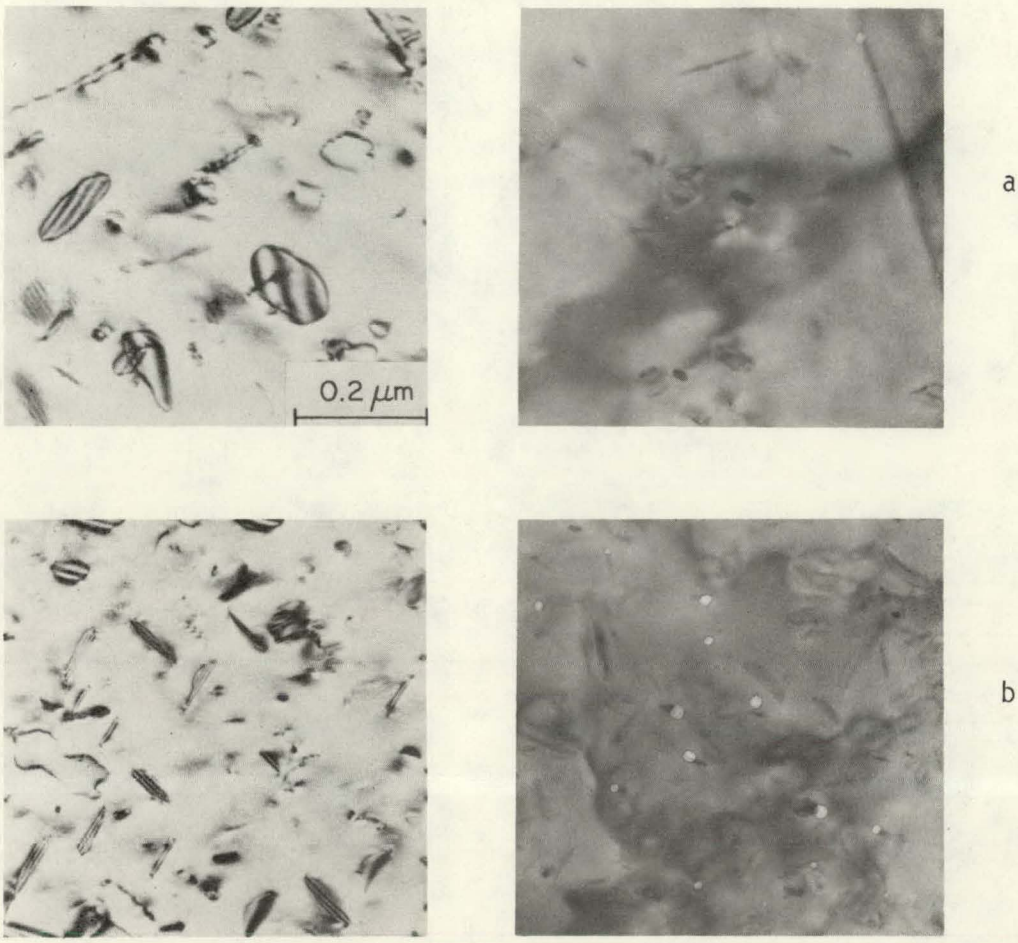

FIGURE 3. Dislocation and Cavity Microstructures in Solution-Annealed and Aged 316 SS Irradiated to 5 dpa at 625°C, a) Schedule 5S and b) Schedule 5D.

addition to the high number density of small cavities, a very low number density of cavities as large as 20 nm. Although the cavity volume fraction is low in both cases, it is clearly higher for the 25SD sample, i.e. the lack of helium at low dose actually enhanced swelling.

5.4 Microstructure of Helium Preinjected Samples

Typical microstructures for 25 dpa hot- and cold-preinjected single-ion irradiated samples of SA, SAA and CW material are presented in Figs. 7, 8 and

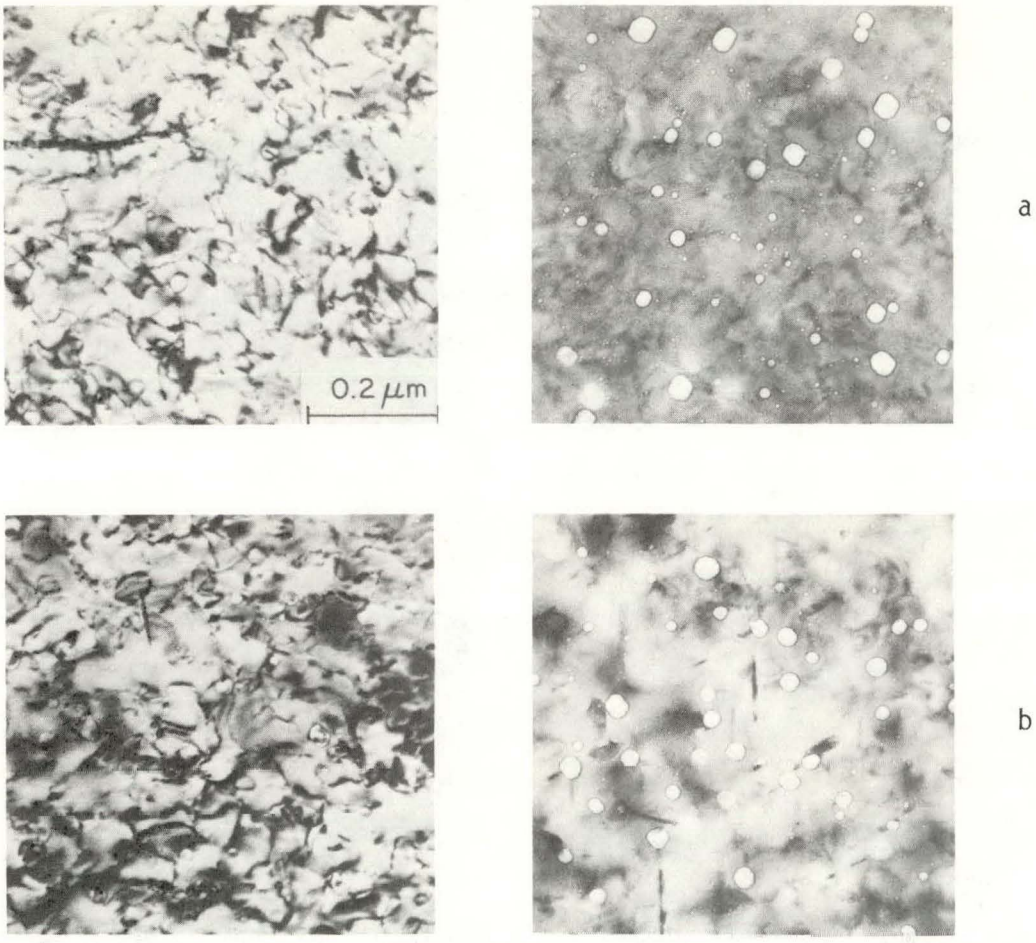

FIGURE 4. Dislocation and Cavity Microstructures in Solution-Annealed and Aged 316 SS Irradiated to 25 dpa, a) Schedule 25SD and b) Schedule 25D.

9 respectively. For easy comparison with dual-ion microstructures we have included 25D dual-ion micrographs in each figure. Beam histories 25CP, 25HP and 25D produced significantly different microstructures in samples with each of the prior thermomechanical treatments; microstructures in SA and SAA material closely paralleled one another but the effect of preinjection on CW material was entirely different.

In SA and SAA samples, Figs. 7 and 8, the dislocation densities in both 25CP and 25HP samples were significantly lower than for 25D irradiation and the fractional contribution of loops was much higher; i.e. the development of

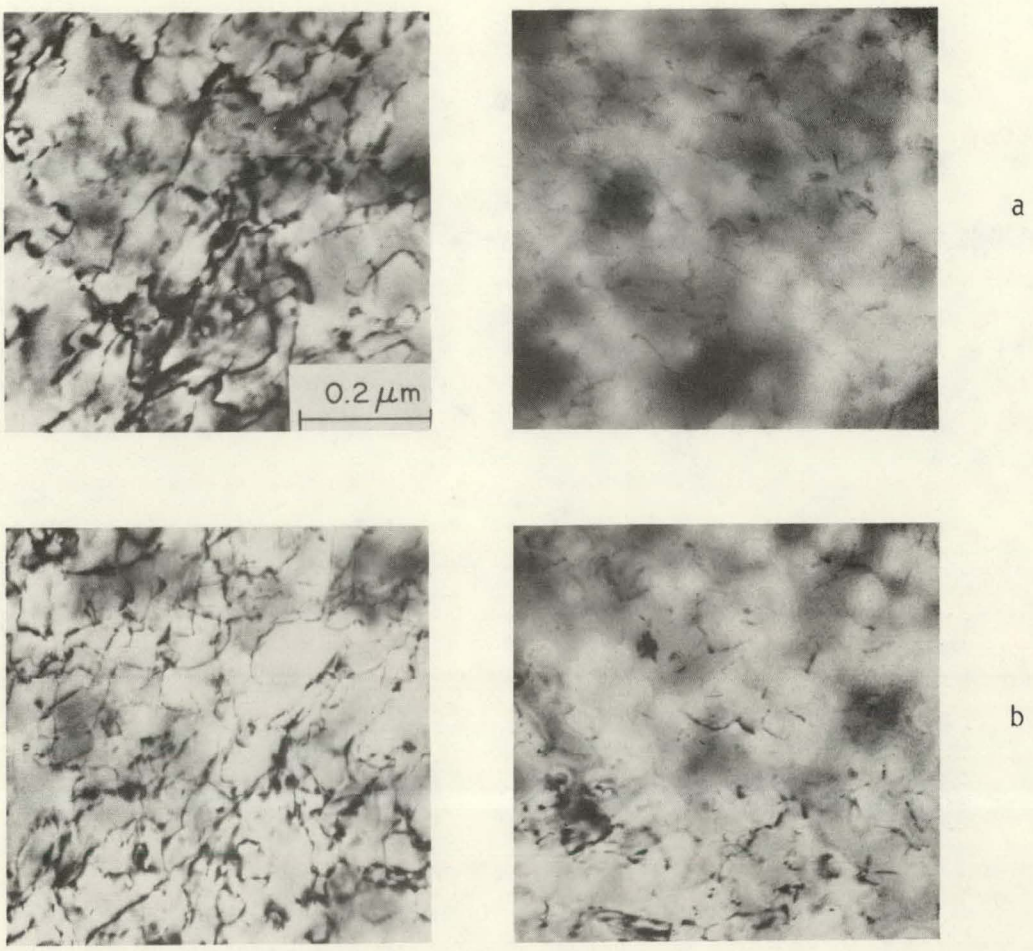

FIGURE 5. Dislocation and Cavity Microstructures in 20% Cold-Worked 316 SS Irradiated to 5 dpa, a) Schedule 5S and b) Schedule 5D.

dislocation microstructure appeared to be significantly retarded in preinjected samples. There were almost no small-cavities in 25 CP or 25 HP samples of SA and SAA material, and large-cavity number densities were a great deal lower than those produced by dual-ion irradiation. The cavity volume fraction was clearly lower in 25CP than in 25D samples, and appeared to be lower in 25HP samples than in 25D samples as well. Cavities in 25CP samples were significantly smaller than the large-cavities in dual-ion samples, while cavities in 25HP samples were significantly larger.

In cold-worked samples, Fig. 9, both hot- and cold-preinjection enhanced

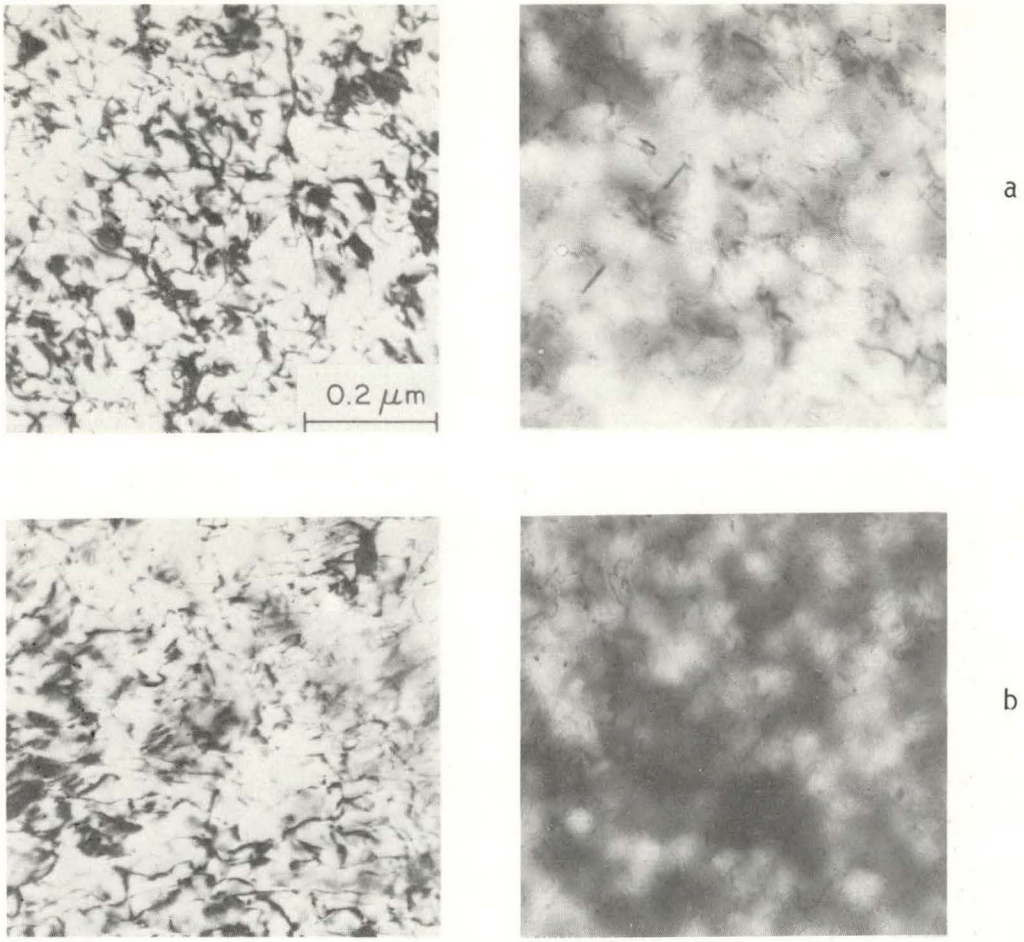

FIGURE 6. Dislocation and Cavity Microstructures in 20% Cold-Worked 316 SS Irradiated to 25 dpa, a) Schedule 25SD and b) Schedule 25D.

swelling relative to dual-ion irradiation instead of retarding it as in SA and SAA material. Dual-ion irradiation produced no large-cavities, Fig. 9c, but cold- and hot-preinjection followed by single-ion irradiation, Figs. 9a and b, produced large-cavities and measurable swelling. What is even more surprising is that swelling in preinjected cold-worked samples appears to be as high as, or even higher than it is in preinjected SA or SAA samples. This unusual feature will require further examination.

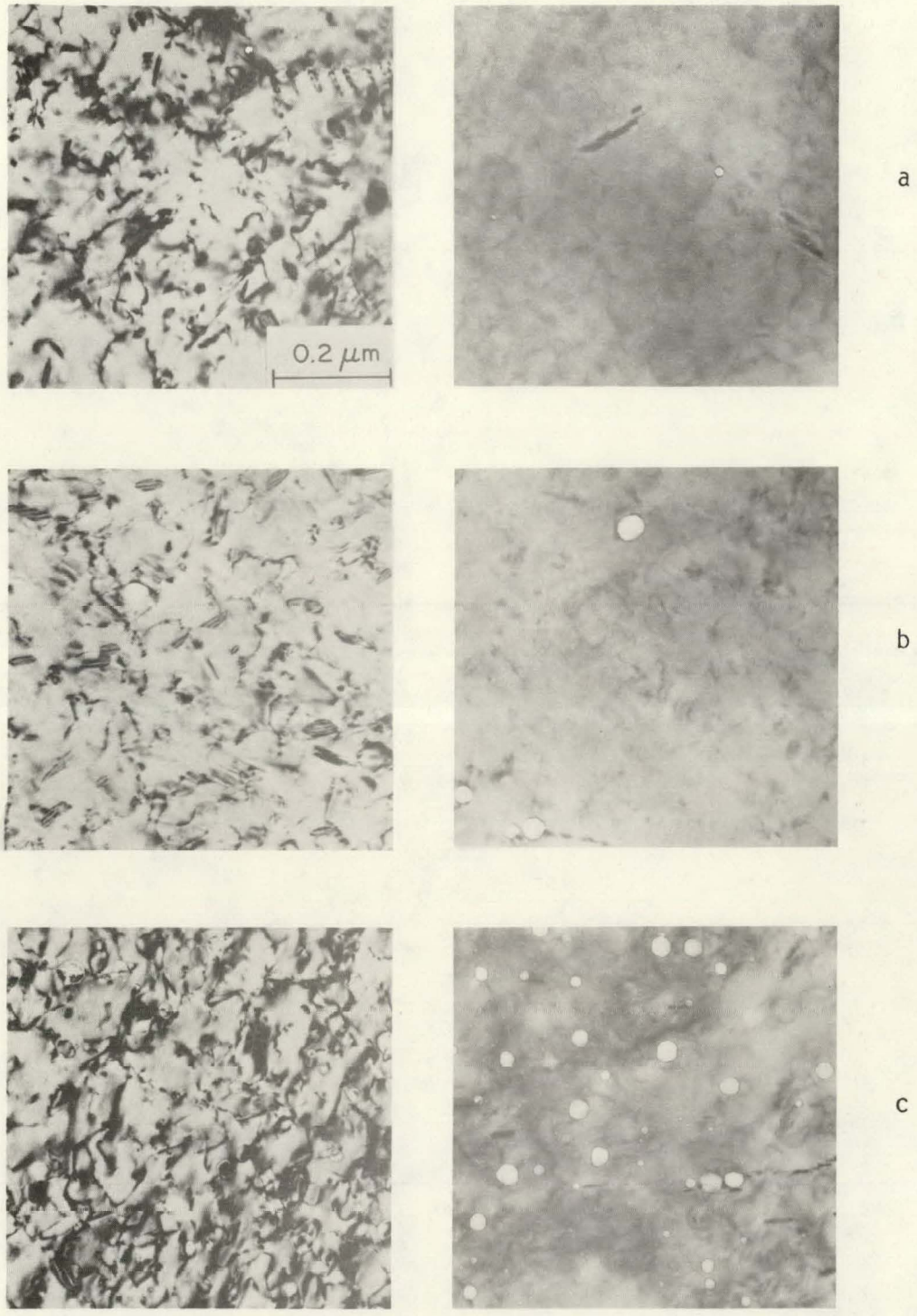

FIGURE 7. Dislocation and Cavity Microstructures in Solution-Annealed 316 SS Irradiated to 25 dpa, a) Cold-Preinjected Schedule 25CP, b) Hot-Preinjected Schedule 25HP and c) Dual-Ion Schedule 25D.

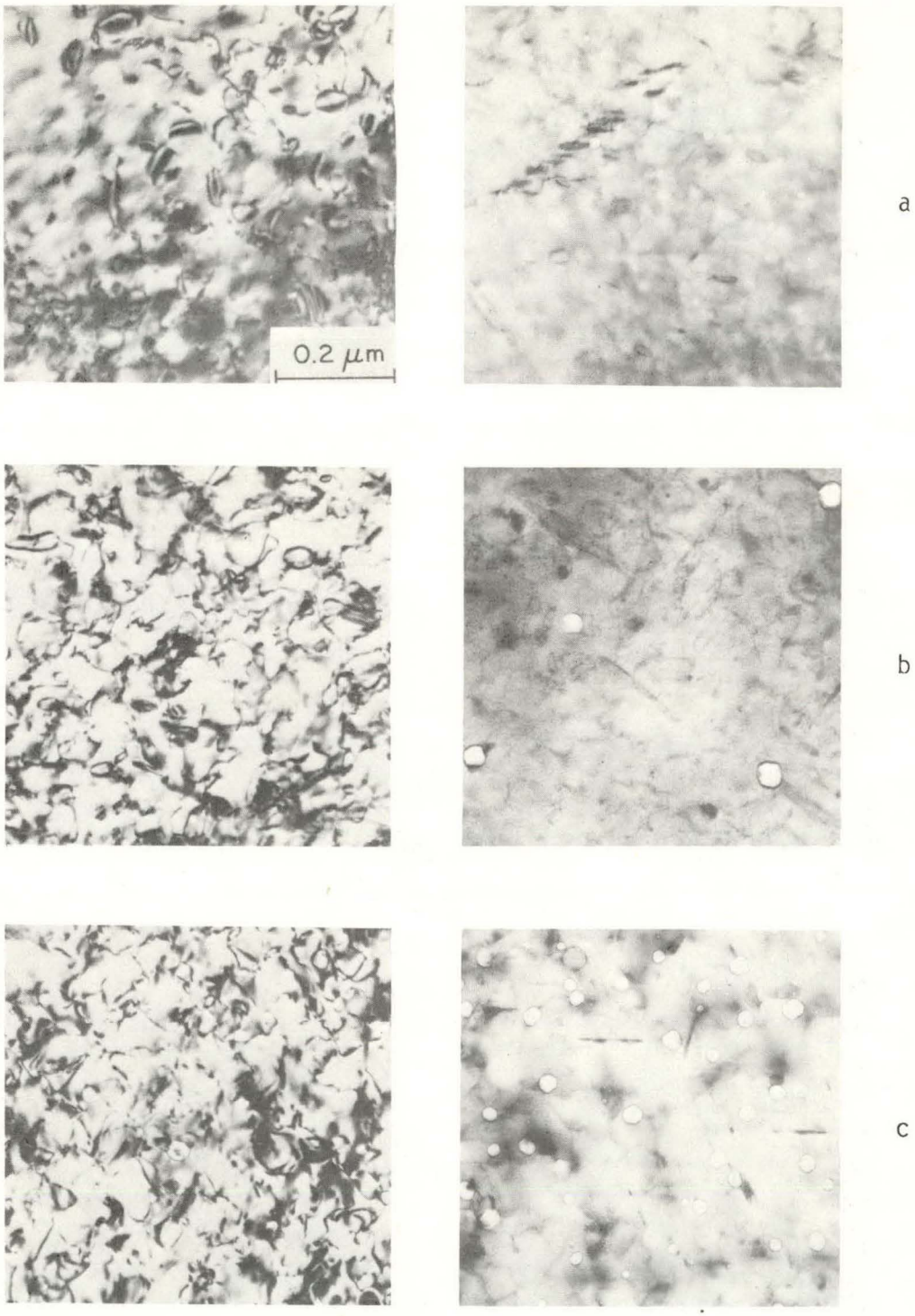

FIGURE 8. Dislocation and Cavity Microstructures in Solution-Annealed and Aged 316 SS Irradiated to 25 dpa, a) Cold-Preinjected Schedule 25CP, b) Hot-Preinjected Schedule 25HP and c) Dual-Ion Schedule 25D.

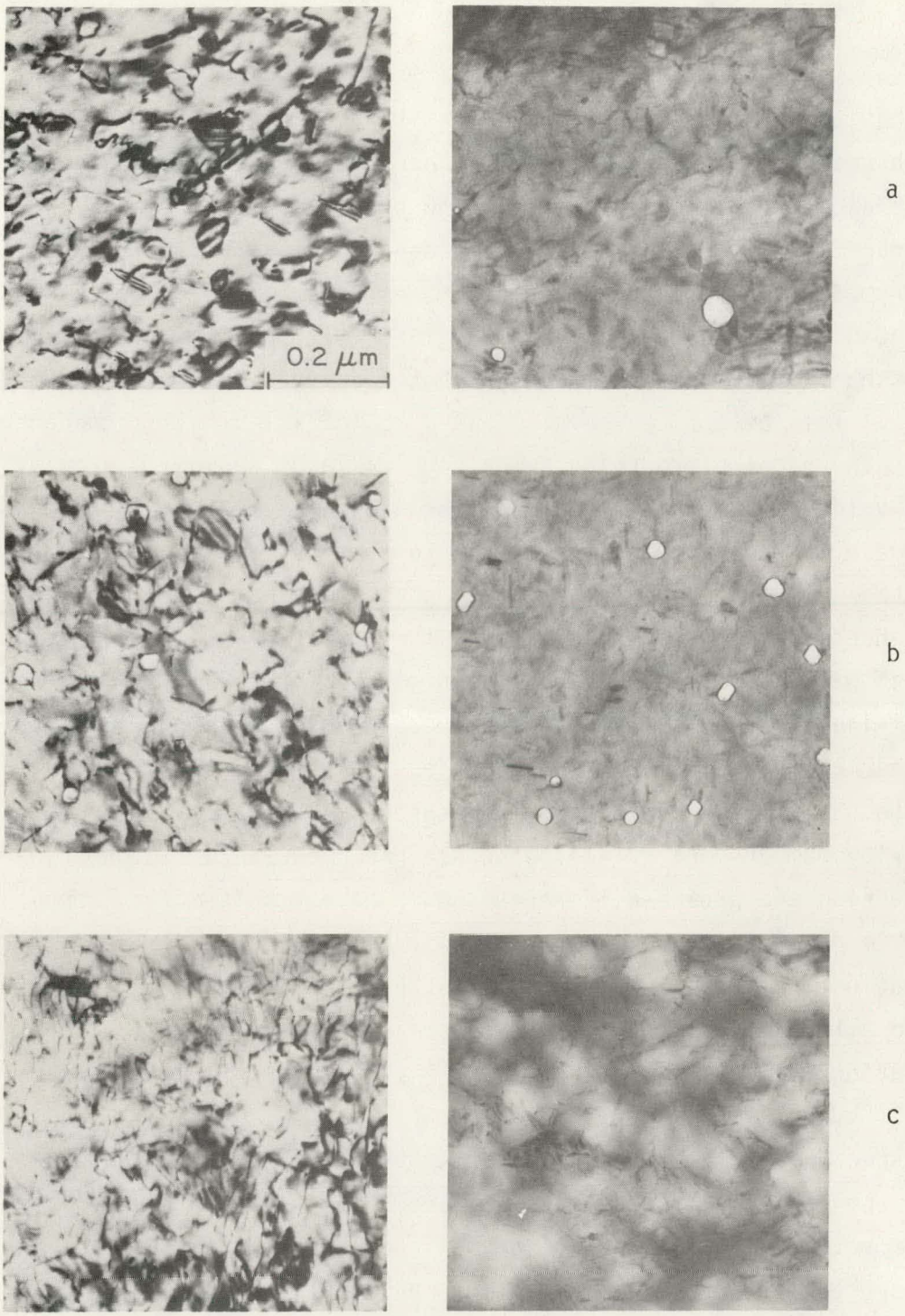

FIGURE 9. Dislocation and Cavity Microstructures in 20% Cold-Worked 316 SS Irradiated to 25 dpa, a) Cold-Preinjected Schedule 25CP, b) Hot-Preinjected Schedule 25HP and c) Dual-Ion Schedule 25D.

5.5 Discussion

The results of this study show that differences in helium concentration and distribution at low dose are quite persistant in affecting the microstructure at high dose. The results also show that the nature of low-dose helium effects are strongly dependent upon the preirradiation microstructure. The most graphic illustration of this is found in comparing hot- and cold-preinjected, single-ion irradiated samples, and comparing both with dual-ion irradiated specimens. In SA and SAA material, both hot- and cold preinjected samples had cavity number densities that were very low compared to dual-ion samples. This effect can be attributed to the lower helium concentration in preinjected samples producing fewer bubbles large enough to grow as bias-driven voids. However the large difference in cavity size between hot- and cold-preinjected samples is difficult to rationalize; clearly the differences persisted well into the cavity growth phase and thus could not be due to cavity nucleation differences alone. The effect of preinjection in CW material was entirely different, first because it enhanced swelling relative to dual-ion irradiation, and second because cold-preinjection caused formation of larger cavities than did hot-preinjection. It is possible that in this case the cavity-size difference was caused by nucleation differences, because the cavity number density following hot-preinjection was higher than for cold-preinjection and growth differences could have resulted from competition for available point defects. Whether this explanation is consistent with the high dislocation densities that would make the dislocations the dominant type of sink in all cases will have to be determined by a rate-theory model calculation.

Microstructure differences between the 25D and 25SD helium schedules were more subtle than the differences caused by cold versus hot-preinjection, but are of more immediate interest because of their direct relationship to MFR versus mixed-spectrum reactor irradiations. The most notable difference between 25D and 25SD samples was the addition of a strong component of mid-size cavities (3-12 nm) to the population in 25SD, SA and SAA samples. Presumably, most or all of these are of sufficient size that their growth is largely bias-

driven. Thus the number densities of cavities in the bias-driven size range may actually be higher in samples where helium was absent at the onset of irradiation. (Results of quantitative analysis will be necessary to confirm this point). Formation of cavities in the 3-12 nm size range also occured in 25SD irradiated CW material, where no cavities larger than ~ 3 nm were present in samples that had been dual-ion irradiated from the start. Thus the behavior in CW material appears to be similar to that in SA and SAA samples. However, the importance of the 3-12 cavities may be greater in the CW material because they are the largest cavities present and their growth should dominate the swelling behavior, whereas in the SA and SAA materials cavities larger than 12 nm are present in both 25D and 25SD irradiated samples.

In summary, we find that differences in the microstructures after irradiation that are caused by differences in helium content and injection schedule are quite complex and surprisingly persistent. Quantitative analysis of the dislocation and cavity microstructures described qualitatively in this report will further elucidate the mechanisms by which these helium effects operate. Results of the quantitative analysis will appear in future reports.

6.0 References

none

7.0 Future Work

Quantitative analysis of dislocation and cavity microstructures in the samples described in this report is now in progress.

CONTINUED EXAMINATION OF THE SWELLING OF "PURE" AISI 316 IRRADIATED IN ORR

H. R. Brager and F. A. Garner (Hanford Engineering Development Laboratory)

1.0 Objective

The objective of this effort is to determine the influence of spectral differences on the evolution of AISI 316 during irradiation and to extrapolate the insight gained to predict the alloy's behavior in proposed fusion devices.

2.0 Summary

Preimplantation of 40-appm helium into "pure AISI 316" prior to irradiation in ORR at 550°C to ∿3 dpa leads to either total suppression of radiation-induced cavities or reduction of their diameters below 1.5 nm.

3.0 Program

Title: Irradiation Effects Analysis (AKJ)
Principal Investigator: D. G. Doran
Affiliation: Hanford Engineering Development Laboratory

4.0 Relevant DAFS Program Plan Task/Subtask

Task II.C.2 Effects of Helium on Microstructure
Task II.C.17 Microstructural Characterization

5.0 Accomplishments and Status

5.1 Introduction

In earlier reports it was shown that the irradiation in the MFE-2 experiment of "pure 316" (Fe-17Cr-16.7Ni-2.5Mo) in the Oak Ridge Research Reactor (ORR)

led to a microstructural evolution that appeared to be sensitive to preirradiation helium implantation but not cold-working.[1-3] However, both density change measurements and postirradiation aging studies suggested that the apparent suppression of swelling by helium preinjection may be misleading.[3] In other words, the cavity density may have been increased sufficiently by preinjection that the voids produced were smaller than the resolution limit (~3.0 nm) of the imaging techniques used in the electron microscope. This conclusion is clouded by the possibility that the small density decrease observed in preinjected specimens may have risen from elemental segregation and not from unresolved cavities. In order to examine this possibility it was decided to extend the resolution limit to smaller sizes by using careful through-focus series of potential cavities under kinematic conditions.

In this type of approach small voids which are essentially invisible by absorption contrast can be imaged. In the underfocus condition the outer boundary of the cavity appears as a black ring surrounding a light area, while in the overfocused condition the inner region is darker than background and surrounded by a white ring.

5.2 Results

In order to define the limit of resolution in the JEOLCO 100X, a preimplanted (40 appm) specimen irradiated at 550°C for ~3 dpa was aged out of reactor for one-quarter hour at 900°C. As shown in Figures 1 and 2 this lead to detectable cavities where none were observed prior to irradiation. The mean diameter is ~3 nm and their density is about 5×10^{15} cm^{-3}. This concentration is similar to that found in irradiated specimens which were not preinjected with helium although the sizes are smaller by factors of 3 to 4.[2] Figure 3 shows that no cavities were detectable at <1.5 nm diameter.

Re-examination of another identical specimen aged one-quarter hour at 700°C yielded a low density ($\leq 10^{14}$ cm^{-3}) of images, some of which were cavities, and some which did not behave as cavities. The latter were probably artifacts on the foil surfaces.

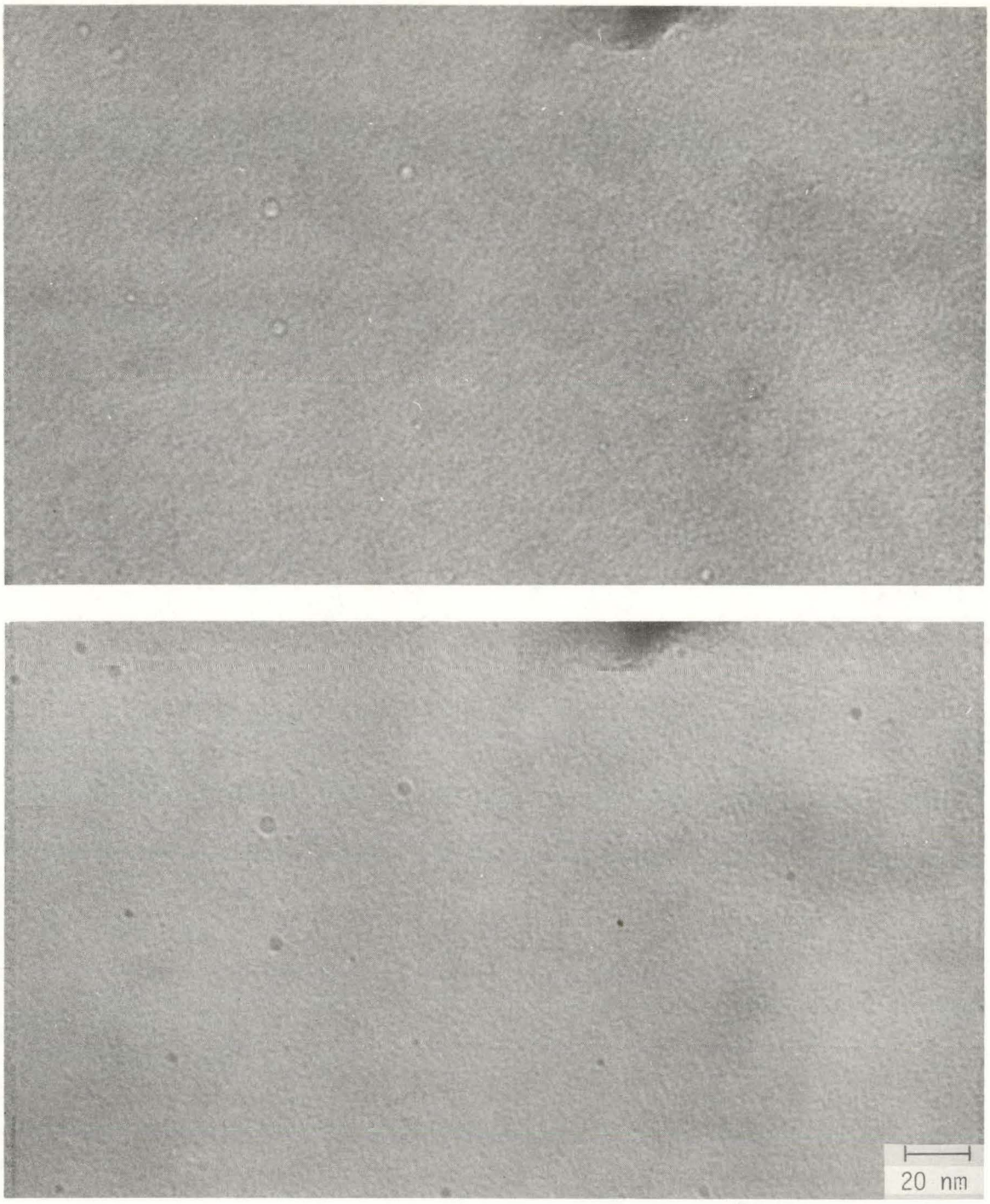

FIGURE 1. Underfocus (Top) and Overfocus (Bottom) Images of Cavities in Annealed Fe-17Cr-16.7Ni-2.5Mo + 40 appm Helium Irradiated in ORR at 550°C for ∿3 dpa and then Aged One-Quarter Hour at 900°C.

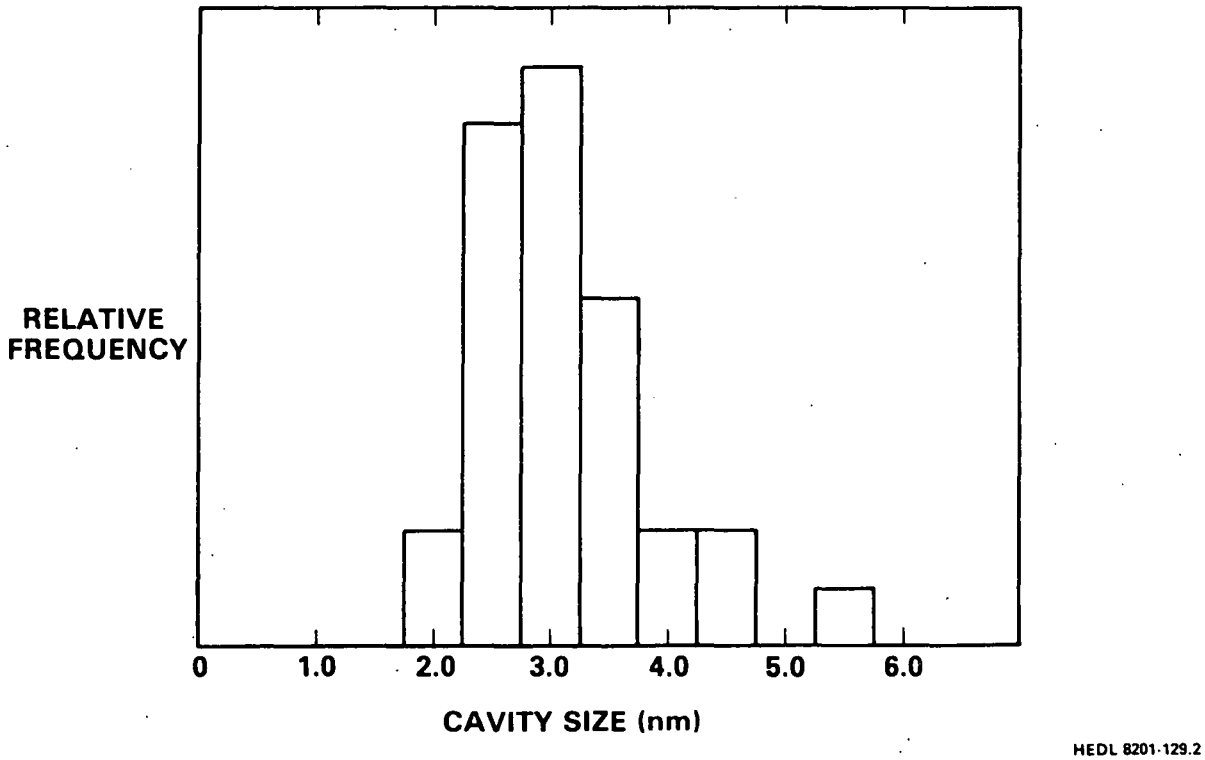

FIGURE 2. Distribution of Visible Cavities Observed in Specimen Described in Figure 1.

Examination of a preimplanted specimen without aging using a careful and extensive through-focus series led to no images which could be attributed to cavities. If indeed cavities exist in this specimen they must possess diameters of $\leq$1.5 nm.

5.3 Conclusions

Preimplantation of 40 appm helium into "pure AISI 316" prior to irradiation in ORR at 550°C to $\sim$3 dpa leads to either total suppression of radiation-induced cavities or reduction of their diameters below 1.5 nm.

6.0 References

1. H. R. Brager and F. A. Garner, "Influence of Cold-Work on Swelling of Pure AISI 316 Irradiated in ORR," DAFS Quarterly Progress Report, DOE/ER-0046/6, p. 148.

2. H. R. Brager, F. A. Garner and R. L. Gaines, "The Influence of Preinjected Helium on Void Nucleation in Fe-17Cr-16.7Ni-2.5Mo," ibid., p. 144.

3. H. R. Brager and F. A. Garner, "Further Examination of Swelling of "Pure" AISI 316 Irradiated in ORR," DAFS Quarterly Progress Report, DOE/ER-0046/7, p. 172.

7.0 Future Work

These specimens as well as preinjected and aged specimens will be examined using positron annihilation in order to determine if cavities exist at diameters below 1.5 nm.

APPENDIX

CRITICAL ASSESSMENT OF DUAL-ION AND CHARGED PARTICLE RESEARCH IN THE FUSION MATERIALS PROGRAM

THIS PAGE

WAS INTENTIONALLY

LEFT BLANK

Critical Assessment of Dual-Ion and Charged Particle Research in the Fusion Materials Program

for

Materials and Radiation Effects Branch
Office of Fusion Energy
Department of Energy

Report of Ad Hoc Task Group on Charged Particle Research

G.R. Odette[1], Chairman
J. Spitznagel[2]
A. Turner[3]
W. Jesser[4]

1 University of California, Santa Barbara
2 Westinghouse Research and Development Center
3 Argonne National Laboratory
4 University of Virginia

Abbreviations Used in the Report

ADIP	Alloy Development for Irradiation Performance Task Group (of the OFE of the DOE)
ANL	Argonne National Laboratory
BNWL	Battelle Northwest Laboratories
BES	Basic Energy Sciences Division of the DOE
CP	Charged Particle
DAFS	Damage Analysis and Fundamental Studies Task Group (of the OFE of the DOE)
DOE	Department of Energy
DPA	displacement per atom
EDX	Energy Dispersive X-ray Analysis
EELS	Electron Energy Loss Spectroscopy
E-19	a Ni - Cr-Fe ternary austenitic alloy
EBR-II	Experimental Breeder Reactor-II (at Idaho National Laboratory)
FFTF	Fast Flux Test Facility (at Hanford Engineering Development Laboratory)
HFIR	High Flux Isotope Reactor (at ORNL)
HVEM	High Voltage Electron Microscopy
MFR	Magnetic Fusion Reactor
OFE	Office of Fusion Energy (of the DOE)
ORNL	Oak Ridge National Laboratory
ORR	Oak Ridge Research Reactor (at ORNL)
PCA	Prime Candidate Alloy (austenitic stainless steel chosen by ADIP as prime contender for that alloy path)
PKA	Primary knockon atom
PMI	Plasma Materials Interaction Task Group (OFE/DOE)

RTNS-II	Rotating Target (14 MeV) Neutron Source (at Lawrence Livermore Laboratory)
SS	Stainless Steel
STA	Solution Treated and Aged
U.-Va.	University of Virginia
U.-Wisc.	University of Wisconsin
U.-Pitt.	University of Pittsburgh
W-R&D	Westinghouse Research and Development Center

Summary

Bombardment with charged-particles, particularly dual beams composed of helium and heavy ions, is a tool increasingly used to study microstructural evolution in structural alloys induced by displacement damage and transmutant gases. A primary motivation for such studies in the fusion materials program is anticipation that this research can contribute to developing a sound physical basis for correlating data from various neutron irradiation environments and to predict behavior in fusion environments which are not available. However, the distinct advantages of these techniques, primarily flexibility and precision in the control of important variables, does not come without significant cost. In particular, there is a concomitant introduction of experimental variables which fall outside the range found for neutron irradiation variables; these variables must be considered in interpreting and utilizing the charged-particle data in fission-fusion neutron correlation efforts. It should be noted, however, that use of neutron data faces similar challenges.

Hence, this report focuses on the status of "interpretational tools" needed to apply the charged-particle results to neutron correlations. We first conclude that there are a finite number of pertinent issues (perhaps

about 10) which are at various stages of resolution. Several of these are nearly solved, while a few others will require 5 to 10 years of additional research. Hence, we believe that there is little near-term (less than 5 years) prospect for direct engineering utilization of charged-particle data. A direct use would be, for example, using charged particle data along with some "correction" factors to specify the void swelling in a particular alloy as a function of neutron exposure in a fusion first wall. However, indirect use of charged particle data can have a critical near-term impact on the fusion materials program in: developing and calibrating models; guiding the interpretation of neutron data; planning neutron irradiation experiments; and chosing among alternate interim engineering correlation positions. Indeed, such indirect use has already taken place. More significantly, such research can provide important information in setting the direction of fusion materials research by addressing several controversial questions of immediate concern, such as the significance and mechanisms of microchemical effects and the influence of pulsing.

Over the intermediate and longer-term more direct use of charged-particle data seems likely. In part, this optimistic conclusion derives from the broad (worldwide) interest in the interaction of ion beams with solids motivated by such diverse technologies as plasma materials interactions and surface modified wear-resistant alloys. Specifically, these programs are developing most of the interpretational tools which are also needed by the fusion materials program.

Hence, we believe that it is in the interest of the fusion program to assure a stable commitment of "reasonable" resources to a sustained charged-particle research effort. If this investment is to be best utilized, however, better coordination, both within fusion-sponsored programs and with other outside groups, is required. Further, there must be some continuing commitment to resolving the underlying interpretational

issues; we particularly note the need to develop better interfaces with modeling efforts.

The program coordination should and need not be overly constraining. Indeed, it should be primarily structured around a consensus on technical issues and mechanisms to resolve them. Hence, we finally offer some tentative suggestions in that vein, noting that it is then a relatively short step to more formalized program plans.

1. INTRODUCTION

Recently, bombardment with ion beams, or charged particles (CP), has been applied in support of fusion materials development. The principal motivation has been a realization that these techniques provide a well-controlled irradiation environment in which key damage variables can be studied singly or in combination in terms of their influence on microstructural evolution; and for light ions, irradiation creep and tensile flow properties. The key variables that can be studied are: displacement per atom (dpa) rate, helium to displacement per atom ratio (He/dpa ratio) and schedule; temperature; stress; and cycling of some or all of these variables. The technique provides access to some variable regimes not readily accessible in neutron experiments -- e.g. high He/dpa ratios and pulsing. Further, the experiments can be conducted for any material (i.e., without the compositional limitation associated with helium generation by neutron reactions). Research supported to date by the Department of Energy's (DOE) Office of Fusion Energy (OFE) has focused on the first three variables (dpa rate, He/dpa ratio and temperature) for engineering or model fusion alloys.

Obtaining these clear benefits is not without challenge; the major issue is interpretation of the CP data in a way which allows it to be used to correlate and extrapolate neutron data to fusion environments in one or more of several ways. These include: direct supplements to neutron data; qualitative assistance in the interpretation and planning of neutron experiments; and providing quantitative information on mechanisms and parameters for models used to correlate neutron and, perhaps, neutron and charged particle data. This issue has been the subject of an American Society for Testing and Materials (ASTM) Recommended Standard Practices[1,2], [one of which is currently undergoing balloting[2]] which provide useful information and background material. However, there have been additional developments since these documents were written. Hence, the Department of Energy's (DOE) Office of Fusion Energy (OFE) requested

that the Damage Analysis and Fundamental Studies (DAFS) Task Group conduct a critical assessment of CP research with respect to both the short and long-term goals of the fusion materials program. We believe that the major issue facing fusion materials CP research are the interpretational tools available for correlating these results with neutron data. Thus, the major body of this report addresses these interpretational tools; indeed, the rate of development of such tools will largely govern the qualitative and quantitative impact of charged particle research both in the short and long-term.

In addition, this brief document attempts to put into current perspective the use of CP bombardment in the DAFS program.* It must be emphasized, however, that this review is by no means definitive. New data generated by these techniques in the DAFS program and a tremendous worldwide increase in research on ion implantation promise to alter many assumptions underlying the use of CP studies.

We have excluded discussion of direct applications of ion beams to the study of Plasma/Materials Interactions (PMI). This subject has been discussed at length elsewhere[3]. It is currently being actively pursued by the PMI Group with few direct ties to CP research in the DAFS program. There is, however, considerable overlap in research interests among the various laboratories involved in DAFS/PMI work. Consequently, a cumulative body of knowledge is evolving regarding near-surface effects from implanted ions that is relevant to the assessment and will be discussed.

---

* Relevant DAFS programs at the time of writing include dual-ion irradiations at Argonne National Laboratory (ANL) and Westinghouse Research and Development Center (W-R&D)/University of Pittsburgh (U.-Pitt.), single heavy ion irradiations at U. Wisconsin (U.-Wisc.) and light ion irradiations at ANL, and helium irradiations coupled to a High Voltage Electron Microscopy (HVEM) at University of Virginia (U.Va.).

Most of what follows is couched in terms of the so-called "dual ion" or "triple ion" beam techniques applied to the study of microstructural effects in potential fusion first-wall materials. This is not meant to detract from the usefulness of bombarding with monatomic high energy heavy ions (U.-Wisc.) or with monatomic light ions (at ANL), sometimes combined with HVEM (at U.-Va.). Such techniques have proven useful in demonstrating changes in properties and microstructure, the degree to which such effects scale with damage energy, and the interaction between applied stress and helium distribution on grain boundary fracture. In fact, most of the arguments presented here are generic to ion implantation in general.

Finally, several suggestions for improving the coordination or general framework of CP and neutron irradiation efforts within the DAFS program are given (with the caveat that overly constrained research would surely be counterproductive).

This report is divided in five parts:

1. Introduction

2. Historical perspective on the use of charged particles to "simulate" or study fast neutron irradiation effects.

3. Discussion of interpretational tools which need to be developed so that CP data can be "used" (in the sense of correlating the data with that from fast and mixed spectrum fission reactor and high energy ex-reactor neutron irradiations).

4. Prospects for "short-term" versus "long-term" impact of CP research on development of fusion reactor first-wall materials.

5. Suggestions for coordinating CP efforts in the DAFS program (encompassing general program philosophies of the participating research groups and experimental/theoretical capabilities).

2. HISTORICAL PERSPECTIVE ON THE USE OF CHARGED PARTICLES TO STUDY FAST NEUTRON DAMAGE EFFECTS IN METALS

Early work at Harwell and elsewhere[4,5] first demonstrated the possibility of using charged particle bombardment to produce microstructural changes similar to those observed under fast neutron ($E \gtrsim 0.1$ MeV) irradiation. The motivation for this work stemmed from three ideas: (1) nearly all atomic displacement events in reactor result from energy transfer among recoiling metal atoms. Under typical fast neutron fluxes of $\sim 10^{14}$ - 10^{15} n/cm^2 sec there are many more atom-atom collisions than neutron-atom collisions per unit volume. Thus, the detailed nature of the initial energy transfer (primary knockon atom or PKA event) should be relatively unimportant in defect production as long as sufficient energy can be transferred to metal atoms in collisional processes. (2) Charged particles have much larger collison cross sections with metal atoms than do neutrons. Thus, it should be possible to compress into hours atomic displacement processes that would take many months in reactor. (3) As long as the energy of the incident particles is less than ~10 MeV/nucleon the atomic displacements can be achieved without making the targets radioactive.

The technique of using ion beams to "simulate" fast reactor conditions gained great popularity in the early 1970's. Unfortunately, the initial conclusion that ion irradiations could be used to simulate neutron irradiation results was based on superficial similarities of microstructures and swelling rates. Very little work was conducted to test the basic assumptions of ideas behind the technique, until more detailed analysis showed significant differences in precipitation behavior and other microstructural features.

In the mid-to-late 1970's the Energy Research and Development Agency (predecessor of DOE) pressure to select and optimize fuel cladding and duct alloy compositions and microstructures for the fast breeder reactor

program in the U.S. gave strong impetus to the use of charged particle techniques. It soon became apparent that successful prediction of alloy behavior under neutron irradiation was not guaranteed by either straightforward application of charged particle results or by simple interpolations or extrapolations of ion or electron bombardment data. There were notable successes, e.g. Johnston's demonstration of the nickel-effect on swelling in face-centered-cubic Fe-Ni-Cr alloys[6] and Okamoto's discovery of irradiation-induced solute segregation[7] (predicted by Anthony[8] of General Electric almost a decade earlier), but there were also failures[9,10,11]. Void and dislocation loop formation often exhibited similar fluence-dependent kinetics under neutron and CP irradiation <u>if</u> the irradiation temperatures were separated by a temperature difference ΔT. The magnitude of ΔT was selected on the basis of relative atomic displacement rates to "normalize" point defect supersaturations. However, such a "temperature-shift" was often accompanied by a precipitate microstructure and a sequence of precipitation[11] which differed from that observed in the corresponding neutron-irradiated specimen. Chemical composition, crystal structure, morphology and stability of the precipitates could all change when the atomic displacement rate was increased by three orders of magnitude, the irradiation temperature raised by an amount $\Delta T \sim 100 - 200°C$, and the irradiation time (time-at-temperature) shortened from $\sim 10^7$ sec to $\sim 10^4$ sec. Interestingly, many of these effects are linked with solute-segregation (sometimes referred to as microchemical evolution[12]) -- a phenomenon discovered and intensively studied by CP bombardment techniques[13].

The difficulties encountered in correlating CP and neutron irradiation data led to disenchantment with the use of charged particle studies in the breeder program, and since experimental breeder reactors were available for continued irradiation studies, most of the CP research activity at the various laboratories directed toward "simulating" fast neutron damage effects was stopped. Basic research studies have continued, in this

country and abroad, related to fusion and other emerging technologies, and using CP techniques to study the effects of atomic displacement damage and implantation of ions with varying degrees of solubility have increased steadily up to the present time[14,15].

Out of the difficulties encountered in attempting to quantitatively correlate CP and fast neutron results there emerged an appreciation of some of the important variables. In particular, questions have been raised about:

Primary recoil energy spectrum effects

Point defect annealing rates and cascade overlap effect at high particle fluxes

Doping of the damage region with implanted interstitials

Introduction of local stresses by ion implantation and inhomogeneous swelling

Loss of point defects to the nearby free surface

Impurity pick-up from the vacuum ambient

Point defect gradient effects arising from a depth dependent atomic displacement rate

Method of implanting helium to simulate helium generation from (n,α) reactions

Acceleration of kinetic processes with different dependencies on atomic displacement rate and temperature

Interfaces between modeling efforts and CP research.

It is precisely in trying to answer these questions that one faces the questions of application, interpolation and extrapolation of charged particle bombardment results to fast neutron damage conditions. Fundamentally, one would like to get as close as possible to neutron irradiation conditions, activating the same basic physical processes and measuring identical responses when the same variables (e.g. temperature,

fluence) are changed. Sometimes this is possible. More often, the advantages of working on a compressed time scale and exploring conditions not achievable with neutron irradiations cause the experimental variables in CP experiments to fall outside the range of normal neutron parameters. Under these conditions it is important to be able to quantify and control the variables singly and in combination to systematically study their influence. Finally, it is necessary to quantify variables, even if they cannot be specifically controlled (e.g. induced stresses).

Not all of these questions bear equal significance. An appreciation of the hierarchy of correlation needs is evident in the way CP experiments have been designed for the DAFS program. Basically, it has been recognized that there are essentially three groups of "atypical" variables:

1) those which can be avoided or minimized by suitable experimental techniques, e.g. injected interstitial effects, impurity pick-up, loss of point defects to the free surface and point defect gradient effects;

2) those which are being addressed in a variety of CP studies (not necessarily related to neutron irradiation effects) which are reasonably close to being quantified, e.g. PKA recoil energy spectra effects, cascade overlap effects, point defect gradient effects and methods of implanting helium or other solutes;

3) those requiring a significant amount of research, including focussed efforts by DAFS programs, e.g., acceleration of kinetic processes with different dependences on atomic displacement rate and temperature, development of appropriate kinetic models for rate effects, and development of reliable techniques for determining the state of stress in an ion implanted solid.

In the following section we discuss each of these variables in more detail and in accordance (roughly) with the above classifications.

3. DISCUSSION OF INTERPRETATIONAL "TOOLS" NEEDED FOR CROSS-CORRELATION OF CHARGED PARTICLE AND NEUTRON IRRADIATION DATA.

This section is primarily a discussion of the basic physical differences between CP and neutron irradiation outlined in the previous section. A lengthy scientific discourse could be given for each item. That will not be done here. Instead we will simply try to summarize the present degree of understanding, relevance to DAFS studies for projected fusion reactor first-wall conditions and possible means of acquiring the knowledge needed to correlate with neutron data.

It must be stated at the outset that the same questions (with the exception of matching (n,α) effects) are of concern in the emerging fields of "surface engineering" implantation metallurgy, semiconductor fabrication for large scale integration and integrated optics. Thus, there are many scientists around the world currently studying these effects. The prognosis for acquiring good physical understanding of most of them within the next 5-10 years is good.

3.1 Doping of the Damage Region with Implanted Interstitials

Anomalously low swelling rates in the vicinity of the peak damage region in self-ion bombarded targets prompted considerable experimental and theoretical work several years ago[16]. It was suggested that the proximity of the damage peak to the mean projected range of bombarding ions resulted in a sufficient imbalance in the concentration of self-interstitials and vacancies that void formation was suppressed. The problem would be compounded if the implanted ion was also a dopant and could alter the chemical composition in the region of observation.

Because this effect can be observed directly and/or avoided by the choice of ion energy and section depth, it is not thought to present a serious impediment to use of CP experiments for elucidating fast neutron damage mechanisms. Many experiments in the DAFS program have avoided this problem by taking data from sections ~0.4μm to 3μm away from the projected range of the heavy ions and analyzing to assure no back-diffusion of the heavy ions to the region of observation.

3.2 Impurity Pick-up From the Vacuum Ambient

Most ion bombardment experiments designed today to approximate fast neutron damage are conducted in high vacuum. This was not always the case, however. Deposition of hydrocarbons on surfaces of ion bombarded foils was a common occurrence for many years (and is still observed if the vacuum degrades to pressures in excess of ~10^{-7} Torr). The influence of these deposits on microstructural development is not known. High temperatures and recoil implantation effects certainly favor carbon transport into the near surface region. Some evidence suggests that carbon may influence nickel and silicon segregation in 316 stainless steel (SS)[17] and copper-vacancy cluster formation in ferritic steels[18] under neutron irradiation. Thus there is reason for concern.

The relevance of this phenomenon to tokamak first wall conditions and the DAFS program is threefold: (1) Even with armor, impurity pick-up effects from the ambient at the first wall as well as at the divertors, limiters and beam dump components may be appreciable. (2) As part of the DAFS effort (and with OFE funding) special experimental capabilities[19] to determine the effects of controlled changes in partial pressures of H, O_2, N_2, CO, CO_2, H_2O, etc. on damage microstructures developed by ion bombardment were constructed. (3) For comparison of bulk radiation effects under ion and fission neutron irradiation it is necessary to quantitatively determine the source and extent of changes in local chemistry in <u>both</u> environments.

The phenomonon is generic to ion implantation, and is controllable and amenable to experimental investigation. It is actively being studied with sophisticated nuclear reaction profiling techniques[20] at several laboratories including Sandia National Laboratory, ORNL, U.-Pitt. and at additional sites abroad. It seems highly likely that sufficient data will be available in 1-2 years to permit some definite conclusions regarding the degree and importance of such contamination.

3.3 Loss of Point Defects to the Free Surface

It was demonstrated a number of years ago that void formation could be inhibited by the proximity of a free surface[20]. The magnitude of the void denuded zone was shown to depend on the ratio of the vacancy diffusivity to the atomic displacement rate for a given foil thickness. Similarly, post-irradiation annealing experiments[21] have demonstrated that cavity shrinkage kinetics can be altered in regions close to the surface. For most of the high energy ion bombardment conditions used in the current DAFS program, experimentally determined void denuded zone widths are small compared to the depth at which data is normally taken. Therefore, it is unlikely that foil surface effects perturb significantly the kinetic processes in the regions being studied.

3.4 Point Defect Gradient Effects Arising from a Depth Dependent Atomic Displacement Rate

The amount of energy per incident ion dissipated in atomic displacement events varies with depth in the specimen. Thus one anticipates gradients in point defect concentrations that could affect kinetic processes. This is, at present, an unresolved concern; however there are indications that it may not be very important. For example, very little decoration of steep damage energy profiles by substitutional solutes has been observed[22,23]. Some enhancement of concentrations of fast-diffusing interstitial elements such as carbon in the vicinity of the damage peak

have been reported [24], but it is not clear whether this is the result of point defect gradients or simply decoration of a varying concentration of defects such as dislocation loops by the fast diffusing species.

In some of the DAFS CP studies, the heavy ion data are obtained from regions well removed from the damage peak where damage energy gradients are minimal. This is being treated as a variable in interlaboratory data comparisons, and if gradient effects prove to be important, all DAFS CP studies will be performed this way.

Combined low energy channeling/Rutherford backscattering and transmission electron microscopy (TEM) techniques are currently being used at a number of laboratories to measure concentration profiles for various solutes resulting from a variety of atomic displacement conditions[25]. The intention is to study diffusion in metals at low temperatures and solute redistribution by cascade mixing and Kirkendall effects. Such studies are clearly relevant to the question of the importance of point defect gradients. Unfortunately they are still in their infancy. Several years of research will be required to obtain definitive evidence.

3.5 Primary Recoil Energy Spectra Effects

The basic difference in the primary recoil spectra (the relative number of primary recoiling atoms having energy T as a function of T) for fast neutrons and ions is the large number of low energy primary recoils in the latter. There is both experimental and theoretical evidence that above a sufficiently large recoil energy (i.e. >10 to 50 keV) the differences in recoil spectra should not be too significant if exposures are calculated in terms of a physically appropriate unit such as damage energy or dpa (26-28). However, it should be noted that while use of damage energy exposure units has "worked" in a number of cases, this expedient has not always been successful; for example, in correlating 14 MeV and fission reactor data in a few instances[27]. Other experimental verification has

been found in studies in which the ion mass/energy has been varied with little observable effect.[29] However, the existence of a large component of low energy recoils (< 10 keV) may have some effect on neutron charged particle correlations (and even on fission neutron - 14MeV/high energy neutron correlations) in a way which is both material and property sensitive. For example, it is known that for some properties, the damage efficiency increases with decreasing recoil energy below ~ 10 keV[30]; on the other hand, properties which are sensitive to defect clusters may show a recoil energy threshold[31].

Nevertheless, most researchers appear to feel that differences in recoil spectra are not as significant as some other variables. However, it is probably most significant that considerable research will be directed at this question in the next several years in connection with DAFS sponsored RTNS-II/fission reactor intercorrelation studies, as well as extensive work in Europe and Japan. It is anticipated that appropriate displacement damage exposure units for neutron charged particle correlations will be available within a period of about five years.

3.6 Point Defect Annealing Rates and Cascade Overlap Effects at High Particle Fluxes

Microstructural evolution depends not only on the the specifics of energy partitioning on the fast collision time scale but also on defect annealing. One criticism that can be leveled at early CP studies is that some beam currents may have been large enough to cause cascade overlap within the time required for vacancy diffusion out of cascade core regions. Detailed effects are not known because few systematic studies have been reported, but some intuitively suspect that this alters the basic "damage physics". Others intuitively feel it is probably a second-order factor. It is, however, an issue implicitly related to underlying damage rate (flux) effects, in general, and is properly an important item for DAFS consideration. Further, it is also related to the

basic stochastic character of radiation damage, particularly in the case where particles produce energetic cascades, viz. - both neutrons and CP irradiations.

The approach taken to date in DAFS CP studies related to fusion conditions is to consider the atomic displacement rate as a key variable. Thus, the different laboratories are using a range of damage rates from ~2 x 10^{-5} dpa/s to ~5 x 10^{-3} dpa/s with overlap experiments at ~10^{-4} dpa/s. The lowest rate approaches that found in some fission reactors and the highest is comparable to that used in earlier CP studies. It is not yet possible to say unequivocally to what extent the damage rate can be increased to accelerate experiments without changing specific mechanisms. Pertinent theoretical work (outside the DAFS program) on time-dependent point defect "wind" effects[32] is currently underway and modeling of rate (flux) effects is planned in the DAFS program. In addition the economic incentive to use high current ion accelerators for "surface engineering" and implantation metallurgy applications is putting strong emphasis on the study of ion beam damage rate effects elsewhere in the scientific community. It is anticipated that a sufficiently detailed understanding of cascade overlap and vacancy annealing phenomenon will be achieved in the next 5-10 years to provide a sound physical basis for treating this effect when extrapolating over several orders of magnitude in damage rate; of course, many short-term studies conducted at lower dose rates will not be significantly constrained by the potential effect of this phenomenon.

3.7 Method of Implanting Helium (and Hydrogen) to Simulate Helium and Hydrogen Generation from (n,α) [(n,p)] Reactions

Various laboratories use somewhat different techniques to implant helium during dual-ion irradiations. For example, in some cases rotating tapered solid degrader foils are used, while in others the specimen is rocked to spread out the helium beam. Further, the helium deposition profile relative to the displacement damage distribution varies between

facilities. The influence of these differences is not expected to be large; however, it is one of the issues that is being specifically addressed in an intercorrelation study involving W-R&D/U.-Pitt., ORNL, ANL and the Battelle Northwest Laboratories (BNWL). Data from this study is currently being assessed. The distribution of implanted helium as well as recoil-induced migration has been studied using α,α scattering and nuclear reaction profiling techniques.[20] Finally, some studies at ORNL have compared the effect of triple (helium and hydrogen) ion versus dual-ion irradiations.[23]

A more significant effect is found for some CP experiments. Prior to the design and construction of the several dual-ion beam facilities available in the world today, some experiments were conducted by preimplanting helium at $\sim$25°C. One of the important contributions of recent CP research has been the demonstration of the importance of the mode of helium injection on microstructural evolution under irradiation. This data is currently being analyzed to deduce helium migration distances and critical cavity sizes for the transition from gas driven to bias-driven cavity growth [33]. Moreover, studies involving various helium implantation schedules are testing for instantaneous versus average He/dpa ratio effects[34,35]. These have a strong bearing on spectral tailoring experiments in mixed-spectrum fission reactors. For alloys containing little or no nickel there is a pressing need, regarding correlation between neutron and CP results, for neutron irradiation experiments on low and high temperature helium preinjected specimens. Additional work with the ion beams to look at nickel doping effects is now in progress. (The purpose of the nickel doping is to produce helium in non-nickel-bearing alloys irradiated in mixed spectrum reactors.) Studies of helium diffusivity from thermal diffusion and collisional processes using "selected area" helium implantation techniques are also needed.

3.8 Acceleration of Kinetic Processes with Different Dependencies on Atomic Displacement Rate and Temperature

This topic currently poses the greatest obstacle in attempting to correlate CP and fast neutron data in complex alloys. We have already briefly described some extreme rate (flux) effects in section 3.6 that are related to changes in the basic point defect annealing processes at very high rates. Additional effects are expected in complex alloys because their response to irradiation depends on a balance between a number of competing processes that can depend in different ways on temperature, time and the radiation produced point defect fluxes.

One example is the likelihood that the kinetics governing the diffusion of the different elements are altered in different ways by radiation and temperature; the evolution of the radiation damage microstructure may follow different paths for different damage rates. It is not necessarily possible in such a system to adjust for the damage rate by a simple temperature shift. Other examples of processes that may affect the damage microstructure evolution are precipitate, void and bubble nucleation, point defect-impurity trapping, and diffusion of point-defect impurity bound complexes. In a complex alloy, such as an austenitic stainless steel, the evolutionary path followed by the alloy is determined by a balance between a number of such processes. A sufficiently large change in either temperature or damage rate can alter this balance in such a way that an entirely different path (e.g. a different sequence of precipitation) is followed. A primary goal of the DAFS damage correlation effort is to establish the temperature and damage rate (flux) limits within which a particular damage sequence is followed, at least for variations in rate (flux) for different neutron experiments.

A complication that arises in pursuing such studies is the existence of chemical composition fluctuations. In complex alloys, it is not uncommon for variations in composition and initial microstructure to exist in

regions tens or hundreds of microns in extent. The primary tool for evaluating damage microstructure evolution in both CP and neutron irradiated samples is transmission electron microscopy (TEM) which examines a region less than a micron thick and a few tens of microns in extent. It is, therefore, essential that local chemistry variations are avoided in correlation experiments. It has been found that repeated CP experiments on small homogeneous laboratory melts conducted over a period of four years yield consistently identical results. However, repeat experiments on 316 SS and titanium modified 316 SS materials in the OFE program have not shown such reproducibility. In order to make meaningful comparisons between neutron and CP experiments or experiments at different rates or temperature, it is essential to either control the homogeneity of the alloy or to characterize the local chemistry of the region from which data were taken, and compare only regions with identical local chemistry.

3.9 Introduction of Stresses During Ion Implantation

An unavoidable consequence of stopping ions in solids is the introduction of centers of dilatation. The undamaged and undoped regions lying beneath and sometimes outside the beam area (if a mask is used) provide a constraint. This can result in theoretically-calculated values of lateral stress sufficiently high to perturb some kinetic processes[36,37]. The problem is mitigated in the case of very high energy ions which pass completely through thin specimens. This is not the way most CP experiments are conducted, however, because of a large number of considerations (very low dpa rates, induced radioactivity, temperature control problems, cost, etc.). In the DAFS program there has been an attempt to both include stress as a significant variable during implantation of helium (i.e. U.-Va. experiments[38]) and to minimize the effect of internally generated stresses in the heavy ion (dual ion) experiments. The latter is accomplished by limiting experiments to low damage levels (low concentrations of implanted ions), sectioning specimens so that data can be taken from a region that could experience appreciable

stress relief from displacement processes above and below it, and (for one laboratory[19]) bathing one entire surface of the specimen with the beam.

This is an area of active investigation at a number of laboratories involved in PMI research activities and at others not connected with OFE activities. It is one of the key areas in understanding and predicting blistering and flaking effects in tokamak near-plasma components. Moreover, the issues of the effects of stress and stress gradients on radiation damage, and the relief of stresses by radiation enhanced creep, are critical to first wall design and the need to resolve these issues is independent of the need to correlate neutron and CP results. In addition, the successful application of ion beams to modify surface-sensitive properties of metals, ceramics, polymers, etc. will require detailed knowledge of the lateral stress build-up accompanying ion implantation. The principal difficulty is the experimental determination of stress and strain levels in very thin layers. Various methods have been proposed[39,40] but at present it is difficult to deduce more than the average integrated lateral stress. Nevertheless, many laboratories are working hard on this problem. The needed information on the magnitude of induced stresses and effects of externally applied stress on microstructure can be anticipated within the next few years.

3.10 Interfaces Between Modeling Efforts and Charged Particle Research

A good interface between CP research and theoretical modeling efforts will be required if both tools are to be used to the maximum possible extent. This is implicit in the generally accepted philosophy that one of the major functions of CP research is to provide mechanisms and parameters needed for modeling efforts. Further, almost all interpretation of charged particle data requires physical models, albeit often qualitative and manifested in terms of "assumptions". Often because of many competing and interacting mechanisms interpretations are not unique; this situation must be clearly recognized. Unfortunately, modeling directed at CP data

analysis and utilization has been insufficient; in part this stems from limited data and its association with potential atypical variables and in part a poor theoretical understanding of complex, real-world phenomena.

A most important goal of future modeling efforts should be to make a local inventory of the transport of various constituent species of interest (i.e. vacancies, interstitials, alloying elements and transmutants such as helium)[41]. Since the transport and consequential reactions are basically kinetic phenomena, such analysis has often used so-called rate theory to take such inventories; unfortunately, due to the inherent complexity of such phenomena, most models to date are highly approximate and incomplete. For example, many studies have been solely focussed on the accumulation of vacancies in clusters (i.e. void swelling) and have neglected often important evolutionary processes such as dislocation structures and microchemistry. Other approaches to modeling have been more empirical and properly focussed on particular mechanisms such as the helium inventory algorithm developed by the W-R&D[42].

In several cases, particularly for simple metal alloys, the models (both theoretical and semi-empirical) have been reasonably successful in predicting several major trends[43]; in other cases, particularly for complex materials, the models have had more limited success[9]. Much more work in the area of compositional/phase stability/local microchemical mass balances is needed.

Nevertheless, such efforts and improvements in turn offer the best verifiable framework of understanding[44]. It must be noted that the lack of quantitative understanding of underlying physical mechanisms is also a serious obstacle to interpreting and correlating neutron data and is a major motivation for CP research. As in the case of neutron research, a more intensive iterative cycle of modeling and experiment is required.

Finally, the bottom line on fusion materials behavior is mechanical properties; clearly, microstructure-property modeling will be needed to exploit CP research in a meaningful way with respect to mechanical behavior.

4. PROSPECTS FOR SHORT-TERM IMPACT OF CHARGED PARTICLE RESEARCH ON TOKAMAK FIRST-WALL MATERIALS DEVELOPMENT

Since their inception, the dual-ion and charged particle irradiation studies in the DAFS program have emphasized detailed studies of damage mechanisms. These studies take advantage of the ability to carefully control the irradiation variables that is characteristic of the CP technique. In most of the work, the emphasis has been on studying the effects of helium on the damage evolution process. This is motivated by the fact that the helium generation rate is a variable which is most difficult to control in reactor irradiations, and the one where fission reactor conditions deviate most significantly from the mgnetic fusion reactor (MFR) environment. Because of the issues discussed above, this work is usually characterized as "long term" research which will increasingly pay off only as phenomena such as helium effects become better understood and can be incorporated into quantitative radiation damage models. There is, however, a short-term benefit to be realized from these experiments. In particular, they can provide important insight in guiding and evaluating the various simulations being carried out using neutron sources. Clearly, anything that helps to guide expensive neutron experiments and planning for faclities, or test of correlation assumptions, can have enormous impact in the short run.

A good example of this is found in a recent effort to analyze the available CP and neutron irradiation data base for purposes of assessing the effect of the He/dpa ratio for developing fission fusion correlations for swelling in 316 stainless steel[45]. The collective results of the CP studies showed a suprising degree of mechanistic consistency with the more

limited neutron data and strengthened the interpretations of these results. In particular, the analysis suggested that the response of swelling to changes in the He/dpa ratio may not be monotonic; and that neutron environments such as the High Flux Isotope Reactor (HFIR), which has a very high He/dpa ratio, and the Experimental Breeder Reactor-I (FBR-II), which has a low He/dpa ratio, may not result in swelling behavior which bounds that for intermediate He/dpa ratios characteristic of a MFR environment. Further, the charged particle data and the mechanisms it highlighted was used to guide the construction of a physical model; the model was then calibrated to the neutron data and used to interpolate to fusion conditons. More significantly, this analysis has led to the identification of additional experiments to test the assumptions underlying the correlation procedures.

Another important example is the need to evaluated helium mobility. Both theory and experiment suggest this variable may be a very important factor as in governing much of microstructural evolution. Thus, "incubation", initial transients in swelling, the scale of loop and cavity nucleation, precipitate-cavity association, segregation, and migration of helium to grain boundaries appear to be strongly affected by helium mobility.[45] Even if some macroscopic properties are not terribly sensitive to helium and helium mobility per-se (perhaps gross swelling in some temperature-dpa regimes), other properties are likely to be very sensitive, e.g., creep rupture behavior. Charged-particle techniques offer excellent flexibility and unique capabilities for evaluating helium partitioning to sinks and obtaining upper and lower bounds in helium migration rates. Using spatially inhomogeneous helium doping (implanting through masks), beam scheduling experiments, and deliberate and controlled temperature changes during irradiation, such experiments provide a powerful means of deducing helium mobilities. On this one point alone the CP studies can have an important near term impact.

Another important example that needs to be highlighted is the demonstration of the limitations imposed on microstructural data from material inhomogeneity constraints discussed previously in section 3.8. First it may be argued that this is a limitation not shared in neutron experiments on bulk mechanical properties which integrate over microscopic variabilities. However, it should be realized that 1) such inhomogeneities do confound fundamental microstructural interpretation of any data set and make extrapolations uncertain, and 2) one direction of alloy development may be to try to produce more homogeneous alloys. The point here is that a very practical issue, homogeneity of the OFE reference program materials, is being raised, in large part as a result of findings in the CP studies. The question is of immediate importance to both DAFS and Alloy Development for Irradiation Performance (ADIP) efforts.

Second, the ability to control the local composition of alloys through implantation microalloying techniques may allow systematic exploration of the competing and interactive effects of microstructural and microchemical evolution in ways not possible using other techniques. This is an area of considerable current controversy, which is strongly flavoring the philosophical approaches to developing fission-fusion correlations in the DAFS program; hence, such studies could have important and far reaching near term impacts on the direction of both DAFS research and selection among alternate data correlations.

Other examples of potential impact of CP work on short-term needs are not difficult to find. Such examples would include: low dose, low temperature effects of microstructure, microchemistry and helium and hydrogen partitioning; the effects of pulsing (dpa, temperature and stress); the effects of adding nickel to enhance (n,α) reactions in HFIR and Oak Ridge Research Reactor (ORR) experiments; and history effects (temperature, flux) on transient phenomena (void incubation, helium bubble growth, microchemistry changes).

The question of whether CP results can be used more directly in engineering data correlations in the near term is more difficult to answer. We note, however, that the goals themselves tend to change on a fairly short time scale. In a somewhat arbitrary fashion then we will define near-term to be less than 5 years, intermediate term as 5-10 years, and long-term to be 10 or more years from now.

In the near-term, CP results will probably not be used directly for fusion engineering data correlations or predictions. (In fairness, it must be said that correlations between fission reactor and fusion reactor properties must themselves face a serious test.) This reflects the need to use models to relate microstructural information or mechanical property data in atypical environments to the mechanical response of the same material under first wall conditions. Simply stated, existing models and data are inadequate. It is thus unlikely that attempts to develop engineering design data from CP results alone within the short-term will prove to be a wise expenditure of money and effort. The short-term benefit from CP studies is thus the insight on mechanisms. However, continuation of these studies has the potential to more direct utilization in the intermediate term. For example, if pulsing effects prove to be significant, the only experimental basis for including them in data correlations will probably be CP studies. While much remains to be done to "calibrate" this tool, the prospect for important long-term impact of CP studies appears to be great. Many laboratories are working on the fundamental issues discussed above for a variety of reasons. Successful delineation of these phenomena and translation of them to fusion reactor conditions will greatly enhance the usefulness of data from both current and future CP research. It will also permit studies of alloy systems not readily amenable to experiments in fission or mixed spectrum environments. It is doubtful that a fusion materials test reactor can be designed and constructed within the 10 years or so it may take to develop the interpretational tools needed for CP studies. Continuity of effort in terms of such experiments and model development should yield an important

return in the long run in the form of well-designed, economically attractive first wall materials.

5. PROGRAM COORDINATION

What emerges from the preceeding considerations of the historical applications of CP techniques, their advantages and limitations, the prognosis for a continual improvement in correlating CP and neutron conditions and their unique capabilities in addressing important DAFS needs are the following:

1. There is a need for continual CP program co-ordination and a definable modeling effort. It is recommended that at a minimum, an ad hoc task group meet about twice a year including Basic Energy Sciences (BES), PMI, implantation metallurgy, and surface engineering and theoretical support group participation. At least one DAFS program should include a component to follow closely progress in BES* and other programs input to the DAFS effort.

2. The coordinated CP effort should always be addressing simultaneously 1) conditions unique to the fusion environment, 2) identification of accessible damage regimes, and 3) basic correlation between CP and fast neutron effects. All three items are compatible with DAFS needs, existing experimental capabilities, participating laboratory philosophies and common sense.

---

*The contribution of the BES-funded programs (at ORNL and BNWL) should be emphasized. In several cases the work has been targeted directly at issues relating to helium effects and pulsing which are of immediate interest to fission-fusion correlation efforts.

One example of a recent initial ad hoc group effort is shown in the following flow charts. From this exercise it is a short step to the development of a coordinated test matrix and detailed milestone tasks in proposals or work schedules. It should be pointed out that much of this effort is already in place in the DAFS program. The principal difference is the construction of an explicit (written) coordinated program rather than the informal, implicit one already in place. Better coordination plans may be possible and clearly can evolve from the existing base. However, this requires a stable commitment of reasonable resources and a continuing, disciplined effort to resolve the fundamental underlying issues.

1. Direct Correlation between Charged Particle and Neutron Irradiations

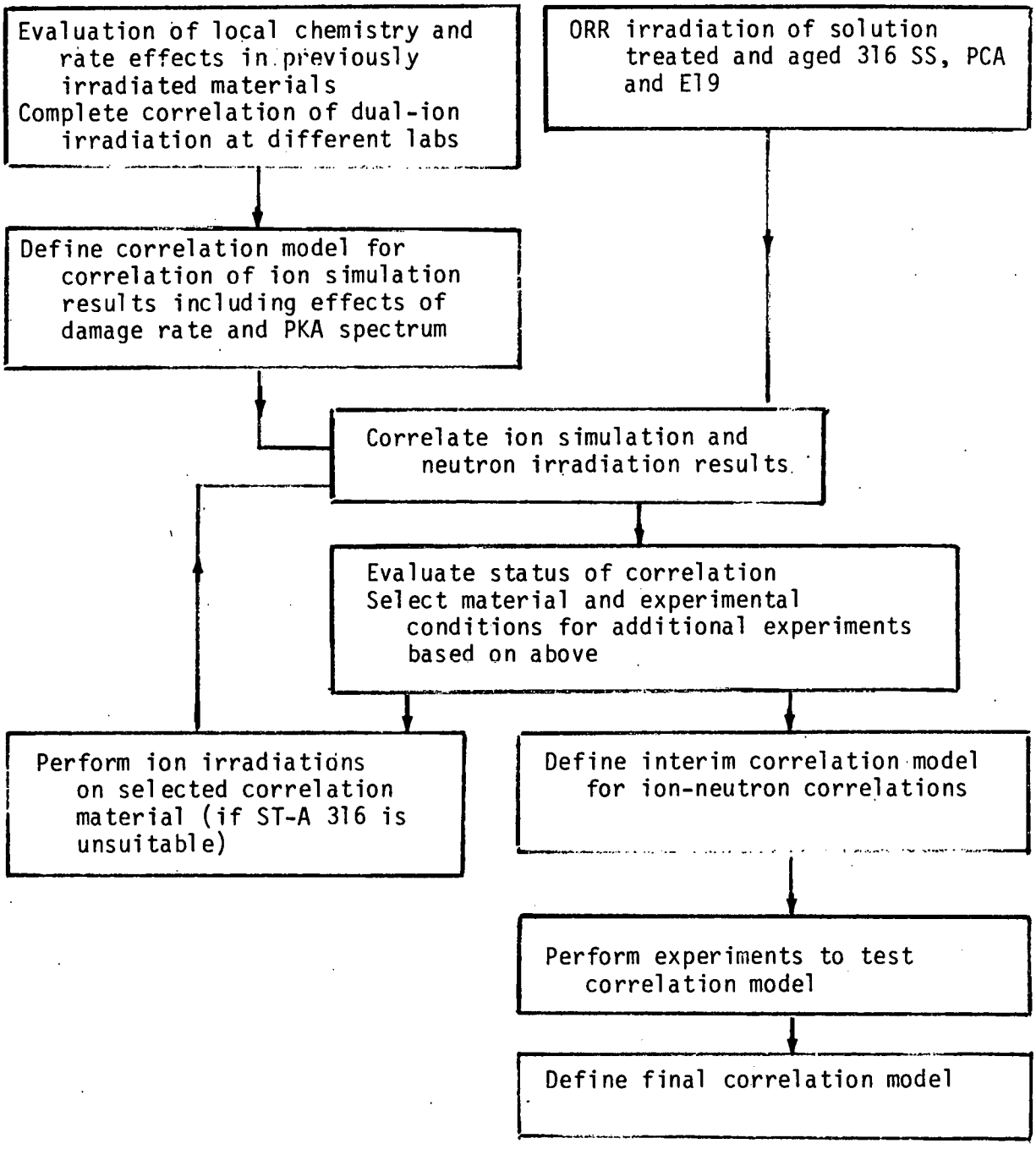

2. Identification of Damage Mechanism Regimes

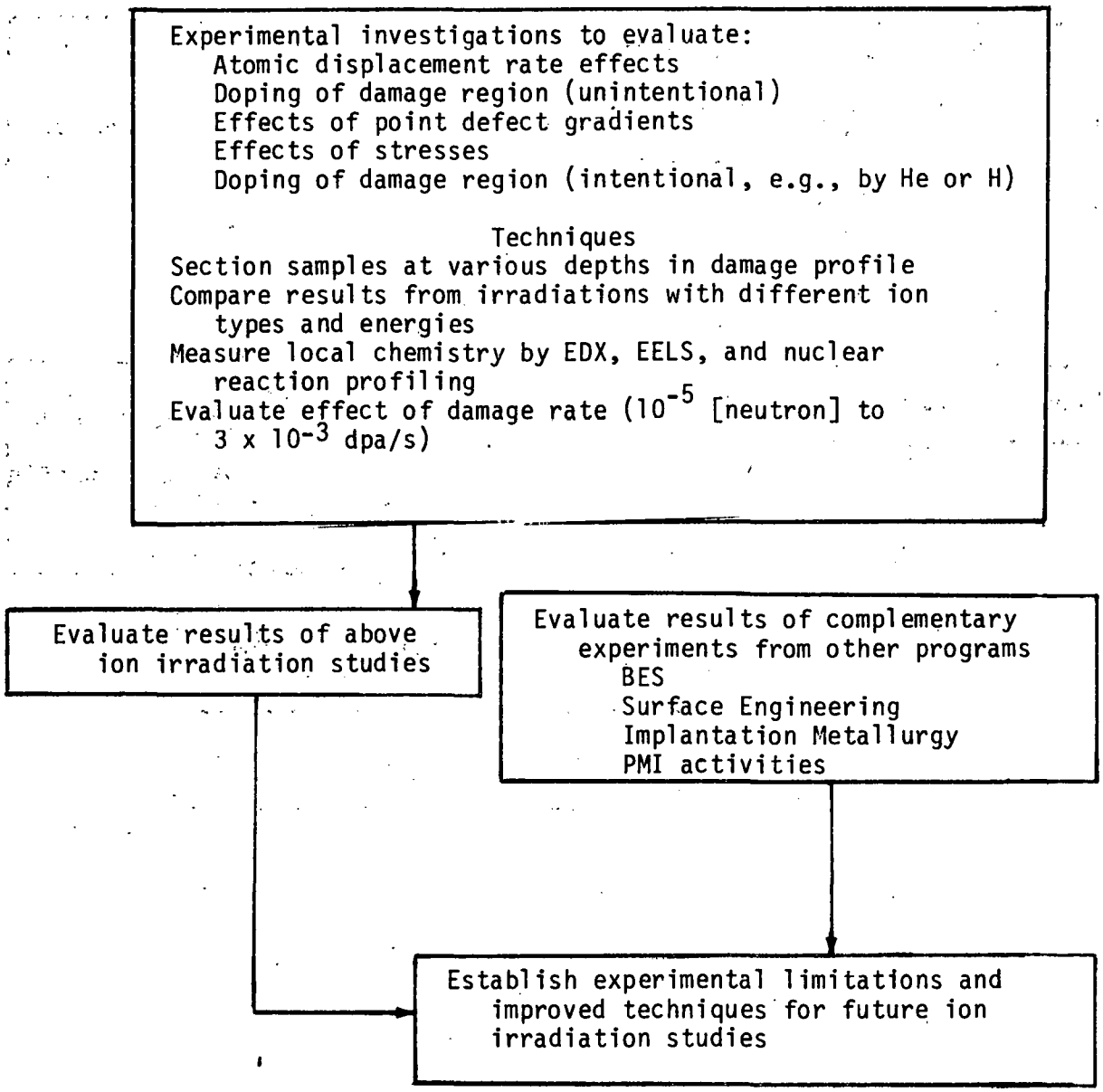

3. Evaluation of Conditions Unique to the MFR Environment

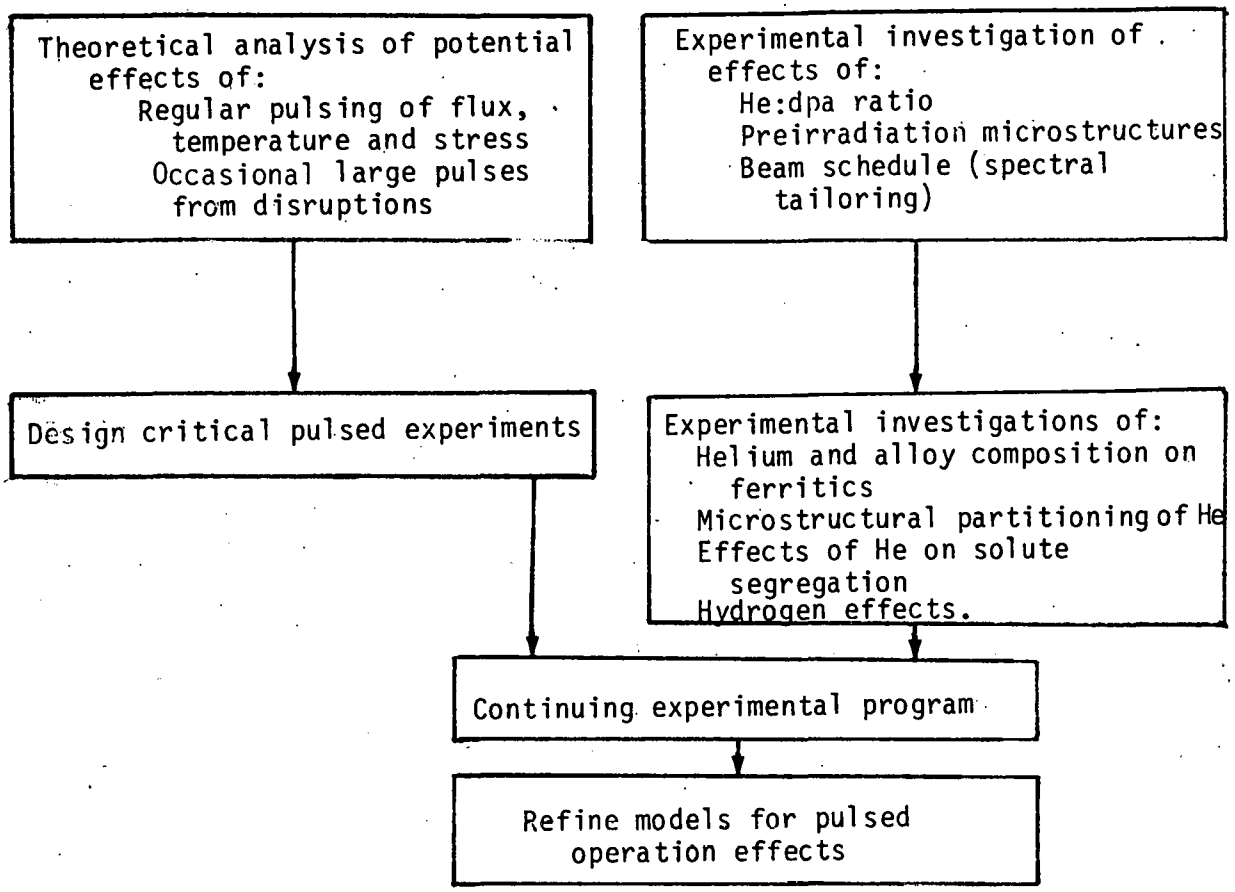

REFERENCES

1. ASTM Standard Recommended Practice for Neutron Radiation Damage Simulation by Charged-Particle Irradiation - Part A, ASTM E521-77. Annual ASTM Standards Part 45, 1087 (1980).

2. ASTM Standard Recommended Practice for Neutron Radiation Damage Simulation - Part B (under ballot).

3. Proceedings of the Third International Conference on Plasma Surface Interactions in Controlled Fusion Devices, G.M. McCracken, P.E. Scott and M.W. Thompson, eds., J. Nucl. Mater., 76 & 77, (1978).

4. R.S. Nelson, D.J. Mazey and J.A. Hudson, J. Nucl. Mater. 37, 1 (1970).

5. Proceedings of the International Conference on Radiation-Induced Voids in Metals, J.W. Corbett, L.C. Ianniello, eds., USAEC CONF-710601 (1972).

6. W.G. Johnston, T. Lauritzen, J.H. Rosolowski and A.M. Turkalo, eds., Properties of Reactor Structural Alloys After Neutron or Particle Irradiation, ASTM STP 570, American Society for Testing and Materials, 525 (1975).

7. P.R. Okamoto, A.T. Santhanam, H. Weidersich, and A. Taylor, Nucl. Technol. 22, 45 (1974).

8. T.R. Anthony, Phys. Rev. B 2, 264 (1970).

9. Proceedings of the Workshop on Correlation of Neutron and Charged Particle Damage, J.O. Stiegler, ed., ERDA CONF-760673 (1976).

10. A.F. Rowcliffe, E.H. Lee and P.S. Sklad, Proceedings of the Symposium on Irradiation Behavior of Metallic Materials for Fast Reactor Components, June 5-14, 1979, Ajaccio, Corsica.

11. E.H. Lee, P.J. Maziasz and A.F. Rowcliffe, Irradiation Effects on Phase Stability", J.R. Holland, L.K. Mansur and D.I. Potter, eds., 191

12. F.A. Garner, Ibid 165.

13. "Proceedings of the Workshop on Solute Segregation and Phase Stability During Irradiation," J.O. Stiegler, ed., J. Nucl. Mater. 83, No. 1 (1979).

14. J.A. Spitznagel, F.W. Wiffen and F.V. Nolfi, J. Nuc. Mater. 85 & 86, 629 (1979).

15. Treatise on Materials Science and Technology Ion Implantation, 18, J.K. Hirvonen, ed., , Academic Press, New York (1980).

16. A.D. Brailsford and L.K. Mansur, J. Nucl. Mater. 71, 110 (1977).

17. W. Möller, Th. Pfeiffer and M. Schluckebier, Nucl. Inst. & Methods, 182/183, (1981).

18. H. Takaku, M. Tokiwai, H. Kayano, Y. Higashiguchi, M. Narui, Y. Suzuki and K. Matsuyama, J. Nucl. Mater. 80, 57 (1979).

19. J.A. Spitznagel, W.J. Choyke, "Radiation Response of Materials", Westinghouse Research Laboratories Report #77-9D2-FUMAT-R2, Contract #EG-77-C-02-4467.A000 (1977), (copies available from ORNL Technical Information Center).

20. F.A. Garner and L.E. Thomas, Effects of Radiation on Substructure and Mechanical Properties of Metals and Alloys, J. Moteff, ed., ASTM STP 529, 303 (1973).

21. S. Wood, Westinghouse Electron Corporation R&D Center, unpublished research (1981).

22. W.J. Choyke, J.A. Spitznagel, J.N. McGruer and J.S. Lally, J. Nucl. Mater. 74, 303 (1978).

23. A.D. Marwick, R.C. Piller and P.M. Sivell, J. Nucl. Mater. 83, 35 (1979).

24. K. Farrell, Oak Ridge National Laboratory, unpublished research (1980).

25. S.M. Meyers, "Implantation Metallurgy-Equilibrium Alloys", Treatise on Materials Science and Technology Ion Implantation, 18, J. Hirvonen, ed., 51, Academic Press (1980).

26. R.M. More and J.A. Spitznagel, "Primary Recoil Spectra and Subcascade Effects in Ion Bombardment Experiments", Radiation Effects, (in press).

27. F.W. Wiffen and J.O. Stiegler, Proceedings of the Second ANS Topical Meeting on the Technology of Controlled Nuclear Fusion, G.L. Kuncinski, ed., USERDA CONF-760935-p. 1, 135 (1976).

28. A.N. Goland, J. Nucl. Mater., 85 and 86, 453 (1979).

29. J.H. Chang, W.J. Choyke, et al., "Experimental Evidence for a Slight Mass Dependence of the Final Damage State Due to Energetic Ions", Radiation Effects (in press).

30. R.L. Simons, DAFS Quarterly Progress Report, July-September 1980, DOE/ER-0046/3, 42 (1981).

31. G.R. Odette and T.O. Ziebold, Nucl. Sci. and Engr. 49, 72, (1972).

32. L.K. Mansur, W.A. Coghlan, A.D. Brailsford J. Nucl. Mater. 85 & 86, 591 (1979).

33. J.A. Spitznagel, S. Wood and W.J. Choyke, DAFS Quarterly Progress Report, January-March 1980, DOE/ER-0046/1, 182 (1980).

34. W.J. Choyke, J.A. Spitznagel, S. Wood, N.J. Doyle, J.N. McGruer and J.R. Townsend, Nucl. Inst. Methods 182/183, 489 (1981).

35. A. Turner, J.A. Spitznagel, G. Ayrault and S. Wood, Proceedings of the DAFS Information Meeting, October 2-3, 1980, Germantown, M.D., 298 (1981).

36. F.A. Garner, G.L. Wire and E.R. Gilbert, Proceedings of the Conference on Radiation Effects and Tritium Technology for Fusion Reactors, J.W. Watson and F.W. Wiffen, eds., ERDA CONF-750989, 1, 474 (1976).

37. B.O. Hall, J. Nucl. Mater. 63, 285 (1976).

38. J.I. Bennetch, J.A. Horton and W.A. Jesser, DAFS Quarterly Progress Report, January-March, 1979, DOE-ET-0065/5, 237 (1979).

39. V.S. Speriosu, H.L. Glass, and T. Kobayashi, Appl. Phys. Lett. 34(9), 539 (1979).

40. E.P. Eernisse and S.T. Picraux, J. Appl. Phys. 48-1, 9 (1977).

41. G.R. Odette, Journ. Nucl. Mat. 85 & 86, 533 (1979).

42. J.A. Spitznagel, S. Wood and W.J. Choyke, DAFS Quarterly Report, DOE/ER-0046/2, April-June, 103 (1980).

43. N.H. Packan, K. Farrell and J.O. Stiegler, J. Nucl. Mater. 78 143 (1978).

44. The Fusion Reactor Materials Program Plan Section II, Damage Analysis and Fundamental Studies DOE/ET-0032/2, July (1978).

45. G.R. Odette, P.J. Maziasz and J.A. Spitznagel, "Fission-Fusion Correlations for Swelling and Microstructure in Stainless Steels: Effect of the Helium to Displacement Per Atom Ratio", elsewhere in this report; also to be published in the Proceedings of the Second Topical Meeting on Fusion Materials, Seattle, WA, August 1981.

DISTRIBUTION

UC-20 (119)

UC-20c (77)

DOE-HQ/Office of Reactor
Research and Technology
NE-530
Washington, DC 20545

PB Hemmig, Safety & Physics

DOE-HQ/Office of
Fusion Energy (2)
Washington, DC 20545

JF Clark, ER-70
JF Decker, ER-54, G-256

DOE-RL/Office of Asst Manager For
Projects and Facilities Management (2)

GM Chenevert, FMITPO

DOE-RL/Office of Asst Manager
for Advanced Reactor Programs

AR DeGrazia, Physical Scientist,
Technology Development

Argonne National Laboratory (5)
9700 South Cass Avenue
Argonne, IL 60439

LR Greenwood
A. Taylor
RE Nygren
APL Turner
H. Wiedersich

Battelle Memorial Institute (3)
Pacific Northwest Laboratory
P.O. Box 999
Richland, WA 99352

JL Brimhall
DA Dingee
TD Chikalla

Brookhaven National Laboratory
Associated Universities
Upton, Long Island, NY 11973

Chairman, Nuclear Energy Dept

Columbia University
Plasma Physics Laboratory
New York, NY 10027

RA Gross

General Atomic Company (2)
P.O. Box 81608
San Diego, CA 92138

GR Hopkins
JR Gilleland

INESCO
11011 Torreyana Rd
San Diego, CA 92121

RD Stevenson

Lawrence Livermore Laboratory (2)
P.O. Box 808
Livermore, CA 94550

MW Guinan
CM Logan

Los Alamos National Laboratory (2)
P.O. Box 1663
Los Alamos, NM 87544

DJ Dudziak
CR Emigh

Massachusetts Institute of Technology (5)
77 Massachusetts Avenue
Cambridge, MA 02139

L. Lidsky
NJ Grant, 8-305
JB Vander Sande, 13-5025
I-W Chen, 13-5118
DB Montgomery, NW21

DISTRIBUTION (Cont'd)

Massachusetts Institute of Technology
Nuclear Reactor Laboratory
138 Albany St
Cambridge, MA 02139

OK Harling, NW12-204

McDonnell-Douglas Astronautics Co.
P.O. Box 516
St. Louis, MO 63166

D. Kummer

Mound Laboratory
P.O. Box 32
Miamisburg, OH 45342

Manager, Tech Appl & Dev

National Bureau of Standards
Gaithersburg, MD 20760

CD Bowman

Naval Research Laboratory (3)
Washington, DC 20375

I. Manning, Code 6672
JA Sprague, Code 6395
LE Steele, Code 6390

North Carolina State University
Department of Nuclear Engineering
Raleigh, NC 26707

JR Beeler, Jr.

Oak Ridge National Laboratory (7)
P.O. Box X
Oak Ridge, TN 37830

Director, Thermonuclear Div,
(Bldg 9201-2)
M. Roberts, Bldg 9204-1
FG Perey C. Weisbin
J. Sheffield FW Wiffen
JO Stiegler

Princeton University (2)
Plasma Physics Laboratory
Forrestal Campus
P.O. Box 451
Princeton, NJ 08544

K. Wakefield
H. Furth

Rockwell International
8900 DeSoto Ave
Canoga Park, CA 91304

D. Kramer

Sandia Laboratories (2)
P.O. Box 5800
Albuquerque, NM 87185

FL Vook, Org 5100

Sandia Laboratories
Livermore, CA 94550

WU Wilson

University of California
Los Angeles, CA 90024

RW Conn

University of Michigan
Nuclear Engineering
Ann Arbor, MI 48109

T. Kammash

University of Missouri
Mechanical & Aerospace Engineering
1006 Engineering Bldg
Columbia, MO 65211

M. Jolles

DISTRIBUTION (Cont'd)

University of Virginia
Dept of Materials Science
Charlottesville, VA 22901

WA Jesser

University of Wisconsin
1500 W. Johnson Drive
Madison, WI 53706

WG Wolfer

Westinghouse
Advanced Reactors Division
P.O. Box 158
Madison, PA 15663

A. Boltax

Westinghouse
Research and Development Center (2)
1310 Beulah Road
Pittsburgh, PA 15235

S. Wood
JA Spitznagel

Commission for the European Communities
200, Rue de la Loi
B-1049 Brussels, Belgium

J. Darvas

(ECN)
Energieonderzoek Centrum Nederland
Westerdionweg 3
NL-1755 ZG Petten, NH, The Netherlands

B. Van Der Schaaf

(EIR)
Swiss Federal Institute
For Reactor Research
CH-5303 Wuerenlingen, Switzerland

WV Green

EURATOM
Joint Research Center Ispra
Materials Science Division
I-21020 Ispra, Varese, Italy

P. Schiller

Hahn-Meitner Institute
fur Kernforschung
Glienickerstrasse 100
D-1000 Berlin,
Federal Republic of Germany

H. Wollenberger

Japan Atomic Energy Research Institute
Physical Metallurgy Laboratory
Division of Nuclear Fuel Research
Fukoku Seimei Bldg
2-2, Uchisaiwai-cho 2-chome, Chiyoda-ki,
Tokyo 100, Japan

K. Shiraishi

(KFA-IFF)
Kernforschungsanlage Jülich GmbH
Postfach 1913
D-517 Julich,
Federal Republic of Germany

H. Ullmaier

(KFK-IMF II)
Kernforschungsaniage Karlsruhe
Institüt für Reaktorbauelemente
Postfach 3640
D-7500 Karlsruhe 1,
Federal Republic of Germany

K. Ehrlich

DISTRIBUTION (Cont'd)

National Research Council
Montreal Road
Ottawa, Canada

EV Kornelson

Osaka University
Dept of Nuclear Engineering
2-1, Yamada-Oka, Suita,
Osaka, 565, Japan

K. Sumita

Science University of Tokyo
Engineering Dept
Kagurazaka, Shinjuku-Ku,
Tokyo, 162, Japan

RR Hasiguti

(SCK/CEN)
Studiecentrum voor Kernenergie
Centre d'Etude de l'Energie Nucleaire
Boeretang 200
B-2400 Mol, Belgium

J. Nihoul

HEDL (38)

HR Brager	W/A-64
WL Bunch	W/B-47
LL Carter	W/B-47
DG Doran (5)	W/A-57
EA Evans	W/C-23
FA Garner	W/A-57
DS Gelles	W/A-64
R. Gold	W/C-39
HL Heinisch	W/A-57
DL Johnson	W/A-4
GD Johnson	W/A-65
NE Kenny	W/C-115
FM Mann	W/A-4
WN McElroy	W/C-39
EK Opperman	W/A-58
NF Panayotou	W/A-65
EF Parker	W/E-17
RW Powell	W/A-64
RJ Puigh	W/A-58
FH Ruddy	W/C-39
FA Schmittroth	W/A-4
WF Sheely	W/C-62
RL Simons	W/A-57
AL Trego	W/E-15
GL Wire	W/A-58
HH Yoshikawa	W/C-44
Central Files (5)	W/C-110
Publ Services (2)	W/C-115
Doc Management	W/C-125

Tokyo Institute of Technology
12-1, 2-Chome, O-Okayama
Meguro-Ku, Tokyo, Japan

K. Kawamura

(UKAEA-Harwell)
United Kingdom Atomic Energy Authority
Atomic Energy Research Establishment
Metallurgy Division
Building 388
Oxfordshire, OX11 ORA, UK

DR Harries

University of Tokyo (3)
Bunkyo-ku,
Tokyo 113, Japan

Naohira Igata
Shiori Ishino
Taijiro Uchida